RESPONSE OF ISOLATED AND INTERFERING SHALLOW FOOTINGS ON SLOPES

A Thesis

Submitted in Partial Fulfillment of the Requirements

for the Degree of

DOCTOR OF PHILOSOPHY

by

Rana Acharyya

Department of Civil Engineering

Indian Institute of Technology Guwahati

Guwahati – 781039, India

February 2019

STATEMENT

I do hereby declare that the matter embodied in this thesis is the result of investigations carried out by me in and with the aid of the Department of Civil Engineering, Indian Institute of Technology Guwahati, Assam, India.

In keeping with the general practice of reporting scientific observations, due acknowledgements have been made wherever the work described is based on the findings of other investigators.

Date: **(Rana Acharyya)**

Place: IIT Guwahati

CERTIFICATE

This is to certify that the thesis entitled **"Response of Isolated and Interfering Shallow Footings on Slopes"** submitted by **Rana Acharyya,** Roll No. 136104007, to the Indian Institute of Technology, Guwahati, for the award of the degree of Doctor of Philosophy in Civil Engineering is a record of bonafide research work carried out by her under my supervision and guidance. The thesis work, in my opinion, has reached the requisite standard fulfilling the requirement for the degree of Doctor of Philosophy.

The results contained in this thesis have not been submitted in part or full to any other University or Institute for award of any degree.

Date:

Place: IIT Guwahati

(Dr. Arindam Dey)
Associate Professor
Department of Civil Engineering
Indian Institute of Technology Guwahati
Guwahati-781039, India

ACKNOWLEDGMENTS

I owe my sincere gratitude to a number of persons whose unending support and patronage enabled me to pursue my research studies and submit the thesis for PhD. First and foremost, I would like to express my heartfelt thanks and deep sense of gratitude to my thesis supervisor and research guide Dr. Arindam Dey, for his meticulous guidance, encouragement, patience and support during my entire PhD study. I am grateful to him for sparing his precious time and efforts throughout the entire work. I am highly obliged to him for all the insightful discussions, affection and kind suggestions, which helped me to complete the work successfully. I have been fortunate and blessed enough to have him as my research guide, whose able guidance and valuable advice will help me a long way in moulding my future career.

My gratitude is extended to doctoral committee members Prof. S. Sreedeep, Prof. Anjan Dutta and Prof. S. Kanagaraj for reviewing my work and providing their valuable inputs that helped in improving my thesis. I would like to express my gratitude to Prof. Krishna Reddy (University of Illinois, Chicago) and Dr. Bappaditya Manna (IIT Delhi) for their contribution in reviewing my thesis and helping it to improve the quality of the same. I would like to express my deepest thanks to Dr. Mousumi Mukherjee (IIT Mandi) for helping in research and modifying the thesis. I would also like to thank the other faculty members of Geotechnical engineering of Civil Engineering Department for their suggestions and support during my PhD. I owe great thanks to the staffs of Geotechnical Engineering, Mr. Hariram Upadhyay, and Mr. Samarjyoti Kalita for kind help in conducting the research. I thank all office staffs of Civil Engineering Department for their help and cooperation in pursuing my work.

I would also sincerely like to thank my friends Nishant, Ardhendu, Dooradarshi, Biplab, Prasun, Joy, Abhishek, Arghadeep Dada, Shankar Dada, Jumrik Didi, Sudheer, Chiranjib, Yagom, Madhulisha, Madhulatha, Sandipan, Mani, Bibhas, Dipjyoti, Janarul, Chinu, Priyanka, Debasmita, Pradeep and many others for their companionship, support and encouragement.

Lastly, but most importantly, I want to acknowledge the greatest supports, love and encouragements received from my parents, my wife (Sulata) and my elder sister (Chaitali) without whom it would never be possible.

Finally, I thank the Almighty for this enriching journey.

Date: **RANA ACHARYYA**

ABSTRACT

This dissertation reports about the overall response of isolated and interfering shallow footings located on or near the slope. 2-D and 3-D Finite element analyses have been resorted to for conducting the numerical investigations for deciphering the bearing capacity and failure mechanisms of the foundations located on slopes. Foremost, the ultimate bearing capacity and failure pattern of square footing resting on dry sandy-soil slope has been investigated by altering the various geotechnical and geometrical parameters. Further recognizing the prevalent presence of c-φ soils in most of the hilly terrains, the study was extended for the square footings resting on such sloped. Apart from square footing, strip footing being the other most common typology of shallow foundations for buildings in hill-slopes, the previous study was further extended to recognise the bearing capacity and failure mechanism of the same. Considering the practical scenarios of building construction in the hill-slopes, it was revealed that single isolated strip or square footing does not represent the building foundation characteristics. In this regard, the impact of interference of strip footings located on crest of c-φ soil slope on their bearing capacity and failure mechanisms has been examined. In all the simulations of various typologies, the influence of the geotechnical and geometrical parameters were vividly studied. With the aid of ANN technique, the quantitative influences of the geotechnical and geometrical parameters were used to develop expressions for bearing capacity prediction. These expressions can serve as a ready-made handy tool for the geotechnical engineers for assessing the bearing capacity of isolated and interfering shallow footings located on the hill-slopes. Additionally, ANN technique had been further used to provide importance ranking of the influencing parameters. Such ranking would help the geotechnical engineers to give due attention to the important parameters while designing and constructing foundations on slopes. Further, with the aid of a case study, the overall stability of a hill-slope supporting an electric transmission tower had been investigated. Based on the outcomes, recommendations to

enhance the bearing capacity commonly adopted isolated footings has been provided through the application of alternative typologies of interconnected shallow footings. The study has been further extended to study the bearing capacity of complex arrangement of shallow footings that may be suitably adopted to harness their benefit of enhanced bearing capacity and lessened outward deformation of slope when placed on the crest of a slope. Finally, the influence of flow-rules (associated and non-associated) and soil dilatancy has been inspected on the bearing capacity, displacement and failure mechanism of strip footing resting on horizontal ground as well as near the sloping ground. Such study aids in the understanding the practical conditions of bearing capacity of foundations on slopes as well as the overall failure mechanisms, which are left unaddressed by the conventional classical bearing capacity theories.

Keywords: Shallow footings on hill-slope; Finite Element modeling; Geotechnical and Geometrical parameter; Interference of footings; Artificial neural network; Bearing capacity predictions; Sensitivity and importance ranking; Flow-rules and soil dilatancy; Footing typologies

TABLE OF CONTENTS

CHAPTER 3: NUMERICAL MODELLING

CHAPTER 4: RESPONSE OF ISOLATED SHALLOW FOUNDATIONS ON SLOPES

CHAPTER 6: APPLICATION OF ARTIFICIAL NEURAL NETWORKS IN PREDICTING BEARING CAPACITY OF FOUNDATIONS ON SLOPES

CHAPTER 7: INFLUENCE OF VARIED TYPOLOGIES OF FOOTINGS LOCATED ON SLOPE CREST

CHAPTER 8: INFLUENCE OF DILATANCY ON FAILURE MECHANISM OF STRIP FOOTING RESTING ON HORIZONTAL AND SLOPING GROUND

LIST OF FIGURES

Figure No.	Figure Caption	Page No.
4.15	Convergence study for square footing resting on sloping ground comprising *c*-φ soil	97
4.16	Typical variation of q_u with cohesion (*c*) and setback ratio (*b/B*)	97
4.17	Typical variation of q_u with angle of internal friction (φ) and setback ratio (*b/B*)	98
4.18	Typical variation of q_u with unit weight of soil (γ) and setback ratio (*b/B*)	99
4.19	Typical variation of q_u with footing width (*B*) and setback ratio (*b/B*)	99
4.20	Typical variation of q_u with slope angle (β) and setback ratio (*b/B*)	100
4.21	Typical variation of q_u with unit weight of soil (D_f/B) and setback ratio (*b/B*)	101
4.22	Development of failure mechanism and interaction of slope face with the passive zones beneath the square footing for various setback ratios (*b/B*)	102
4.23	Typical convergence study for determining the optimum mesh element size	104
4.24	Validation of the 2D FE model with the aid of experimental outcomes	105
4.25	Comparison of pressure-displacement patterns obtained from numerical model and experimental model	105
4.26	Mesh convergence analysis for strip footing located at the crest of *c*-φ slope	107
4.27	Influence of cohesion of soil (*c*) on $q_u/\gamma H_s$	107
4.28	Influence of slope inclination (β) on $q_u/\gamma H_s$	108
4.29	Influence of footing width (*B*) on $q_u/\gamma H_s$	109
4.30	Influence of angle of internal friction of soil (φ) on $q_u/\gamma H_s$	110
4.31	Impact of embedment depth ratio (D_f/B) on $q_u/\gamma H_s$	110
4.32	Representative development of failure mechanisms underneath the footing for different setback ratios (*b/B*)	111
5.1	Typical convergence study for interfering strip footings resting on horizontal ground	123

Figure No.	Figure Caption	Page No.

LIST OF TABLES

CHAPTER 1

INTRODUCTION

1.1 General

The bearing capacity of the foundations is a primary concern in the field of foundation engineering. Design of foundations on a horizontal ground surface depends on the mechanical characteristics of the soil such as unit weight, shear strength etc., and the physical properties of the foundation such as its depth, width, and shape. There are two primary considerations to decide the allowable bearing pressures for shallow foundations; the safety factor against ultimate shear failure must be adequate and the settlements under allowable bearing pressures should not exceed tolerable limits. Several theories are available to predict the bearing capacity of foundations resting on or in level grounds (Terzaghi 1943; Meyerhof 1963; Hansen 1970; Vesic 1975; Michalowski 1997; Huang and Menq 1997). Several experimental studies have been carried with respect to footings resting on both unreinforced and reinforced horizontal grounds.

Foundations are sometimes located on slopes or near the edges of slopes. Examples of such practice are buildings or roads constructed in hilly regions (Figure 1.1) and electric transmission towers built on mountain slopes, foundations for bridge abutments resting on granular fill slopes. The bearing capacity of a foundation constructed near the edge of a slope assumes its importance in view of the fact that performance of the structure depends on the stability of the slope and the soil bearing capacity. As compared to the foundations constructed and resting on a horizontal ground surface, a shallow footing placed on top of a slope and subjected to a variety of loading (axial, inclined, eccentric, coupled moments or their combinations) experiences a reduction in ultimate bearing capacity (Meyerhof 1957; Shields et al. 1977; Bauer et al. 1981). This is primarily attributed to the incomplete development of the passive zone near the slope face, where there is not enough lateral restraint on the soil to resist it outward lateral movement.

Figure 1.1 Buildings right at the verge of steep slopes (Photo courtesy: Arindam Dey, 2015)

It is understood that the stability of a foundation located on or near a slope is affected by several factors. These factors include the location of footing, the loading pattern, the edge distance from the slope face, the slope angle, the depth of embedment of the foundation, the shear strength characteristic of the foundation soil and other environmental conditions (rainfall and saturation of the slope material). The loading characteristics play a vital role in the deformation and failure of the foundation on a slope in regard to their direction of application. Load acting towards the slope face will lead to a further reduction in the bearing capacity in comparison to the one acting away from the slope face. The more close a footing towards the face of the slope, the lesser is the lateral restraint over the soil movement taking place in the passive direction, and hence more jeopardized is the safety of the footing and the associated structure. A footing located on the crest of the slope near to the slope face will be more vulnerable to failure than the one which is located far away from the slope face, and beyond a particular edge distance, the effect of the presence of the slope face will be completely diminished.

The saturation condition of the slope will be definitely governing the shear strength characteristics and shear strength parameters of the founding material, and hence the presence of water table, seepage, percolation of water depending on the rate of precipitation and infiltration will be one of the guiding parameters to ascertain the slope stability condition. Hilly areas of the North-Eastern regions of India suffer from frequent landslides and movement of the slope primarily due to two major reasons, the torrential incessant rainfall and frequent seismicity. Moreover, due to increasing urbanization, the North-eastern regions is experiencing massive outgrowth in the number of habitations leading to widespread construction of residential and commercial buildings (Figure 1.2).

Figure 1.2 Residential habitations on hill slopes (Photo courtesy: Arindam Dey, 2015)

Due to scarcity of proper land areas, the construction are being carried out the slopes, either using berm or terraces (where the foundations are laid in the crest or crown of the slope) or placed directly on the slope itself (were the foundations lie directly on the sloping ground) (Figure 1.3). Many closely spaced low-rise residential buildings, schools, offices, military barracks (Figure 1.4), hospitals or other not-so high-rise structures are being built with shallow foundations, many of them lacking proper geotechnical outlook or adequate geotechnical supervision.

Figure 1.3 Foundation being laid and building constructed on slope face (Photo courtesy: Arindam Dey, 2015)

Figure 1.4 Closely spaced buildings on the hill slopes at same or different elevations (Photo courtesy: Arindam Dey, 2015)

Foundations are laid unscrupulously without paying proper heed to the effect it would produce on the stability of the slope or on the adjacent structures. A common feature which can be seen in such regions are that foundation placed at different levels with different depths of embedment, the analyses of which does not follow the conventional bearing capacity theories. Thus, a thorough study in this aspect is vividly important with regard to safety of the upcoming projects in the NE regions and its hill-slopes.

1.2 Motivation of the Present Study

Based on the thorough literature review conducted for this study, it has been understood that most of the studies reported are experimental works done in the laboratory mostly targeting to comprehend the effect of various parameters on the stability of the footings. A major lack in the knowledge remains with such experimentation is that all the studies conducted are based on a single footing located at various positions and embedment depths. There has not been a single study which attempted to explore the effect of multiple footings present adjacent to each other, which is the most common scenario for a structure located on a hill slope and affecting its stability. Moreover, all the studies conducted have considered dry soils, while the effect of saturation of slopes on the bearing capacity of foundation on slopes remains aloof of exploration. In addition, all the articles visited have referred to the results of experimental investigations in regard to strip footings (apart from Castelli and Lentini 2012, which presented a very preliminary study on square footing), which largely deviates from the actual practical considerations where most of the foundation on slopes would be of other shapes than a strip. Even combined footings are quite common in the hill slopes which have not been explored at all in the conducted studies. All the above stated variants of footing typologies and arrangements on the hill-slopes affect the stability and future consequences. Hence, it is utterly necessary to investigate the various features and responses of shallow foundations on hill-slopes, and devise some recommendations related to the enhancement in bearing capacity of such foundations through suitable construction practices. The existing lacunae in the current practices of analysis and field implementation related to buildings resting on shallow foundation on hill-slopes has provided the motivation to conduct a thorough investigation on this subject.

1.3 Outline of the Dissertation

This dissertation is organized into nine chapters as per the following outline:

- **Chapter 1** presents a general introduction to the subject matter and motivation of the dissertation work on 'Response of Isolated and Interfering Shallow Footings on Slopes'.
- **Chapter 2** deals with the background study and comprehensive literature review. Based on the critical appraisal of the reviewed literature and gap areas, the precise objectives and the scope of the study have been listed.
- **Chapter 3** provides the details of the methodologies adopted in the present study for numerical simulation.
- **Chapter 4** describes the influence of different geotechnical and geometrical parameters specifically, angle of internal friction, cohesion, unit weight of soil, width of foundation, embedment depth of foundation, setback distance and slope angle on the bearing capacity and failure mechanism of square and strip footings resting on sloping ground.
- **Chapter 5** clarifies the influence of interference on the bearing capacity and failure mechanism of strip footings located at the crest or face of slope.
- **Chapter 6** elaborates the integration of soft computing through Artificial Neural Network (ANN) to provide the bearing capacity prediction expressions for isolated and interfering footings located on the slope crest. Further, the relative importance of the different geotechnical and geometrical parameters on the estimated bearing capacity is also recognized.
- **Chapter 7** presents the influence of the interaction of various footing typologies located on the slope of crest, based on which the recommendations are provided for locating foundations on slopes.

- **Chapter 8** illustrates the impact of associated and non-associated flow rule son the bearing capacity, displacement and failure mechanism for shallow footing resting on horizontal ground and sloping ground.
- **Chapter 9** lists out the important conclusions and recommendations as an outcome of the present dissertation. The scope of the future work for further enhancement of research knowledge is also presented here.

The chapters are finally followed by a list of related references considered for the comprehending and preparation of the dissertation. A list of publications produced from the knowledge gain from the dissertation is also presented.

CHAPTER 2

LITERATURE SURVEY

2.1 General

Bearing capacity (q_u) of footing defines the maximum load that the foundation can carry without failure within allowable limits of settlement. The load carrying capacity of foundation depends on geotechnical and geometrical characteristics. Geotechnical characteristics comprise the shear strength and deformation parameters of soil. Geometrical characteristics include the size, depth and shape of the footing. In order to design an adequate foundation for superstructures, bearing capacity is the key for geotechnical engineers. In the hilly regions, as the construction permits, footings are mostly located on the crest of a slope (with some setback distance) or on the slope face itself, for e.g. footings of mobile and electric transmission towers, overhead water tanks, and bridge abutments. The bearing resistance of such footings is necessarily lower than the same placed on horizontal surface, attributed to the curtailed passive resistance zone developed towards the sloping face. For footings located on or near steeper slopes, the bearing resistance is substantially reduced. This chapter presents the detailed review of literatures on the responses of shallow foundation located on or near sloping surface. Further, discussions have been categorized based on the literature on bearing capacity of footing placed on or near the sloping ground considering: (1) Experimental approach (2) Theoretical and Numerical approaches. Finally, the critical appraisal of the literature reviewed and a detailed objective of the present study have concluded the chapter.

2.2 Footing on Horizontal Ground

The conventional technique to determine the ultimate bearing capacity of a surface or embedded strip footing on horizontal ground is based on several assumptions (Terzaghi 1943;

Meyerhof 1951). The theoretical analysis, as developed, considers the footing to be shallow and rigid, sharing a rough interface with the underlying soil. The foundation soil has been assumed to be homogeneous, elastic, semi-infinite, isotropic and incompressible (Terzaghi, 1943; Murthy, 2008). The foundation soil has been considered to undergo a general shear failure when it is subjected to vertical and centric loading applied on the footing. The postulated theory was based on a pre-assumed symmetric failure mechanism with well-defined formations of various failure zones beneath the footing (Terzaghi 1943). The ultimate failure load, expressed in terms of the shearing resistance mobilized along the pre-defined failure planes, was estimated based on the static equilibrium of the active wedge immediately beneath the footing. The estimation is assumed to be governed by the principle of superposition considering the theory of elasticity to be valid until failure. Based on the analysis, three bearing capacity factors (N_c, N_q and N_γ) were proposed as a function of the angle of internal friction of soil (φ). Figure 2.1 describes the schematic diagram of the failure surfaces as proposed by (Terzaghi 1943).

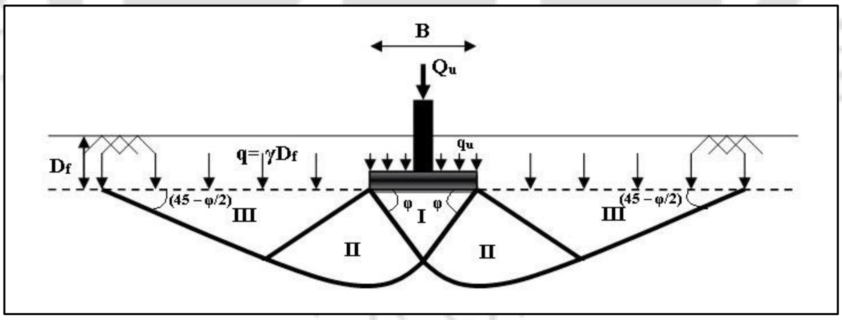

Fig. 2.1 Schematic representation of the conventional failure mechanism of a shallow strip footing undergoing general shear failure

Based on the laboratory and field investigations related to shallow footings on saturated clay, Skempton (1951) expressed N_c, to be dependent on the shape and the depth of the foundation.

Meyerhof (1951) extended Terzaghi's bearing capacity theory to the embedded strip footings in homogeneous soil, wherein the slip surface for the passive zone was considered to be extended up to the ground surface. Although the bearing capacity expression was considered the same as proposed by Terzaghi (1943), different expressions for the bearing capacity factors were proposed. Hansen (1970) proposed a general bearing capacity expression having identical bearing capacity factors as proposed by Meyerhof (1951), additionally incorporating the effects of shape and depth of the footing along with the inclination of applied load as various accompanying factors. Vesic (1973) proposed a bearing capacity theory having similar failure surfaces (Fig. 2.1) as proposed by Terzaghi (1943), however with a different wedge angle inclination for Zone I. Further modifications in the bearing capacity theory have been achieved mostly based on suitable adjustment in the bearing capacity factors (Meyerhof 1978; Hanna 1982; Cerato and Lutenegger 2006).

As reported in several literature, the applicability of the postulated bearing capacity theories depend on the outcomes of the experimental and numerical investigations on model strip footings resting on sandy or clayey beds, subjected to axially vertical or inclined load (Hanna and Meyerhof 1981; Meyerhof and Koumoto 1987; Loukidis et al. 2008). While maintaining the basic form of bearing capacity expression, the experimental investigations primarily target to establish the depth, shape, inclination and compressibility factors. In many cases, the effect of shape and depth of footing is directly incorporated to define modified bearing capacity factors (Hanna and Rahman 1990). Numerical investigations have elucidated the effect of variation in the soil strength parameters (cohesion and adhesion) with depth on the bearing capacity of shallow foundation on clayey medium (Reddy et al. 1991). Instead of utilizing conventional bearing capacity factors, based on the analytical procedures, to define the collapse mechanism of strip footings resting over a two-layered foundation soil system (sand or clay), generalized design charts have been developed for the direct estimation of the bearing capacity governed by the strength parameters of the layered media (Michalowski and Shi 1995). The effects of shear dilatancy on bearing capacity, bearing capacity factors and failure mechanism have been numerically investigated by several researchers (Vermeer and de-Borst 1984; Nova and Montrasio 1991; Drescher and Detournay 1993; Bolton and Lau 1993; Manoharan and Dasgupta 1995; Manzari and Nour 2000; Yin et al. 2001; Erickson and Drescher 2002; Shiau et al. 2003; Xiao et al. 2007; Loukidis and Salgado 2009; Benmebarek et al. 2012). The influence of groundwater conditions on the bearing capacity of shallow foundations, considering the effect of seepage during drained loading conditions, resulting in inhomogeneous unit weight, have been investigated using the kinematic approach of limit analysis (Ausilio and Conte 2005). The effect of locally placed horizontal confinement walls on the ultimate bearing capacity of a smooth strip footing has also been reported (Zhao et al. 2014). Such an enclosure results in the formation of a confined, but constricted, passive zone, thus leading to an altered bearing capacity governed by the clear distance of the adjacent confinements from the footing, and is expressed in terms of a correction on the bearing capacity factor N_γ. The effect of a rigid basement confinement on the ultimate bearing capacity of rough strip footing using upper-bound finite element method with rigid translatory moving elements (UBFEM-RTME) has been reported by (Yang et al. 2016).

2.3 Foundation on slopes

Rapid growth of urbanization in the North-Eastern hilly regions of India has resulted in myriads of residential and commercial constructions. The foundations of such constructions are mostly shallow, and are located either on the crest or on the benched face of the slopes. Apart from the urban constructions, mobile tower, transmission towers, water tanks, retaining walls, footings for bridge abutments, and even foundations for transportation links are mostly located on the slopes. Foundation on slopes is a challenging and complex problem for the geotechnical engineers. The stability of a footing located on or near a slope is affected by its location, the loading pattern, the edge distance from the slope face, the slope angle, the depth of embedment of the footing, the shear strength characteristics of the foundation soil and other factors, such as the rainfall, seismicity and saturation level of the foundation material. For footing placed near to face of a slope, a reduction in the bearing capacity of the foundation is expected due to the curtailed zone of passive resistance developed towards the slope face.

2.3.1 Experimental investigations and development

2.3.1.1 Model testing

Shields et al. (1977) conducted experimental investigations to estimate the bearing capacity of vertically loaded strip footings located at various depths of a sand-fill in the crest region of slope. The objective of the investigation idea was to verify the bearing capacity estimates as provided by the earlier theory proposed by Giroud (1971). Few comparisons were also made with the test results obtained by Lebegue (1973). The experimental model involved a 0.3m wide strip footing placed across the width of a sand box of dimension 2 m (width) ×15 m (length) × 2.2 m (height).The aspect ratio of footing as chosen was able to generate a plane strain condition. Crushed uniformly graded quartz sand had been used for the investigation that was deposited in the sand box in an air-dry condition by means of rotating drum spreader. Two sand samples having dry unit weights 14.85 kN/m^3 (compacted) and 15.75 kN/m^3 (densified) corresponding to relative densities (D_r) 70% and 90% respectively. A standard slope of 2H:1V was used for the sand-fill. The experimental bearing capacity factor values were presented in the form of contours (Fig. 2.2 and 2.3).

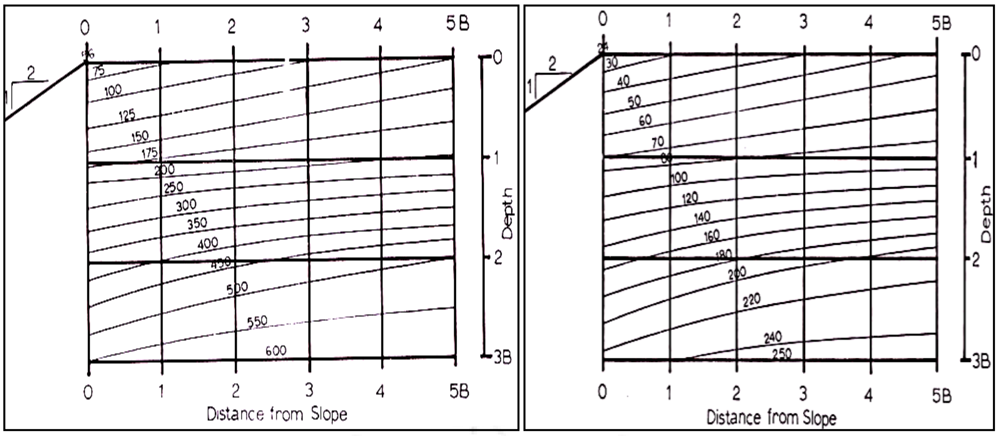

(a) (b)

Fig. 2.2 Contours of (a) Experimental bearing capacity and (b) Bearing capacity factor (compact sand) (Shields et al. 1977)

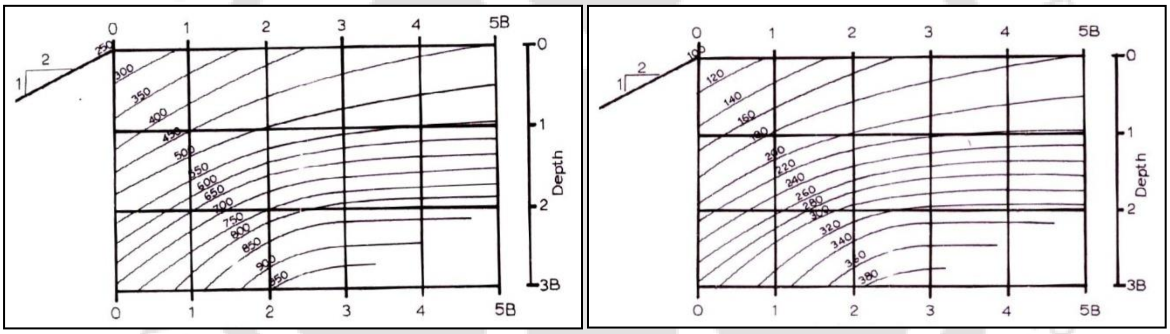

(a) (b)

Fig. 2.3 Contours of (a) Experimental bearing capacity and (b) Bearing capacity factor (dense sand) (Shields et al. 1977)

It has been reported in Shields et al. (1977) that bearing capacity factor obtained from the tests for footing located at the surface adjacent to the slope showed an agreeable match with the earlier conducted tests (Lebegue, 1973). From the investigation and comparative study, it was observed that Giroud's theory (Giroud 1971) overestimates the bearing capacity magnitudes of spread footing located near the slope. The experimental investigation conducted by Shields et al. (1977) had been extended by Bauer et al.(1981) to study the scale effect of footing on its bearing capacity. Rough-base rigid strip footings of two different widths (0.3m and 0.6m) had been used for the purpose. Apart from the locations as considered by Shields et al. (1977), footings were also placed at various locations in the slope face with varying magnitudes of embedment depth. Footing was placed across the width of a sand box or test bin of dimension 2m (*B*) × 15m (*L*) × 2m (*H*). The test setup closely followed as was adopted by Shields et al. (1977). Crushed uniformly graded quartz sand was deposited in the sand box with 100% proctor density by means of bucket elevator and sand spreading machine. The sand sample having angle of internal friction (φ) as 45° and dry density (γ_d) as 1610 kg/m^3 has been used. A standard slope of 2H:1V was used for the sand slope. The footings were subjected to both centric vertical loading and inclined loading. The load inclination was maintained at 15º with the vertical acting towards the slope. From the investigation, it was observed that for footings located at a depth 2*B* below the surface and subjected to vertical or inclined loadings, the bearing capacity factor ($N_{\gamma q}$) increased by 2-3 times (with respect to that obtained from a surface footing). Based on the experimental investigations, a scale factor $\left[S = \dfrac{N_{\gamma q(0.6m)}}{N_{\gamma q(0.3m)}}\right]$ was proposed, given as a ratio of bearing capacity factor for 0.6m footing size with respect to a 0.3m footing size (which is also conventionally termed as Bearing Capacity Factor, BCF). It was noticed that the scale factor attained an average value of 0.8 for footings located beyond a distance of 3*B* from the slope subjected to a vertical loading condition. This indicates that the bearing capacity factor for a narrower footing is more than that of a wider one. For inclined loading conditions, the scale factor attained an average value of 1.39, thus indicating that the bearing capacity factor for a wider footing is more in comparison to narrower one. An inclination factor $\left[i_\gamma = \dfrac{N^*_{\gamma q(\text{inclined})}}{N_{\gamma q(\text{vertical})}}\right]$ was also described based on the obtained results. In comparison to the vertical load condition, it had been seen that the bearing capacity factor reduced by 0.7 when footing was subjected to an inclined load. This reduction of bearing capacity was attributed to the observed shallower depth of the obtained failure surface under inclined loading condition.

Keskin and Laman (2013) have investigated the ultimate bearing capacity of strip footing located on the crest of sand-slope through experimental and numerical approaches. The parameters investigated were the effect of setback distance of the footing to the slope crest, slope angle, relative density of sand and footing width on the ultimate bearing capacity of strip footings. The investigation had been done with model footings of 70 mm and 50 mm in width, 465 mm in length and 20 mm in thickness, fabricated from mild steel were used. The footings were located on the sand slope inside the tank of dimension 1.140 m (length), 0.475 m (width) and 0.500 m (depth).Static vertical loads were applied to the model footings by a motor-controlled hydraulic jack system. The system attached to the loading frame located above the test box has a loading rate of 0.5 mm/min. The soil used for the model tests was uniform, clean and fine sand obtained from Cakit River bed. Using the Unified Soil Classification System, the material was determined to be poorly graded sand (SP). The specific gravity of the soil particles was 2.68, determined by pycnometer test. The maximum and minimum dry unit weights of the sand were measured as 17.9 kN/m^3 and 15.5 kN/m^3, and corresponding values of the minimum and maximum void ratios were calculated as 0.729 and 0.497 respectively. The experimental tests were conducted on samples prepared with average unit weights of 16.5, 17.0 and 17.5 kN/m^3. The corresponding relative densities of the samples were 45%, 65% and 85%, respectively. The estimated internal friction angles of the sand were 40.6°, 41.8° and 43.5°, respectively. Model sand slopes with slope angles (β) of 20°, 25° and 30° were prepared by using the identical compaction procedure in layers of 50 mm thick sand. From the investigation, it was observed that the ultimate bearing capacity increased with increasing setback distance of the footing from the slope crest. When the footing was moved away from the slope crest (*b/B*=0) to the setback distance of *b/B*=1.0, there was remarkable increase in bearing capacity (an average value of 70%). Moreover, the rate of increase in bearing capacity decreased with increasing distance of setback until *b/B*=5.0, beyond which the ultimate bearing capacity of the footing on slope approached that of a footing on level ground (Fig. 2.4 a). It was perceived the ultimate bearing capacity decreased with an increase in slope angle (Fig. 2.4 b).

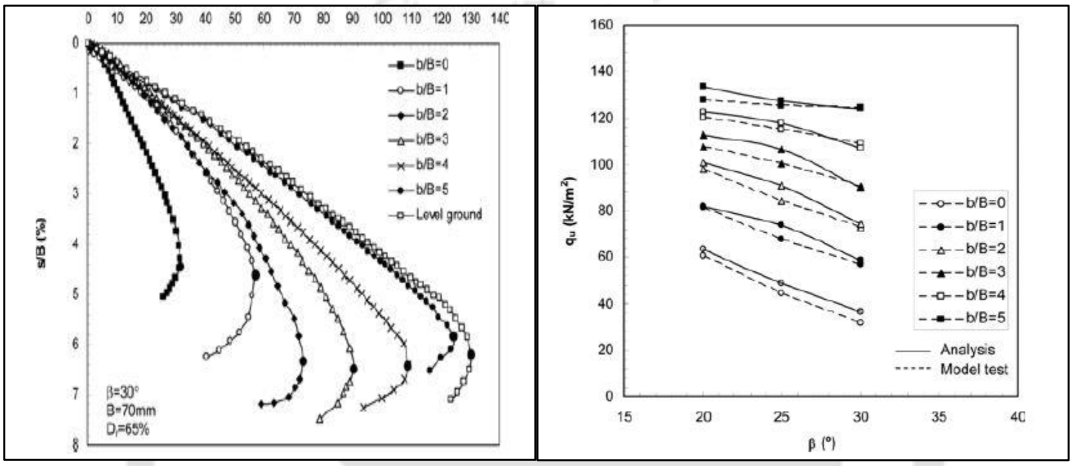

(a) (b)

Fig. 2.4 Effect of (a) Setback distance (b) angle of inclination of slope on bearing capacity (Keskin and Laman 2013)

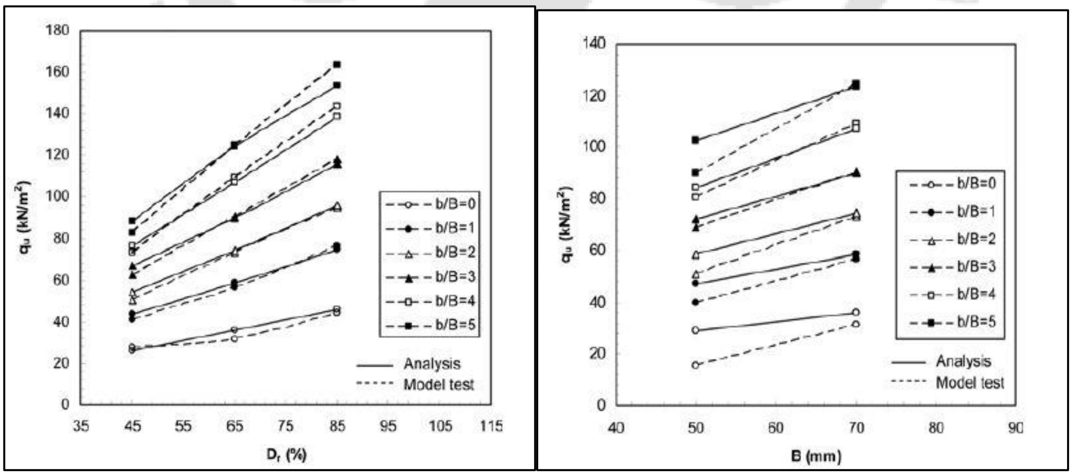

(a) (b)

Fig. 2.5 Effect of (a) Relative density of sand (b) Width of footing on bearing capacity (Keskin and Laman 2013)

It was noted that that the bearing capacity of the footing on a slope was significantly increased with increasing relative density (D_r) (Fig. 2.5 a). It had been seen that the ultimate bearing capacity increased with increasing the width of the footing (B) (Fig. 2.5 b).

The effect of the bearing capacity of shallow foundations on slopes had been experimentally investigated by researchers (Castelli and Lentini 2012**)**. The investigation had been performed with square footings of dimension 6 cm, 8 cm and 10 cm width (B), and strip footings of dimension 4 and 6 cm, the width and constant length of 45 cm resting on the sand slope inside the tank of dimension 100 cm long, 45 cm wide and 40 cm high. Load was applied incrementally by a hydraulic jack and maintained manually with a hand pump. The vertical displacements were measured by means of displacement transducers. Settlement data were recorded using a data acquisition system with a precision of 0.025 mm. All the tests were performed on specimens of Playa Catania (Italy) sand. A series of standard drained shear tests were carried out to evaluate the internal friction angle of the model sand using specimens prepared by dry tamping. The estimated internal friction angle at the relative density of 87% was approximately φ=38°, and the maximum dry unit weight was γ_{dmax} =17.50 kN/m^3. Test soil bed was constructed in layers and the sand was set up to form a slope angle of 30°. It had been observed that the threshold distance [a threshold distance d_t at which the effect of the sloping ground vanishes] increased as the friction angle increased. For a strip footing, it varied between d_t/B=1.5 for a value of the friction angle φ=20° to d_t/B = 3.5 for a value of the friction angle φ= 40° (Fig. 2.6).

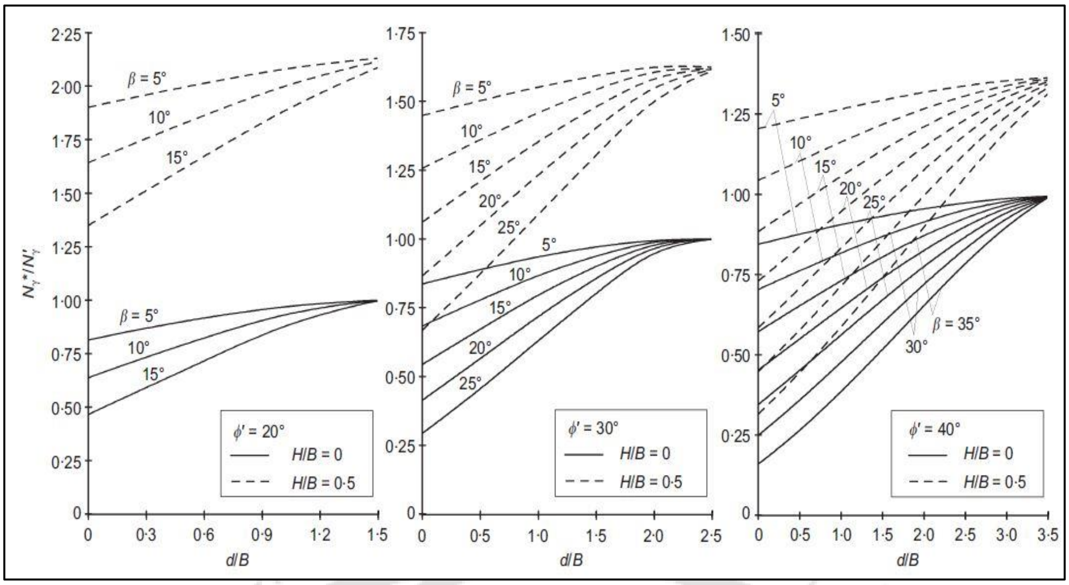

Fig. 2.6 Effect of setback distance and angle of internal friction on bearing capacity factor (Castelli and Lentini 2012)

The behaviour of a strip footing with structural skirts adjacent to a sand slope had been investigated experimentally and numerically by Azzam and Farouk (2010). The studied parameters include the skirts depth (*L/B*), location of the skirted footing relative to the slope crest (*b/B*) and the slope inclination (β). The investigation had been done with the rigid footing model, made of a solid steel section of dimension 10 cm (width) × 2 cm (thickness) × 59 cm (length) resting on the crest of a slope inside the tank of dimension 205 cm length, 60 cm width and 90 cm height. The loading system was designed and manufactured to apply vertical loads to the model footing. The sand used in this research was medium to coarse sand. The internal friction angle related to the same relative density used in the model tests was found 41°. Structural skirts were fabricated in this study using steel sheets made of 3 mm in thickness and they were fixed directly to the footing edges along each side by welding. A slope height of 50 cm was fixed in all tests, while the slope angle, β, was varied between 20°, 26.56° and 30°. It has been reported that the footing with the structural skirts improved the performance of the footing by increasing the bearing capacity and reducing the settlement of the system. It had been seen that improvement occurred from 1.4 to 2 times of the footing without skirts. The improvement had taken place for the skirt length of 2*B*, beyond that the improvement was not significant. The capability of rigid strip one-sided micro-piled footings in stabilizing sand slopes had been investigated experimentally by Elsaied (2014). The investigation had been done with a model footing, prepared using a stiff steel plate of dimension 150 mm (width) × 12 mm (thickness) × 295 mm (length) resting on the crest of sand slope in the rigid steel tank of inner dimensions of 2000 mm (length) × 300 mm (width) × 800 mm (depth). A rigid loading frame was used to apply the load to the model strip footing through hydraulic jack and 50 KN proving ring. The implemented sand was dense and it is classified as poorly graded sand (SP) according to the Unified Soil Classification system. The grain size distribution was 45% coarse sand, 50% medium sand, and 5% fine sand. The sand had maximum dry density of 18.2 kN/m^3, minimum dry density of 15.7 kN/m^3 and specific gravity of 2.51. The sand was kept dry during model tests and the bulk density is 17.5 kN/m^3. All the model tests were conducted at a relative density of 75%, for which the friction angle from a direct shear test was found to be 38°. Experimentation included five groups of high tensile steel bars with 20 mm diameter and with different lengths. Each group contained five micro-piles with the same length. The depths of the micro-piles after fixation on the footing base were 75 mm, 150 mm, 300 mm, 450 mm, and 600 mm. In the experiment, three different sets of tests were carried out: the first test set comprising of vertical centric load on the footing, the second test set was performed under eccentric loading of e/B of 0.133 and 0.266 in the direction of the slope crest and the third test set was carried out to investigate the effect of centric oblique loading with inclination angle with the vertical (i =10°) on the micro-piles footing system behaviour. It has been reported that the ultimate bearing capacity increased as the footing is placed far from the slope crest [setback distance (X/B)] as well as with the decrease in slope inclination angle and eccentricity of footing for vertical and eccentric loading conditions. It has been mentioned that vertical loading condition, the footing pressure decreased with increasing the depth of micro-piles up to L=B. It has been declared that for eccentric loading condition, increasing the micro-piles depth leads to an increase in the bearing capacity. It has been stated that in case of oblique loading (i=10°) condition, footing pressure capacity increased and horizontal displacement of the footing decreased with increasing the setback distance and length of micro-pile. Azzam and El-Wakil (2015) executed laboratory and numerical model tests on the influence of soil confinement on the behavior of circular footings resting on the crest of slope. The considered parameters include the cell-embedment depth, slope angle, and subgrade density. The considered sand was dry medium siliceous sand of specific gravity 2.64, the maximum and minimum dry densities were 18.55 and 15.60 kN/m^3, respectively, and the corresponding values of the minimum and the maximum void ratios are 0.305 and 0.593. Three uniform relative densities were considered of 80%, 55%, and 35%. The corresponding angles of internal frictions were found 41°, 33°, and 29°, respectively. The outcomes specify that the bearing load capacities of circular footings at any edge distance from the slope crest can be significantly increased by soil confinement. The influence of slope face on the ultimate bearing capacity can be ignored when the cell-footing system is placed at setback distance with cell embedment depth around two times the cell diameter. The enhancement in the bearing capacity reached 4, 2.2, and 1.9 times the footing without cell with subgrade relative densities of 80%, 55%, and 35%, respectively, when the cell-footing system is located directly on a steep slope crest. Shukla and Jakka (2017) have found some major ambiguities in the study done by Azzam and El-Wakil (2015). In the discussion, it has been exposed that Azzam and El-Wakil (2015) in their experimental investigation have made a sand slope of sloping angle 45° with loose sand having angle of internal friction (φ) 29° and relative density (D_r) 35%. It has been also mentioned that the slope used in the experiment found to be unstable with a stability factor of 0.56. It has been concerned that Azzam and El-Wakil (2015) made two contradicting statements in the results and discussions of their experimental study. Initially it has been stated that the gradual decrease in the bearing capacity ratio was observed when the slope angle and the relative density of the subgrade were increased and afterwards it has been specified that the increase of subgrade density much improve the shear strength and increases bearing capacity ratio. It has been enunciated that Azzam and El-Wakil (2015) used axisymmetric elasto-plastic finite-element (FE) modeling to determine the ultimate capacity of circular footing, although an axisymmetric model is valid only for circular footing resting on level ground. The present problem as a whole cannot be considered as an axisymmetric problem, because slope has considerable influence on the pressure bulb as well as the failure pattern of footing. It has also been articulated that a three-dimensional (3D) FEM model is necessary to predict the behavior of circular footing resting on slope crest.

Islam and Gnanendran (2013) had experimentally investigated the change in ultimate bearing capacity and permanent deformation due to applying vertical cyclic load for strip footing located adjacent to slope. The soil used in the investigation was poorly graded sand. The maximum dry density (MDD) of the soil was 1770 kg/m^3 with respective optimum moisture content (OMC) was 5.2%. The cohesion (c) and angle of internal friction of soil were 3 kPa and 34° respectively. In the experiment two different slope, mild (1V:2H) and steep (1V:1.5H) had been considered. The model slope had been prepared on the model tank of dimension 1100 mm (length) x 500 mm (width) x 800 mm (height). The model strip footing of dimension 490 mm (length) x 130 mm (width) had been considered on the crest of the slope. In the investigation, low-frequency vertical cyclic loading had been applied. The amplitude had been varied from 6 kN to 10 kN and applied on each model footing for approximately 100000 cycles. It had been declared that the bearing capacity and stiffness of soil significantly improved due to applying the cyclic loading. It had been mentioned that for both the slope the bearing capacity had been increased by 44% for 100000 load cycles. Moreover, the lateral movement of the model footing in slope direction was significantly reduced for considering cyclic loading.

2.3.1.2 Centrifuge testing

Gemperline (1988) carried out 215 centrifuge tests on model footings located on the crest of a cohesionless slope**.** Based on the above test results, an equation was proposed to determine the bearing capacity of a foundation near slope. None of the tests was carried out on footing placed on the face of the slope. The tests were conducted for various footing width to length ratio (the width was varied from 0.6 m to 1.81m) and for two different slope inclinations (i.e. 2H:1V and 3H:2V). Based on the experimental results, an equation was proposed to determine the bearing capacity of foundation (Eq. 2.1 and Eq. 2.2):

$$q_u = \frac{1}{2}\gamma B N_{\gamma q} \tag{2.1}$$

where $N_{\gamma q} \approx f_{(\phi)} \times f_{(B)} \times f_{(D/B)} \times f_{(B/L)} \times f_{(D/B,B/L)} \times f_{(\beta,b/B)} \times f_{(\beta,b/B,D/B)} \times f_{(\beta,b/B,B/L)}$

$$\left.\begin{aligned}
f_{(\phi)} &= 10^{(0.1159\phi-2.386)} \\
f_{(B)} &= 10^{(0.34-0.2\log_{10} B)} \\
f_{(D/B)} &= 1+0.6(D/B) \\
f_{(B/L)} &= 1-0.27(B/L) \\
f_{(D/B,B/L)} &= 1+0.39(D/L) \\
f_{(\beta,b/B)} &= 1-0.8\left[1-(1-\tan\beta)^2\right]\left\{2/\left[2+(b/B)^2\tan\beta\right]\right\} \\
f_{(\beta,b/B,D/B)} &= 1+0.6(B/L)\left[1-(1-\tan\beta)^2\right]\left\{2/\left[2+(b/B)^2\tan\beta\right]\right\} \\
f_{(\beta,b/B,B/L)} &= 1+0.33(D/B)\tan\beta\left\{2/\left[2+(b/B)^2\tan\beta\right]\right\}
\end{aligned}\right] \tag{2.2}$$

However, the Eq. 2.2 has some limitations. The above equation is invalid for slope angle more than 45°. Moreover, the effect of load inclination and load eccentricity were also not considered in the analysis. The expression also ceases to be valid when λ and η become greater than 2, where λ, η are the distance of footing from the crest and depth of embedment, respectively. The experimental result obtained from the Shields et al. (1977) and Bauer et al. (1981) have been compared with the experimental result proposed by Gemperline (1988) (Shields et al. 1990). The $N_{\gamma q}$ obtained from the Gemperline equation was normalized with the $N_{\gamma q}$ value of the foundation on a level ground, and it was defined as the bearing capacity factor ratio. A contour of bearing capacity factor ratio was plotted (for a slope of 2H:1V) with embedment depth as shown in Fig. 2.7.

The value obtained from Shields et al. (1977) and Bauer et al. (1981) propositions had been normalized with the bearing capacity of a foundation on a horizontal ground. The comparison of the Gemperline (1988) results with the results obtained by Shields et al. (1977) and Bauer et al. (1981) are shown for a slope of 2H: 1V in Fig. 2.8. Gemperline's curve for footings located on the slope face, was extended as a straight-line tangent as shown in the Fig. 2.9.

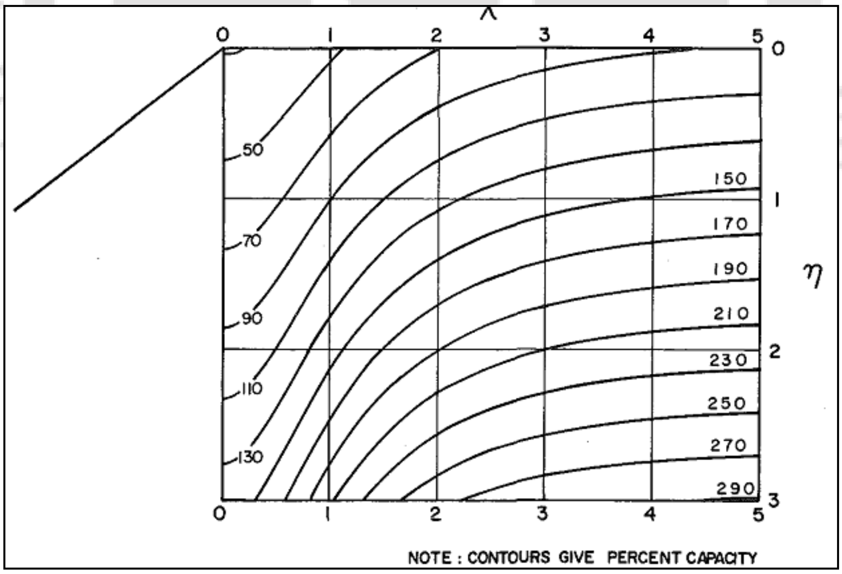

Fig. 2.7 Bearing capacity factor ratio contours as per Gemperline's (1988) prediction expressions for 26.6° slope (Shields et al. 1990)

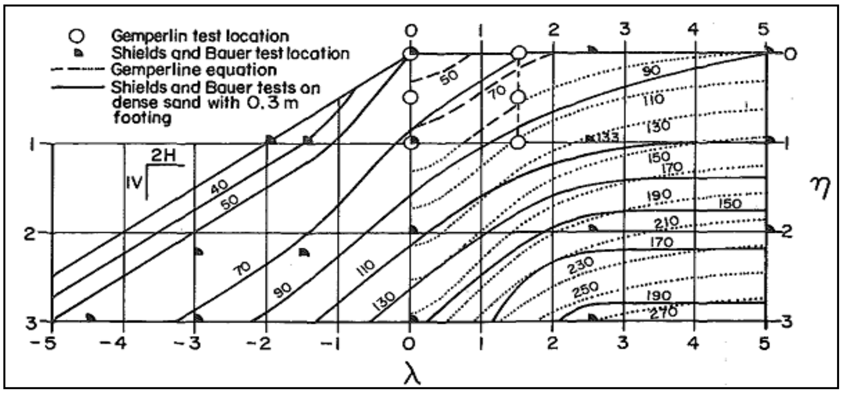

Fig. 2.8 Comparison of percentage bearing capacity values obtained from Gemperline (1988) expressions with that of Shields and Bauer (1977) results (Shields et al. 1990)

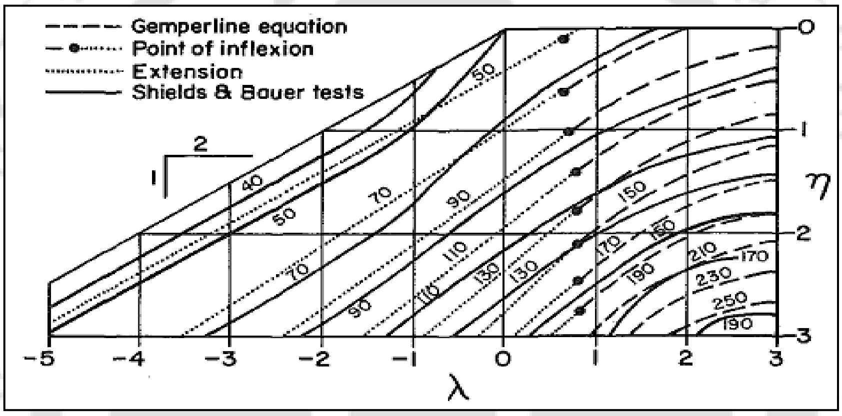

Fig. 2.9 Comparison of percentage bearing capacity values obtained from extended Gemperline (1988) expressions with that of Shields and Bauer (1977) results (Shields et al. 1990)

Although the results were proposed on the basis of tests conducted on a limited location of footings, the results reported in Gemperline (1988) were validated for a wide range of footing location. Moreover, near the slope face, the bearing capacity ratio obtained by Gemperline (1988), Shields et al. (1977) and Bauer et al. (1981) findings were in good match.

2.3.1.3 Prototype testing

Clark et al. (1988) conducted full-scale field testing for the bearing capacity and stability of inclined footings with anchors on a colluvial slope near the east portal of the Rogers Pass tunnel in British Columbia. A series of four soil (D_1, D_2, W_1, W_2) anchor tests was carried out to verify the anchor capacity and measure the response of the reaction footings on the 35° colluvial slope. The reaction footings, 1.07 m square and 0.5 m thick, were cast parallel to the slope on a surface excavated to undisturbed natural soil. The anchors and reaction footings were loaded and unloaded in five stages using increments and decrements of 111 kN applied by calibrated jacks. From the investigation, it had been reported that the elastic and deformation responses both remain linear with increasing load levels. The deformation modulus normal to the slope for the anchor reaction footings averages about 75 MPa. The elastic modulus averages 228 MPa, three times the deformation modulus (Table 2.1).

Table 2.1 Results for anchor test reaction footings (Clark and Mckeown, 1988)

No.	Soil water content (%)	Elastic modulus (MPa)	Deformation modulus (MPa)	Ratio of elastic/deformation modulus
D2	-	310	117	2.6
D3	6.5	250	75	3.3
W1	9.5	126	43	2.9
W2	-	225	65	3.5
Average		228	75	3.0

2.3.2 Theoretical investigation and developments

2.3.2.1 Analytical study

One of the earlier attempts to find the bearing capacity of footing placed on the vicinity of a slope was done by Meyerhof (1957). The conventional theory was modified to include the effect of slope on the stability of foundation. The failure zone was assumed to comprise of an elastic zone, a radial shear zone and a mixed shear zone. When footing is placed very near to a slope, the plastic zone on the side of the slope is not fully developed as it does when the footing is placed on a level ground. Fig 2.10 shows the failure surface assumed by Meyerhof. Thus, the bearing capacity of the foundation is significantly reduced due to the improper formation of failure surface.

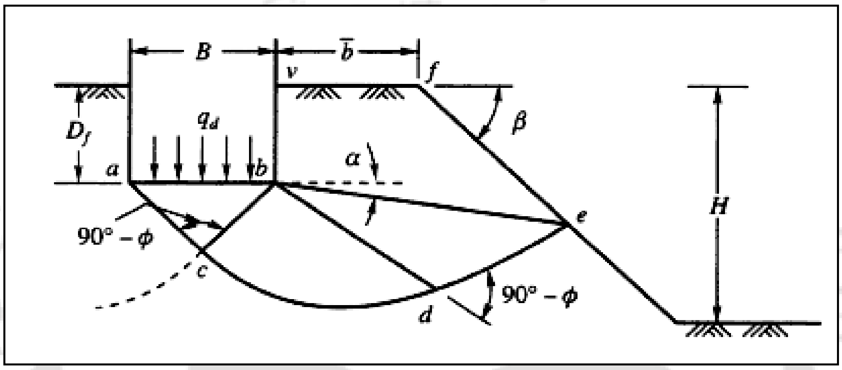

Fig. 2.10 Continuous foundation on top of the slope (Meyerhof 1957)

The ultimate bearing capacity proposed by Meyerhof (1957) for footing resting on crest as well as on slope surface through following expression (Eq. 2.3):

$$q_u = cN_{cq} + 0.5\gamma BN_{\gamma q} \tag{2.3}$$

The bearing capacity factors N_{cq} and $N_{\gamma q}$ obtained depend on (i) Distance of footing from crest (d_e) (ii) Slope angle (β) (iii) Angle of internal friction of soil (φ) (iv) Depth to footing width ratio ($\frac{d_f}{B}$), and (v) Stability number ($\frac{\gamma H}{c}$). The bearing capacity factors were presented in the form of chart for various values of depth of footing, distance of footing from crest of the slope, slope angle and angle of internal friction of the soil as shown in Fig 2.11. However, different sets of charts were provided for the bearing capacity factors for footing resting on slope face as shown in the Fig 2.12. It was found from the analysis that at a distance of 2-6 times the foundation width, the bearing capacity becomes independent of slope angle and follows the theory of a foundation on a horizontal ground.

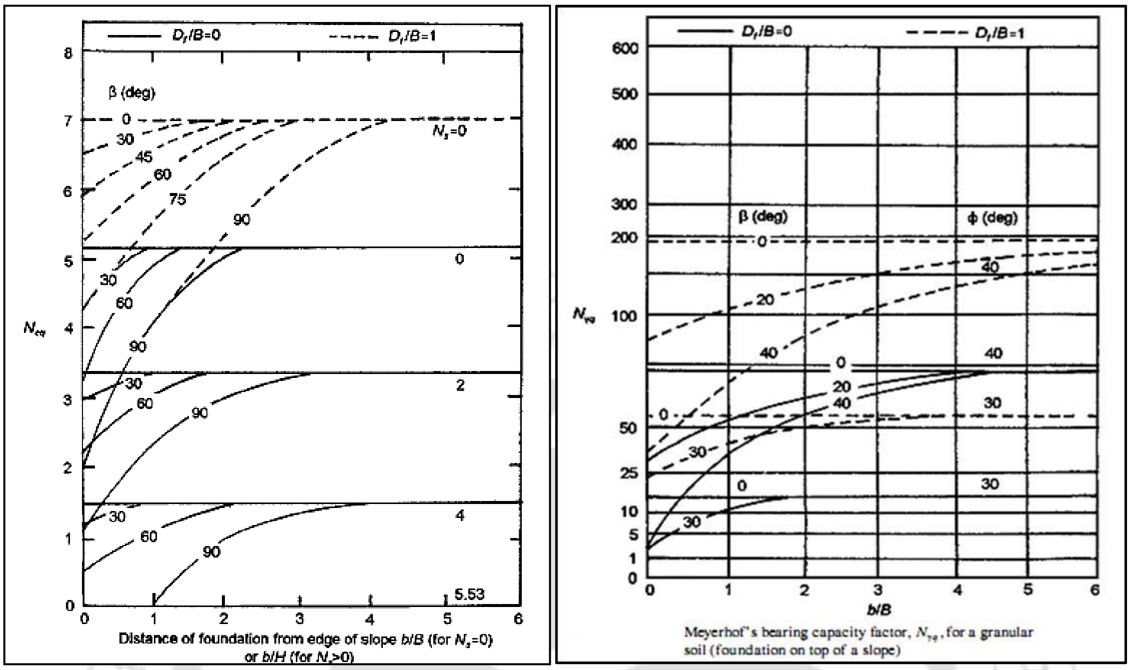

(a) (b)

Fig. 2.11 Meyerhof's bearing capacity factors (a) N_{cq} (b) $N_{\gamma q}$ (footing on top of the soil) (Meyerhof 1957)

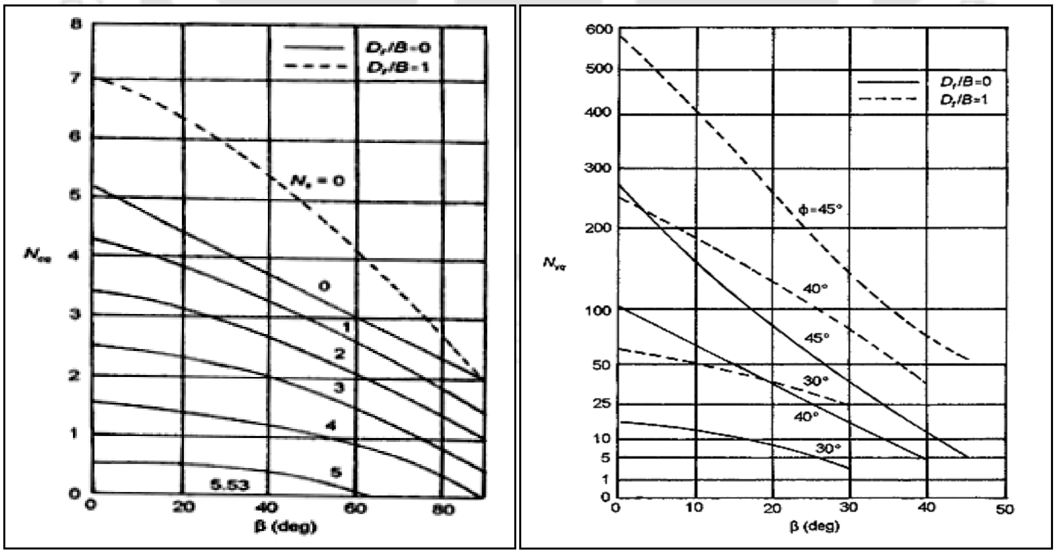

(a) (b)

Fig. 2.12 Meyerhof bearing capacity factor (a) N_{cq} (b) $N_{\gamma q}$ (footing on face of the slope) (Meyerhof 1957)

The bearing capacity of a strip footing placed on the crest of a cohesionless soil slope has been determined by Mizuno et al. 1960. It was assumed that at the instant of failure, three zones exist in the soil underneath the footing (active pressure wedge, transition zone and passive pressure zone). The transition zone was divided into a number of small wedges. For each wedge, the equilibrium condition of force was applied, subsequently Mohr's circles were drawn, and then, by finding the critical stress state, the ultimate bearing capacity was estimated. The failure zone proposed by Mizuno et al. (1960) is shown in Fig 2.13.

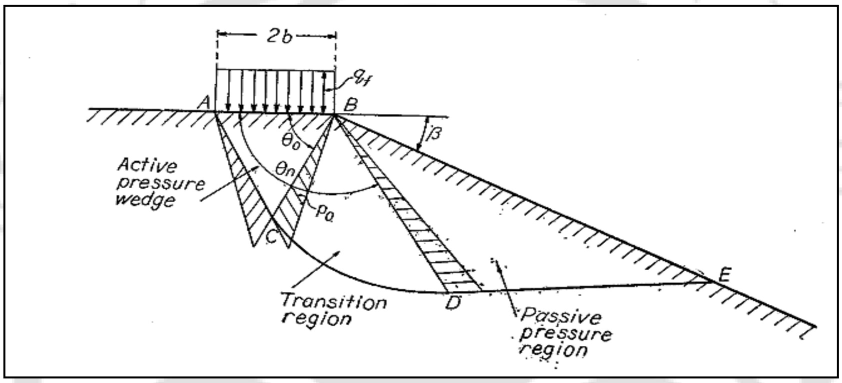

Fig. 2.13 Failure zones for footings located on the crest and at the edge of slope face (Mizuno et al. 1960)

It was assumed that resistance against the sliding is caused only by the weight of the soil and that the stress in the passive region is proportional to the depth below the sloping surface. To check the failure surface obtained with the actual failure plane, an investigation had been done in which small cylindrical bamboo sticks of 5mm diameter were used to find the position of the slip line. For different values of slope angle (β = 10° and β = 15°) it was found that the sliding surface was exactly similar to the slip line obtained by the analytical solution proposed (Fig. 2.14).

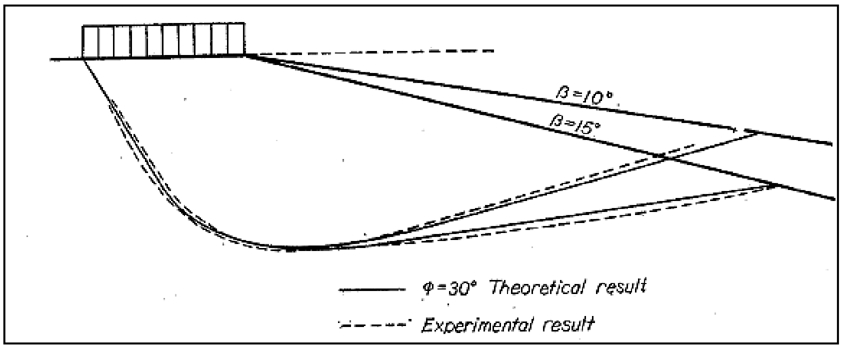

Fig. 2.14 Comparison of theoretical and experimental failure planes (Mizuno et al. 1960)

Afterwards, researchers (Hansen 1970; Vesic 1975) had extended the theoretical investigation that had been done by Meyerhof (1957). Researcher had given ultimate bearing capacity expression and different slope factors ($\lambda_{c\beta}$, $\lambda_{q\beta}$ and $\lambda_{\gamma\beta}$) for rough strip footing resting on crest of slope with zero setback distance (b). However, when the bearing capacity value obtained from this analysis was compared with the result obtained from the Saran et al. (1989), it was found that the Mizuno et al. (1960) solution seriously underestimates the bearing capacity of the soil and thus leads to an oversafe design. Narita and Yamaguchi (1990) had investigated the normalized bearing capacity ($q/\gamma B$) of strip footing located on crest of sloping ground with aid of log-spiral method. In the analysis the input parameters specifically, setback distance ($L = \lambda B$), slope angle (β), angle of internal friction (φ) and slope height ($H = \eta B$) were altered. The outcomes were compared with the results of past analytical and experimental works. It had been reported that the results obtained from log-spiral method were overestimated compared to upper-bound technique and Bishop's method for cohesionless soil. It had been declared that for cohesive soil (φ=0), the slip surface beneath the footing had been degenerated from log-spiral to circle and results found from log-spiral method was close to outcomes obtained from analytical solution. The bearing capacity of rectangular and square footing located crest of slope had been inspected by researches (De-Buhan and Garnier 1998) through kinematic method with aid of three-dimensional analyses. In the investigation, various geotechnical parameters (φ and $\gamma H/c$) and geometrical parameters [normalized length (B/L), slope angle (β), normalized setback distance (D/B) and normalized slope height (H/B)] had been considered for estimating the bearing capacity of footing. Moreover, the obtained result from kinematic method had been compared with experimental outcomes (Bakir 1993). It had been reported that there was excellent match between results fond from kinematic approach and experimental outcomes. It had been also mentioned that the effect of slope on bearing capacity of footing was vanished beyond a normalized setback distance (D/B) of 3.

2.3.2.2 Numerical study

The bearing capacity of embedded strip footing located on the crest of the slope had been investigated by Jao et al. (2008) with aid of finite element analysis based on the theory of elasto-plasticity. For the investigation, three slope angles (18.4°, 26.6° and 45°), six footing locations [0 (at the crest) to 6B], two soil types (Kaolin and Silty clay) and three loading positions over footing [E = -B/6 (eccentricity towards slope), E = 0 (centric vertical load) and E = +B/6 (eccentricity away from slope); B is the width of footing)] had been considered. It had been reported that eccentricity of loading having insignificant effect on load bearing-settlement behaviour as shown in Fig. 2.15. It had been declared that the magnitude of bearing capacities of the footing obtained from eccentricity of E = -B/6 greater than bearing capacities found from eccentricity of E = +B/6 for different slope angles and footing locations (Fig. 2.16 and Fig. 2.17).

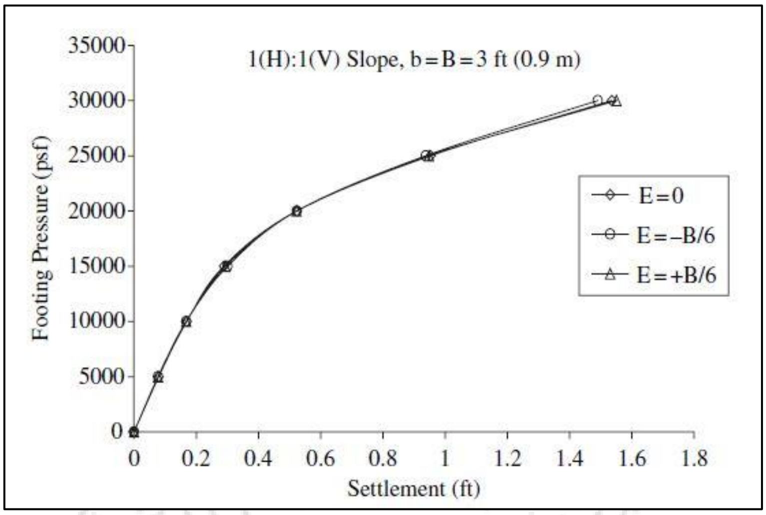

Fig. 2.15 Pressure-settlement behaviour of footing located on slopes and subjected to different eccentricity (Jao et al. 2008)

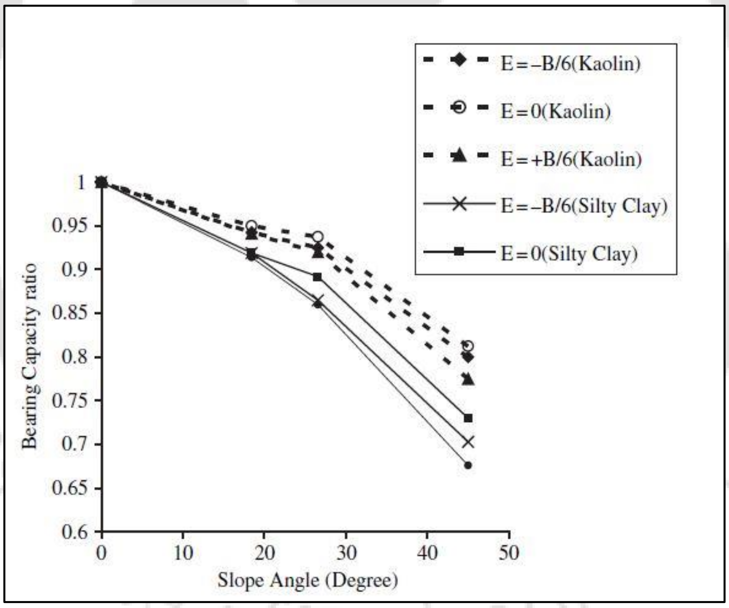

Fig. 2.16 Bearing capacity behaviour of footing located on slopes and subjected for different eccentricity and slope angles (Jao et al. 2008)

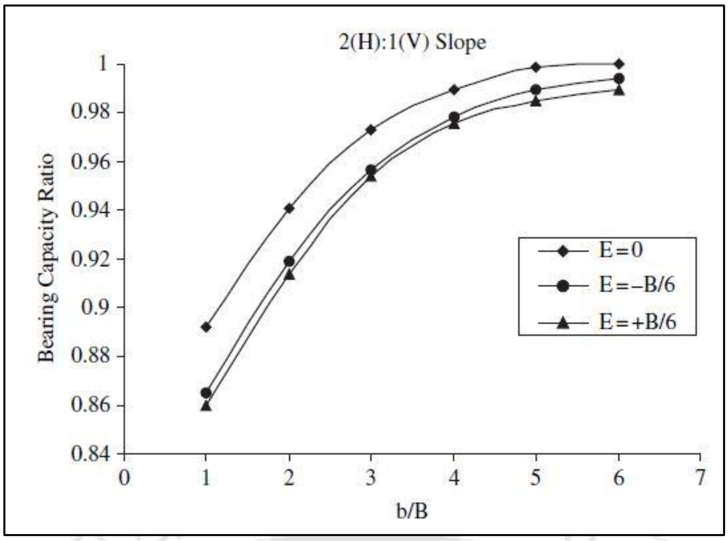

Fig. 2.17 Bearing capacity behaviour of footing located on slopes and subjected to different eccentricity and footing locations (Jao et al. 2008)

Shiau et al. (2011) had investigated the normalized bearing pressure [$p/\gamma H$, p is the pressure on footing, γ is the unit weight of soil and H is the height of slope] for smooth and rough strip footings located on crest of slope or vertical cut made of clay with aid of finite element upper and lower bound methods. For the sake of investigation, input parameters specifically, normalized setback distance (L/B), slope angle (β), normalized undrained strength ($c_u/\gamma B$), normalized surcharge ($q/\gamma B$) and normalized slope height (H/B) had been varied. In the article, various design charts were provided for estimating the normalized bearing pressure by altering input parameters. Moreover, authors had provided the design procedures to calculate the normalized bearing pressure as follows:

1. Determine the magnitude of geotechnical and geometrical parameters namely, c_u, γ, $c_u/\gamma B$ and L/B.
2. Estimation the magnitude of $(c_u/\gamma B)_{\text{critical}}$ in which slope failure can occur (Eq.2.4).

$$(c_u/\gamma B)_{critical} = N_f \frac{H}{B} \tag{2.4}$$

where, $N_f = c_u/\gamma H F_s$ obtained from Taylor's chart by providing $F_s = 1$.

3. If $(c_u/\gamma B) \le (c_u/\gamma B)_{critical}$, then overall slope failure has occurred. If $(c_u/\gamma B) > (c_u/\gamma B)_{critical}$, then the slope is stable and the normalized bearing pressure ($p/\gamma H$) can be obtained from the design charts.

The undrained bearing capacity factor N_c had been investigated by Georgiadis (2010) for surface strip footing located on crest of clayey soil-slope with aid of finite element analysis. In the research, the input parameters namely normalized setback distance (λB), slope angle (β), normalizes slope height (H/B) and normalized cohesion ($c_u/\gamma B$) had been altered for estimating undrained bearing capacity factor N_c. It had been reported that the undrained bearing capacity factor was affected by normalized slope height within range of 0.25 to 0.75, beyond which the effect of H/B was negligible. Various design charts had been provided for calculating the magnitude of N_c for various combinations of input parameters. Moreover, design expressions for N_c had been given as follows (Eq.2.5 – Eq. 2.8).

$$N_{c0} = 5.14 - \frac{2\beta}{1 - \frac{\gamma B}{5.14 \times c_u}} \quad (\beta \text{ in radian}) \tag{2.5}$$

where, N_{c0} is the undrained bearing capacity factor at crest ($\lambda = 0$), B is the footing width and γ is the unit weight of the foundation soil.

In the investigation, Georgiadis (2010) had determined the critical normalized setback distance (λ_0) beyond which the effect of slope diminished.

$$\lambda_0 = \left(\frac{5.14}{2}\right)^{\beta} \tag{2.6}$$

$$\text{For } \lambda > \lambda_0,\ N_c = N_{c0} + (5.14 - N_{c0}) \times \frac{\lambda}{\lambda_0} \times \left[1 + \frac{\beta}{2} \times \left(1 - \frac{\lambda}{\lambda_0}\right)\right] \tag{2.7}$$

$$\text{For } \lambda \ge \lambda_0,\ N_c = 5.14 \tag{2.8}$$

The bearing capacity factors N_c, N_q, N_γ and the associated failure mechanism had been investigated by Chakraborty and Kumar (2013) with aid of lower bound finite element limit analysis and nonlinear optimisation for strip footing resting on cohesionless sloping surface. The bearing capacity factors and associated failure mechanism beneath the footing had been examined and compared for rough and smooth base strip footings. For sake of analysis, the angle of internal friction (φ) and slope angle (β) had been varied. It had been reported that the magnitudes of bearing capacity factors N_c, N_q, N_γ obtained from rough strip footing were higher than bearing capacity factors fond from smooth strip footing as shown in Fig. 2.18. It had been presented that the size of the passive zone around the footing base was bigger for the rough footing compared to smooth footing. Moreover, authors had compared their outcomes with results of available literature (Kumar and Rao 2003; Hjiaj et al. 2005; Kumar 2009) and presented that there was excellent agreement of results.

The ultimate bearing capacity of surface strip footing resting on crest of c-φ soil slope had been investigated through limit analysis with discontinuity layout optimization (DLO-LA) technique by Leshchinsky (2015). In the analysis, different parameters specifically, angle of internal friction (φ), slope angle (β), stability factor (N_s) [$N_s = \frac{\gamma H}{c}$, γ is the unit weight of soil, H is the slope height and c is the soil cohesion] and slope height ratio (B/H) had been varied. The results obtained from DLO-LA technique had been compared with the results of researchers Kusakabe et al. (1981) and Georgiadis (2010), and it had been presented that there was excellent match of results. The outcomes of DLO-LA technique were presented in terms of reduction coefficient (RC_{BC}) factor (Eq.2.9 and Eq. 3.0).

$$RC_{BC} = \frac{Q_{ult}(DLO - LA)}{Q_{ult}} \tag{2.9}$$

$$Q_{ult}(DLO - LA) = cN_c RC_{BC} + 0.5\gamma B N_\gamma RC_{BC} \tag{2.10}$$

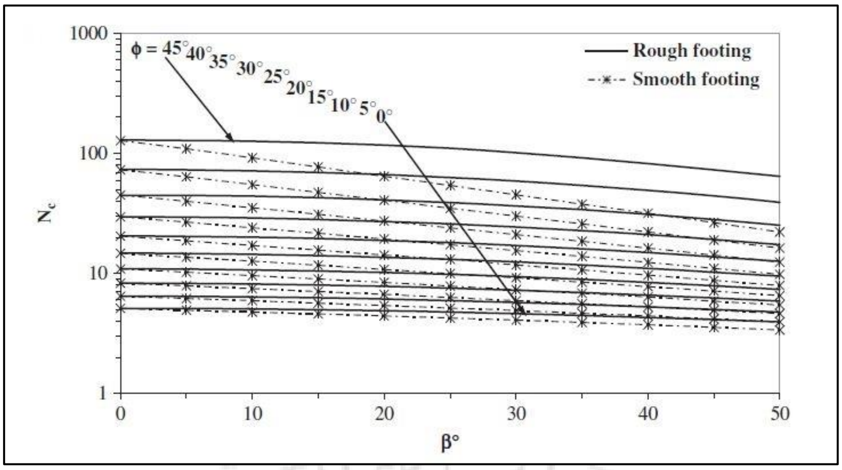

(a)

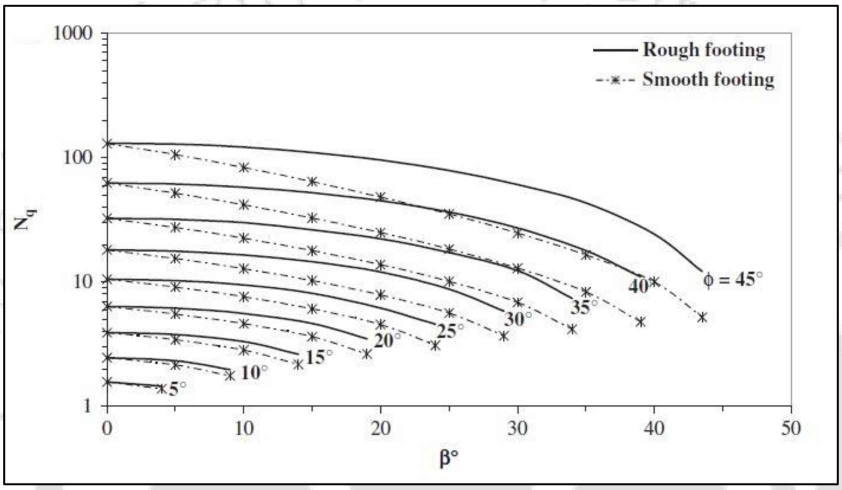

(b)

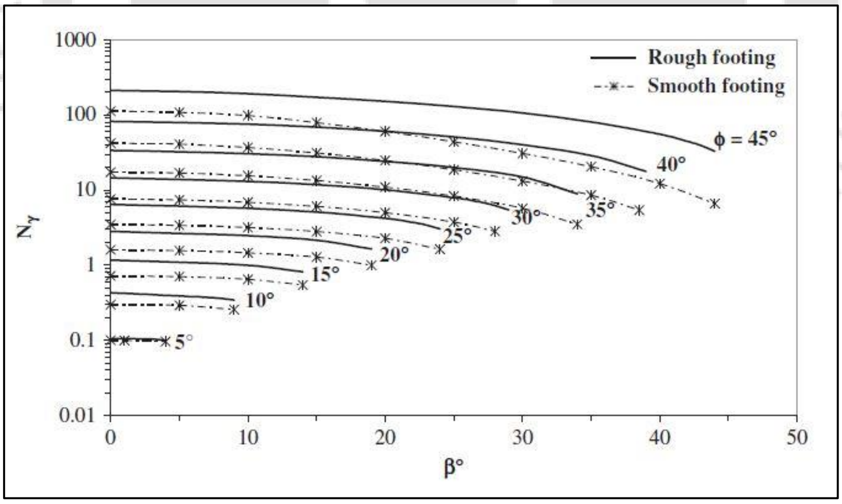

(c)

Fig. 2.18 Comparison of bearing capacity factors for rough and smooth footing for different slope angle and angle of internal friction (Chakraborty and Kumar 2013) where, Q_{ult} (DLO-LA) is the ultimate bearing capacity of strip footing resting on slope from DLO-LA technique, Q_{ult} is the ultimate bearing capacity of strip footing resting on horizontal ground obtained from AASHTO (2012), and N_c and N_γ are the bearing capacity factors. Moreover, design charts are provided for estimating the ultimate bearing capacity of strip footing located on slope crest with aid of reduction coefficient (RC_{BC}) factor by altering various input parameters. Thereafter, DLO technique, combined with upper-bound limit analysis, had been considered by Zhou et al. (2018) to estimate the ultimate bearing pressure of strip footing resting on crest of slope. In the analyses, same geotechnical and geometrical (additional parameter was normalized setback distance, λ) parameters were considered as taken by Leshchinsky (2015). In the investigation, the obtained values of bearing capacity factor N_c had been compared with analytical solutions given by researches (Kusakabe et al. 1981; Georgiadis 2010) and the obtained magnitudes of bearing capacity factor N_γ had been compared with researches (Meyerhof 1957; Leshchinsky 2015). It had been reported that there was excellent match of outcomes between DLO technique and available analytical solutions. In the literature, different design charts ware provided for estimating the bearing capacity of strip footing. It had been also mentioned that the influence of normalized setback distance (λ) was substantial for determination of bearing capacity and failure mechanism of strip footing resting on crest of slope.

2.3.2.3 Soft computing approaches

Moayedi and Hayati (2018) had investigated the ultimate bearing capacity of strip footing resting on crest of dry-sandy slope with the aid of finite element analysis. The results of finite element analysis had been considered for soft computing based models, specifically, feed-forward neural network (FFNN), radial basis neural network (RBNN), general regression neural network (GRNN), support vector machine (SVM), tree regression fitting model

(TREE) and adaptive neuro- fuzzy inference system (ANFIS). In the analysis, different types of soils, setback distances, and slope angles were considered for evaluating the bearing capacity. The data were trained and tested in every model (FFNN, RBNN, GRNN, SVM, TREE and ANFIS) to check the prediction capability of the models. The prediction ability of the models had been verified through regression plots of training and testing stages and statistical parameters (R^2, the coefficient of correlation, and MSE, the mean square error. It has been reported that FFNN was the most efficient model to predict the output.

2.3.3 Code of practice for design and construction of foundations on or near slope

IS-1904 (1986) has provided various design guidelines for the construction of shallow footing resting on slope face. For footings located adjacent to the sloping ground in such a manner that the bottom of the footings of the same or adjacent structure are at different levels, the depth of the footings shall be such that the difference in footing elevations shall be subjected to the following limitations.

a. When the ground surface slopes downward adjacent to a footing, the sloping surface shall not intersect a frustum of bearing material under the footing having sides which make an angle of 30° with the horizontal for soil and horizontal distance from the lower edge of the footing to the sloping surface shall be at least 60 cm for rock and 90 cm for soil foundations (Fig. 2.19).

b. In the case of footings in granular soil, a line drawn between the lower adjacent edges of adjacent footings shall not have a steeper slope than 1V:2H (Fig. 2.20).

c. In case of footing of clayey soils, a line drawn between the lower adjacent edge of the upper footing and the upper adjacent edge of lower footing shall not have a steeper slope than 1V:2H (Fig. 2.20).

The above mentioned guidelines are not applicable under following conditions:

a. Where adequate provision is made for the lateral support (such as with retaining walls) of the material supporting the higher footing.

b. When the factor of safety of the foundation soil against shearing is not less than four.

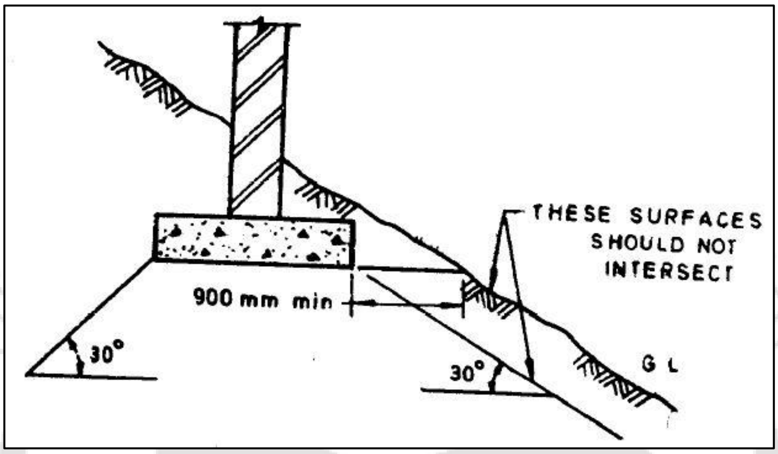

Fig. 2.19 Footing in sloping ground (IS: 1904-1986)

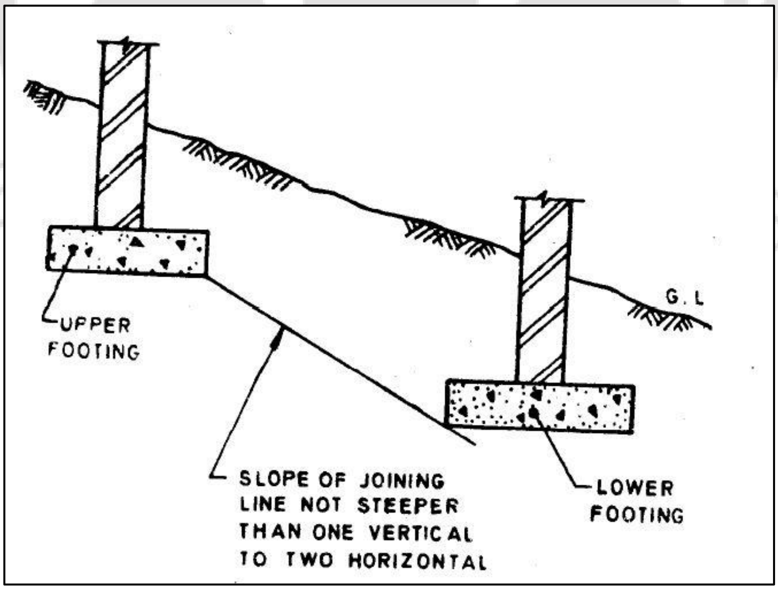

Fig. 2.20 Footing in granular soil or clayey soil (IS: 1904-1986)

AASHTO (2012) has given various design charts for shallow footings resting on or near the sandy or clayey slope. The ultimate bearing capacity of footing has been defined by Eq. 2.11.

$$q_u = cN_{cq} + 0.5\gamma BN_{\gamma q} \tag{2.11}$$

where, q_u is the bearing resistance (ksf), c is the cohesion (ksf), N_{cq} and $N_{\gamma q}$ are the bearing capacity factors, B is the width of footing (ft) and γ is the unit weight of soil (kcf). N_{cq} and $N_{\gamma q}$ are evaluated from Fig. 2.21 and Fig. 2.22.

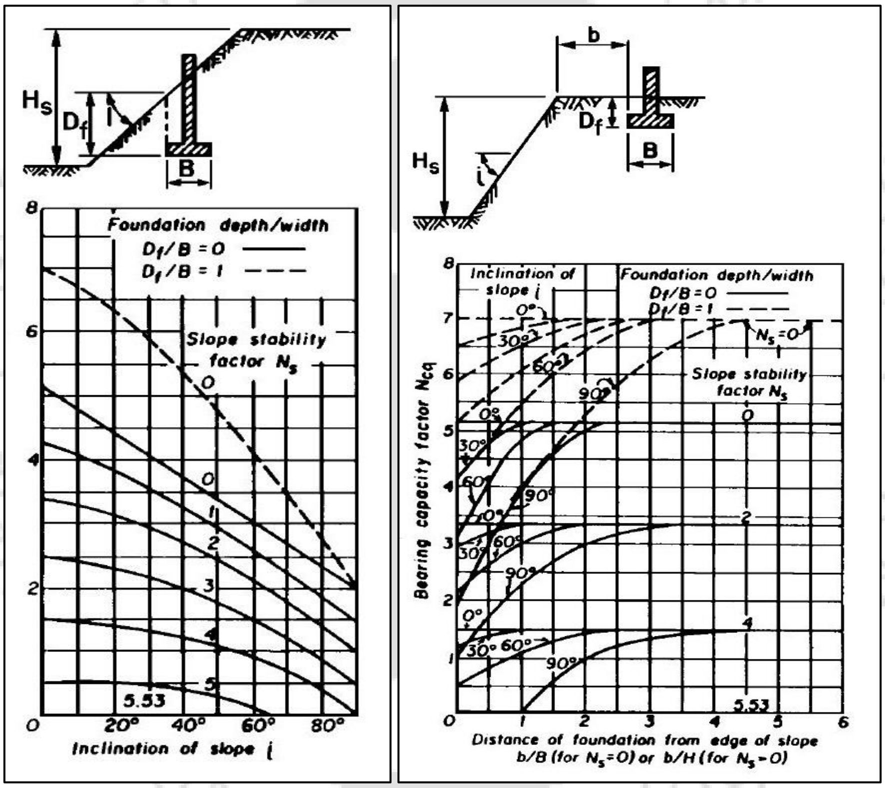

Fig. 2.21 Footing in cohesive soils and on or adjacent to sloping ground (AASHTO 2012)

In Fig. 2.2, the slope stability factor, N_s, can be obtained by following expressions

a. For $B < H_s$, $N_s = 0$ (2.12)

b. For $B \geq H_s$, $N_s = \dfrac{\gamma H_s}{c}$ (2.13)

where, H_s is height of slopping ground mass (ft)

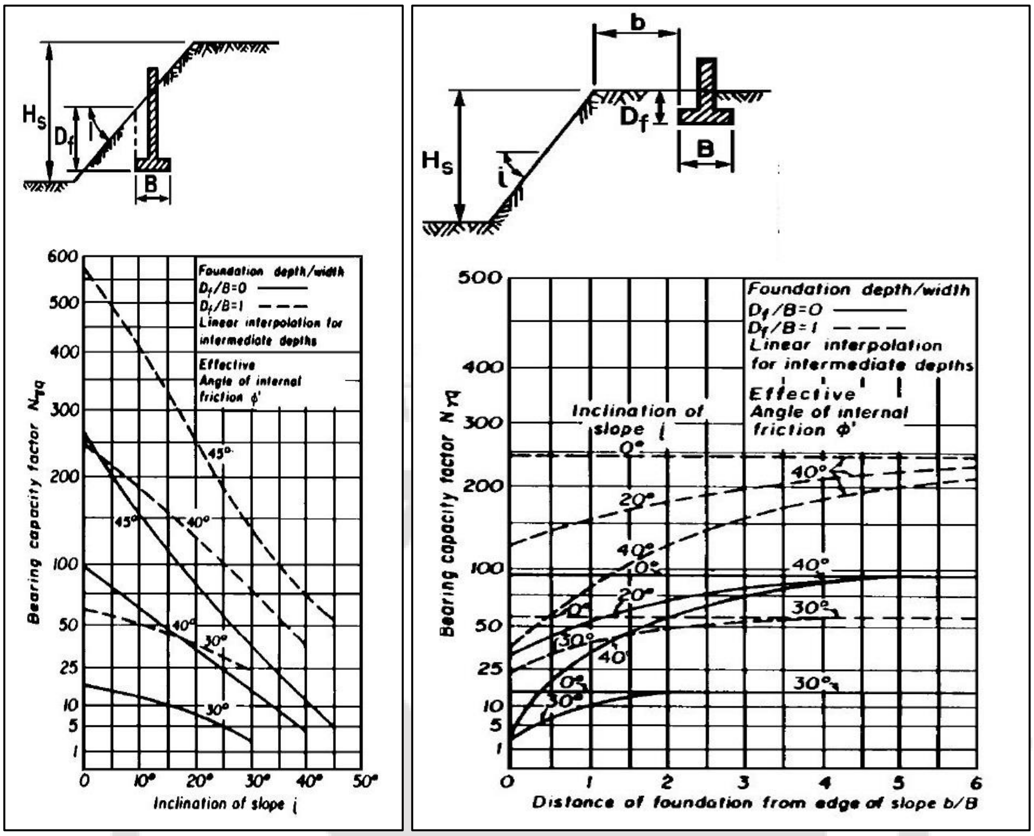

Fig. 2.22 Footing in cohesionless soils and on or adjacent to sloping ground (AASHTO 2012)

2.4 Critical Appraisal of the Literature and Gap areas

It is well understood that gradually increasing unplanned and unscientific hill-slope constructions lead to gradual or sudden failure of the existing slopes, and thus it is imperative to understand the scientific geotechnical mechanisms leading to the ultimate behavior of the foundations on slopes. In this context, review of the existing literature is carried out and the following inferences are drawn:

- The detailed literature review highlights that in comparison to the research conducted for estimating the bearing capacity of isolated or interfering shallow footings located on horizontal ground, the estimation of the bearing capacity of such foundations located on slopes did not receive ample attention.

- Most of the available research, conducted to identify the theoretical bearing capacity of shallow strip footings on slopes, is based on the experimental investigations on surface strip footings located on the crest of dry sand slopes. The prime focus have been laid on the estimation of the failure load, or bearing stress, from the load-settlement curves, and use the test results to device a prediction expression for bearing capacity considering the influences of various geotechnical and geometrical parameters. Footings of various shapes and sizes, having various embedment depths, can be located on the crest or face of the slope. It is important to study the behavior of isolated footings of various shapes resting on c-φ soils forming the hill-slopes, which has not been conducted until date.
- In actual practice, presence of multiple typologies of footings, coexistent with each other, and located on slopes comprising mostly c-φ soils, lead the problem to be a more complicated one. Closely spaced footings result in the increase in the foundation stresses due to the overlap of the pressure bulbs formed beneath the footing, which can lead to unaccounted exceedance of the shear strength of the soil, leading to slope collapse. It is immensely important to study the response of such interfering footings; however, there has been no literature available which are related to theoretical or numerical studies of interfering shallow foundations on slopes.
- All the existing theoretical expressions providing the bearing capacity of shallow foundations on slopes are based on the stress-equilibrium based approaches, wherein the soil is considered elastic until failure is achieved. Even though such assumptions might hold good for footings resting on horizontal ground due to the presence of apt lateral resistance against deformation, the same is not true for foundations on slopes. For footings located on or near the slope face, the bearing capacity of the footing is guided by the deformation of slope face, and thus, the bearing failure of footing and

stability failure of slopes are inseparable. Under such circumstances, it is important to estimate the bearing capacity based on a coupled stress-deformation analysis, which has not been paid much attention until date.

- In all the existing researches, importance has only been given to the attained failure load, without paying due attention to the evolution of failure mechanism. However, the latter is immensely important to be understood, as it will aid in the assessment of the progressive development of failure modes in the presence of multiple footings. Evolution of failure mechanism provides the detailed development of strains in the slopes, which would help to dictate proper mitigation steps long before failure stresses and strains are achieved. Further, such coupled stress-deformation analysis is likely to form the basis of displacement-induced failures, which are more prevalent in cases of foundations on slopes, rather than adopting conventional stress-based failure approaches.
- All the existing theoretical techniques consider general shear failure conditions and full mobilization of soil dilatancy during shearing and development of failure surface. However, soil dilatancy plays a major role in governing the stresses and strains generated in the foundation when subjected to footing load. Especially for sloping grounds, depending upon the location of the footing, where the slope face results in inadequate passive resistance against failure, soil dilatancy should substantially affect the bearing capacity and evolving failure mechanism. However, until date, no research has been directed in this regard.
- It is important to provide prediction expressions to estimate bearing capacity based on the influencing parameters, which would provide an aid to the designers and practicing engineers. It has been a common practice in the existing literature to extend Terzaghi's or Meyerhof's basic expressions for bearing capacity of footings located on horizontal

grounds. However, it is to be understood that failure mechanism of the footings located on slopes is quite different from that observed for footings located on horizontal grounds, especially due to the improper development of the confining passive zone towards the slope face. In such case, as mentioned earlier, the failure stress will be justifiably guided by the displacement-based mechanism. Thus, simple extensions of the existing theories by incorporating the influencing parameters would not suffice owing to the basic difference in the failure mechanisms for two different classes of problems. In this regard, advanced soft computation techniques may be resorted to; however, until date, no attempt has been made to devise such computation based bearing capacity prediction expressions, which is the need of the hour.

2.5 Objective of the Present Study

Based on the detailed literature review, and the critical appraisal of literature, the primary objectives of present work are formulated as follows:

- Assessment of bearing capacity and evolution of failure mechanism of isolated and interfering shallow footings located on the crest or face of slopes.
- Development of prediction expressions for bearing capacity of footings on slopes based on their FE coupled stress-deformation analysis based responses.
- Provision of technical recommendations about the choice of footing typologies to be adopted on hill-slopes for coexisting or interfering foundations.

2.6 Scope of the Present Study

In order to meet the stated objectives, the scopes of the current work are listed as follows:

- Conducting 2D and 3D Finite Element analysis to decipher the evolution of failure mechanism of the shallow footings located on hill-slopes.

- Validation of the developed numerical models with the aid of outcomes of experimental investigation and theoretical prediction available in literature.
- Inferring the influences of various geometrical (size, shape and embedment depth of footing, slope inclination, spacing between interfering footings and setback distance) and geotechnical (angle of internal friction, cohesion, unit weight, angle of dilatancy, elastic modulus of soil and footing) parameters on the bearing capacity and failure mechanism of isolated or interfering footings resting on crest or face of a slope.
- Application of Artificial Neural Network approach to develop bearing capacity prediction equations for various cases of isolated and interfering footings resting on the crest of a slope, based on the weights and biases of the corresponding trained networks. Further, the trained network is to be used to produce an importance ranking of the influencing parameters
- Study and assess the impact of coexisting footings of different shapes and arrangements, resting on crest of a slope, on its load carrying capacity and evolution of failure mechanism.
- Assessment of the importance and influence of soil dilatancy and flow rules (associated or non-associated) on the bearing capacity and failure mechanism of strip footings resting on horizontal and sloping grounds.

CHAPTER 3

NUMERICAL MODELLING

3.1 General

A numerical model is a mathematical simulation to a real physical process. A numerical model is different from a physical model prototype or a full-scaled field modelling. Other than being quick and providing the user a higher conditional variability, the numerical modelling is also very safe and many boundary conditions can be investigated using it. In recent decades, the Finite Element Method has been used increasingly for the analysis of stress, deformation, structural forces, bearing capacity, stability and ground water flow in geotechnical engineering applications. The development in mathematics along with the increase in the calculation power of computer has led to development of various robust and user-friendly software tools. In present study, the problem of estimation of bearing capacity of footings resting on the face, on or near the crest of the slope is modelled using two commercially available Finite Element program; and Plaxis 2D *v*2015.02 and Plaxis 3D *v*AE.01.

Plaxis 2D and 3D are finite element tools, used for two-dimensional and three-dimensional analysis of ground water flow, stability and deformation in geotechnical engineering (Plaxis Reference Manual 2015). The calculation is fully automated and is based on robust numerical procedures. Since its evolution in 1987 (Plaxis Reference Manual 2015), it has served the geotechnical engineers in solving simple to very complex problems. It is capable to deal with numerous intricate aspects of geotechnical structures. Plaxis 2D and 3D comprises advanced constitutive models for analysis of non-linear, anisotropic and time-dependent behaviour of soil or rock. Necessary attentions have to be taken for dealing with non-hydrostatic and hydrostatic pore pressure in soil.

3.2 Geometry and Boundary Condition

Plaxis 2D has been considered for two-dimensional finite element (FE) simulation. 2D finite element models may be either plane-strain or axisymmetric. A plane-strain model is used for geometries with a uniform cross-section along the longitudinal direction (perpendicular to the cross-section), and is assumed subjected to identical stress state and loading scheme along the longitudinal direction. The displacements and strains developed in the longitudinal direction are assumed zero; however, the normal stresses in longitudinal direction are fully taken into consideration. An axisymmetric model is considered for circular or cylindrical systems possessing a uniform radial cross-section and loading scheme around the central axis, where the deformation and stress state are assumed identical in any radial direction.

In Plaxis 2D analysis, plane-strain criterion has been considered for modelling strip footing resting on horizontal ground, located on the slope crest, or located near the slope face. In Plaxis 3D analysis, the plane-stress criterion is not necessary for modelling, as the entire footing can be modelled as per its aspect ratio. Theoretically, when B/L [B = width of footing and L = length of footing] is nearly equal to zero ($L = \infty$), a plane-strain case will exist in the soil mass supporting the foundation. For most practical cases, when $B/L \leq 1/5$ - $1/6$, the plane strain theories will provide a fair result (Das 2009), even though the problem is actually a 3-D problem. Hence, in the present investigation, following the given guideline, even though the strip footings ($B/L \leq 1/6$) could have been modelled using a plane-strain condition, in order to comprehend the actual response of the interfering strip footings resting on slope, a 3-D analysis has been adopted (as elaborated in Chapter 5).

3.2.1 Representation of horizontal ground through FE model

A strip footing of width B has been considered to be resting the ground surface of a homogeneous soil. For establishing an optimum model dimension, sensitivity analysis has been carried out for various widths and depths of the domain, the results of which are illustrated in Fig. 3.1. It is perceived that the non-dimensional bearing capacity ($q_u/\gamma B$) remains unaffected beyond an optimal domain dimension (depth and width), which is obtained as $(d_D/B)_{optimal}$ = $(b_D/B)_{optimal}$ = 3 [q_u is the ultimate bearing capacity, γ is the unit weight of the soil, B is the width of the footing, d_D is the domain depth, and b_D is the clear distance between the footing and the vertical boundary of the domain]. Figure 3.2 provides the optimum domain definition of the numerical model used in the present study, where the width and depth of the model geometry have been taken as 7B and 3B, respectively. Standard fixities have been used for the numerical model, wherein the vertical edges of the model are restricted from horizontal deformation and the bottom boundary is considered non-yielding along both horizontal and vertical directions.

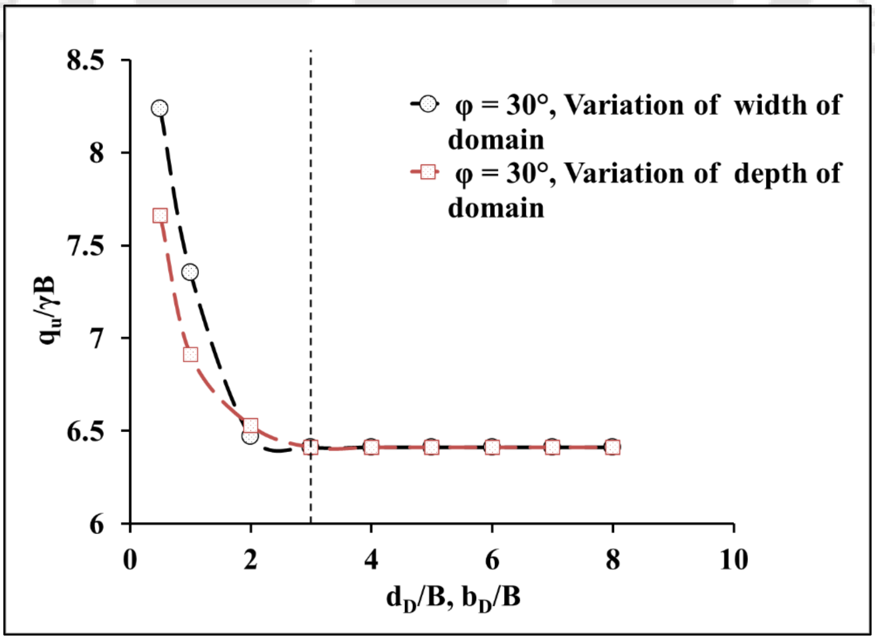

Fig. 3.1 Sensitivity analysis to determine the optimum dimensions of the model

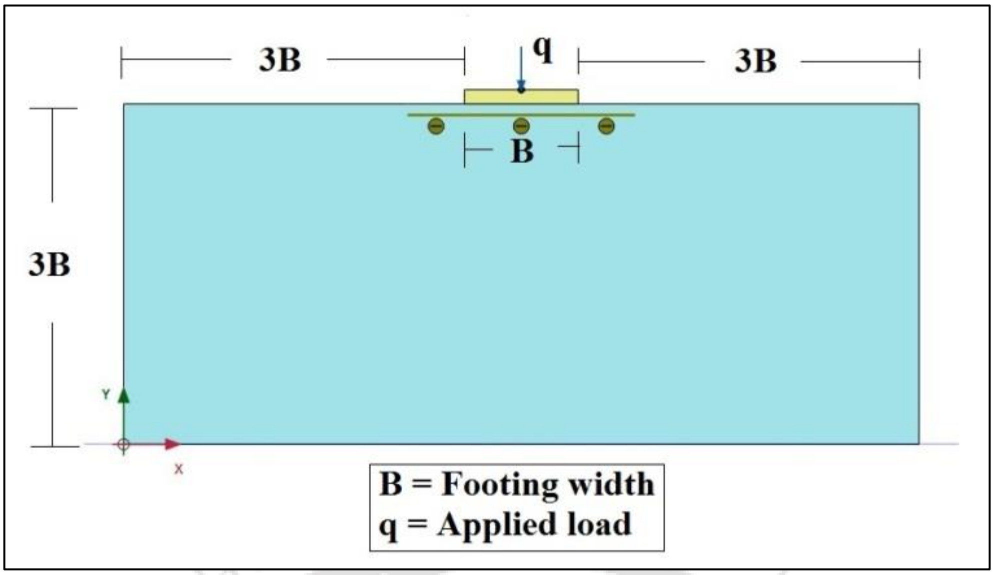

Fig. 3.2 Typical representation of the optimum model geometry

3.2.2 Representation of sloping ground through FE model

The model geometry has been developed for footing located on the crest or the face of the slope, as shown typically in Fig. 3.3 for isolated strip and interfering strip footings. In accordance to the Boussinesq's elastic stress theory, the ''0.1*q*'' (*q* is the stress applied on the footing up to its failure) stress contour represents the outermost significant isobar, beyond which the effect of the applied stress is considered negligible. The model dimensions have been so chosen that the significant isobar is not intersected by the model boundaries (Fig. 3.3).

In the numerical model, ''standard fixity'' condition has been employed. Horizontal fixity was applied to the lateral vertical edges, while the bottom edge of the model is assumed non-yielding and restrained from both vertical and horizontal movements. The inclined slope face is devoid of any fixity, allowing free deformation subjected to its own weight and loading of the footing.

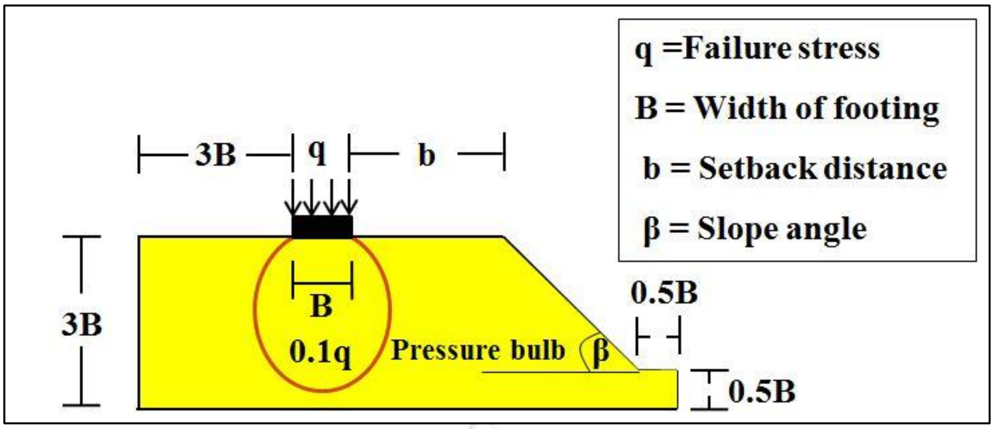

(a)

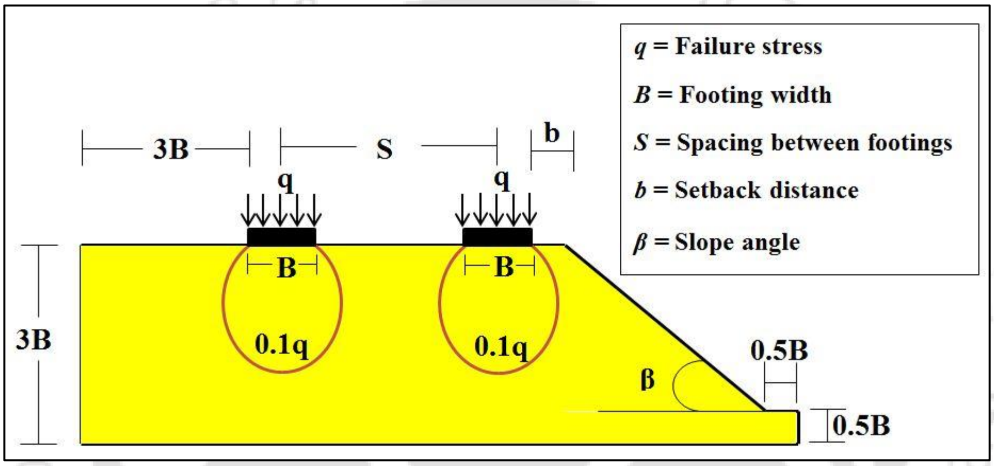

(b)

Fig. 3.3 (a) Typical model diagram of isolated strip footing placed near slope (not to scale); (b) Typical geometry for of interfering strip footings located near slope (not to scale)

3.2.3 Locations of the footing

Figure 3.4 portrays the various positions of strip footings located near the sloping surface, with or without embedment depth. For every position of footing, the geotechnical and geometrical parameters have been varied for evaluation of bearing capacity and failure mechanism developed underneath the footing.

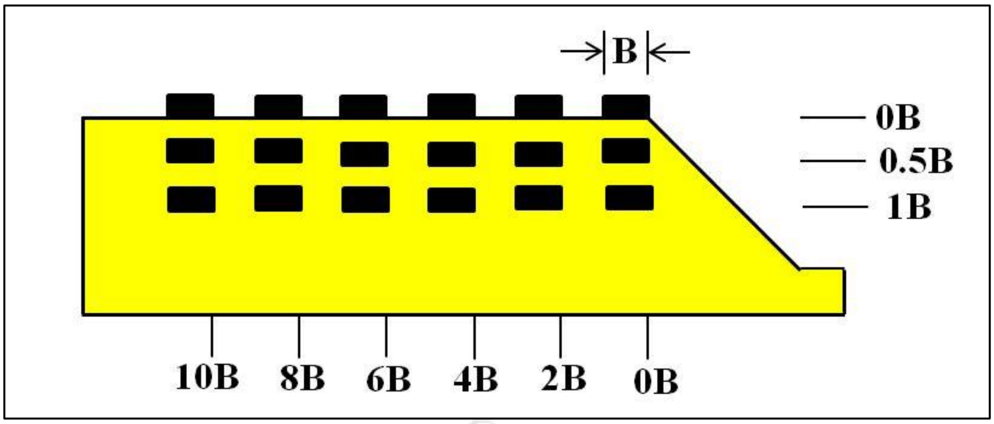

Fig. 3.4 Typical positions of footings near the slope as considered in the present study

3.3 Meshing and Discretization

3.3.1 2D Meshing and discretization scheme

To perform the finite element analysis, the model geometry is discretized into smaller finite number of elements. For the Plaxis 2D finite element mesh, the basic soil elements are the 6-noded and 15-noded triangular elements. In the present investigation, 15-noded triangular elements were used (Fig. 3.5) as it provides more precision to the determination of displacements and stresses since higher number of nodes and Gauss points are available as compared to the 6-noded triangular elements. Plaxis 2D program allows for a fully automatic generation of finite element meshes using the 'robust triangulation scheme'. In Plaxis 2D, five basic meshing schemes are available, namely 'Very coarse', 'Coarse', 'Medium', 'Fine', and 'Very fine', governed by their associated 'Mesh coarseness factor'. The mesh should be sufficiently and optimally fine to obtain accurate numerical results. A very coarse mesh fails to capture the important characteristic responses of the domain. Beyond optimally fine meshes, there are chances of the accumulation of numerical errors, thereby producing inaccuracy in the obtained information. Moreover, very fine meshing should be avoided since it will take excessive time for calculations. Any basic meshing scheme can be adopted, with further provisions of local refinements, as demanded by the merit of the problem and the location of the response points in the numerical simulation. A detail of the element formulation in PLAXIS 2D and 3D is provided in (Plaxis Reference Manual 2015).

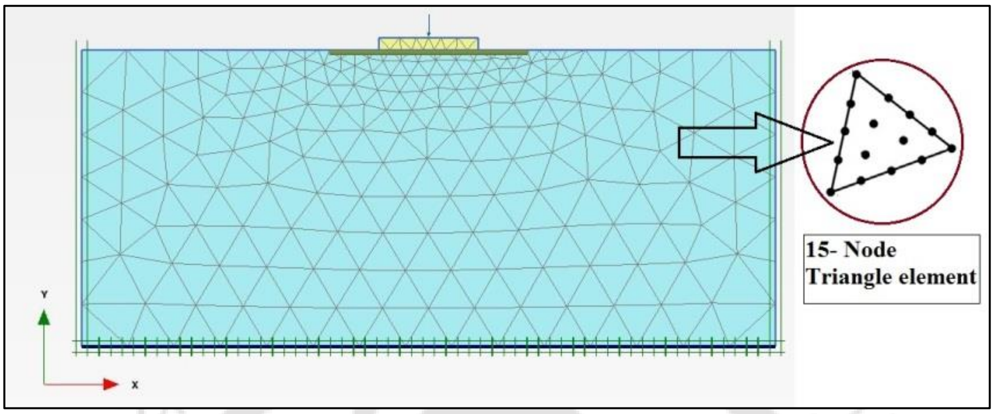

(a)

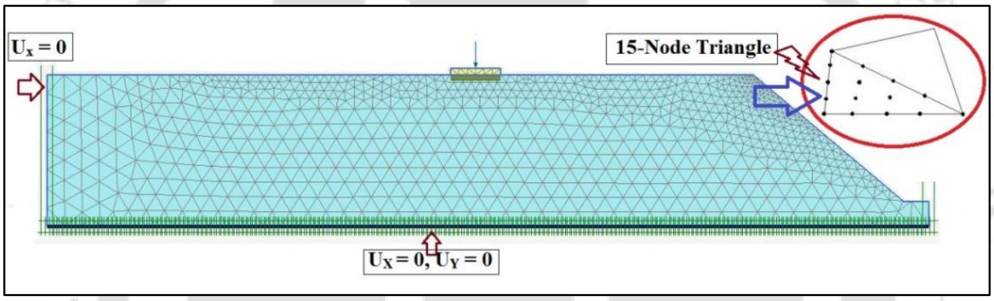

(b)

Fig. 3.5 (a) Typical meshing scheme adopted for 2D horizontal ground; (b) Typical meshing scheme adopted for 2D sloping ground

In Plaxis 2D, only triangular elements are available for modelling as a result to consider the influence of other element types available in GeoStudio 2007 Sigma/W module has been considered. Sigma/W is Finite Element module that is integrated with GeoStudio-2007 and can be considered to perform stress and deformation analysis of soil. 'Rectangular grid of Quads', 'Triangular grid of Quads' and 'Quad and Triangular' are the meshing patterns available in this module. It is possible to analyse both simple and complex problems with the help of Sigma/W. It is formulated for 2D plane-strain or axisymmetric problems. It is equipped with different analysis types such as in-situ analysis, stress redistribution, load deformation, volume change and dynamic deformation analysis. A wide range of material model is also available specifically linear elastic, hyperbolic non-linear elastic, anisotropic elastic and elastic plastic models. The working principle of Sigma/W is formulated for incremental analysis. For each load step, incremental displacement at each node resulting from the incremental load is computed and added to the displacement at the beginning of the load step to give the total displacement.

3.3.2 3D Meshing and discretization scheme

In the 3D finite element investigation, the domain of the geometry has been discretized into finite number of elements. In order to determine accurate displacements and stresses, 10-noded tetrahedral elements was considered as it offers more nodes and Gauss points (Fig. 3.6). Plaxis 3D program generates automatic finite element meshes with aid of ‘robust triangulation technique’. Plaxis 3D provides five basic meshing schemes specifically, ‘very coarse’, ‘coarse’, ‘medium’, ‘fine’, and ‘very fine’. Each meshing scheme can be progressively refined with user defined mesh coarseness factor. The adopted mesh should be adequately and optimally fine to attain precise numerical outcomes.

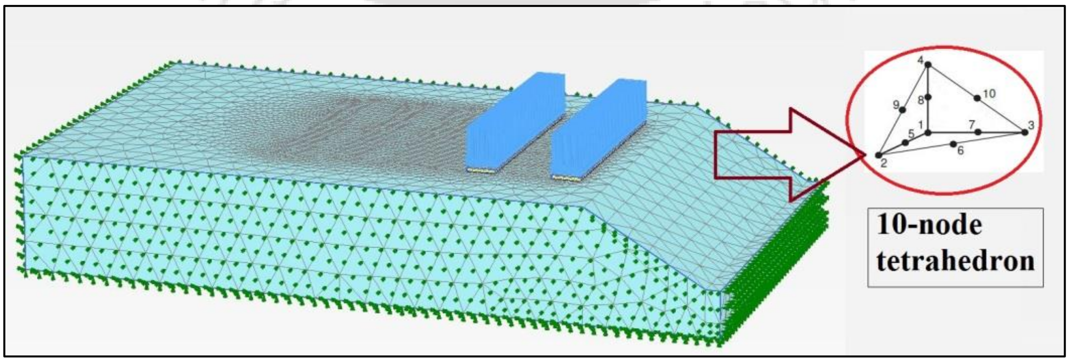

Fig. 3.6 Typical meshing scheme for 3D sloping ground

3.3.3 Basic mesh refinement: Global coarseness

The mesh generator needs a global meshing parameter that signifies the average element size, l_e. In Plaxis 2D, l_e can be evaluated from the outer geometry dimensions (X_{min}, X_{max}, Y_{min}, Y_{max}). In Plaxis 3D, this parameter can be estimated from outer geometry dimensions (X_{min}, X_{max}, Y_{min}, Y_{max}, Z_{min}, Z_{max}). The final element dimension has been evaluated according to Eqs. 3.1 and 3.2.

For Plaxis 2D, $$l_e = r_e \times 0.06 \times \sqrt{(X_{\max} - X_{\min})^2 + (Y_{\max} - Y_{\min})^2} \quad (3.1)$$

For Plaxis 3D, $$l_e = r_e \times 0.05 \times \sqrt{(X_{\max} - X_{\min})^2 + (Y_{\max} - Y_{\min})^2 + (Z_{\max} - Z_{\min})^2} \quad (3.2)$$

The average element size is determined based on a parameter called Relative element size factor (r_e). The element distribution is made based on the five global levels (very coarse, coarse, medium, fine and very fine). The magnitudes of the 'Relative element size' (for Plaxis 2D, it is $r_e \times 0.06$, and, for Plaxis 3D, it is $r_e \times 0.05$) for the different discretizations is given in Table 3.1. The multiplying factors, 0.06 and 0.05, as mentioned earlier, are fitting constants that are used for determination of relative element size.

Table 3.1 Magnitude of relative element size factor for different meshing schemes

Meshing schemes	Relative element size
Very coarse	2.00
Coarse	1.33
Medium	1.00
Fine	0.67
Very fine	0.50

The exact number of elements depends on the shape of the geometry and optional local refinement setting. The number of elements is not influenced by the type of elements parameter. 2D Meshing composed with 15-noded elements provides a much finer distribution of nodes and hence much more accurate outcomes than a similar mesh made of an equal number of 6-noded elements. However, the use of 15-node elements is more time consuming than considering 6-node elements, although the present computational facilities overcomes the computational time issues. In a similar manner, 3D analysis, 10-noded tetrahedron elements have been considered for simulation.

3.3.4 Enhanced mesh refinement: Local coarseness

The mesh should be sufficiently and optimally fine to produce accurate result from the numerical investigation. Apart from adopting global refinement as dictated by the user, Plaxis applies automatic or user-defined local mesh refinement strategies around structural elements, loads and prescribed displacements. Local refinement is necessary in the model geometry clusters where large stress concentrations are expected to occur. The enhanced mesh refinement is used to automatically generate a good quality mesh, which is qualitatively defined as a mesh having elements with the least amount of skewness and distortion. These automatic refinements, with the aid of an implicit local element size-multiplication factor, are applied in following cases:

- Structural elements, loads, prescribed displacements: The coarseness factor will be 0.25, except when prescribed displacements or loads have been applied along a whole edge of the geometry.
- The distance between points or lines is rather close, which requires a smaller element size to avoid large aspect ratio.
- An angle between geometry lines, other than a multiple of 90°, to allow for more accurate stresses around geometry discontinuities. The local element size factor will be multiplied according to Fig. 3.7.

In a model geometry, when two geometry lines are perpendicular or oriented to 180º to each other, the local element size factor will automatically be set to 1, and hence there would be no requirement of further enhanced local refinement. The angles of 90º, 180º and 270º conforms to the maximum exposed geometry in a Cartesian quadrant system. When two geometry lines nearly overlap (0º or 360º), the minimal exposed geometry condition is generated. Under such case, the size and skewness of the already generated element are further reduced to smallest, and thus the least magnitude of the enhanced refinement is used. For any other intermittent angles, the enhanced mesh refinement factor is interpolated as per Fig. 3.7. The enhanced mesh refinement value is used as a scalar multiplier to alter the already generated local element from the basic refinement scheme.

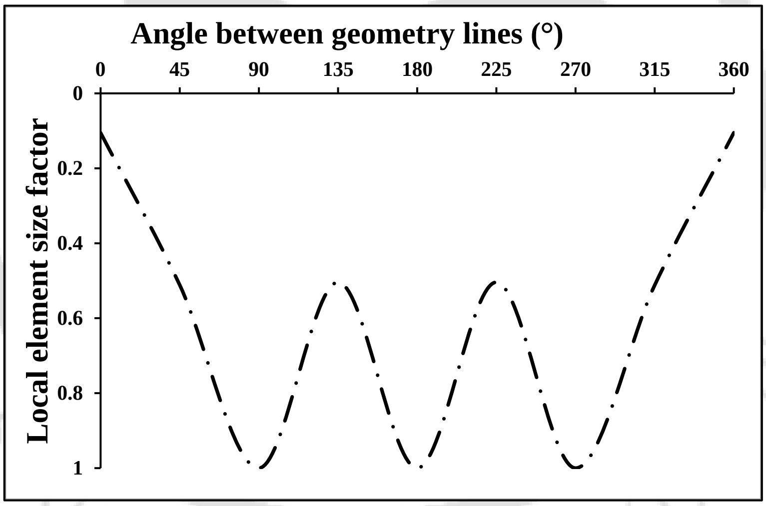

Fig. 3.7 Local element size factor for geometry lines at different angles

3.4 Material Models

In Plaxis FE analysis, various material models are available to represent the stress-strain behaviour of the soils, specifically, Linear elastic model (LE), Mohr-Coulomb model (MC), Hardening Soil model (HS), HS small model (HSsmall), Modified Cam-Clay model (MCC), Soft Soil model (SS), Soft Soil creep model (SSC), NGI-ADP model, UDCAM-S model, Sekiguchi-Ohta model, and UBC-3D PLM model. LE model is used either for representing stiff structures embedded within the soil, or the soil itself, on the condition that the generated stresses are not expected to exceed the elastic limit of the soil. MC model is a first-order approximation of soil or rock behaviour with constant stiffness. HS model is used for simulating the behaviour of sands and gravel, as well as softer types of soil such as clays and silts, specifically for incorporating stress-dependent stiffness moduli. HSsmall model is considered for simulating the different response of soil to small strains (strain level below 10^{-5}) and large strains (strain level above 10^{-3}); this model accounts for the stiffer response of soil at small strains and its degradation with the increased straining, as well as includes hysteretic material damping during cyclic straining. SS model is a cam-clay type model especially meant for primary compression of near normally consolidated clay-type soils, including peat. SSC model is used to simulate the secondary compression or the time-dependent creep behaviour of soft soils like normally consolidated clays, silts and peat, and can be used for the analysis of the foundation and embankment settlements. Modified Cam-Clay model is an elastic plastic strain-hardening model that is used to simulate the behaviour of normally consolidated soft soils, incorporating the variation of strength with the void ratio of the soil. NGI-ADP is an anisotropic undrained shear strength model that finds its usage in the onshore and offshore applications in undrained silts and clays. UDCAM-S model is a simplified undrained cyclic accumulation model that is used to deal with the undrained soil behaviour and the degradation of strength and stiffness in cyclic loading of clay or very low permeable silty soils. Sekiguchi-Ohta model incorporates anisotropic yield contours and can be used as a time-independent inviscid model, or, a time-dependent viscid model. UBC3D-PLM model is an advanced model for simulation of the liquefaction behaviour under dynamic applications. Each of the models has their own specific usage and limitations. The choice of a model to be used in the simulation depends on the attributes of the problem to be solved.

Moreover, the application of the model also depends upon the parameters assessed for the geomaterial. In most cases until date, estimation of the MC shear strength parameters has been more common and popular for the representation of the constitutive behaviour of the soil. In the present study as well, maintaining the simplicity of usage of the MC model, the same has been used for the rest of the study.

3.4.1 Constitutive behavior of soil

In the present study, elastic-perfectly plastic Mohr-Coulomb (M-C) model has been considered for soil model. M-C model includes 5 inputs specifically, strength parameter (cohesion c, angle of internal friction φ and ψ as dilatancy angle) and deformation parameters (Elastic modulus E and Poisson's ratio v). Concept of plasticity theory confirms that, if the dilatancy angle is not similar to the friction angle, the material shows a non-associated flow rule. The dilatancy angle varies from zero to the soil friction angle. Correspondingly, dilative coefficient, η, which relates the dilatancy angle to the soil friction angle, is defined as $\eta = \psi / \varphi$, where, φ is the friction angle and ψ is the dilatancy angle. Theoretically, the magnitude of dilative coefficient is $0 \leq \eta \leq 1$. The case η =1 directs that the material follows an associated flow rule (Vermeer and de-Borst 1984; Nova and Montrasio 1991; Drescher and Detournay 1993; Bolton and Lau 1993; Manoharan and Dasgupta 1995; Manzari and Nour 2000; Yin et al. 2001; Erickson and Drescher 2002; Shiau et al. 2003; Xiao et al. 2007; Loukidis and Salgado 2009; Benmebarek et al. 2012). In the present investigation, for most of the cases, associated flow rule has been taken into account, except for Chapter 8, which highlights the influence of non-associated flow rule on some typical observed responses, thus elucidating the importance of non-associated flow rules in geotechnical responses. The typical soil types and their parameters considered in the present study (Arora 2011) is given in Table 3.2, while some specific parameters wherever used are mentioned in their respective sections.

Table 3.2 Typical soil parameters

Soil types	Cohesion (c) (kPa)	Angle of internal friction (φ)°	Dry unit weight (γ) (kN/m^3)	Modulus of elasticity (E) (MPa)	Poisson's ratio (ν)
Dense sand	0	40	19	40	0.3
Medium dense sand	0	30	17	20	0.28
Loose sand	0	20	16	15	0.25
c-φ soil	20	30	18	20	0.3

3.4.1.1 Shear strength parameters of soil

For the constitutive model chosen for soil, the governing shear strength parameters, as already mentioned, are angle of internal friction (φ), cohesion (c), and angle of dilatancy (ψ). Angle of internal friction is the most important strength parameter of sand. The variation of angle of internal friction (φ) on the ultimate bearing capacity of the footing has been studied for various scenarios of foundation on slopes with the aid of FE analysis and the results are presented in the corresponding sections. In general, the influence of the variation of angle of internal friction of soil has been studied for the range of 10° to 40°, with some variations as and wherever required. Cohesion governs the strength characteristics of the c-φ soils. To study the effect of cohesion on the ultimate bearing capacity of the footing for different scenarios, analyses have been carried out for different values of cohesion in the range of 5 kPa to 80 kPa, with suitable variations as and whenever required. In Plaxis, even for cohesionless sand at low stress level, e.g. near ground surface, it is good to give a nominal cohesion value for numerical stability in finite element calculations otherwise truncation error may occur in numerical computation. Some numerical issues may also be observed such as node of the soil undergoes extreme displacement, e.g. shoot off, which can be observed in the output results. The error 'soil body seems to collapse' may also be displayed due to excessive settlement and premature collapse due to the absence of cohesive bond. Therefore, a nominal cohesion value of 1kPa was adopted in the modelling.

In the current investigation, the impact of dilatancy on ultimate bearing capacity and failure mechanism of footing resting on horizontal ground or resting near the slope has been investigated. Concept of plasticity theory confirms that, if the dilatancy angle is not similar to the friction angle, the material shows a non-associated flow rule. The dilatancy angle varies from zero to the soil friction angle. Correspondingly, dilative coefficient, η, which relates the dilatancy angle to the soil friction angle, is defined as $\eta = \psi / \varphi$, where, φ is the friction angle and ψ is the dilatancy angle. Theoretically, the magnitude of dilative coefficient is $0 \leq \eta \leq 1$. The case η =1 directs that the material follows an associated flow rule (Vermeer and de-Borst 1984; Nova and Montrasio 1991; Drescher and Detournay 1993; Bolton and Lau 1993; Manoharan and Dasgupta 1995; Manzari and Nour 2000; Yin et al. 2001; Erickson and Drescher 2002; Shiau et al. 2003; Xiao et al. 2007; Loukidis and Salgado 2009; Benmebarek et al. 2012). In the present investigation, for most of the studies, associated flow rule has been taken into account, i.e. for each value of friction angle φ, dilation angle ψ has been considered equal to φ. However, for few specific scenarios, the effect of non-associated flow rule has been investigated, wherein the angle of dilatancy is considered different from the angle of internal friction of soil.

3.4.1.2 Stiffness parameters of soil

Plaxis considers the Young's modulus as the basic stiffness modulus in the Mohr-Coulomb model. For a particular set of values of other soil parameters, the effect of change in the value of Young's modulus of soil (*E*) on the ultimate bearing capacity of the footing has been studied and presented in the corresponding sections. The magnitude of Young's modulus of soil (*E*) has been varied in range of 10 MPa to 90 MPa. The Poisson's ratio for various types of soil has been representatively considered as provide in Table 3.2.

3.4.1.3 Unit weight of soil

Plaxis provides the options of saturated and unsaturated weight of the soil material to be used for the FE analysis. The saturated unit weight (γ_{sat}) refers to the total unit weight of the soil skeleton including the fluid in the pores, while the unsaturated unit weight (γ_{unsat}) refers to the total unit weight when the pores are partially filled with air. The unsaturated weight γ_{unsat} applies to all material above the phreatic level, while saturated weight γ_{sat} or the submerged unit weight γ_{sub} applies to all material below the phreatic level. The dry unit weight of the soil γ_d forms a special case of the unsaturated condition wherein the pores are completely filled with air. In the current investigation, water table has not been considered; as a result, the simulation has been carried out with γ_d, the magnitude of the dry unit weight has been used as γ_{unsat}. In the simulations, wherever required, the value of γ_d has been varied from 12 kN/m^3 to 21 kN/m^3 to check the influence of dry unit weight on ultimate bearing capacity of footing.

3.4.1.4 Slope inclination (β)

In the analysis, various slope angles have been considered to check the impact of slope angles on bearing capacity and failure mechanism of footing located on or near slope. The slope angles have been considered in the analysis in the range of 10° to 40°. For same stiffness and strength parameters of the slope, the steepness of the slope controls the volume of soil that would be subjected to displacement due to the loading of the supported footing.

3.4.2 Footing

In the present investigations, the footing has been modelled in two different techniques. For most of the studies, the footing is modelled with the aid of geometry lines as per the shape of the footing required for various scenarios. The thickness of the footing is considered 250 mm throughout the investigation, based on the building surveys conducted in the North-eastern regions of India (NDMA 2013). The material for the footing is considered concrete of required specification, as described in following sections. For some of the studies, the footing has also been modelled as equivalent plate element, whose axial and bending stiffness are adjusted according to the chosen section of the footing as used in practice, while maintaining the same thickness of 250 mm. The thickness of the footing is so chosen that the footing do not exhibit bending behaviour when subjected to loading. Thus, the footing has been considered as a rigid footing for the present investigation.

3.4.2.1 Footing width (B)

The effect of footing width (*B*) on the ultimate bearing capacity and failure mechanism has been examined for all the footing locations as mentioned previously. Three different footing widths (B = 0.5 m, 1 m and 2 m) has been considered in the analysis.

3.4.2.2 Embedment depth of footing (D_f)

In the analyses, various embedment depth of the footing has been considered to check its influence on the ultimate bearing capacity and failure mechanism of footing. The embedment depth of footing has been varied from 0 (footing resting on surface) to 1.5B, so that the condition of shallow foundations are maintained.

3.4.2.3 Setback distance (b)

The setback distance is the distance between the edge of footing and the slope crest. In the simulations, the influence of setback distance on ultimate bearing capacity of footing and failure mechanism has been investigated. The setback distance and the slope inclination simultaneously controls the development of the confining passive zone and the resulting displacement developed towards the face of the slope, which in turn governs the failure mechanism of the footing. In this regard, the setback distance has been varied from 0 to 10B for different scenarios and types of footings.

3.4.2.4 Constitutive model for footing

The rigid rough strip footing, formed with M_{20} concrete material, is represented by using linearly elastic (LE) model. LE model signifies Hooke's law of isotropic linear elasticity. The model includes two elastic stiffness parameters, specifically Young's modulus, *E*, Poisson's ratio, *ν*. Since the footing is considered rigid and stiff enough, which does not exhibit bending and any permanent deformation in itself due to the subjected loading, the linear elastic model is justified to represent the behaviour of the footing. The parameters of the LE model that are used to represent the footing are tabulated in Table 3.3.

Table 3.3 Material parameters used to represent the LE footing

Unit weight (γ) (kN/m^3)	Modulus of elasticity *E* (GPa)	Poisson's ratio (ν)
25	22	0.15

3.4.2.5 Non-porous behaviour

In non-porous criterion, neither initial nor excess pore pressures will be taken into account in the designated geometry cluster. This behaviour is appropriate in the modelling of concrete or structural behaviour. Non-porous behaviour has been often considered in combination with the Liner elastic model. The input of saturated unit weight and permeability is not applicable for non-porous materials. In the present analysis, the footing has been modelled as non-porous material.

3.4.2.6 Interface and interface strength (R_{inter})

The interface elements are required in the simulation to establish proper soil-structure interaction in the presence of two different materials in the model domain. The interface is considered at the contact of two different materials that are expected to generate extreme stresses during relative shearing. The interface elements derive their properties from the adjacent materials in contact. The prime interface parameter is the strength reduction factor R_{inter}. Coulomb method has been considered to differentiate between elastic behaviour, where small displacement can arise within the interface, and plastic interface behaviour when permanent slip may occur.

For interface to remain elastic, the shear stress τ is given by Eq. 3.3 and Eq. 3.4.

$$|\tau| < \sigma_n \tan \varphi_i + c_i \tag{3.3}$$

$$|\tau| = \sqrt{\tau^2_{s1} + \tau^2_{s2}} \tag{3.4}$$

where, τ_{s1} and τ_{s2} are shear stress in the two (perpendicular) shear directions and σ_n is the effective normal stress.

For plastic behaviour, τ is given by Eq. 3.5.

$$|\tau| = \sigma_n \tan \varphi_i + c_i \tag{3.5}$$

where, φ_i and c_i are the angle of friction and cohesion (adhesion) of the interface. The strength properties of interfaces are linked to the strength properties of a soil layer. Each data set has an associated strength reduction factor for interfaces (R_{inter}). The interface properties are calculated from the soil properties in associated data set and the strength reduction factor by applying the following rules given by Eqs.3.6 - 3.8.

$$c_i = R_{inter} c_{soil} \tag{3.6}$$

$$\tan \varphi_i = R_{inter} \tan \varphi_{soil} \leq \tan \varphi_{soil} \tag{3.7}$$

$$\psi_i = 0° \text{ for } R_{inter} < 1, \text{ otherwise } \psi_i = \psi_{soil} \tag{3.8}$$

An appropriate value of interface strength reduction factor (R_{inter}) has been chosen for simulating interface parameters. The same elastic modulus and shear strength parameters have been assumed for interface elements as considered for the adjacent soil elements (R_{inter} = 1); therefore the footing exhibits rough strip footing. As a result, no slip mechanism has been incorporated between footing and soil. The failure mechanism generated beneath the footing resting on horizontal ground has been postulated by Terzaghi (1943) on the basis of the assumption that the base of the footing is rough. In the same fashion, the base of the footing has been considered as rough base by taken into account R_{inter} = 1 to comprehend the failure mechanism of footing resting on or near the slope. Such interface definition ensures full contact and no-slippage mechanism in the numerical model, which ensures the soil and the structural node move together without the generation of any relative displacement. In the present numerical investigation, only vertical load has been considered over the footing as assumed by Terzaghi (1943). In case of practical situation, vertical load, horizontal load and moment are acted over the footing and hence the slip may happen between footing and soil. Even with the vertical load, if the footing moves toward the direction of the slope face, slippage may occur in practice. Such slippage mechanism would be more vivid in the case of surface footing, while restrictive with the increment in the embedment depth.

The stiffness matrix of interface can be determined by Newton-Cotes integration points (Nasr 2014). The interaction between the soil and the bottom surface of the shallow footing will be described by embedded interface elements (Plaxis Reference Manual 2015). These interface elements are based on 3-noded line elements with pairs of nodes instead of a single node. The interaction can be represented by a skin traction $\underline{t}^{skin}$. The development of the skin traction can be regarded as an incremental process (Eq. 3.9).

$$\underline{t}^{skin} = \underline{t}_0^{skin} + \Delta \underline{t}^{skin} \tag{3.9}$$

In Eq. 3.9, $\underline{t}_0^{skin}$ denotes initial skin traction $\Delta \underline{t}^{skin}$ denotes the skin traction increment. The constitutive relation between the skin traction increment and relative displacement increment is formulated as Eq. 3.10.

$$\Delta \underline{t}^{skin} = \underline{\underline{T}}^{skin} \Delta \underline{u}_{rel} \tag{3.10}$$

In Eq. 3.10, $\underline{\underline{T}}^{skin}$ denotes the material stiffness of the embedded interface element in the global coordinate system. The increment in relative displacement vector $\Delta \underline{u}_{rel}$ is defined as the difference in the increment of the soil displacement and the increment of the footing displacement (Eq. 3.11-3.13).

$$\Delta \underline{u}_{rel} = \Delta \underline{u}_f - \Delta \underline{u}_s = \underline{\underline{N}}_f \Delta v_f - \underline{\underline{N}}_s \Delta v_s = \underline{\underline{N}}_{rel} \Delta v_{rel} \tag{3.11}$$

where, $$\underline{\underline{N}}_{rel} = \left[\underline{\underline{N}}_f - \underline{\underline{N}}_s \right] \tag{3.12}$$

$$\Delta v_{rel} = \left[\Delta v_f - \Delta v_s \right] \tag{3.13}$$

The traction increment at the bottom skin of the footing can be described as Eq. 3.14.

$$\int \Delta \underline{u}_{rel}^T \Delta \underline{t}^{skin} \, dS = \delta \underline{v}_{rel}^T \int \underline{\underline{N}}_{rel}^T \underline{\underline{T}}^{skin} \underline{\underline{N}}_{rel} \, dS \Delta \underline{v}_{rel} = \underline{\underline{K}}^{skin} \Delta \underline{v}_{rel} \tag{3.14}$$

In this Eq. 3.14, the element stiffness matrix $\underline{\underline{K}}^{skin}$ represents the interaction between the base of the footing skin and the soil and consists of four parts (Eq. 3.15).

$$\underline{\underline{K}}^{skin} = \begin{bmatrix} \underline{\underline{K}}_{ff}^{skin} & \underline{\underline{K}}_{fs}^{skin} \\ \underline{\underline{K}}_{sf}^{skin} & \underline{\underline{K}}_{ss}^{skin} \end{bmatrix} \tag{3.15}$$

The matrix $\underline{\underline{K}}_{ff}^{skin}$ represents the contribution of the footing nodes to the interaction, the matrix $\underline{\underline{K}}_{ss}^{skin}$ represents the contribution of the soil nodes to the interaction and the matrices $\underline{\underline{K}}_{fs}^{skin}$ and $\underline{\underline{K}}_{sf}^{skin}$ are the mixed terms (Eq. 3.16a-3.16d).

$$\underline{\underline{K}}_{ff}^{skin} = \int \underline{\underline{N}}_f^T T^{skin} \underline{\underline{N}}_f \, dS \tag{3.16a}$$

$$\underline{\underline{K}}_{fs}^{skin} = -\int \underline{\underline{N}}_f^T T^{skin} \underline{\underline{N}}_s \, dS \tag{3.16b}$$

$$\underline{\underline{K}}_{sf}^{skin} = -\int \underline{\underline{N}}_s^T T^{skin} \underline{\underline{N}}_f \, dS \tag{3.16c}$$

$$\underline{\underline{K}}_{ss}^{skin} = \int \underline{\underline{N}}_s^T T^{skin} \underline{\underline{N}}_f \, dS \tag{3.16d}$$

These integrals are numerically estimated using equation Eq. 3.17.

$$\int_{\xi=-1}^{1} F(\xi) d\xi \approx \sum_{i=1}^{k} F(\xi_i) w_i \tag{3.17}$$

where $F(\xi_i)$ is the value of function F at position ξ_i and w_i is the weight factor for point i. Here, Newton-Cotes integration has been considered. In this method the points ξ_i are chosen at the position of the nodes, given in Table 3.4. The type of integration to be used for the embedded interface elements is according to No. 3 given in Table 3.14. In case of plastic deformations of embedded interface elements only the elastic part of the interface stiffness will be used in the stiffness matrix whereas the plasticity is solved for iteratively.

Table 3.4 Characteristic features of Newton-Cotes integration

No.	Nodes	ξ_i	w_i
1	2 Nodes	±1	1
2	3 Nodes	±1, 0	1/3, 4/3
3	4 Nodes	±1, ±1/3	1/4, 3/4
4	5 Nodes	±1, ±1/2, 0	7/45, 32/45, 12/45

3.5 Types of Loading Inputs and Staged Construction

In Plaxis, various loading and displacement inputs are available. In Plaxis 2D, loading can be provided with the aid of line load, point load, line displacement and point displacement options are available. In Plaxis 3D, surface load, point load, point displacement and surface displacement are the options for loading mechanism. In the present study, for 2-D investigations, point loading and line displacement have been used. In case of Plaxis 3D, surface loading and point loading have been considered.

Staged construction is the technique available in Plaxis to provide sequential loading and excavation inputs. In this feature, it is possible to change the geometry and load configuration by deactivating or reactivating loads, volume clusters or structural objects as created in the geometry input. Staged construction enables an accurate and realistic simulation of various loading, construction and excavation processes. The option can also be used to reassign material data sets to change the water pressure distribution in the geometry. To carry out a staged construction calculation, it is first necessary to create a geometry model that includes all of the objects that are to be used during calculation. Objects that are not necessary at the start of the calculation should be deactivated in the initial geometry configuration at the end of the input program.

3.6 Calculation Types

The first step in Plaxis FE analysis is defining a calculation type of any analysis phase. To generate initial stress state of soil for the initial phase, the options available are 'K_0-procedure' and 'Gravity loading'. The option for activating the ground water flow can be used only if ground water flow analysis is to be performed. For any subsequent deformation analysis, the calculation types available are 'Plastic analysis', 'Consolidation analysis', 'Safety analysis', 'Dynamic analysis' and 'Fully coupled flow-deformation analysis'. In the current simulations, the initial stresses have been generated by adopting 'Gravity loading' for footing located on sloping ground and 'K_0-procedure' for footing located on horizontal ground. 'Plastic analysis' have been considered for the deformation analyses, while 'Safety analysis' have been adopted for estimating the stability against impending failure.

3.6.1 Generation of initial stresses

Many problems in geotechnical engineering require the generation of initial stresses. These stresses, caused by gravity, represent the equilibrium state of the undisturbed soil or rock body. In Plaxis simulations, these initial stresses need to be specified. Two possibilities remain for the specification of these stresses, namely 'K_0-procedure' and 'Gravity loading'. As a rule, *K_0-procedure* should be used in case of horizontal surface and with any soil layer and phreatic lines parallel to the surface. For all other circumstances, *Gravity loading* should be used as shown for various cases in Fig.3.8. The details of the two procedures are described in the following subsections.

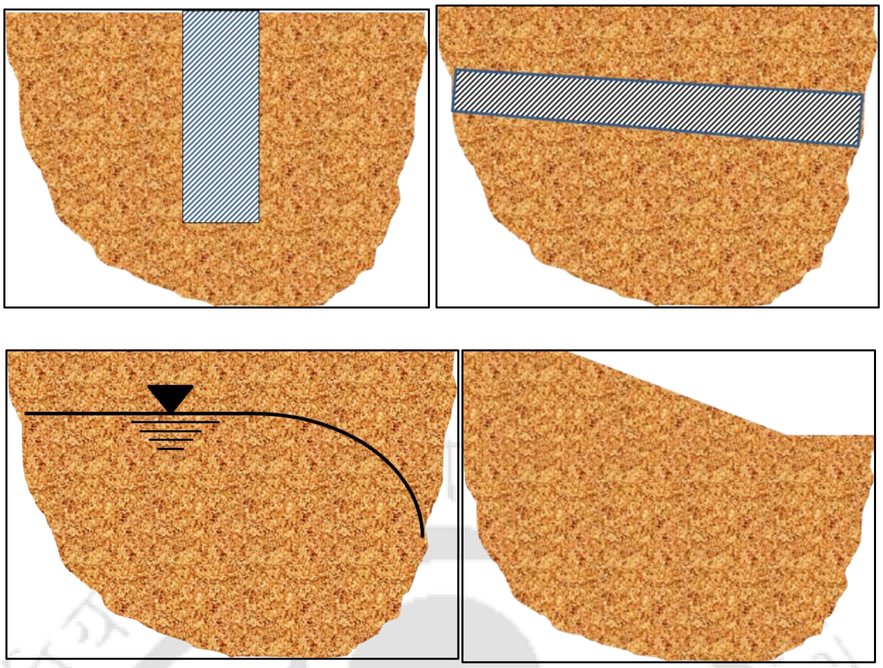

Fig. 3.8 Examples for non-horizontal geometrical profiles where 'Gravity loading' is to be used for the generatio of initial stresses in the system

3.6.1.1 K_0-Procedure

When selecting this procedure, it is possible to enter magnitudes for coefficient of lateral earth pressure for each individual soil cluster. The coefficient K_0 signifies the ratio of the horizontal and vertical effective stresses, and is bascially the coefficient of at-rest earth pressure. The expressions has been given by Eqs. 3.18 - 3.20.

For 2D analysis: $$K_0 = \frac{\sigma'_{xx}}{\sigma'_{yy}} \tag{3.18}$$

For 3D analysis:

K_0 for x-direction: $$K_{0,x} = \frac{\sigma'_{xx}}{\sigma'_{zz}} \tag{3.19}$$

K_0 for y-direction: $$K_{0,y} = \frac{\sigma'_{yy}}{\sigma'_{zz}} \tag{3.20}$$

In practice, the value of K_0 for a normally consolidated soil is often assumed to be related to the friction angle by the following the empirical expression given by Eq. 3.21a (Plaxis Reference Manual 2015).

$$K_0 = 1 - \sin\varphi \tag{3.21a}$$

In case of over-consolidated soil, K_0 would be larger than the magnitude given by expression Eq. 3.21b (Mayne and Kulhawy 1982).

$$K_0 = (1 - \sin\varphi) OCR^{\sin\varphi} \tag{3.21b}$$

where, φ is the angle of internal friction and OCR is the over consolidation ratio.

Considering very low or very high K_0-value in the K_0 procedure may lead to stresses that violate the Coulomb failure principle. Plaxis autometically reduces the lateral stresses such that the failure condition is followed. It is generally desirable to generate an initial stress field which does not contain plastic points. It has been shown that to avoid the development of soil pasticity, the magnitude of K_0 is provided by Eq. 3.22.

$$\frac{1-\sin\varphi}{1+\sin\varphi} < K_0 < \frac{1+\sin\varphi}{1-\sin\varphi} \quad \text{(Cohesionless soil)} \tag{3.22a}$$

$$K_0 = \frac{v}{1-v} \quad \text{(Clayey soil)} \tag{3.22b}$$

where, v is the Poisson's ratio.

When the K_0-procedure is taken into account, Plaxis generates vertical stresses that are in equlibrium with the self-weight of the soil. Horizontal stresses are calculated from the specified value of K_0.

3.6.1.2 Gravity loading

If Gravity loading is taken into account, then the initial stresses (corresponding to initial phase) are zero. The initial stresses, in this case, are set up by considering the soil self-weight in the first calculation phase. In case of Mohr-Coulomb model, the final value of K_0 depends strongly on the assumed values of Poisson's ratio. It is important to choose magnitude of Poisson's ratio that provides realistic values of K_0. For one-dimensional compression, an elastic computation will be provided by Eq. 3.23.

$$K_0 = \frac{v}{(1-v)} \tag{3.23}$$

If a magnitude of K_0 of 0.5 is essential, then it is required to specify a value of Poisson's ratio of 0.333.

3.6.2 Deformation analysis

This section highlights the two types of deformation analysis that has been adopted in the present study, namely the Plastic calculation and Phi-c reduction technique. A detail of the finite element calculations associated with the deformation analysis is provided in (Plaxis Scientific Manual 2015).

3.6.2.1 Plastic calculation

A plastic calculation should be considered to carry out an elastic-plastic deformation analysis in which the decay of excess pore pressures with time is not an influential factor. In general, the calculation is performed as per the small deformation theory, and hence, the stiffness matrix in a normal plastic calculation is based on the original undeformed geometry. This type of calculation is appropriate in most practical geotechnical applications. A plastic calculation is primarily used to analyse a fully undrained behaviour, with the aid of various types of 'undrained' options, e.g. influence of quick loading on saturated clay soils. However, a fully drained analysis can also be conducted for the assessment of long-term settlements, although the precise loading history is not followed and the consolidation is not dealt explicitly as the calculation typology is independent of time.

3.6.2.2 Phi-C reduction

'Phi-c reduction' is a technique incorporated in Plaxis to compute global safety factors. In 'Phi-c reduction' approach, the strength parameters, φ and c, of the soil are successively reduced until the failure of the FE model takes place. The strength of interfaces is reduced in the same fashion. The strength of structural objects like pates and anchors is not influenced by 'Phi-c reduction'.

The total multiplier $\sum M_{sf}$ has been considered to define the value of the soil strength parameters at any given stage during the analysis given by Eq. 3.24.

$$\sum M_{sf} = \frac{\tan \varphi_{input}}{\tan \varphi_{reduced}} = \frac{c_{input}}{c_{reduced}} \tag{3.24}$$

where, the strength parameters with the subscript 'input' stands for the properties entered in the material sets and parameters with the subscript 'reduced' refer to the reduced values considered in the analysis. Initially, $\sum M_{sf}$ is 1.0 at the start of a calculation to set all material strengths to their input values. The incremental multiplier M_{sf} is considered to specify the reduction of the strength of the first calculation step. This increment is generally set to 0.1, which is found to be a good starting value. The strength parameters are successively reduced with an automated scheme. The number of additional steps is considered 100, but a larger value up to 1000 may be taken, if required. The factor of safety is given by Eq. 3.25.

$$SF = \frac{\text{Available strength}}{\text{Strength at failure}} = \text{Value of} \sum M_{sf} \text{ at failure} \tag{3.25}$$

3.6.3 Maximum number of iterations

This value signifies the maximum allowable number of iterations within any individual calculation step. In general, the solution procedure will restrict the number of iterations that take place. The parameter is required only to ensure that computer time does not become excessive due to the accumulation of during the calculation phase. The standard value of maximum iteration is 60; however, the number may be altered within the range of 1 to 100. If the maximum allowable number of iteration is reached in the final step of a calculation phase, then the result may be inaccurate. Such a situation rarely happens when the solution process does not converge. This may have various causes, but it is mostly indicated as an input error, and has to be rectified by increasing the 'Number of additional steps' in the analysis.

3.6.3.1 Automatic error checks

During each calculation step, Plaxis performs a series of iterations to reduce the out-of-balance errors in the solution that are originated due to the sudden change in the loading conditions or abrupt change in geometry during the calculation phase. It is necessary to automatically estimate the out-of-equilibrium errors at every stage during the iterative process, so that the same can be utilized to terminate this iterative procedure when the errors are acceptable. Two separate error indicators are used for this purpose. One of these is based on a measure of the global equilibrium error and other is a local error check. The magnitudes of both of these indicators must be below predetermined limits (described later) for iterative procedure to terminate.

3.6.3.2 Global error check

The global error checking parameter in Plaxis is related to sum of the magnitudes of the out-of-balance nodal forces. 'Out-of-balance nodal forces' is the difference between the external loads and the forces that are in equilibrium with the current stresses. For obtaining the global error, the out-of-balance loads have been made dimensionless as given in Eq. 3.26.

$$\text{Global error} = \frac{\sum \lVert \text{Out of balance nodal forces} \rVert}{\sum \lVert \text{Active loads} \rVert + CSP \times \lVert \text{Inactive loads} \rVert} \tag{3.26}$$

where, CSP is the current value of the stiffness parameter. The 'Active loads' are the load difference between the ongoing calculation and the previous calculation phase, while the 'Inactive loads' are the active loads from the previous calculation phase. The stiffness parameter provides an indication of amount of plasticity that occurs in the calculation. The stiffness parameter is defined in Eq. 3.27 as:

$$Stffness = \int \frac{\Delta\varepsilon . \Delta\sigma}{\Delta\varepsilon D^{e} \Delta\varepsilon} \tag{3.27}$$

where, $\Delta\varepsilon$, $\Delta\sigma$ and D^{e} are defined as strain increment, stress increment and elastic material matrix. When the solution is fully elastic, the stiffness is equal to unity, whereas, at failure, the stiffness approaches zero.

3.6.3.3 Local error check

Local errors refer to the errors at each individual stress or Gauss point. To comprehend the local error checking procedure considered in Plaxis, it is necessary to consider the stress changes that occur at a typical stress point during the iterative process. The variation of a typical stress component during the iteration procedure is shown in Fig. 3.9.

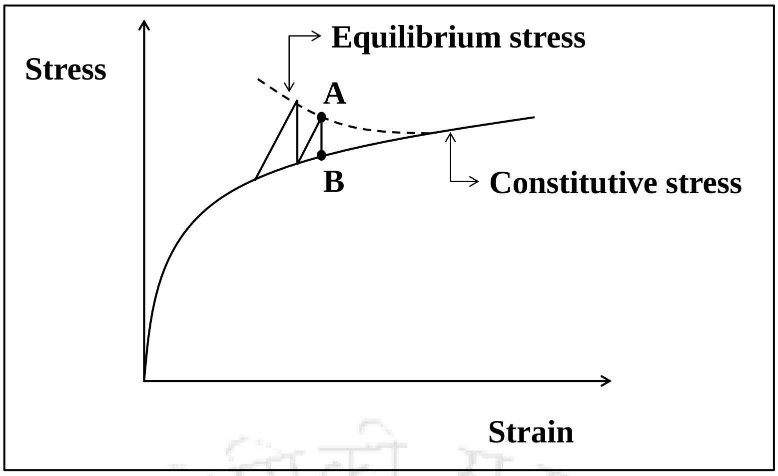

Fig. 3.9 Equilibrium and constitutive stresses with respect to local error checks

At the end of the each iteration, two important magnitudes of stress are calculated by Plaxis. The first of these, the 'equilibrium stress', is the stress calculated directly from the stiffness matrix (Point A on Fig. 3.9). The second important stress, the 'constitutive stress' is the value of stress on the material stress-strain curve at the same strain as the equilibrium stress, point B on Fig. 3.9. The dashed line represents the path of equilibrium stress. In general, the equilibrium stress path depends on the nature of the stress field and applied loading. For the case of a soil element following Mohr-Coulomb criterion, the local error for the particular stress point at the end of the iteration is defined by Eq. 3.28.

$$\text{Local error} = \frac{\left\| \sigma^e - \sigma^c \right\|}{T_{\max}} \tag{3.28}$$

In Eq. 3.20, the numerator is a norm of the difference between the equilibrium stress tensor, σ^e, and constitutive stress tensor, σ^c. This norm is defined by Eq. 3.29.

$$\left\| \sigma^e - \sigma^c \right\| = \sqrt{\begin{aligned}&(\sigma_{xx}{}^e - \sigma_{xx}{}^c)^2 + (\sigma_{yy}{}^e - \sigma_{yy}{}^c)^2 + (\sigma_{zz}{}^e - \sigma_{zz}{}^c)^2 \\ &+(\sigma_{xy}{}^e - \sigma_{xy}{}^c)^2 + (\sigma_{yz}{}^e - \sigma_{yz}{}^c)^2 + (\sigma_{zx}{}^e - \sigma_{zx}{}^c)^2\end{aligned}} \tag{3.29}$$

The denominator of the equation for the local error is the maximum value of the shear stress as defined by the Coulomb failure criterion. In case of the Mohr-Coulomb model, T_{max} is defined as following expression Eq. 3.30.

$$T_{\max} = \max\left[0.5(\sigma_1 - \sigma_3), c\cos\varphi\right] \tag{3.30}$$

where, σ_1 and σ_3 are the major and minor principal stresses. c and φ are the cohesion and angle of internal friction of the soil. When the stress point is located in an interface element, the local error has been computed by considering the following expression Eq. 3.31.

$$\text{Local error} = \frac{\sqrt{(\sigma_n{}^e - \sigma_n{}^c)^2 + (\tau^e - \tau^c)^2}}{c_i - \sigma^c{}_n \tan\varphi_i} \tag{3.31}$$

where, σ_n and τ signifies the normal and shear stress respectively in the interface. To aptly quantify the local accuracy, the 'inaccurate plastic points' need to be assessed. A plastic point is said to be inaccurate when the local error exceeds the user-defined tolerated error.

3.6.3.4 Tolerated error

In any non-linear analysis, where a finite number of calculation steps are used, there will be some shift of numerical solution from the exact solution, as shown in Fig. 3.10. The purpose of a solution algorithm is to ensure that the equilibrium errors, both locally and globally, remain within acceptable bounds. The calculation program continues to carry out iterations until the calculated errors are smaller than the specified value, within each step. If the tolerated error is set to a high value, then the calculation will be relatively quick, although may be inaccurate. If a low tolerated error is adopted, then the computational time may become excessively large. In general, the standard value of 0.01 (for both local and global) has been used in the simulation that is suitable for most calculations. If a plastic calculation phase provides failure loads that tend to reduce unexpectedly with increasing displacement, then it might be a possible indication of excessive drift of the finite element results from the exact solution. In such cases, the calculation should be repeated using lower value of the tolerated error.

3.6.3.5 Termination of iteration

During the execution of any FE analysis in Plaxis, in order to terminate the iterations in the a particular load step, all the following three error checks must be satisfied (Vermeer and van Langen 1989), as illustrated by Eqs. 3.31 - 3.34.

1. $\text{Global error} \leq \text{Tolerated error}$ (3.32)

2. $\text{No. of inaccurate soil points} \leq 3 + \dfrac{\text{No. of plastic soil points}}{10}$ (3.33)

3. $\text{No. of inaccurate interface points} \leq 3 + \dfrac{\text{No. of plastic interface points}}{10}$ (3.34)

3.6.4 Output from FE analysis

In Plaxis, various options are available to see the outputs or results after the calculation phase. These are specifically classified as total displacement, incremental displacement, total Cartesian strain, incremental Cartesian strain, total strain, incremental strain, principal effective stress, principal total stress, pore pressure, ground water flow, plastic points and load-displacement pattern. In the current investigation, the outcomes have been revealed in form of graphical representation of bearing capacity and failure mechanisms through total displacement, incremental displacement, incremental strain (deviatoric strain) and load-displacement curves.

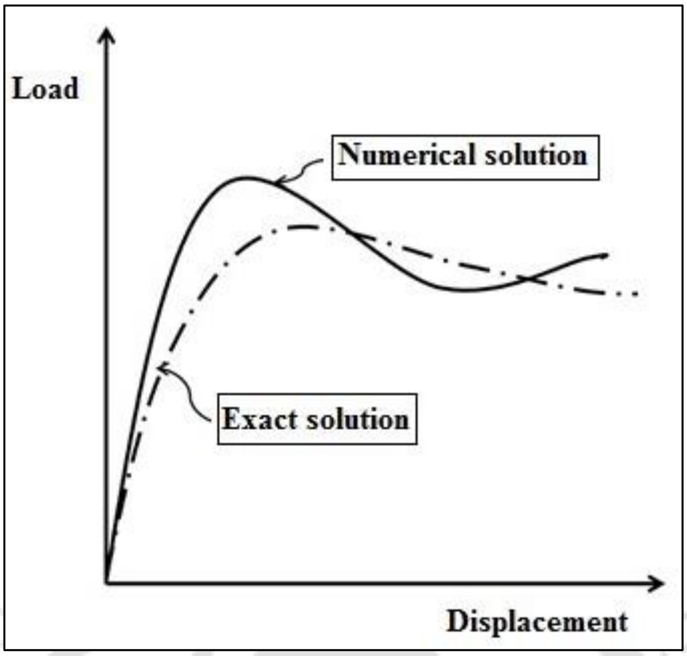

Fig. 3.10 Drift of computed solution from exact solution observed during numerical analysis

3.6.4.1 Total displacement

The total displacements are the absolute accumulated displacements $|u|$, combined from horizontal ($|u_x|$ for 2D analysis, and, for 3D analysis, $|u_x|$ and $|u_y|$) and vertical ($|u_y|$ for 2D analysis and for 3D $|u_z|$) displacement components at all nodes at the end of the current calculation step, and are displayed on the plot of the geometry. The displacements are presented in the form of contours, arrows and shadings.

3.6.4.2 Incremental displacement

The total increments are the absolute displacement increments of the current step $|\Delta u|$, combined from the horizontal and vertical displacement increments at all nodes as calculated for the current step, displayed on a plot of the geometry. Similar, the horizontal increments and vertical increments are, respectively, the horizontal ($|\Delta u_x|$ for 2D analysis and for 3D $|\Delta u_x|$ and

$|\Delta u_y|$) and vertical ($|\Delta u_y|$ for 2D analysis and for 3D $|\Delta u_z|$) displacement increments at all nodes as calculated for the current step. The displacement increments are presented as arrows and shadings by selecting the appropriate option. The contours of total increments are particularly useful for the observation of localization of deformations within the soil when plastic failure occurs.

3.6.4.3 Incremental strain

The incremental strains option contains different strain measures based on strain increments as calculated for the current calculation step, and is displayed in a plot of the geometry. A further selection has to be made between the volumetric strain $(\Delta\varepsilon_v)$ and deviatoric strain $(\Delta\varepsilon_q)$. In the analysis, incremental deviatoric strain has been taken into account as output, presented in the form shadings, representing the strain concentrations and slip lines at failure.

3.6.4.4 Load-displacement curves

Load-displacement curves can be used to visualize the relationship between the applied loading and resulting displacement of a certain point in the geometry. The points at which the curves will be generated must be selected before starting the calculation process. In the results presented for this study, the load level (Multiplier) is plotted in the x-axis, while the y-axis relates to the displacement of a particular node. The type of displacement can be either the length of the displacement vector ($|u|$) or one of the individual displacement components (u_x, u_y or u_z). The displacements are expressed in the unit of length (mm or m). The selection of multiplier must be completed with the selection of the desired load system, represented be the corresponding multiplier. In the current analysis, the total multiplier ($\sum M_{stage}$) has been considered. The total multiplier ($\sum M_{stage}$) provides the proportion of a construction stage and the corresponding load that has been completed in the preceding phases. The value of $\sum M_{stage}$ is always zero at the start of a staged construction analysis. At the end of the analysis, $\sum M_{stage}$ will generally be 1.0 if failure does not takes place; however, in case of a failure, the reached value of $\sum M_{stage}$ will provide the proportion of the applied load that has resulted in the failure.

3.7 Summary

In this chapter, discussions have been provided on the methodologies involved in numerical modelling as used in the present study. It has been revealed that model dimension plays vital role for estimation of bearing capacity of footing. Boundary dimension should be optimum to get accurate result. The boundary width and depth should be at least 7*B* and 3*B*, respectively, to estimate the bearing capacity of footing without any influence of domain boundary (*B* is the width of the footing). In the simulation, standard fixity has been considered. Horizontal fixities have been provided to vertical boundaries, vertical and horizontal fixities have been given to bottom of the domain and slope face devoid of any fixity. Mohr-Coulomb and Linear elastic model have been considered for simulating the behaviour of soil and footing. The coupled stress-deformation analysis has been achieved through 'Plastic calculation', while the safety analyses have been achieved by adopting 'Phi-c reduction technique'. The outputs will be checked through various representations of stress, strains and deformations generated with the model domain due to applied loading and failure conditions, if any. A description of the various intricacies of the FE modelling, analyses and solution strategies is also elaborated.

CHAPTER 4

RESPONSE OF ISOLATED SHALLOW FOUNDATIONS ON SLOPES

4.1 General

It is a common practice to adopt various types of shallow foundations on the hill slopes to support urbanization, among which strip and isolated square footings are frequently adopted (NDMA 2013). In this regard, it is imperative to understand the response of such shallow foundation located on the slopes and the factors affecting their response. The present chapter addresses the estimation of bearing capacity (q_u) and the associated failure mechanisms of square and strip footings located on dry cohesionless slopes (comprising predominantly granular material) or c-φ soil slopes (the commonly found characteristic hill-slope constituent). 2-D and 3-D finite element (FE) modelling, employing coupled stress-deformation analysis has been employed to carry out the numerical simulations. The impact of various geotechnical and geometrical parameters over bearing capacity, namely the angle of internal friction of soil (φ), cohesion (c), unit weight of soil (γ), setback distance (b), slope inclination (β), footing width (B) and the depth of embedment (D_f or D) of the footing, have been investigated. The following subsections provide the detailed documentation of the influences.

4.2 Square Footing on Dry Cohesionless Soil Slopes

4.2.1 Validation of the developed FE model

Castelli and Lentini (2012) experimentally investigated the effect of the bearing capacity of shallow footings on slopes. The investigation had been performed with square footings of width 6 cm, 8 cm and 10 cm, resting on the sandy slope inside a model tank of dimension 100 cm long, 45 cm wide and 40 cm high. Three setback distances have been used during the experiment (b = 0.04 m, 0.12 m, 0.21 m). The load was applied incrementally by a hydraulic jack and was maintained manually with a hand pump. The vertical displacements were measured by means of displacement transducers. Settlement data were recorded using a data acquisition system having a precision of 0.025 mm. All the tests were performed on specimens of Playa Catania (Italy) sand. A series of standard drained shear tests were carried out to evaluate the internal friction angle of the model sand using specimens prepared by dry tamping. The internal friction angle (φ) of the sand, at a relative density of 87%, was estimated approximately to be 38°, and the maximum dry density (γ_{dmax}) was obtained to be 17.50 kN/m^3. The test soil bed was constructed in layers, forming a slope angle of 30° at the face.

A 3D FE numerical model is developed to represent the experimental work reported by Castelli and Lentini (2012). In order to identify the optimal meshing configuration for the numerical model, a convergence study had been carried out (considering different footing locations and sizes) using the standard meshing schemes described earlier. The schemes are represented by their non-dimensional average element length, which is defined as the ratio of the average element length to the largest geometrical dimension of the model. Figure 4.1 represents the result of the convergence study for a typical footing location (b = 0.04 m), and exhibits that beyond a fine mesh, the obtained results are nearly identical. Similar results have been obtained for other configurations as well; however, those are not presented here for the sake of brevity. Based on the observations, the fine mesh (non-dimensional average element length approximately 0.086) is considered to be optimum.

In order to validate the numerical model considering the optimal mesh size, various geometrical configurations related to the footing location and setback distances have been considered for the study. The model dimensions and the material properties have been adopted identical to that of the experimental model considered by Castelli and Lentini (2012). As the stiffness parameters for the soil used in the experimental model was not explicitly specified in the literature, the magnitudes of the modulus of elasticity of soil (E_s = 15 MPa) and its Poisson's ratio (ν = 0.3) has been chosen in accordance to the standard references (Keskin and Laman 2013; Naderi and Hataf 2014).

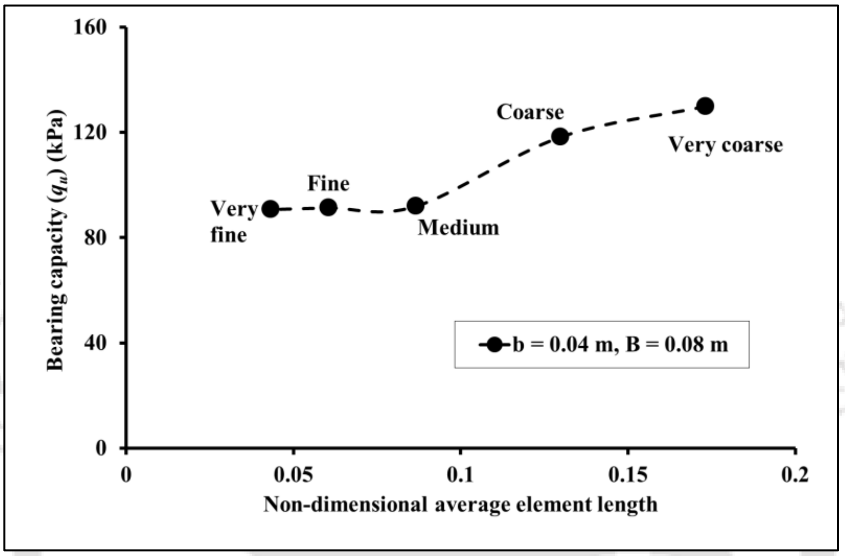

Fig. 4.1 Convergence study for determining the optimum mesh size for FE analysis

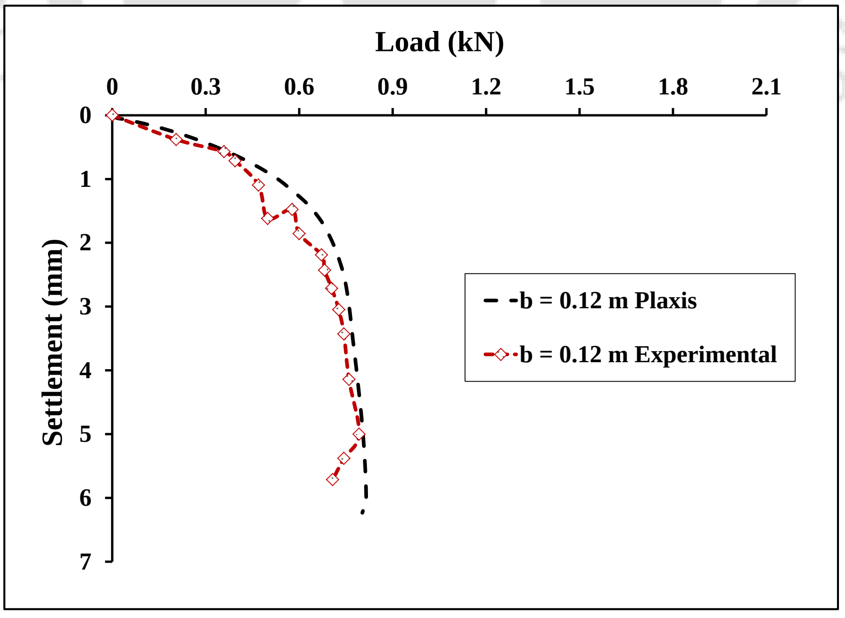

Fig. 4.2 Validation of the load-settlement curve obtained from numerical simulation with that of experimental investigations by Castelli and Lentini (2012)

Figure 4.2 represents the comparison of the load-settlement behaviour for a typical geometrical configuration (B = 0.08 m, b = 0.12 m). A good agreement between the experimental and numerical results can be observed, thus indicating the suitability of the developed numerical model for representing the response of such foundations.

4.2.2 Parametric studies

For footing resting on a sloping ground, the setback distance is perceived as one of the most important governing parameter in the assessment of bearing and deformation characteristics of the footing. The lesser the setback distance, higher is the possibility of failure of the footing exhibiting conditions of distress due to the deformation of the slope face. Hence, in order to highlight the effect of various parameters, a detailed parametric study has been conducted keeping the setback distance as one of the contributing parameters of the simulation. For a footing resting on a sloping ground, five different setback ratios were considered in the analysis, namely b/B = 0, 0.5, 1, 2 and 3.

As earlier, the numerical simulation of footings resting on sloping ground, with various setback ratios (b/B) and embedment ratios (D/B) had been checked for mesh convergence, the results of which are illustrated in Fig. 4.3. It can be observed that beyond a medium mesh (average non-dimensional mesh size of nearly 0.14), the obtained results are nearly identical, and hence, all the further studies for the sloping ground have been carried out with the same. The non-dimensional mesh size has been found with respect to the height of the model (H_s) that has been considered 6 m, which remains invariant for all the simulation scenarios.

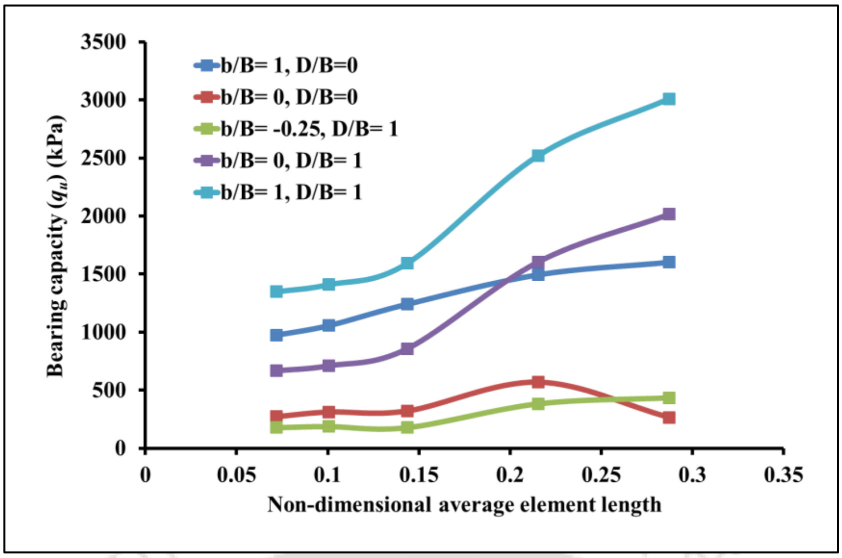

Fig. 4.3 Convergence study for square footing resting on sloping ground comprising φ-soil

4.2.2.1 Influence of angle of internal friction of slope material (φ)

Figure 4.4 illustrates the effect of variation of angle of internal friction (φ) on the bearing capacity (q_u) of a surface footing. It can be observed that the combined variation of setback ratio and angle of internal friction have significant effect on the above estimates. It can be noticed that for any setback ratio, the increase in φ resulted in the increase in the magnitudes q_u, the effect being more prominent at higher values of φ.

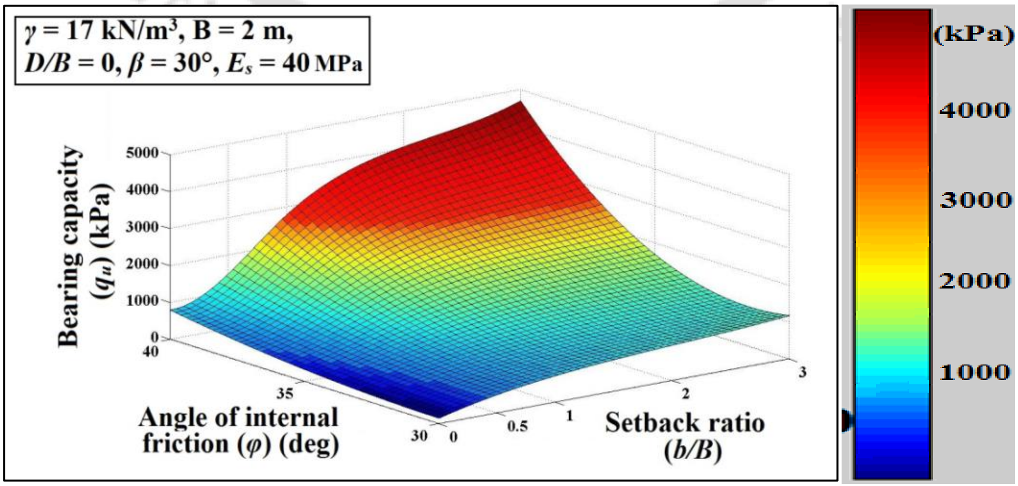

Fig. 4.4 Typical variation of q_u with angle of internal friction (φ) and setback ratio (b/B)

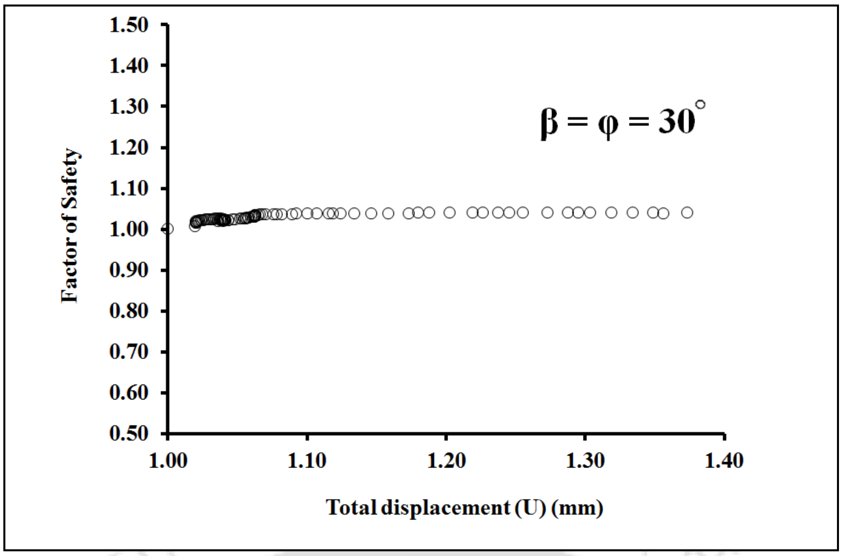

Fig. 4.5 Safety analysis of a typical slope, $\beta = \varphi = 30°$

A special case of the variation of angle of internal friction is presented for the case when the magnitude of the same becomes equal to the slope angle. Such a slope remains to be just stable at the verge of failure, and exhibits a factor of safety (FOS) equal to 1 (one) in its natural state, as shown in Fig. 4.5. Figure 4.6 shows the total displacement pattern of such slope in its natural state, exhibiting minimal deformation of the slope face. Such a slope, when subjected to minimal loading, exhibits an overall failure of the slope, as exhibited in Fig.4.7.

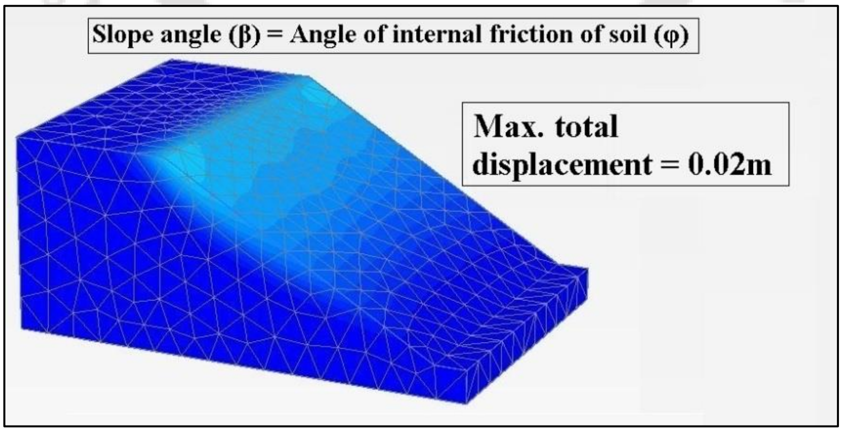

Fig. 4.6 Total displacement pattern for a slope at its natural state (at incipient failure)

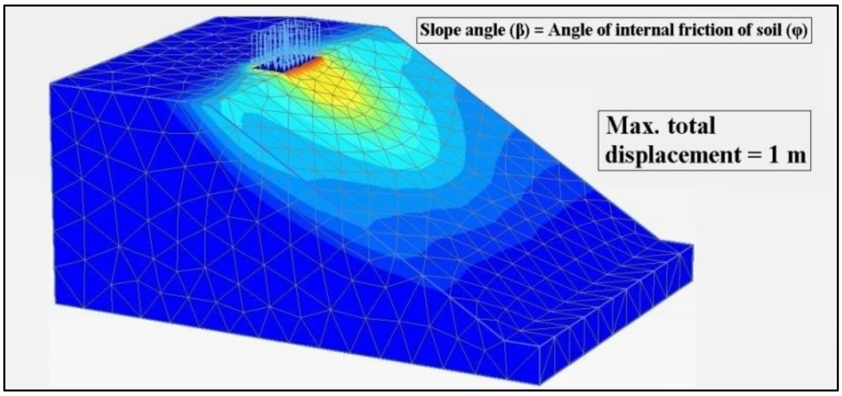

Fig. 4.7 Overall failure of a slope ($\beta = \varphi$) after implementing load on square footing

4.2.2.2 Influence of slope inclination (ß)

Change in the slope angle (β) can significantly alter the stability conditions and bearing capacity characteristics of the footing resting on the sloping ground. A footing exhibits a higher bearing capacity while resting on or near a slope with lesser inclination. Moreover, the natural stability of the slope is governed by the slope angle in relation to the angle of internal friction of the constituent material. For the present study, three different slope angles have been considered namely β = 30°, 35° and 40°. It can be observed from Fig. 4.8 that q_u decreases with the increase in the angle of inclination of the slope. This is attributed to the fact that more steeper is the slope, the volume of soil contributing to passive zone becomes smaller and hence, less resistance towards failure will be offered by the soil located towards the slope face.

4.2.2.3 Influence of embedment ratio (D/B)

Figure 4.9 depicts the various position of square footing on or near the slope. The crest of the slope has been set as zero setback distance. The setback distances which are away from the slope, have been denoted as positive setback distance, and those on the slope side, have been marked as negative setback distances. In this particular investigation, the depth of footing has been denoted as *D* because the embedment depths of footings are not same for a particular elevation for footings locate on or near the slope. For further investigations where the footings are considered only to be located on the crest of slope, the depth of embedment has been solely denoted as D_f.

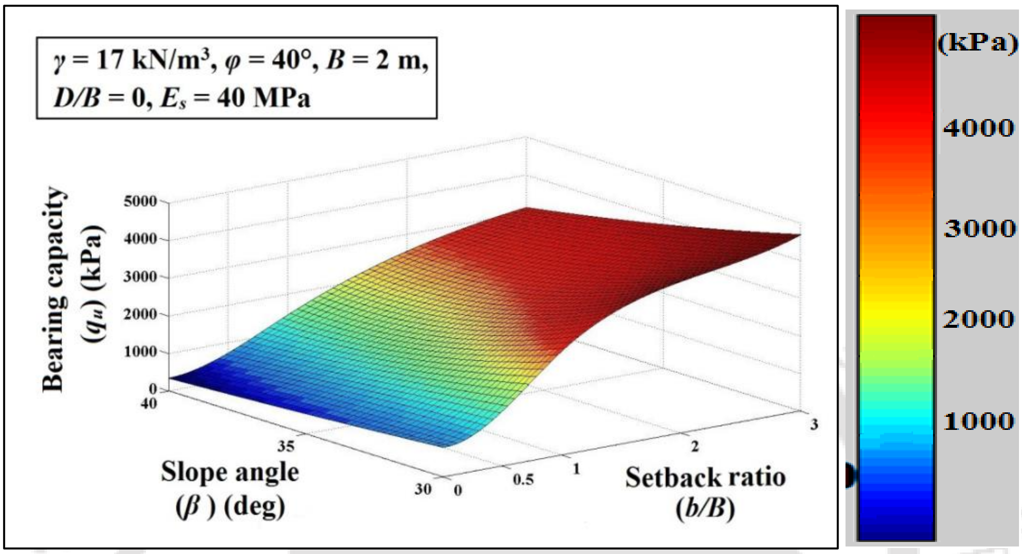

Fig. 4.8 Typical variation of q_u with slope angle (*ß*) and setback ratio (*b/B*)

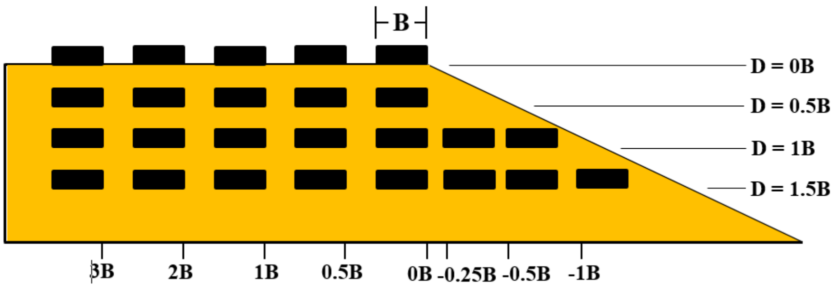

Fig. 4.9 Locations of surface and embedded footing in a sloping ground

For footing resting on the crest of the sloping ground, three different *D/B* were considered as 0.5, 1 and 1.5, so that the footings can be approximately considered to behave as shallow footings. Figure 4.10 shows that for any setback distance, the bearing capacity (q_u) increases with the increase in the embedment ratio of footing (*D/B*), the effect being more prominent when the footing is located away from the face of the slope i.e. the footing exhibits a higher setback distance. The negative setback distances are for the footings located on the face of the slope. Such locations exhibit comparatively low bearing capacity due to the immensely curtailed development of the passive resistance zone towards the slope face.

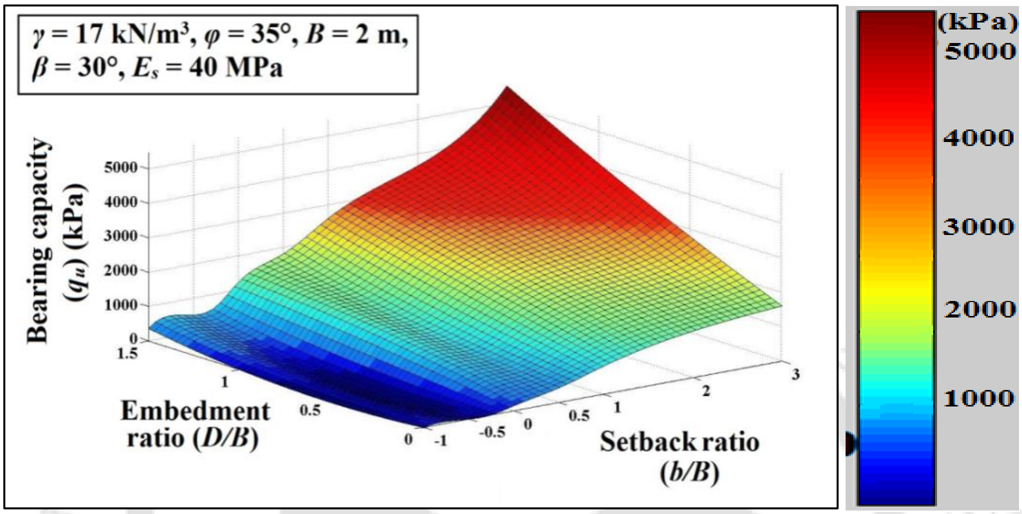

Fig. 4.10 Typical variation of q_u with embedment ratio (D/B) and setback ratio (b/B)

4.2.2.4 Influence of footing width (B)

Four different footing widths have been chosen namely B = 0.5 m, 1 m, 1.5 m and 2 m. Figure 4.11 shows the variation of ultimate bearing capacity (q_u) for various footing widths. Increase of ultimate bearing capacity reconfirms the fact that a greater footing width involves a larger soil domain to support the incumbent load.

4.2.2.5 Influence of unit weight of soil (γ)

Three different unit weight of the soil has been chosen namely γ = 15 kN/m^3, 17 kN/m^3 and 19 kN/m^3. Variation of unit weight of soil did not produce significant effect on the bearing capacity (q_u), as exhibited in Fig. 4.12.

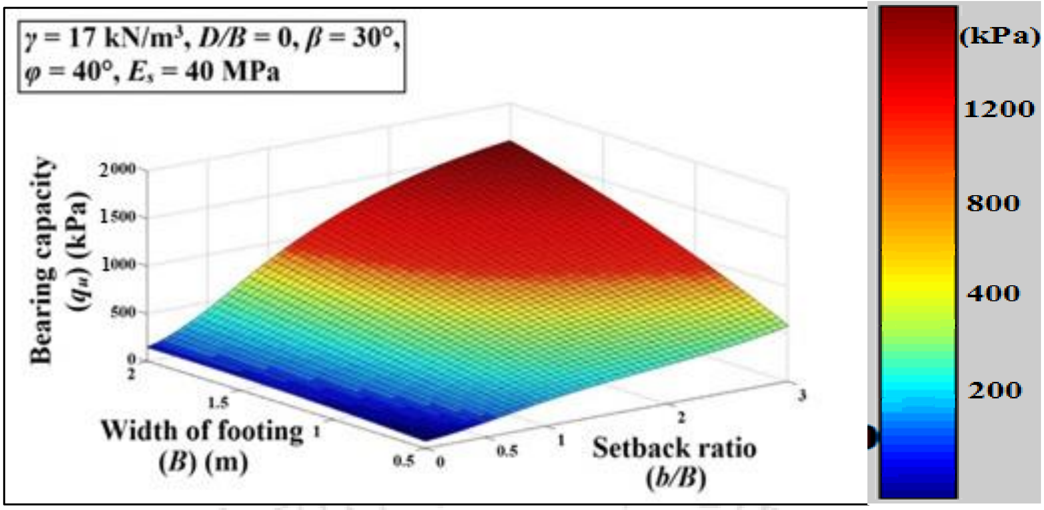

Fig. 4.11 Typical variation of q_u with footing width (B) and setback ratio (b/B)

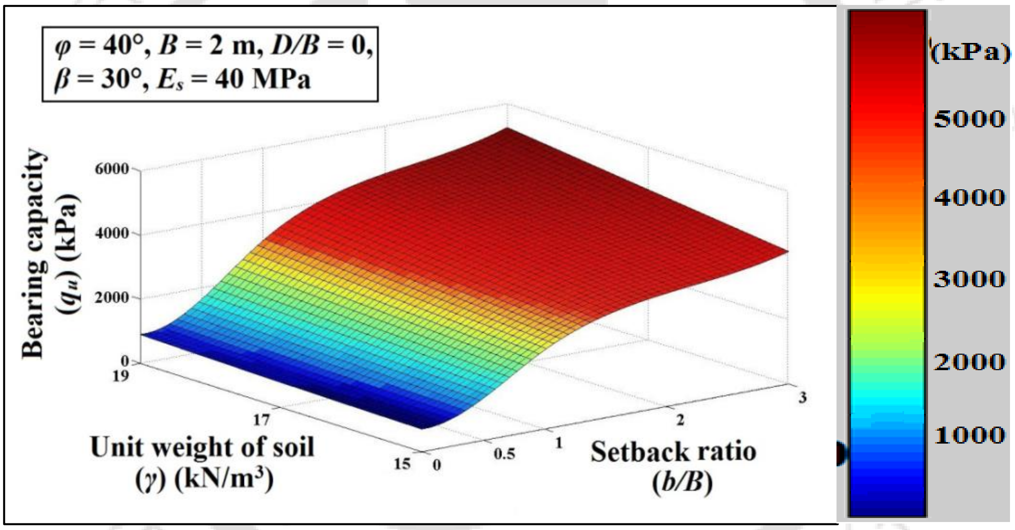

Fig. 4.12 Typical variation of q_u with unit weight of soil (γ) and setback ratio (b/B)

4.2.2.6 Influence of elastic modulus of soil (E_s)

Figure 4.13 highlights the effect of varying modulus of elasticity on the bearing capacity. It is perceived that the elastic modulus of soil (E_s) has insignificant effect on bearing capacity (q_u) of soil. It can be seen that the bearing capacity increases with the increase in the setback ratio (b/B), which is rather obvious. From the Figs. 4.4, 4.8, 4.10, 4.11 and 4.12, it is clear that for a footing located with a lesser setback distance (i.e. located near to the face of the slope), any application of load results in the incomplete development of the resisting passive zone beneath the footing. This is due to the presence of the sloping boundary that fails to provide enough passive confinement. With the increase in the setback distance, the formation of the passive zones attains completeness, thus provides more restriction to the lateral movement of the foundation, and largely inhibits the loss of confinement. Hence, an increase in the setback distance clearly manifests the increment in the bearing capacity of the footing.

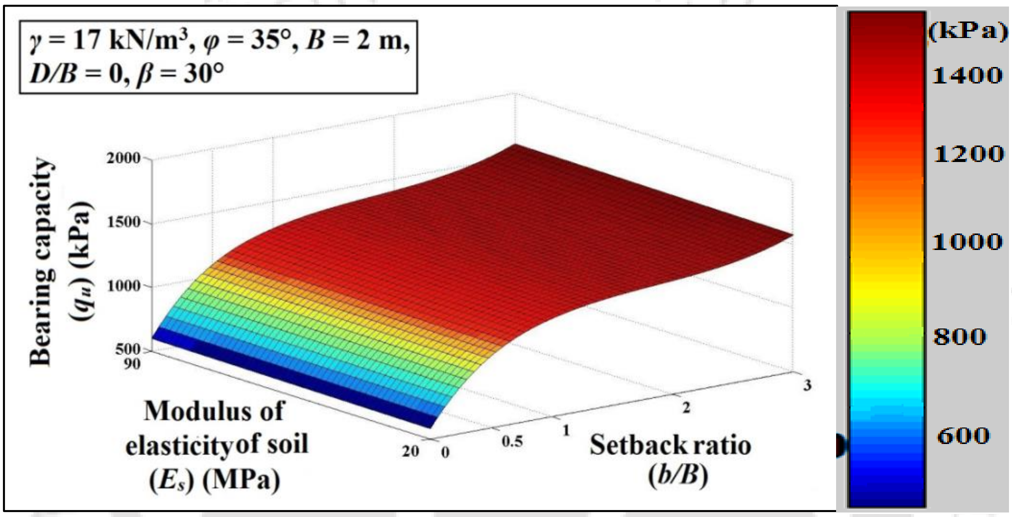

Fig. 4.13 Typical variation of q_u with elastic modulus of soil (E_s) and setback ratio (b/B)

4.2.3 Failure mechanism of foundations on slopes

For footings placed at various setback distances from the slope face, Figure 4.14 depicts the role of the sloping face in intersecting the resisting passive zone beneath the footing, thus reducing the bearing capacity and governing the failure of the foundation.

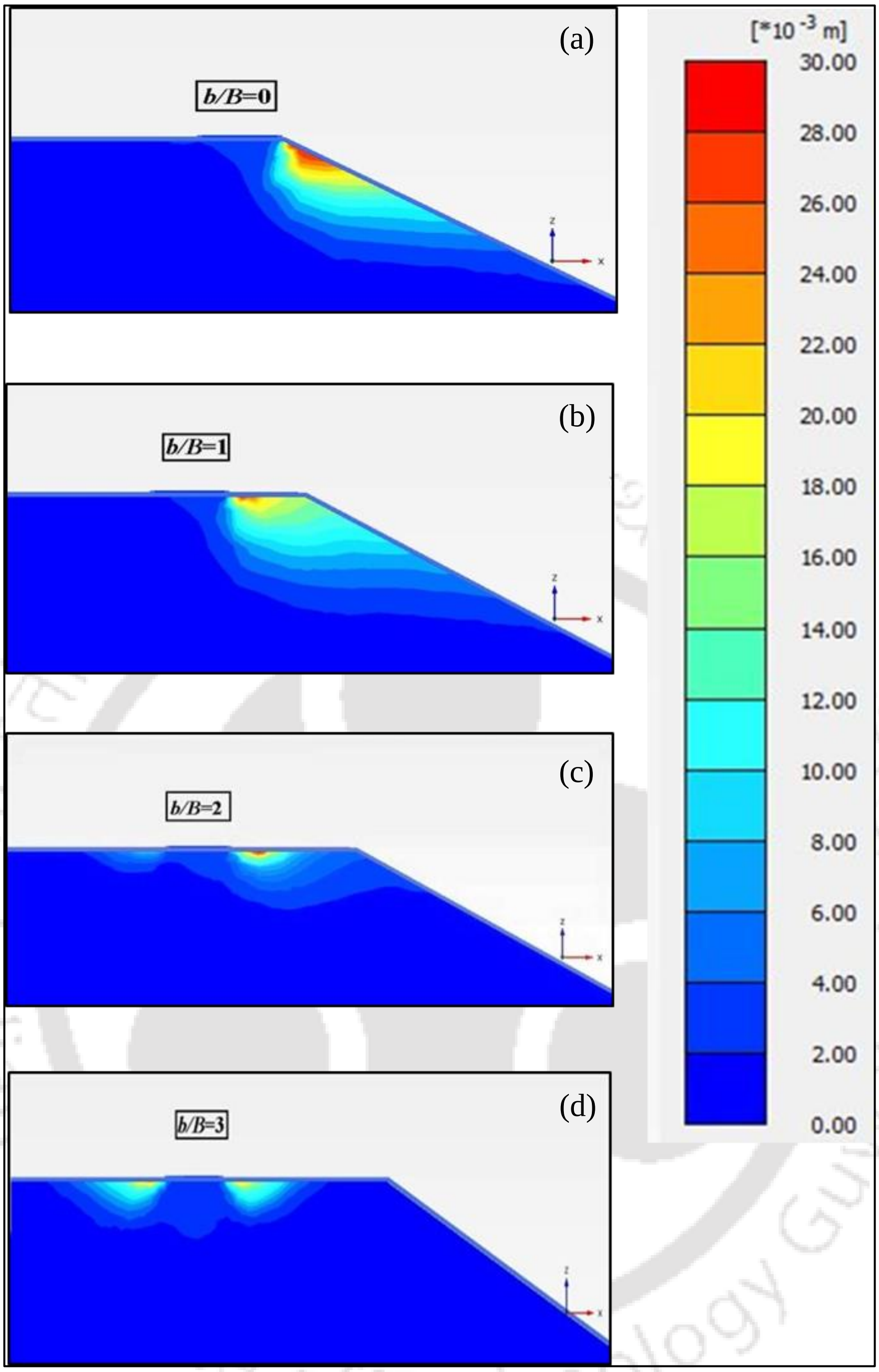

Fig. 4.14 Development of failure mechanism and interaction of slope face with the passive zones beneath the footing for various setback ratios (*b/B*)

It is observed that for a footing placed at the crest of the slope (*b/B* = 0), the formation of passive zone is largely one-directional and curtailed by the slope face, due to the dominant free deformation of the soil upon loading of the footing to failure. This phenomenon results in a substantial reduction of the confinement pressure, and hence, diminution of the bearing capacity. As the setback ratio increases, the influencing effect of the slope face on the development of the passive mechanism gradually diminishes, as can be observed from Fig. 4.14. It is noted that beyond a critical setback ratio $(b/B)_{critical}$ of 3, the footing behaves as if resting on horizontal ground for, wherein the developed stress contours for the passive zone remains unaffected from the influence of the slope face for any angle of slope. It is worth mentioning that for the cases in which the footing is placed at the crest with larger setback distances such that the slope face do not interact with the developed passive zones beneath the footing at its ultimate condition, the achieved failure condition and the estimated bearing capacity is solely related to the foundation failure. However, for footings with lesser setback distances, the developed passive zone intersects with the slope face, and the ultimate bearing capacity of the footing is an inevitable result of combinatorial failure of the foundation and slope face. In such cases, it is not possible to decouple the failure phenomenon, and hence, the estimated bearing capacity becomes a function of setback distance and slope inclination. A typical result of square footing resting on crest of sandy slope has been tabulated in Table 4.1.

Table 4.1 Typical results for square footing resting on crest of sandy slope (Fig. 4.14)

c (kPa)	φ (°)	γ (kN/m^3)	B (m)	b/B	β (°)	$q_u/\gamma H_s$
0	40	17	2	0	30	9.4
0	40	17	2	1	30	35.2
0	40	17	2	2	30	49.4
0	40	17	2	3	30	56.4
0	40	17	2	4	30	56.4
0	40	17	2	5	30	56.4
0	40	17	2	6	30	56.4
0	40	17	2	7	30	56.4
0	40	17	2	8	30	56.4
0	40	17	2	9	30	56.4
0	40	17	2	10	30	56.4

4.3 Square Footing on Dry *c-φ* Soil Slopes

4.3.1 Parametric studies

Natural hill-slopes primarily consist of *c-φ* soils, having varying combinations of angle of internal friction and cohesion characteristics. It is imperative that the failure characteristics of the footings resting on such slopes are thoroughly studied for their failure mechanism and the bearing capacity estimations. As earlier, in order to highlight the effect of various geotechnical and geometrical parameters, a detailed parametric study has been conducted, keeping the setback distance as one of the contributing parameters of the simulation. For a footing resting on a sloping ground, different setback ratios were considered in the analysis, namely b/B = 0-10.

The numerical simulation of footings resting on sloping ground, with various setback ratios (b/B), slope angles (β), footing widths (B) and embedment ratios (D_f/B) had been checked for mesh convergence, the results of which are illustrated in Fig. 4.15. As observed earlier, fine mesh (average non-dimensional mesh size of nearly 0.18) proves to be the optimal, and hence, all the further studies for the sloping ground have been carried out with the mesh configuration. The non-dimensional mesh size is estimated in terms of the height of the model (6 m) that remains invariant for all the simulation scenarios.

4.3.1.1 *Influence of cohesion of slope material (c)*

The influence of cohesion (c) on the ultimate bearing capacity (q_u) of a surface footing is exhibited in Fig. 4.16. As obvious, higher values of cohesion resulted in higher shear strength, and hence, higher bearing capacity of the foundation. Moreover, it is noted that for any chosen value of cohesion, the bearing capacity increases up to setback ratio 4, and further exhibits an asymptotic response.

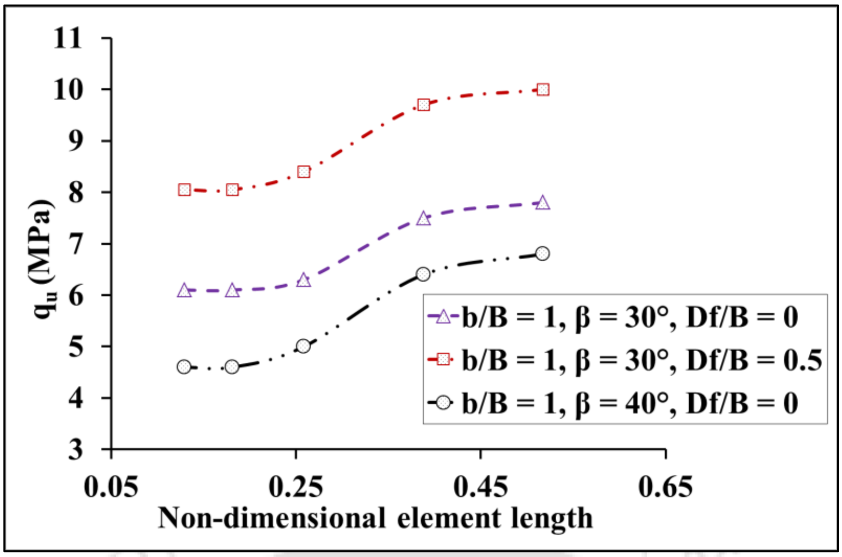

Fig. 4.15 Convergence study for square footing resting on sloping ground comprising *c*-*φ* soil

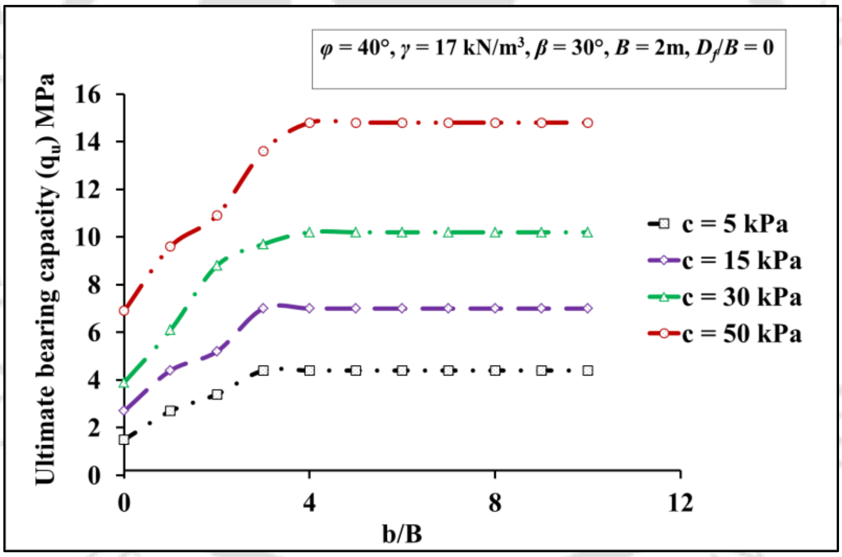

Fig. 4.16 Typical variation of q_u with cohesion (*c*) and setback ratio (*b/B*)

4.3.1.2 Influence of angle of internal friction of slope material (φ)

Figure 4.17 demonstrates the effect of variation of angle of internal friction (φ) on the ultimate bearing capacity (q_u) of a surface footing. An increase in angle of internal friction involves increased inter-particle frictional contact, thus enhancing the shear strength of foundation soil, which in turn, increases the ultimate bearing capacity of the footing. In this case as well, the effect of varying setback distance remains prominent until b/B = 2-4.

4.3.1.3 Influence of unit weight of soil (γ)

Four different unit weight of the soil has been chosen for the parametric study, namely γ = 12 kN/m^3, 15 kN/m^3, 17 kN/m^3 and 21 kN/m^3. Fig. 4.18 exhibits that variation of unit weight has negligible effect on the ultimate bearing capacity of the footing.

4.3.1.4 Influence of footing width (B)

Three different footing widths have been selected, namely B = 0.5 m, 1 m and 2 m. A larger footing width involves a larger soil domain to support the incumbent load, and the same is reflected in Fig. 4.19 that shows a higher ultimate bearing capacity for larger footing widths.

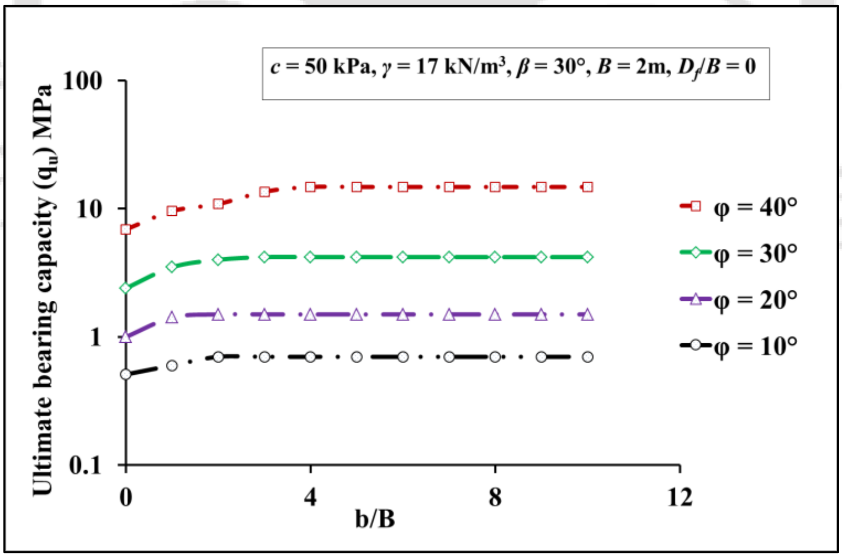

Fig. 4.17 Typical variation of q_u with angle of internal friction (φ) and setback ratio (b/B)

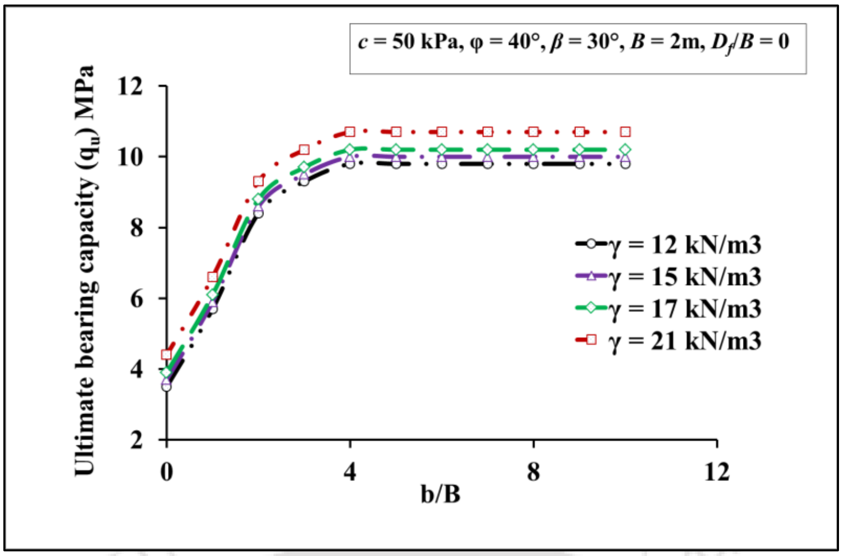

Fig. 4.18 Typical variation of q_u with unit weight of soil (γ) and setback ratio (*b/B*)

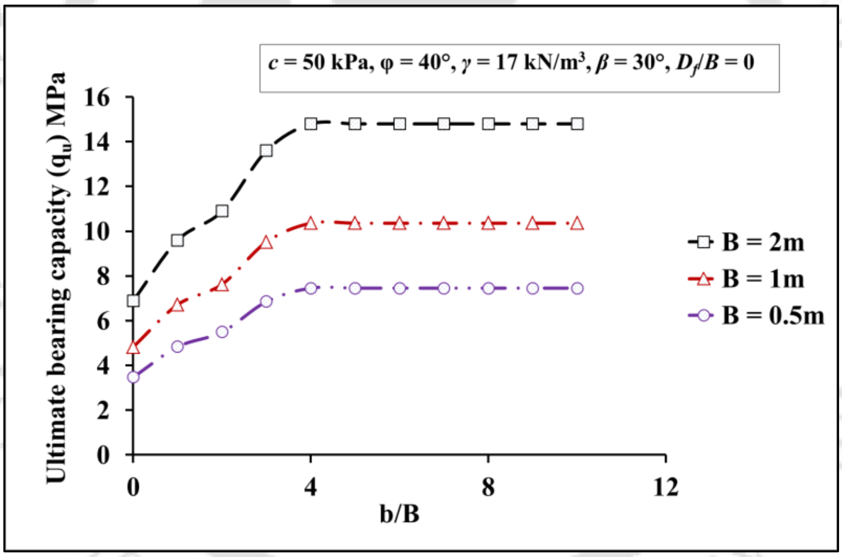

Fig. 4.19 Typical variation of q_u with footing width (*B*) and setback ratio (*b/B*)

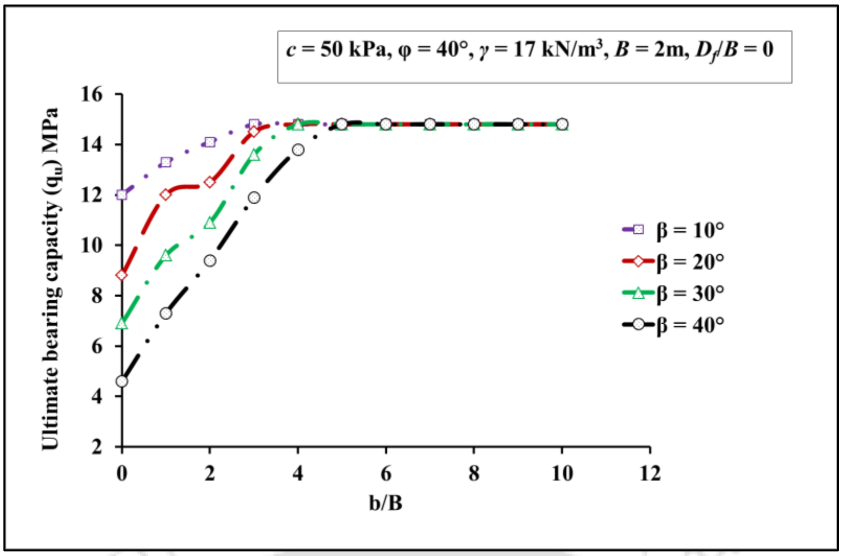

Fig. 4.20 Typical variation of q_u with slope angle (β) and setback ratio (b/B)

4.3.1.5 Influence of slope inclination (β)

Change in the slope angle (β) can significantly alter the stability conditions and bearing capacity characteristics of the footing resting on the sloping ground. A footing exhibits a higher bearing capacity while resting on or near a slope having lesser inclination. Moreover, the natural stability of the slope is governed by the slope angle in relation to the shear strength parameters of the constituent material. For the present study, four different slope angles have been considered namely β = 10°, 20°, 30° and 40°. It can be observed from Fig. 4.20 that q_u decreases with the increase in the slope inclination. This is attributed to the fact that steeper is the slope, the zone of outward passive resistance beneath the footing will be smaller and, hence, will offer less resistance towards outward soil movement and easily succumb to failure.

4.3.1.6 Influence of embedment ratio (D_f/B)

Three different embedment ratios (D_f/B= 0 m, 0.5 m and 1 m) were chosen for footing located on the crest of a sloping ground. The embedment ratio was restricted to 1, so that the footings can be considered to behave as shallow footings. Figure 4.21 shows that the ultimate bearing capacity (q_u) increases with the increase in the embedment ratio of footing (D_f/B), attributed to the higher confinement effect restricting the soil movement. The effect is more prominent when the footing is located away from the face of the slope due to reduced influence of the slope face.

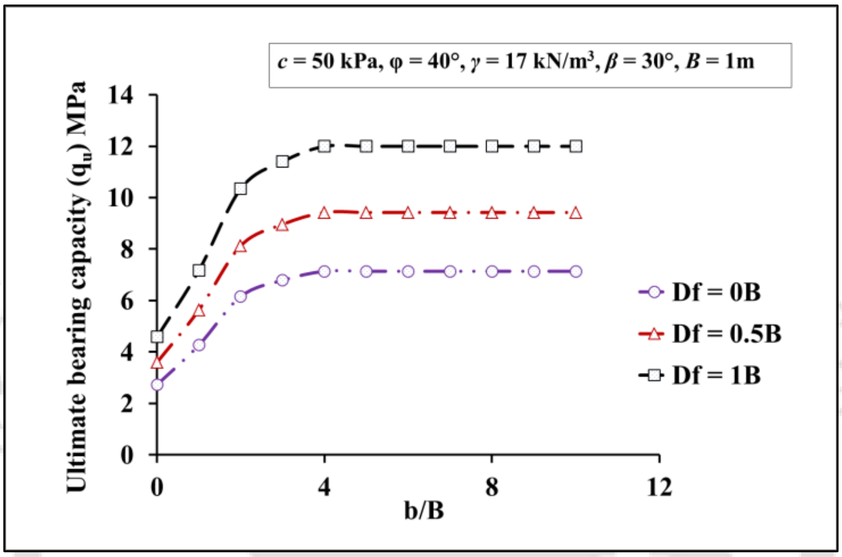

Fig. 4.21 Typical variation of q_u with unit weight of soil (D_f/B) and setback ratio (b/B)

4.3.1.7 Influence of setback distance (b/B)

Based on all the variations as exhibited in Figures 4.15-4.21, it can be aptly noted that beyond a setback distance b/B = 4, the variations are nearly asymptotic, thereby indicating least influence of the slope face on the soil movement beneath the loaded footing. It can be witnessed that for a footing placed at the crest of the slope (b/B = 0), the formation of passive zone is largely one-directional, due to the predominant free deformation of the soil towards the slope face due to the load applied on the footing. This phenomenon results in a considerable decrease of the confinement pressure, and hence, lessening of the bearing capacity. As the setback ratio increases, the influencing effect of the slope face on the development of the passive mechanism gradually reduces. Hence, b/B = 4 can be conclusively stated to the limiting or critical setback, beyond which the response of a loaded footing will be the same as obtained as it rests in homogeneous semi-infinite medium. For footings positioned at various locations on the crest, Figure 4.22 portrays the influence of setback distance of the development of the resisting mechanisms beneath a loaded footing. It can be observed that the outward passive zone (towards the slope face) is substantially affected by the nearness of the footing to the slope face. Lesser is the setback distance, lesser is the resistance offered by the passive zone since it is largely intersected by the slope face, leading to the reduction in the bearing capacity. A typical result of square footing resting on crest of *c*-*φ* slope has been tabulated in Table 4.2.

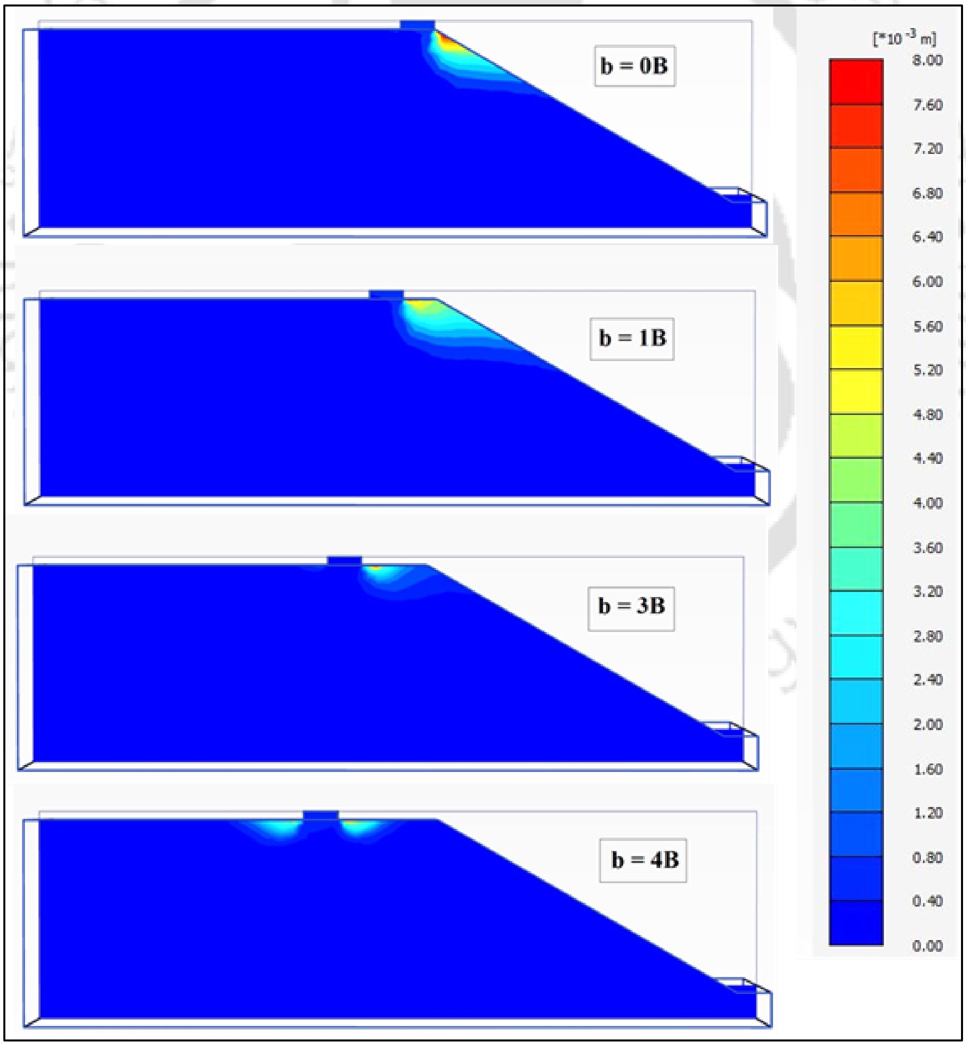

Fig. 4.22 Development of failure mechanism and interaction of slope face with the passive zones beneath the square footing for various setback ratios (*b/B*)

Table 4.2 Typical results for square footing resting on crest of c-φ slope (Fig. 4.31)

c (kPa)	φ (°)	γ (kN/m^3)	B (m)	b/B	β (°)	$q_u/\gamma H_s$
30	40	17	2	0	30	32.7
30	40	17	2	1	30	51.2
30	40	17	2	2	30	73.9
30	40	17	2	3	30	81.5
30	40	17	2	4	30	85.7
30	40	17	2	5	30	85.7
30	40	17	2	6	30	85.7
30	40	17	2	7	30	85.7
30	40	17	2	8	30	85.7
30	40	17	2	9	30	85.7
30	40	17	2	10	30	85.7

4.4 Strip Footing on Dry c-φ Soil Slope

4.4.1 Validation of the FE model

In the present numerical investigation, the experimental research done by Castelli and Lentini (2012) has been considered for validation of the developed numerical model. Castelli and Lentini (2012) have estimated ultimate bearing capacity (q_u) and bearing capacity factors for strip footings located at the crest of slope. Two strip footings of varying widths 4 cm and 6 cm were considered for the investigation. The reinforced test box of size 100 cm long, 45 cm width and 40 cm height has been used in their experimental investigation. The angle of slope was 30°. Researchers have considered Italy sand for constructing the sloping ground. The friction angle (φ), relative density (D_r) and dry unit weight (γ_d) of soil were 38°, 87% and 17 kN/m^3, respectively. The bearing capacity of strip footing for different setback distances were measured, specifically for 16 cm, 30 cm and greater than 30 cm. Vertical load has been provided over the footing up to its failure, and the load carrying capacity of the footing has been evaluated.

The numerical models developed with the aid of 2-D finite element analysis has been validated with the experimental findings. Before conducting the validation investigation, a convergence analysis has been carried out for selecting optimum mesh size. The convergence analysis has been done for different footing sizes and various setback distances. Figure 4.23 describes the results of the typical convergence analysis, in terms of non-dimensional average element size (NAES, ratio of average element length and the height of the model). It can be observed that the outcomes of the convergence study are nearly similar beyond NAES$\approx$0.04, and the same has been used for the estimation of bearing capacity for further studies. In order to verify the numerical study, the same model dimension and similar soil properties have been considered as used by Castelli and Lentini (2012) for the experimental studies. In this regard, a strip footing with width of 4 cm located at crest of the slope with setback distance of 30 cm has been modelled. The validation study has been represented in terms of load-settlement pattern. Figure 4.24 illustrates that there is a significant match between numerical outcomes and results obtained from experimental investigation, thus validating the FE model.

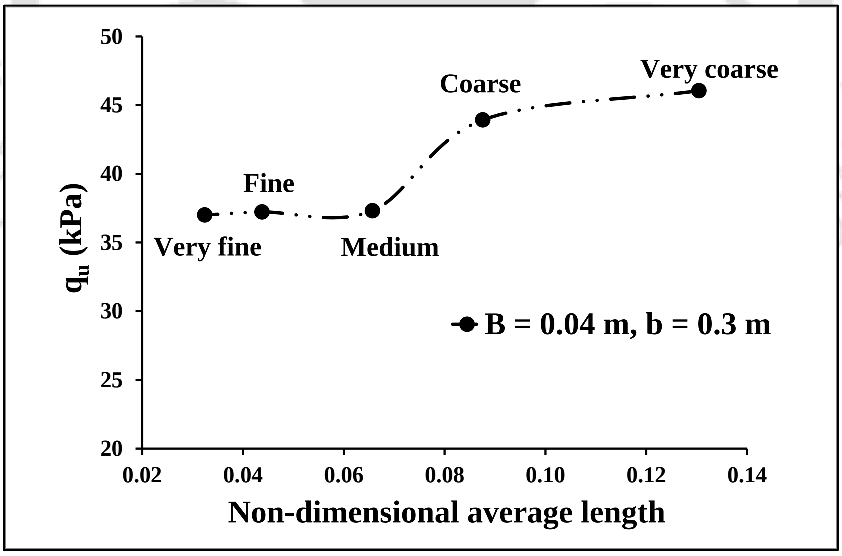

Fig. 4.23 Typical convergence study for determining the optimum mesh element size

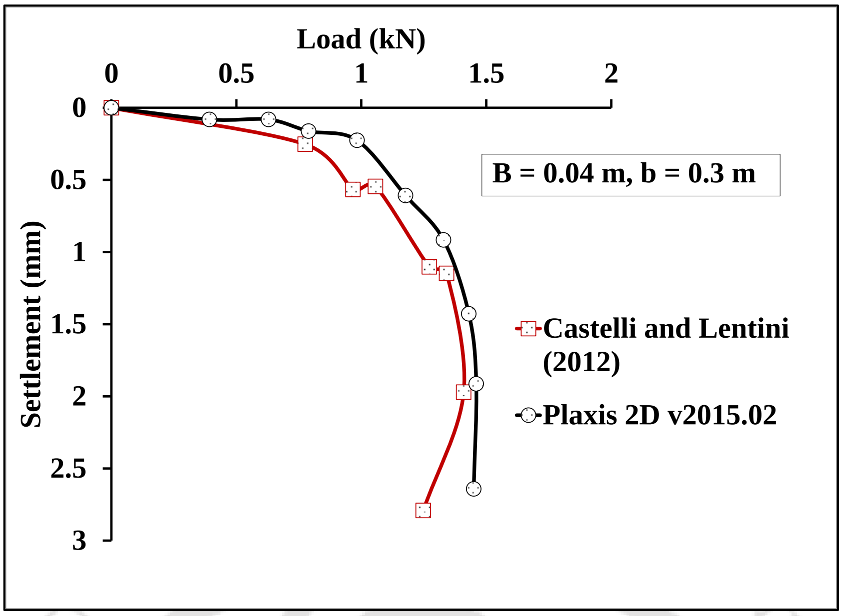

Fig. 4.24 Validation of the 2D FE model with the aid of experimental outcomes

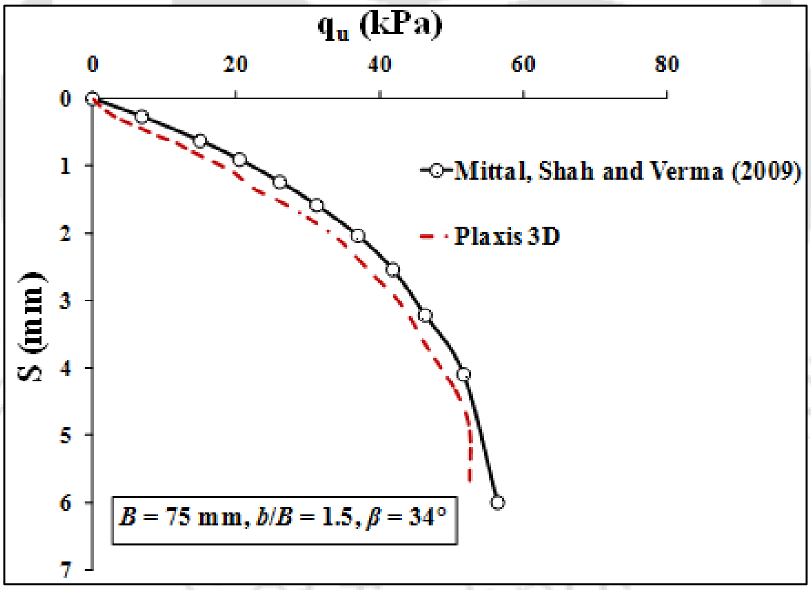

Fig. 4.25 Comparison of pressure-displacement patterns obtained from numerical model and experimental model

Furthermore, to validate the numerical model, another experimental work done by Mittal et al. (2009) has been taken into consideration. Mittal et al. (2009) had experimentally investigated the q_u of a strip footing (B = 75 mm) located on the crest of unreinforced and reinforced sandy slopes having an angle of inclination 34º. The dry unit weight and angle of internal friction of the soil were 16.3 kN/m^3 and 36° respectively. Figure 4.25 depicts the load-settlement behavior of the strip footing located on the slope crest. It can be perceived that there is an excellent agreement in pressure-settlement patterns, as well as the bearing capacity, obtained from present numerical investigation and those estimated from the experimental investigations.

4.4.2 Parametric investigations

In the present study, various geotechnical and geometrical parameters are varied to realize the impact of parameters over the estimation of bearing capacity of strip footing located at the crest of a dry c-φ slope. In the parametric investigation, the influence of the parameters on the bearing capacity of footing has been manifested in terms of the dimensionless ultimate bearing capacity ($q_u/\gamma H_s$) for different setback ratios (b/B).

Before conducting the parametric study, a convergence analysis has been performed. In order to perform the mesh convergence test, different slope angle, footing position and embedment depth of footing have been considered. It has been revealed that the magnitudes of obtained dimensionless ultimate bearing capacity ($q_u/\gamma H_s$) are same beyond an average non-dimensional mesh size of 0.047, conforming to fine mesh, as shown in Fig. 4.26. The model height of 6 m, which has been maintained constant for all the simulations, has been considered to calculate the non-dimensional mesh size. Furthermore, all the successive investigation has been conducted considering fine mesh.

4.4.2.1 Influence of cohesion of slope material (c)

Figure 4.27 exhibits the influence of cohesion (c) of soil over the load carrying capacity of footing positioned over the crest of slope. It has been realized that the dimensionless ultimate bearing capacity ($q_u/\gamma H_s$) enhances with increase in cohesion in soil. It defines the fact that increase in cohesion results in the improvement of shear strength of soil, and hence the load carrying capacity of footing increases.

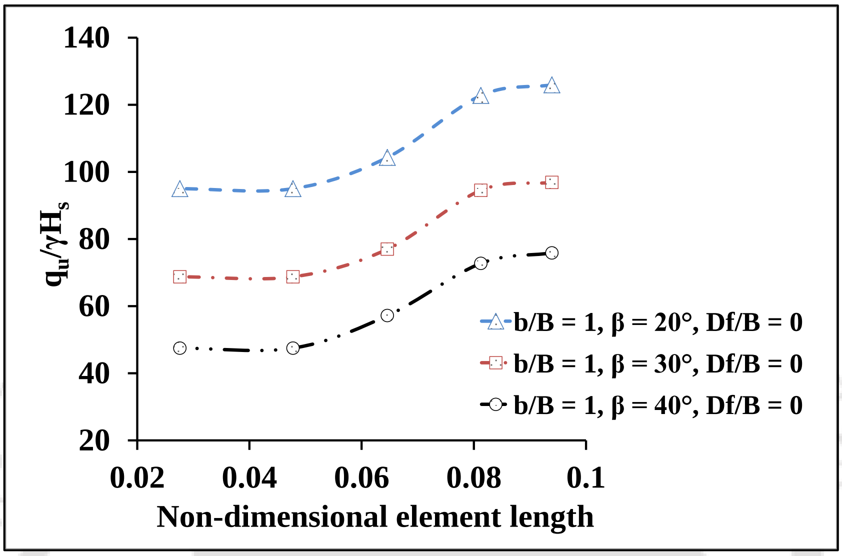

Fig. 4.26 Mesh convergence analysis for strip footing located at the crest of c-φ slope

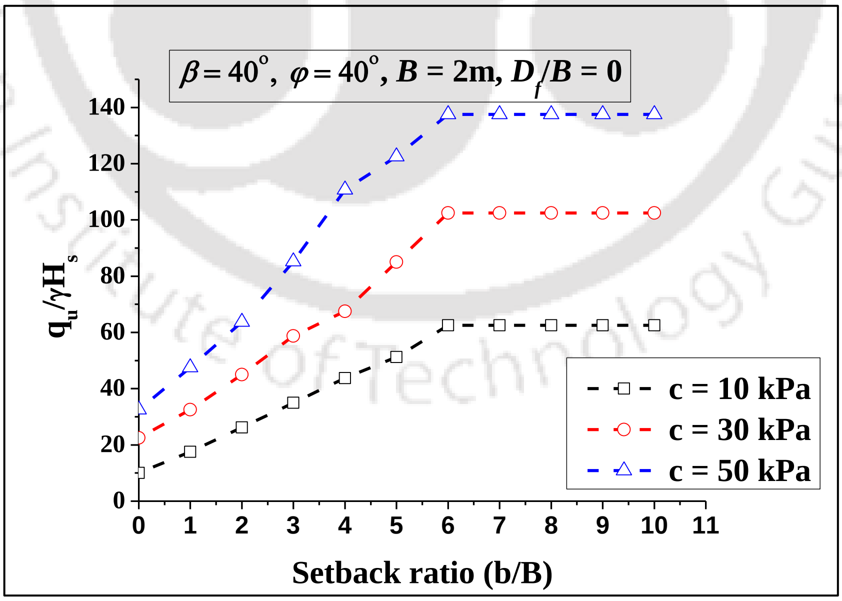

Fig. 4.27 Influence of cohesion of soil (c) on $q_u/\gamma H_s$

4.4.2.2 Influence of slope inclination (β)

Figure 4.28 elucidates the effect of slope inclination on the assessment of bearing capacity of footing positioned at crest of slope. In order to check the influence of slope angle, different slope angles were considered specifically ranging from 10° to 40°. It has been revealed that the dimensionless ultimate bearing capacity ($q_u/\gamma H_s$) reduces with increase in slope inclination. The outcomes reveal that the resistance of outward lateral movement of soil beneath the footing reduces due to increase in slope angle; therefore, the load carrying capacity of footing decreases. It has been perceived that beyond a setback back distance of 6*B*, the impact of slope inclination over the estimation of bearing capacity diminishes, and the footing on slope illustrate a response similar to that exhibited by an isolated strip footing on horizontal ground.

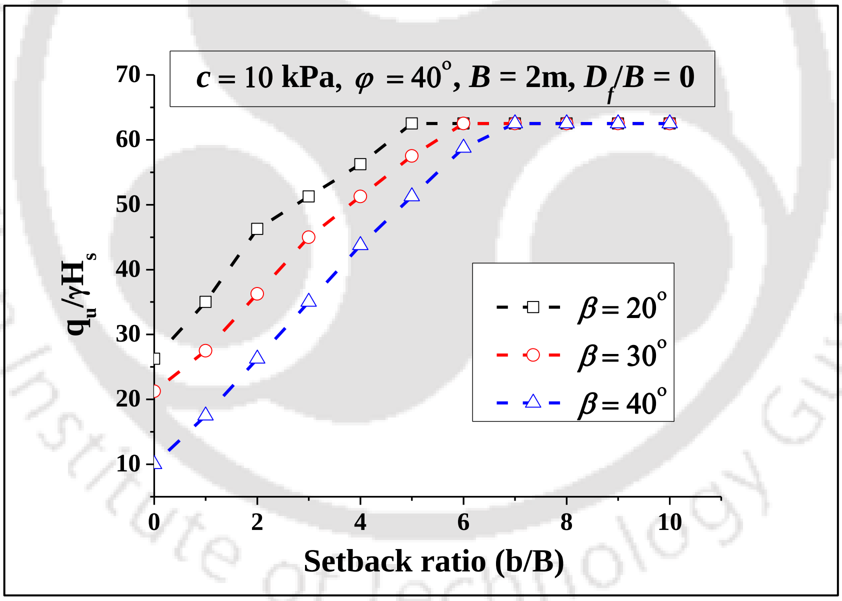

Fig. 4.28 Influence of slope inclination (β) on $q_u/\gamma H_s$

4.4.2.3 Influence of footing width (B)

Figure 4.29 illustrates the influence of footing width (*B*) over the estimation of bearing capacity of footing located on the crest of slope. In this respect, the size of footing width has been varied from 0.5 m to 2 m. It has been perceived that the dimensionless ultimate bearing capacity

($q_u/\gamma H_s$) enhances with increase in footing width. It explains the fact that with the increase in footing width, the load on the footing will be spread over the larger area in the subsoil, and hence the bearing capacity improves.

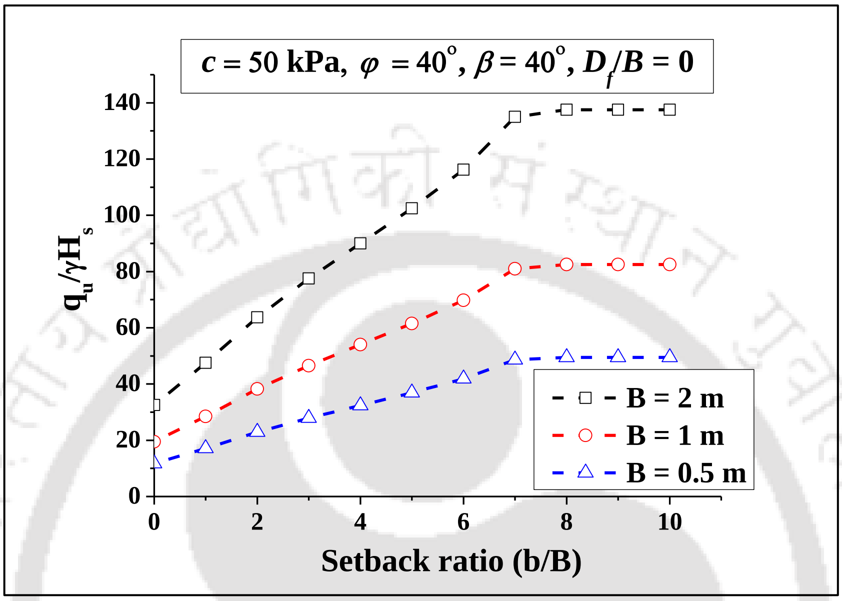

Fig. 4.29 Influence of footing width (B) on $q_u/\gamma H_s$

4.4.2.4 Influence of angle of internal friction of slope material (φ)

Figure 4.30 portrays the influence of angle of internal friction (φ) on the estimation of bearing capacity of footing placed on the crest of slope. It can be observed that the dimensionless ultimate bearing capacity ($q_u/\gamma H_s$) increases with increase in angle of internal friction of soil. The results illustrate that the passive resistance of soil increases for the increase in angle of internal friction of soil due to higher inter-particle shearing, thus enhancing the load carrying capacity of footing.

4.4.2.5 Influence of embedment depth ratio of footing (D_f/B)

Figure 4.31 depicts the influence of embedment depth of footing positioned near the slope on the estimation of bearing capacity. In this regard, different embedment ratio (D_f/B) have been taken, ranging from 0 to 1. It has been perceived that the dimensionless bearing capacity ($q_u/\gamma H_s$) increases with increase in embedment depth ratio (D_f/B). The outcome describes the fact that any increase in embedment depth, the confinement increases in foundation soil and hence load carrying capacity of footing improves. It has also revealed that the obtained dimensionless bearing capacities are identical for setback distances beyond 6*B*.

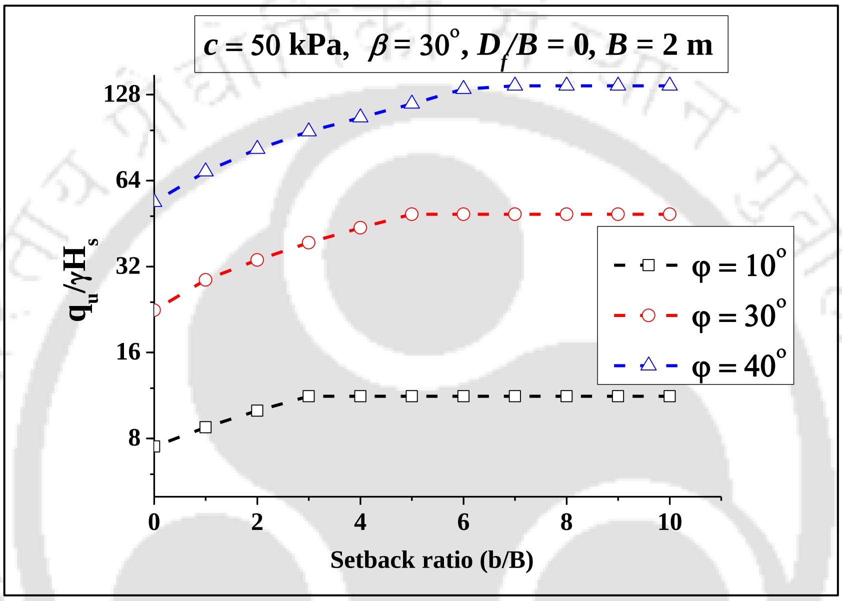

Fig. 4.30 Influence of angle of internal friction of soil (φ) on $q_u/\gamma H_s$

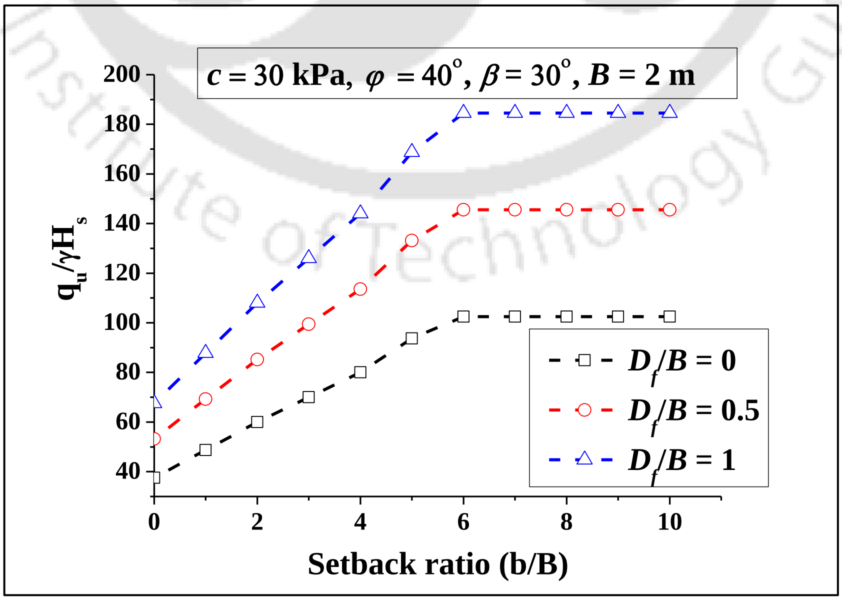

Fig. 4.31 Impact of embedment depth ratio (D_f/B) on $q_u/\gamma H_s$

4.4.2.6 Influence of setback ratio (b/B)

In the present numerical investigation, the failure mechanism developed beneath the strip footing placed at the crest of slope has been investigated for different setback distances.

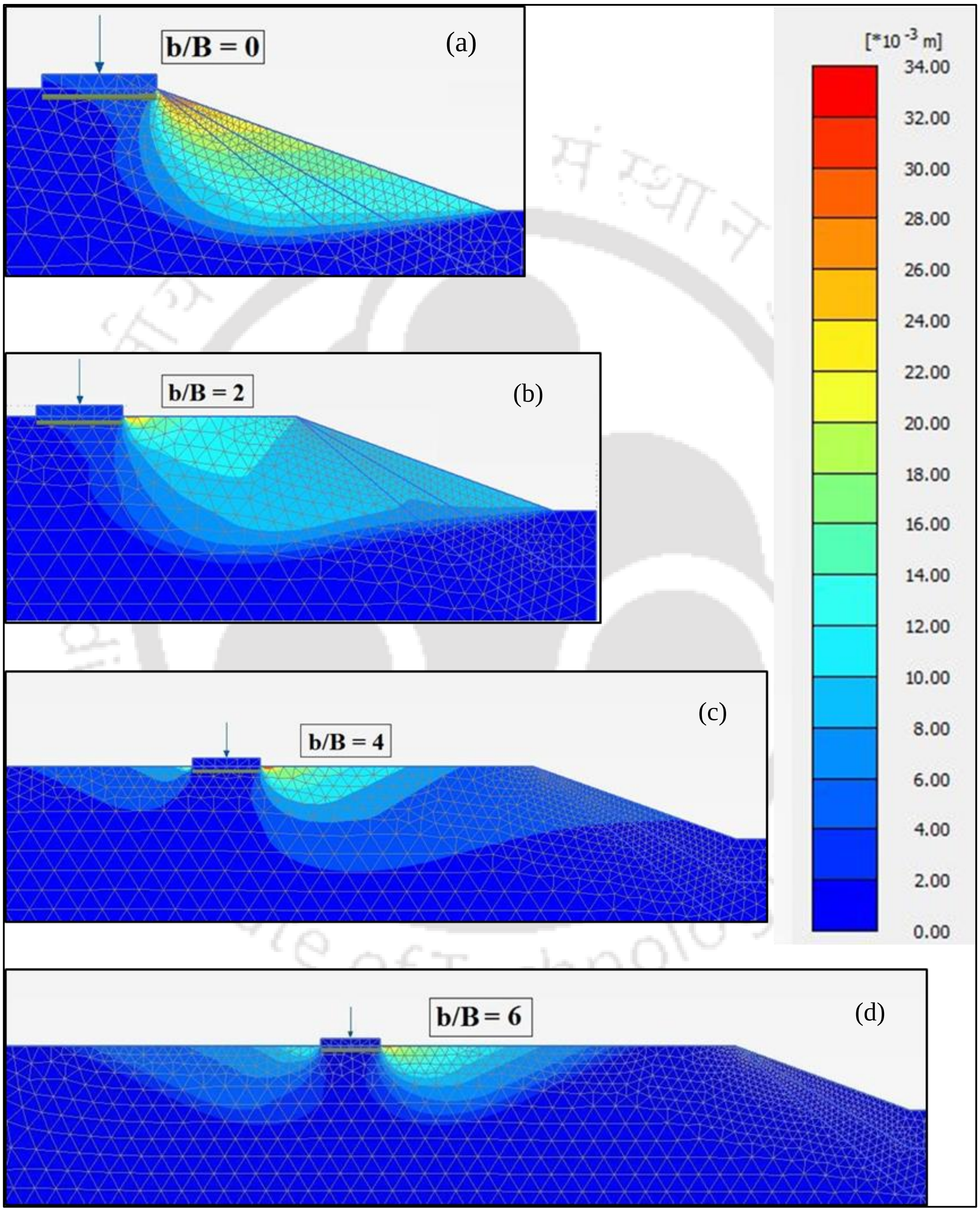

Fig. 4.32 Representative development of failure mechanisms underneath the footing for different setback ratios (*b/B*)

Figure 4.32 exhibits that the passive zone formed beneath the footing is significantly affected by the nearness of the footing to the slope face, the effect being more noticeable for lesser setback distances. The more close a footing to the sloping surface, the load carrying capacity of the footing reduces due to inadequate generation of passive confinement towards the sloping face. In the present research, the failure mechanism has been checked up to setback ratio (b/B) of 10. It has been found that the developed failure mechanism beneath the footing gets affected by the slope face up to a setback ratio b/B = 6. The influence of slope face on governing the failure mechanism beneath the footing completely disappears with further increase of setback ratio. Beyond the critical setback ratio b/B = 6, the developed failure mechanism underneath the footing is observed to be identical to the failure mechanism generated beneath an isolated strip footing located on horizontal ground. As concluded earlier, for lower setback distances, the failure mechanism is a combined effect of footing and slope failure, while, beyond the critical setback ratio, the failure is only governed by the foundation failure. A typical result of strip footing resting on crest of c-φ slope has been tabulated in Table 4.3.

Table 4.3 Typical results for strip footing resting on crest of c-φ slope (Fig. 4.31)

c (kPa)	φ (°)	γ (kN/m^3)	B (m)	b/B	β (°)	$q_u/\gamma H_s$
30	40	17	2	0	30	37.5
30	40	17	2	1	30	48.75
30	40	17	2	2	30	60
30	40	17	2	3	30	70
30	40	17	2	4	30	80
30	40	17	2	5	30	93.75
30	40	17	2	6	30	102.5
30	40	17	2	7	30	102.5
30	40	17	2	8	30	102.5
30	40	17	2	9	30	102.5
30	40	17	2	10	30	102.5

4.5 Efficacy of the FE Approach over the Existing Theories of Bearing Capacity of Footings on Slopes and their Shortcomings

There are few existing theories that addresses the estimation of bearing capacity of shallow footings on slopes. Meyerhof (1957) was the earliest to propose a theory for the estimation of bearing capacity of shallow continuous footings resting on the face or crest of the slope. The classical theory for bearing capacity of footings on horizontal ground was extended to include the effects of slope inclination and depth of embedment of foundation. Bearing capacity factors for footing resting on either purely cohesionless or purely cohesive soils were proposed. Considering principle of superposition to be valid, an expression was provided for the estimation of the bearing capacity of footing on slopes as

$$q_u = cN_{cq} + 0.5\gamma BN_{\gamma q} \tag{4.1}$$

where, N_{cq} and $N_{\gamma q}$ are the bearing capacity parameters dependent on the angle of internal friction of soil (φ), slope inclination (β), Stability number ($N_s = \gamma H/c$), height of slope (H), and depth of embedment of footing (D_f). The primary limitation of this methodology lies in the consideration of the magnitudes of bearing capacity factors that are found independently for purely cohesionless or purely cohesive soils, and do not address the condition for a c-φ soil, where the shear strength is governed by both the parameters, and thus would affect the estimation of the bearing capacity parameters. Moreover, Meyerhof (1957) has considered only one-sided rupture on the side of the slope and has inherently considered the mirror image of the failure mechanism for the other side of the footing, thus considering a symmetric slope on both sides of the footing. Thus, this assumption leads to the symmetric failure of the slope from both sides of the shallow footing, when loaded progressively. Hence, under such case, the bearing capacity of the foundation is substantially reduced. Further, for footings resting in cohesive soils, the foundation load is replaced by a uniform surcharge on the horizontal top surface, thus neglecting the influence of the setback distance on the estimated bearing capacity.

Lastly, Meyerhof's approach does not consider the influence of footing shapes on the bearing capacity estimation, and is restricted only for strip footings. For some typical combinations of shear strength parameters of a soil slope, setback distance, size and embedment depth of strip footings, as considered in the present study, Table 4.4 presents a comparative of the bearing capacity estimated by the Meyerhof's (1957) approach and that obtained through FE numerical simulations from the present study.

Table 4.4 Comparison of theoretical and finite element based bearing capacities of typical strip footings located on slopes

Type of footing	Geotechnical and geometrical configuration	Ultimate bearing capacity q_u (kPa)			
		Meyerhof (1957)	Hansen (1970)	Saran et al. (1989)	FE analyses (Present study)
Surface strip footing on edge of crest	c = 10 kPa, φ = 40°, β = 40°, B = 1 m, b/B = 0, D_f/B = 0	61.25	25.86	428.5	340
Embedded strip footing on edge of crest	c = 10 kPa, φ = 40°, β = 40°, B = 1 m, b/B = 0, D_f/B = 1	315	54.23	1378.6	918
Surface strip footing on top of crest	c = 10 kPa, φ = 40°, β = 40°, B = 1 m, b/B = 1, D_f/B = 0	305	-NA-	905	510
Embedded strip footing on top of crest	c = 10 kPa, φ = 40°, β = 40°, B = 1 m, b/B = 1, D_f/B = 1	576	-NA-	2037.8	1606

In contrary to Meyerhof's approach, the FE simulations do not assume any predefined formation of the rupture surfaces beneath the footing, and allows for the evolution of the failure mechanism die to the progressive loading. Moreover, unlike Meyerhof's approach, the FE simulations allow for coupled stress-deformation analysis, instead of only a stress-based approach as adopted by the former method. Guided by the above-stated reasons, Table 4.4 illustrates that for various typical locations of footing on slopes, the bearing capacity estimate by Meyerhof's approach is consistently lesser than that obtained from FE analyses. Mizuno et al. (1960) proposed a similar approach to determine the bearing capacity of shallow footings resting on the crest of cohesionless soil slope.

Hansen (1970) was the pioneer to provide the estimate of bearing capacity of shallow footing resting on a c-φ slope. However, based on limit equilibrium analysis, Hansen (1970) provided the estimate for only a special case when the footing is located right on the edge of the slope without any setback distance (i.e. $b/B = 0$). The estimate was provided as the modified form of bearing capacity prediction expression for strip footings on slopes as

$$q_u = cN_c\lambda_{c\beta} + qN_q\lambda_{q\beta} + 0.5\gamma BN_q\lambda_{\gamma\beta} \tag{4.2}$$

where, N_c, N_q, N_γ are the bearing capacity factors, q is the overburden pressure, and $\lambda_{c\beta}$, $\lambda_{q\beta}$, $\lambda_{\gamma\beta}$ are the slope factors given as

$$\begin{aligned} &\lambda_{q\beta} = \lambda_{\gamma\beta} = (1-\tan\beta)^2 \\ &\lambda_{c\beta} = \frac{N_q\lambda_{q\beta}-1}{N_q-1} \quad \text{for } \phi > 0 \\ &\lambda_{c\beta} = 1-\frac{2\beta}{\pi+2} \quad \text{for } \phi = 0 \end{aligned} \tag{4.2a}$$

Based on the above expressions, the estimate for the bearing capacity of two typical footing conditions are listed in Table 4.1, which shows even lower values than compared to Meyerhof's analysis. This is due to the fact that the bearing capacity factors used by Hansen (1970) is estimated considering the dual effect of the shear strength parameters, which has lower influence than the independent estimation technique adopted by Meyerhof (1957). Siva Reddy and Mogaliah (1976) proposed a modification of the Meyerhof's (1957) approach by including the effects of non-homogeneity and anisotropy of cohesion in the slope material, while the failure analysis was carried out considering the friction circle method.

Using upper bound theorem of limit analysis, Kusakabe et al. (1981) calculated the bearing capacities of slopes load on the top surface. The failure mechanism was considered to comprise an elastic triangular wedge, a log-spiral and a smooth line joining the log-spiral smoothly and passing through the inclined slope face. As in the earlier approaches, in this case, also, the failure surface has been considered only on the side of the slope, and the influence of the soil on the other side of the footing has been much neglected. In this regard, based on limit equilibrium and limit analysis approach, Saran et al. (1989) provided a solution to determine the upper bound bearing capacity of shallow continuous foundations located on the top of a slope. In this approach, apart from the full formation of the rupture surfaces towards the slope, the passive influence of the soil from the other side of the footing was also taken into account by considering partial mobilization of the shear resistance of the soil. The bearing capacity factors (N_c, N_q, N_γ) were determined from the analytical expressions as a function of setback ratio, embedment depth and angle of internal friction and slope inclination. The corresponding bearing capacity estimate is provided as

$$q_u = cN_c + qN_q + 0.5\gamma BN_q \tag{4.3}$$

Based on the above expression, and the corresponding bearing capacity factors, for the typical footing locations, Table 4.4 provides the bearing capacity estimates as obtained from Saran et al. (1989). It can be observed that the findings based on this technique is the highest, as expected from the upper bound estimates.

In a nutshell, Meyerhof's (1957) analysis for foundation resting on slopes does not recognize the actual development of the failure mechanism beneath the footing resting on the crest of the slope. A one-directional rupture surface that develops towards the face of the slope is accounted, and the same rupture phenomenon is considered towards the other side of the footing, thus generating a symmetric rupture mechanism beneath the footing. In this process, the full mobilization of resistive passive mechanism developed towards the interior of the slope (away from the face) is not fully appreciated, thus resulting in lowered magnitude of the bearing capacity. Hansen's (1970) limit equilibrium approach of determining the bearing capacity of the footing resting on the edge of the crest (exactly on the verge of the face) of a slope comprising c-φ soil, is a very restrictive slope-stability approach used for a special case analysis. In this technique, only one-directional rupture surface is considered in the analysis, and thus provides further lesser magnitudes of bearing capacity for the degenerated problems as listed in Table 4.4. Saran et al. (1989) approach considers the upper bound limit analysis approach to determine the bearing capacity of footings on slopes and establishes the maximum resistance offered by the slope against the foundation or slope failure. Moreover, Saran et al. (1989) approach incorporates full formation of rupture surface, both towards the slope face, and towards the other side of the footing. As a consequence, as per the characteristics of the upper bound theorem, the method regularly proposes a higher bearing capacity. Further, all the classical or theoretical techniques described herein are characterized by a predefined assumption of a probable rupture surface, based on which the bearing capacity is determined. Further, all the techniques are conditioned by stress-based approaches without incorporating the deformations induced in the slope during the progressive loading of the footing leading to its failure. Hence, only foundation failure is taken into consideration by the stated classical approaches, while the constitutive behaviour of soil is completely neglected. Further, all the classical approaches are developed only for continuous strip foundations. Keeping these limitations in mind, the FE analysis approach supersedes all these shortcomings, on the condition that a proper constitutive model is chosen to represent the material behaviour. The

FE analysis does not depend on the predefined assumptions of failure surfaces. Rather, based on the constitutive relationships of the involved materials, the failure mechanism evolves as a function of the progressive loading. Further, the coupled stress-deformation approached adopted in the FE analysis aids in the comprehension of simultaneous foundation failure and slope instability, and their effects on each other. Moreover, FE analysis can easily incorporate any footing shape in the analysis and uncover its progressive failure mechanism when loaded. Thus, it is essential to conduct FE analysis to establish the comprehensive understanding of the response of shallow foundations on slopes. The outcomes of the FE analysis would be further used to develop bearing capacity prediction expressions. Owing to the complex involvement of too many influencing parameters as well as the coupled stress-deformation response affecting the bearing response of shallow footings on slopes, soft computing technique will be adopted for developing the bearing capacity expressions, which will be discussed in detail in Chapter 6.

It can be noted that the validation problem presented in this chapter (or, similarly in the later chapters) involve miniature laboratory models, while the developed FE model is extended later to include the prototype footings of higher sizes, and consequently higher model dimensions. It is worthy to mention here that scaling effects do agree for different sizes of experimental setups. Specifically, the influence of scaling can be vividly noticed when the miniature centrifuge models are compared to the large-dimension prototype testing. The effect of scaling is mostly pertinent due to alteration of the relative stiffness at various material and their interfaces in different model sizes. In actual experiments, any change in the dimension of the model or its components in effective in changing the relative stiffness of the system. This is primarily attributed to the fact that absolute and relative stiffness are not independent parameters, rather derived parameters dependent on several dimensions of the system components. However, such scaling effect is not present in the numerical modeling. In any numerical modeling, the stiffness of system components are provided as parameters independent of the actual dimensions of the model. For example, when a footing is represented by a plate element, the change in the stiffness only changes the virtual thickness of a plate element, and the plate element of same width is applicable. Similarly, plates of higher sizes can be given lower stiffness by controlling the virtual thickness. Such virtual parameters does not affect the results from the numerical modeling. Thus, numerical models of different sizes can be efficiently used without any scaling effect. The effect of scaling related to load and deformation might still be an issue; the same load can limit the results in elastic regime for bigger size model, while it can generate plastic regime in the lower dimension models. However, for problems related to bearing capacity and slope stability, which deals with collapse and failure mechanisms, plastic regime is anyways developed at the end of the simulation, and hence, any load and deformation scaling, which might be present is overcome by the automatic load-advancement and load-stepping schemes.

4.6 Summary

In the context of presently growing urbanization in the hill-slopes, it is essential to study the behaviour and response of typical typologies of footings commonly adopted as shallow foundations in the residential and commercial buildings on the hillslopes. In this regard, this chapter reports the outcome of 2D and 3D FE studies carried out to study the behaviour and influence of a shallow square and strip footings located on dry homogeneous cohesionless and *c-φ* soil slopes. It has been highlighted that several geotechnical and geometrical parameters related to the slopes and supporting foundations affect the bearing capacity and the evolution of failure mechanisms of such foundations. It has been found that the setback distance, which governs the nearness of the footing to the slope face, largely influences the developed failure mechanism and the bearing capacity of the footing. With increasing setback distance, the influence of slope face reduces, and beyond a critical distance, the footing behaves as if located on horizontal ground. The bearing capacity reduces with increasing steepness of slope, and increases with the embedment depth, footing sizes and the shear strength parameters of the slope material. The present study highlights the limitation of the existing classical theories of prediction of the bearing capacity of foundations on slopes, and illustrates how the FE analyses is capable in providing a robust solution to the problem.

CHAPTER 5

RESPONSE OF INTERFERING FOOTINGS LOCATED ON SLOPES

5.1 General

From the point of view of urbanized localities on hill-slopes, the mechanism of a single footing does not necessarily address the presence of footings of various shapes, sizes and embedment depths, in vicinity to each other. However, such situation is quite common in hilly regions due to several constructions, whether residential or commercial structures, crammed into congested locations on the crest or face of the hilly slopes. Survey conducted in the inhabited hilly terrains of the North-Eastern (NE) areas of India reveal the dominant presence of shallow strip foundations on unreinforced hill slopes or terraces of the same (NDMA 2013). With the passage of time, growing inhabitation and changing trends of the building structures (from light-weight Assam-type housing to multi-storied concrete structures) is gradually appending to the changing deformation and instability of the slopes in the North-eastern India due to inadequate knowledge about the behaviour of foundation placed near the sloping surface. It has been witnessed from the background check that no work has been done regarding the interference effect of strip footings on hill slope. As a result, this investigation attempts to estimate the load carrying capacity of interfering strip footings located at sloping surface. In this regard, 2D and 3D FE simulations have been attempted with the aid of Plaxis software to comprehend the load bearing behaviour of such interfering strip footings and their corresponding failure mechanisms.

5.2 Validation of the Developed FE model

In the present research, the ultimate bearing capacity of interfering strip footings located on the crest of the slope has been investigated through 3-D finite element analysis with the aid of

Plaxis 3D. In various sections of the study, the response of interfering strip footings have been determined when they are located wither parallel to slope face (Chapter 4) or perpendicular to slope face (Chapter 7). The investigation of strip footings located parallel to slope face on crest of slope can be simulated in 2-D finite element analysis by following plane strain condition. However, the same 2D analysis cannot be adopted for the simulation of strip footings located perpendicular to slope face, as the response cannot be addressed by plane strain condition. Hence, to maintain the consistency of the investigation, 3-D finite element analysis has been considered for analysing the interfering strip footings located on the crest of the slope. The details of the 3D FE analysis has already been mentioned in Chapter 3.

Das and Larbi-Cherif (1983) had investigated the interference effect of strip footing on horizontal ground through laboratory experimentations. Dry sand having relative density of (D_r) of 54%, dry density of 15.88 kN/m^3, and angle of internal friction (φ) of 38°, had been used to fill a test box of dimension 1.524 m × 0.305 m × 0.914 m. Steel footings, connected by frames, each having dimension 50.8 mm × 304.8 mm, were placed over the crest of the sand slope. The centre-to-centre distance between the footings has been considered as the footing spacing (S). For the purpose of validation, a 3-D numerical model has been developed in the present study that conforms to the exact dimensions used in the experimentation program (Das and Larbi-Cherif, 1983). The numerical simulations have been developed for different spacing of the interfering footings, ranging from 1B to10B, where B is the width of an individual footing. Any FE model should achieve numerical stability before they can be used for definitive validation or prediction studies. It is well understood that the finite element studies of engineering problems are sufficiently affected by the mesh size and number of elements. This influence is mainly attributed to the refinement associated to the numerical computation. As in this case, the FE model represents a continuum medium, it is imperative that the entities of the response of the medium (i.e. stress, strain, deformation etc.) should be computed as precise as possible, while taking care of redistribution of stresses and strains in the attractor or concentration zones (mostly at the interfacial corners of the model elements). Keeping this in mind, any FE numerical model has to be numerically stabilized by choosing the apt mesh size, thus providing the optimal mesh element numbers. Following the same, to achieve a numerically stable FE model and selecting the optimum mesh configuration, a mesh convergence analysis has been conducted for a representative spacing of the interfering footings (*S/B* = 1.5). Figure 5.1 describes the results of the convergence analysis in terms of non-dimensional average element size (NAES, ratio of average element length and the height of the domain), which shows that the outcomes are nearly similar beyond NAES ≈ 0.05, and the same has been used for the estimation of the numerical results from the validation model. Fig. 5.2 shows that there is a significant match between the numerical results with those obtained from experimental investigations (Das and Larbi-Cherif, 1983), thus rendering the developed numerical model to be validated.

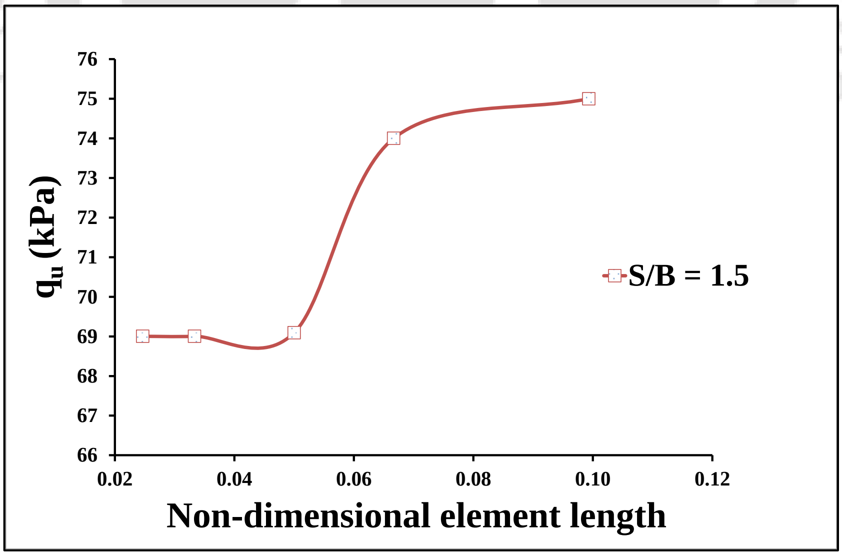

Fig. 5.1 Typical convergence study for interfering strip footings resting on horizontal ground

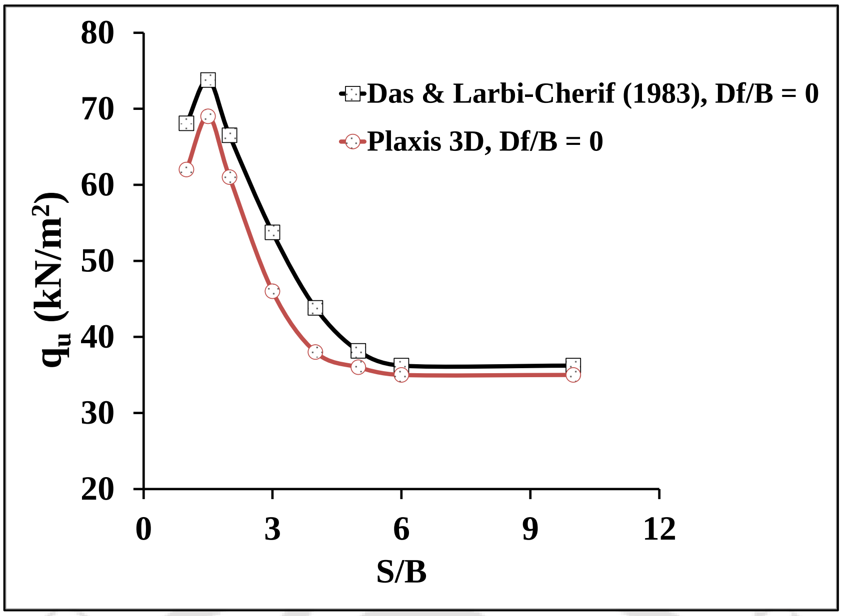

Fig. 5.2 Validation of the numerical model with experimental investigation by Das and Larbi-Cherif (1983)

The interference mechanism has been checked through slip mechanisms generated beneath the footing in terms of incremental displacement. Figure 5.3 portrays that the footings spaced within a distance of 6*B* can be considered to have mutual influences on their stress and settlement characteristics and can be termed as closely-spaced interfering footings. Beyond this spacing, the interaction effects of the footings cease to exist, and hence, the footings can be considered as isolated footings. The results obtained from numerical simulation of the validation study have also been compared with those obtained from theoretical formulations (Stuart 1962), and the comparative have been tabulated in Table 5.1. It can be observed that the outcomes of FE analysis well conform to the findings of Stuart (1962), thus providing confidence on the developed FE model which can be further used to study the response and failure mechanism of interfering footings on slopes. It is worth mentioning that until date, neither any experimental investigation has been carried out nor any theoretical formulation has been developed to predict the response of interfering footings resting on the crest or face of a slope, in terms of their bearing capacity or failure mechanism. In this regard, this study proves to be pioneering in providing the bearing response and failure mechanism of interfering strip footings on slope crest.

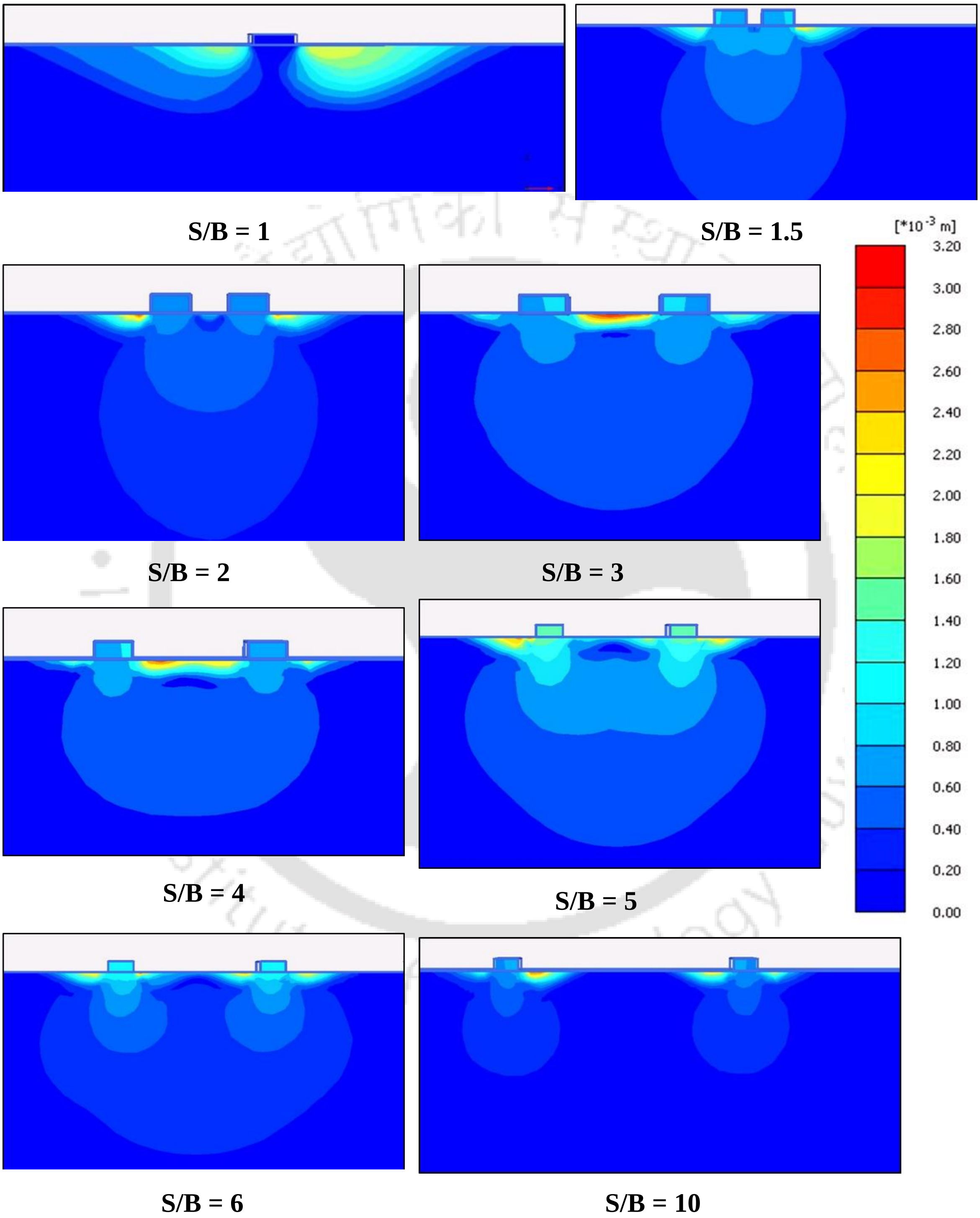

Fig. 5.3 Typical interaction mechanism of interfering strip footings for various spacing ratios

Table 5.1 Comparison of the bearing capacities of interfering surface strip footings resting on horizontal ground obtained from the FE analyses and theoretical formulation

Spacing ratio (S/B)	q_u (kPa) (Stuart 1962)	q_u (kPa) (FE analysis)
1	63.41	62.20
1.5	85.61	70.15
2	69.75	61.23
3	47.56	46.05
4	39	38.13
5	31	36.30
6	31	35
10	31	35

5.3 Interfering Strip Footings Located on Slope Crest

This section describes the influence of various parameters on the bearing capacity and failure mechanism of the interfering strip footings located on the crest of a slope.

5.3.1 Influence of setback distance on the failure mechanism of a single strip footing located on slope crest

The effect of setback distance (b) on ultimate bearing capacity and failure mechanism has been studied for isolated strip footing resting on the crest of c-φ soil slope, and has already been elaborated in Chapter 4. The numerical simulation of strip footings resting on sloping ground, with various setback ratios (b/B), slope angles (β) and footing widths (B) had been checked for mesh convergence, the typical results of which are illustrated in Fig. 5.4. It can be observed that the obtained results are nearly identical beyond a fine mesh (average non-dimensional mesh size of nearly 0.04), and the same is used in the further studies with sloping ground. It is depicted in Fig. 5.5 that the dimensionless ultimate bearing capacity increases with increasing setback ratio (b/B) up to 6, beyond which no substantial changes are noted.

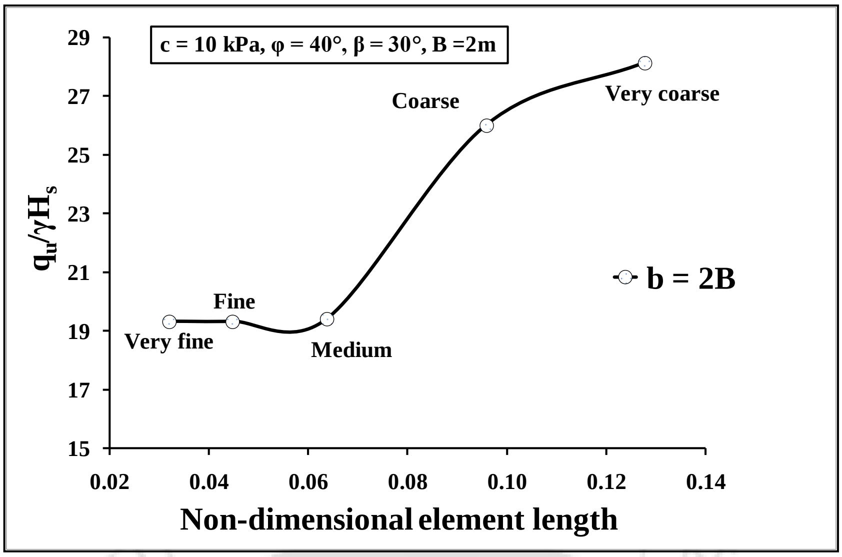

Fig. 5.4 Typical convergence study for strip footing resting on slope crest

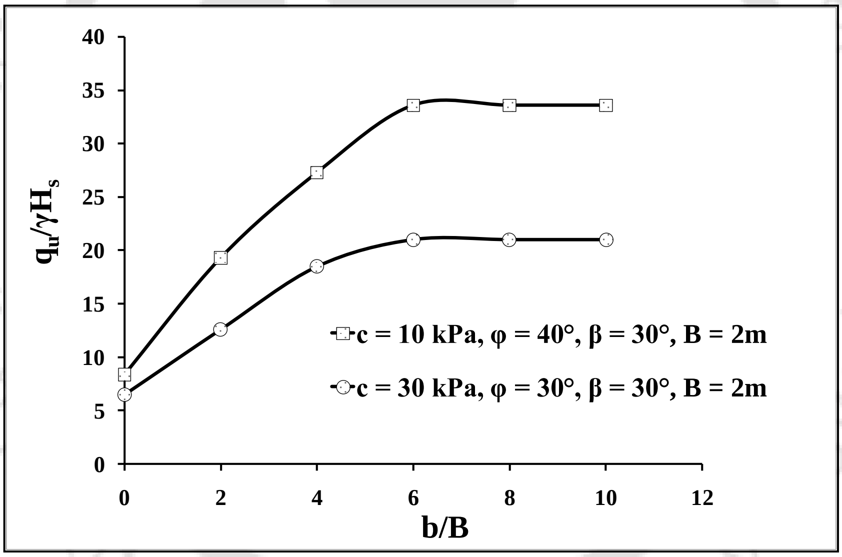

Fig. 5.5 Typical variation of ultimate bearing capacity of strip footing with setback distance

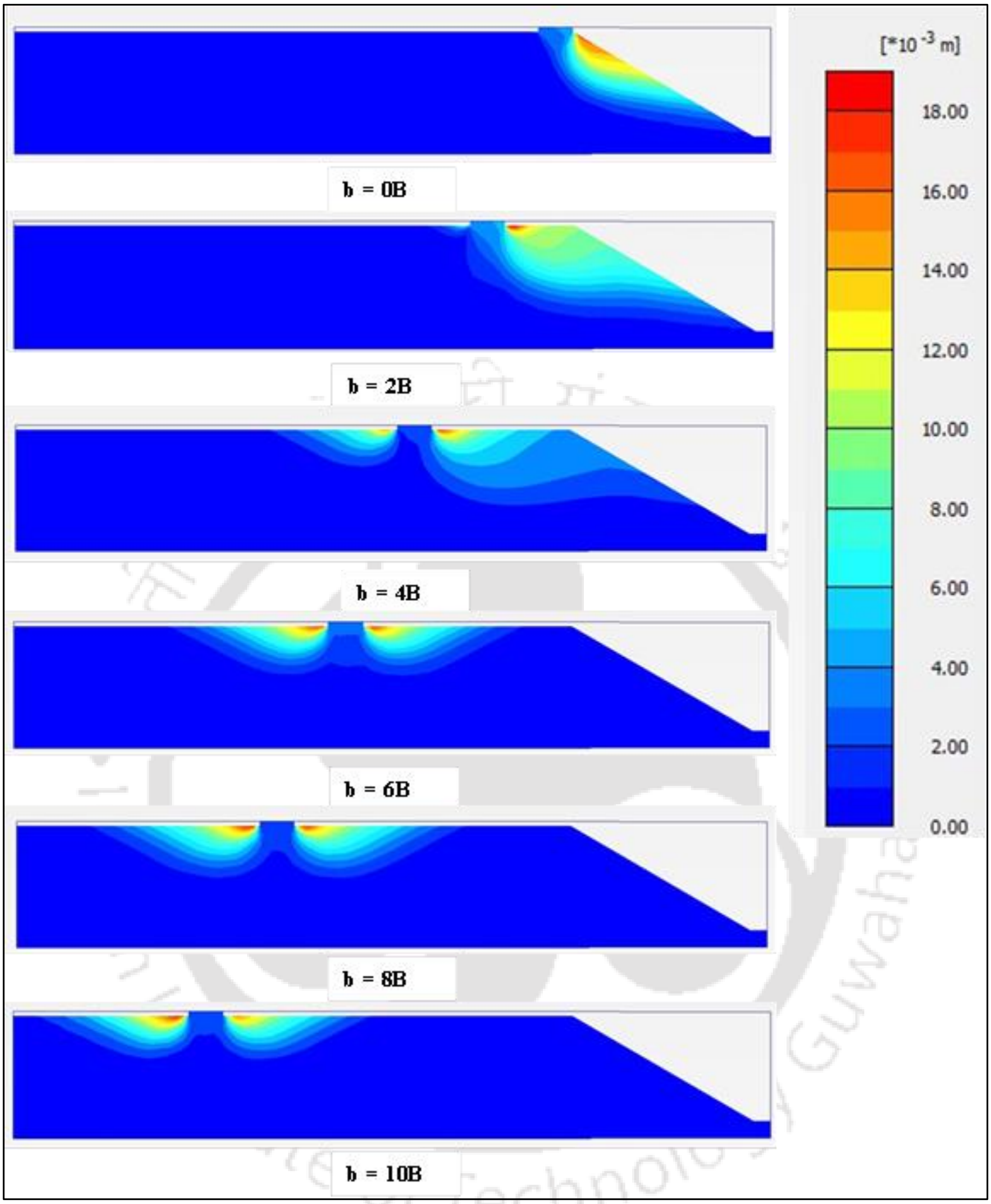

Fig. 5.6 Typical formation of passive zones and failure mechanisms beneath the strip footing located on slope crest having various setback ratios

For strip footings located at various setback distances from the slope face, Fig. 5.6 highlights the influence of sloping face in reducing the bearing capacity by intersecting the resisting passive zone formed toward the slope face. It can be witnessed that the developed passive zone is largely one-directional and curtailed by the slope face when the footing is located at the crest of the slope (b/B= 0), which is attributed to the dominant free deformation of the soil due to the loading of the footing until failure. This phenomenon results in a considerable decrease of the confinement pressure, and hence, attenuation of the bearing capacity. As the setback ratio increases, the dominant influence of the slope face on the development of the passive mechanism gradually reduces, as shown in Fig. 5.6. It is observed that beyond a critical setback ratio of 6, the footing behaviour corresponds to that of the same resting on horizontal ground. For such cases, the developed displacement contours, representing the passive zone, remains unaffected.

5.3.2 Influence of spacing, slope angle and setback distance on the response of interfering strip footings located on slope crest

Figure 5.7 portrays the effect of spacing (S) on bearing capacity of interfering strip footings located near the slope for various setback distances (b) and slope angles (β). It has been perceived that the dimensionless ultimate bearing capacity (q_{un} = $q_u/\gamma H_s$) increases up to spacing 1.5B, followed by a progressive reduction until 3B, beyond which the magnitude remains asymptotic for further spacing ratios. For S = 1B, the footings act as a single footing of increased width (2B). At the spacing S = 1.5B, the interference of pressure bulbs beneath the two footings result in a larger zone of foundation soil participating in the bearing resistance of the footing, leading to an enhanced magnitude of the dimensionless ultimate bearing capacity ($q_u/\gamma H_s$). It has been perceived that, on an average, q_{un} decreases by 15% per 10° increment of slope angle (β). Concerning the setback distance (b), on an average, q_{un} increases by 25% for increasing setback distance up to 2B, while the same increases by 7% upon further increasing the setback distance (b) up to 6B. Beyond 6B, the bearing capacity approaches that obtained for an individual isolated footing and the influence of setback distance ceases to exist.

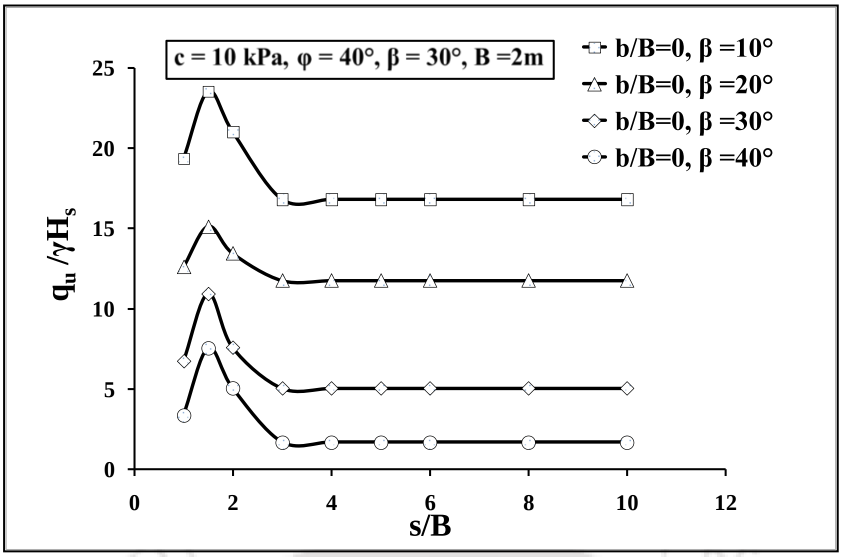

c = 10 kPa, φ = 40°, β = 30°, B =2m
b/B=0, β =10°
b/B=0, β =20°
b/B=0, β =30°
b/B=0, β =40°
$q_u / \gamma H_s$
s/B
0
5
10
15
20
25
2
4
6
8
10
12

(a)

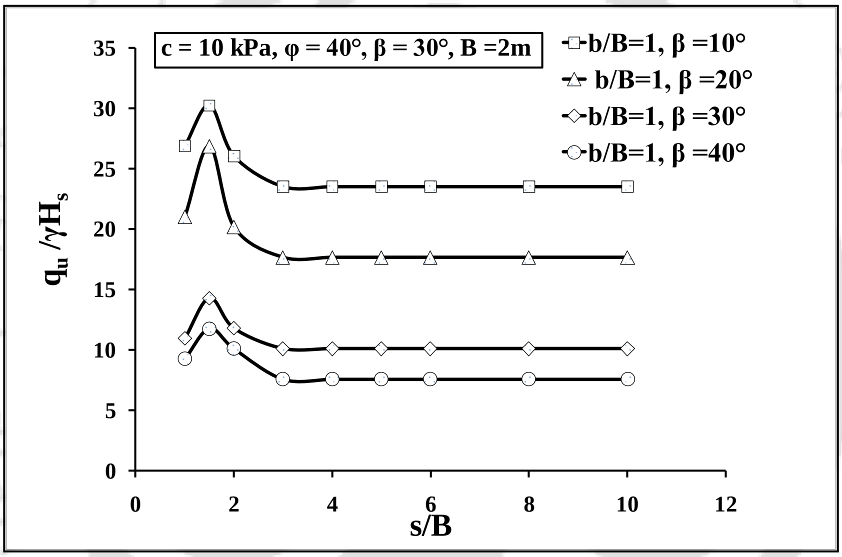

c = 10 kPa, φ = 40°, β = 30°, B =2m
b/B=1, β =10°
b/B=1, β =20°
b/B=1, β =30°
b/B=1, β =40°
$q_u / \gamma H_s$
s/B
0
5
10
15
20
25
30
35
2
4
6
8
10
12

(b)

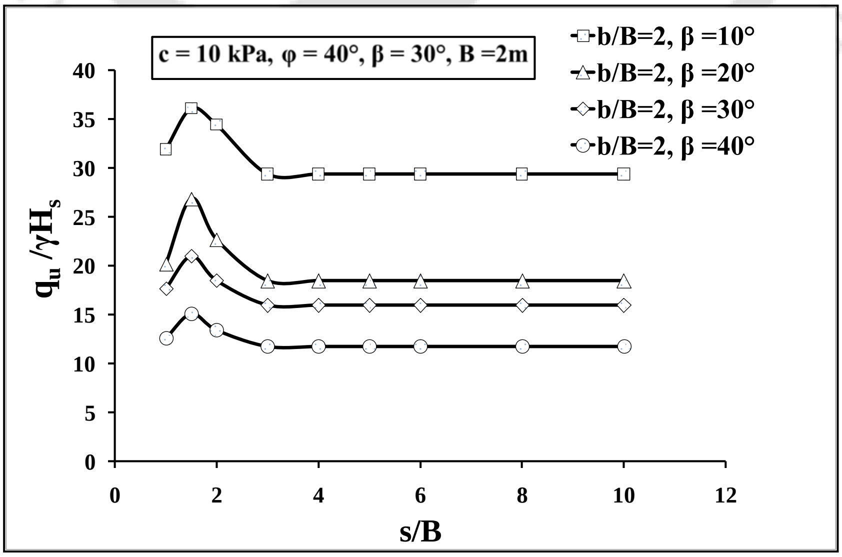

c = 10 kPa, φ = 40°, β = 30°, B =2m
b/B=2, β =10°
b/B=2, β =20°
b/B=2, β =30°
b/B=2, β =40°
$q_u / \gamma H_s$
s/B
0
5
10
15
20
25
30
35
40
2
4
6
8
10
12

(c)

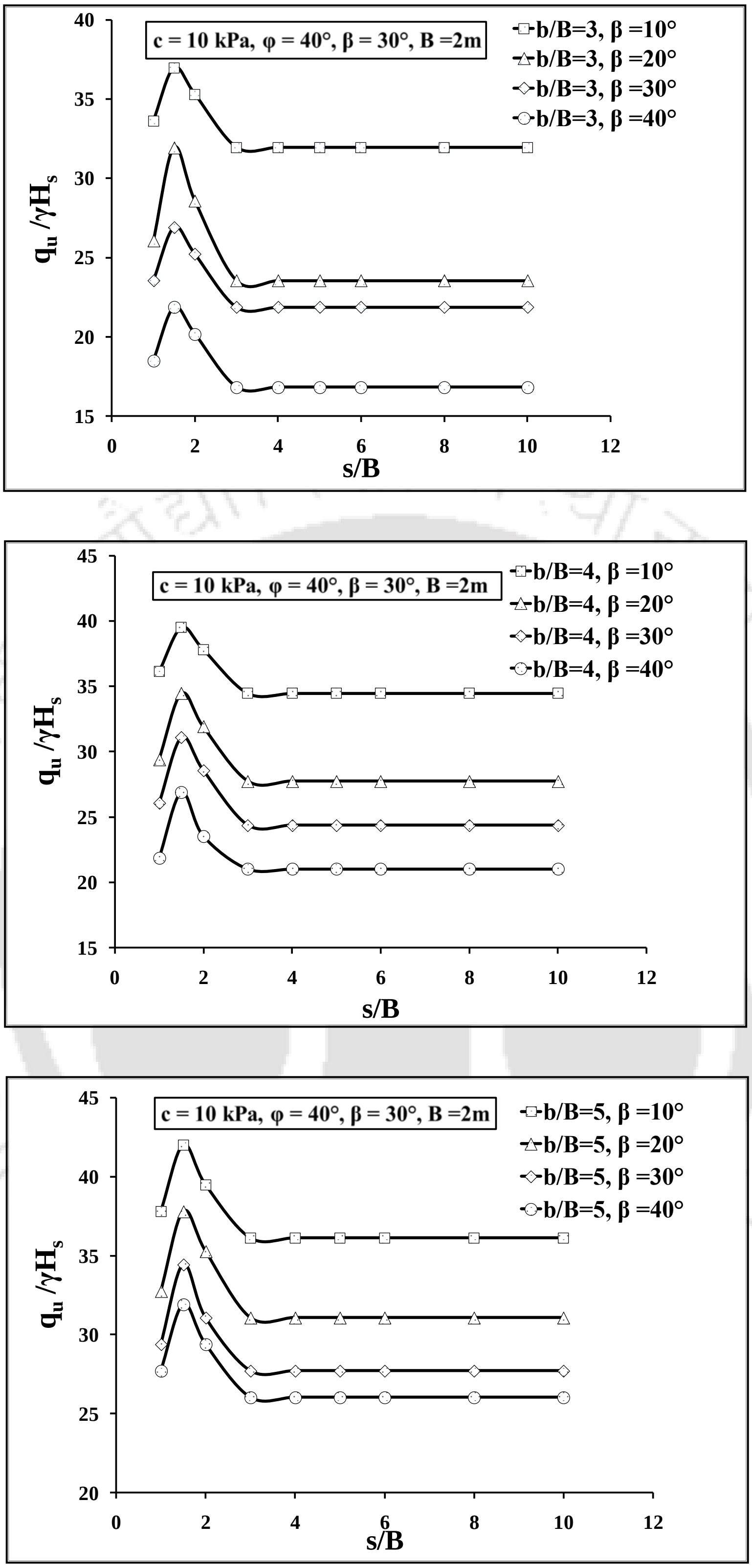

Fig. 5.7 Effect of setback distances and slope angles on ultimate bearing capacity of interfering strip footings located on the crest of a slope (a) *b*/*B* = 0 (b) *b*/*B* = 1 (c) *b*/*B* = 2 (d) *b*/*B* = 3 (e) *b*/*B* = 4 (f) *b*/*B* = 5

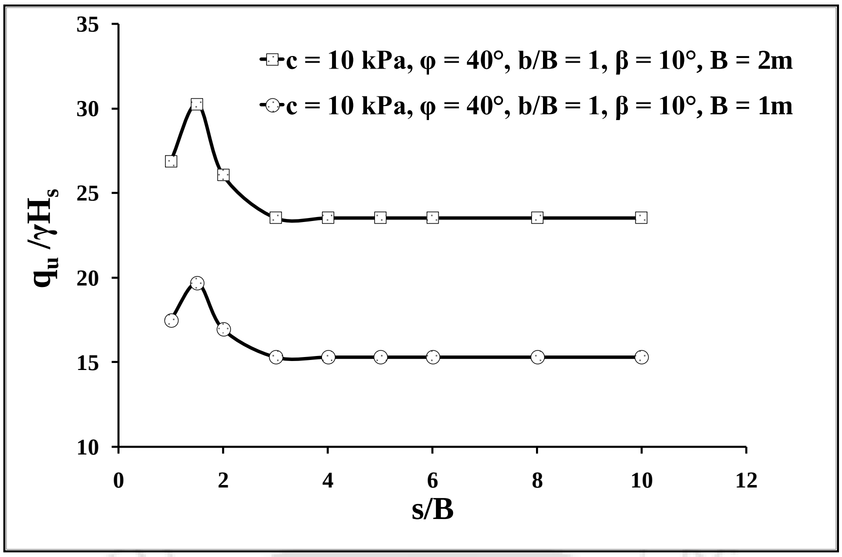

Fig. 5.8 Effect of footing widths on ultimate bearing capacity of interfering strip footings

5.3.3 Influence of footing width on interfering footings on the crest of slope

Figure 5.8 depicts the influence of footings widths on the bearing capacity of interfering strip footings. It is observed that $q_u/\gamma H_s$ reduced with decreasing footing width, which is attributed to the fact that a wider footing involves a larger zone of foundation soil to participate in the resisting mechanism, thereby increasing the bearing capacity. The effect of spacing of the interfering strip footings remains the same as highlighted in the previous section. On an average, $q_u/\gamma H_s$ increases by 35% as the footing width is doubled, while the same decreases by 15% for each 10° increment of slope angle.

5.3.4 Influence of soil types on interfering footings on the crest of slope

Figure 5.9 illustrates the effect of different types of foundation soil on the bearing capacity of interfering strip footings. It is seen that the maximum value of $q_u/\gamma H_s$ has been obtained for soil having higher friction angle, while soil having lower angle of internal friction depicts the lowest $q_u/\gamma H_m$. This observation highlights that the trend of variation of $q_u/\gamma H_s$ with the soil types is primarily governed by the variation in φ. Based on the results obtained with various types of soils as the slope material, it is observed that a spacing of $S = 3B$ can be considered as limiting spacing beyond which the interference effect completely disappears.

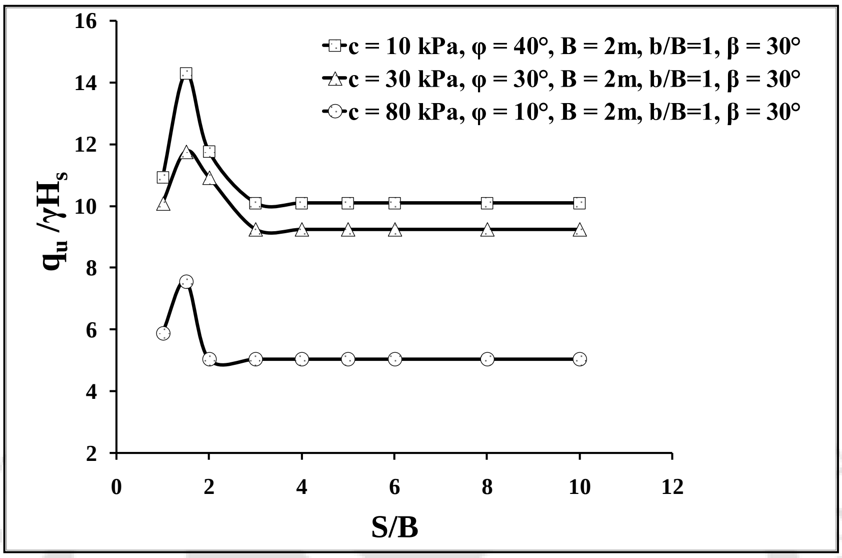

Fig. 5.9 Effect of soil types on ultimate bearing capacity of interfering strip footings

5.3.5 Interaction mechanism for footings resting on the crest of a slope

Figure 5.10 portrays the interaction mechanism of strip footings resting on the crest of a slope and separated by various spacing ratios (S/B). There exist two common and frequently interchangeable practices to represent the spacing between two footings. One practice adopts the clear spacing, while the other adopts the center-to-center spacing between the footings. The present study adopts the latter. Under such condition, if the footing widths are B, a clear spacing of $1B$ is identical to a center-to-center spacing of $2B$. Similarly, if two footings of width B are in contact with each other, the spacing between the footings is zero as per the former approach, while the spacing is $1B$ as per the latter approach.

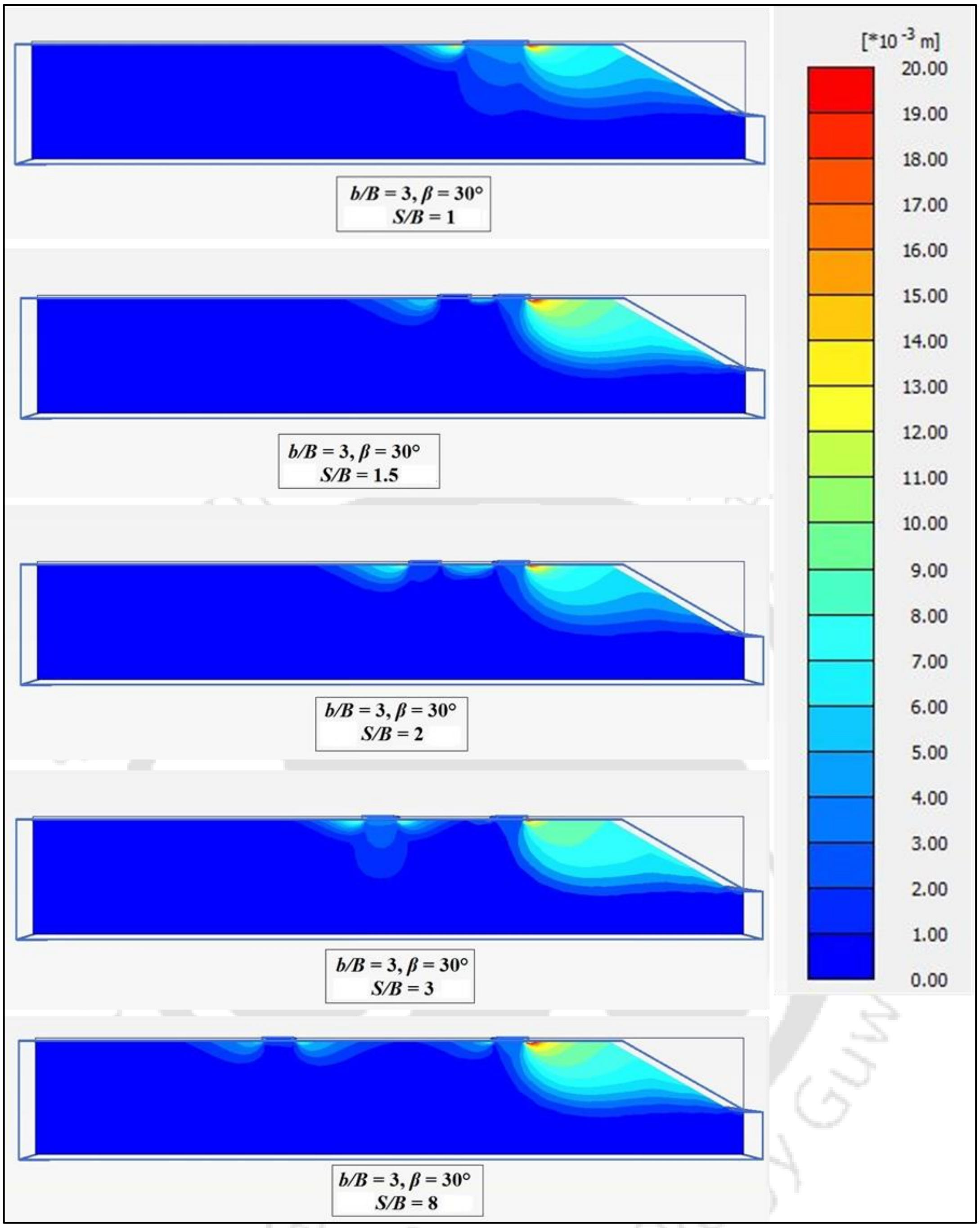

Fig. 5.10 Typical interaction mechanism for interfering footings having various spacing ratios (S/B) for b/B = 2

Thus, S/B = 0 as used in Nainegali et al. (2013) and S/B = 1 as used in present study (Fig. 5.10) is primarily identical; Nainegali et al. (2013) adopts the practice of clear spacing between footing, while the present study adopts center-to-center spacing between footings. As S/B

increases, the influential effect of each footing on the generation of failure zones progressively reduces. In the present research, the formation of failure mechanism has been investigated up to spacing ratio (S/B) of 8. It was observed that the overlap of the displacement contours totally disappears beyond S/B = 3, and that the footing located afar from the slope face exhibited a bearing phenomenon similar to an isolated strip footing placed on a horizontal semi-infinite medium.

5.4 Interfering Strip Footings Located on Slope Face

It is common to experience the presence of adjacent buildings located in the slope face, especially in the North-eastern mountainous terrains. Foundations located on such slope faces, especially the interacting ones located in close spacing, are quite instrumental in influencing the stability of the slopes, which in turn, affects the failure mechanism and bearing capacity estimation of such footings. Hence, considering both the theoretical and practical importance, a study has been conducted to determine the failure mechanism and bearing capacity estimates of such footing located on the face of a slope. In the investigation, strip footings have been placed parallel to the slope length on the slope face. In the research, no other footing position has been considered on the slope face. The investigation of strip footings located parallel to slope length on face of slope can suitably be addressed in 2-D finite element analysis through plane strain condition. Hence, the ultimate bearing capacity of interfering strip footings located on the slope face has been investigated with the aid of Plaxis 2D.

5.4.1 Problem statement

A 55m high hill slope has been modelled in the PLAXIS 2D to represent a typical field slope geometry. A shallow strip footing is considered located at the slope face, 10 m below the crest level. The location is so maintained that the stress-strain mechanism developed beneath the foundation remain unaffected by the fixed boundaries of the domain; in other words, the position of the footing is so chosen that only the effects of the loading and slope boundary comes into consideration. The footing has been placed in such a way that the height between the near-end of the footing to the slope surface is 1 m, which ascertains the minimum embedment depth of the footing within the slope. The intention was to provide a nominal soil cover of 1 m as shown in Fig. 5.11. Further, in order to incorporate multiple footings, one footing has been fixed at 10 m below the crest (as already mentioned), while the other footings are placed at various elevations (in terms of footing width below the level of 1^{st} footing), as shown in Fig. 5.12. In order to investigate the interaction of footings located on the slope boundary, the simulation has been done for 7 different scenarios of footing location, the maximum relative elevation of the footing being considered as 10*B*. In the present study, horizontal fixity was given to the vertical edges of the model (NB: The inclined face of the sloping ground is not provided with any boundary fixity, as a footing located on or near the slope face will be affected by the deformation of the same). In the bottom edge of the model, both vertical and horizontal fixity were applied, as the base of the model is assumed non-yielding. As stated earlier, fine mesh has been used for all further studies of footings located on a slope. The simulations have been carried out for three different varieties of soil (Medium dense sand, Dense sand and c-φ soils), the properties of which have been tabulated in Table 5.2. In the present investigation, the footing has been subjected to displacement based failure mechanism, where the failure displacement given to the strip footing is considered as 20% of the footing width (*B*).

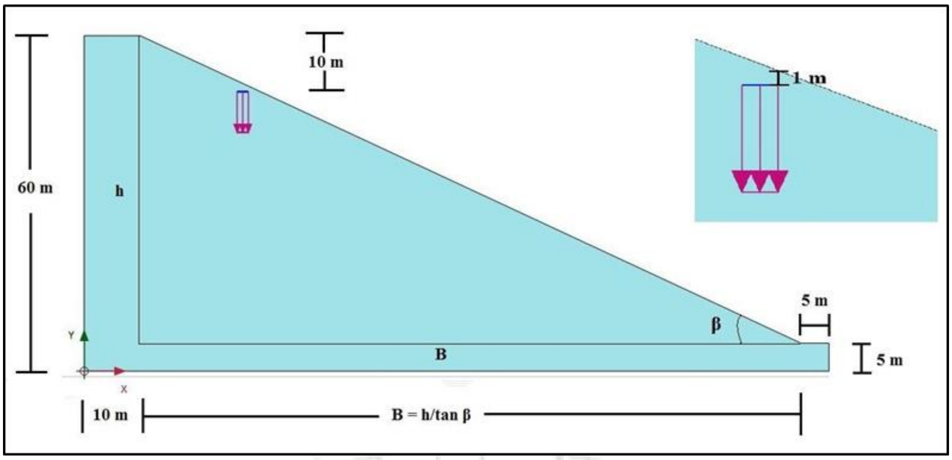

Fig. 5.11 Representative schematic diagram of a strip footing located on a slope face

Table 5.2 Different types of foundation soil as used in the present investigation

Soil types	Cohesion (c) (kPa)	Angle of internal friction (φ)°	Unit weight (γ) (kN/m^3)	Modulus of elasticity (E) (MPa)	Poisson's ratio (ν)
Dense sand	0	40	19	40	0.3
Medium dense sand	0	30	17	20	0.28
c-φ soil	20	30	18	20	0.3

5.4.2 Interpretations and discussions

As stated, the simulation has been conducted for 7 different scenarios of interacting footings. As a benchmark problem, the response of an isolated strip footing has also been investigated; this problem is termed as 'h = 0 B' condition. This section discusses about the influence of various parameters on the bearing capacity and failure mechanism of interfering strip footings located on the crest of a slope.

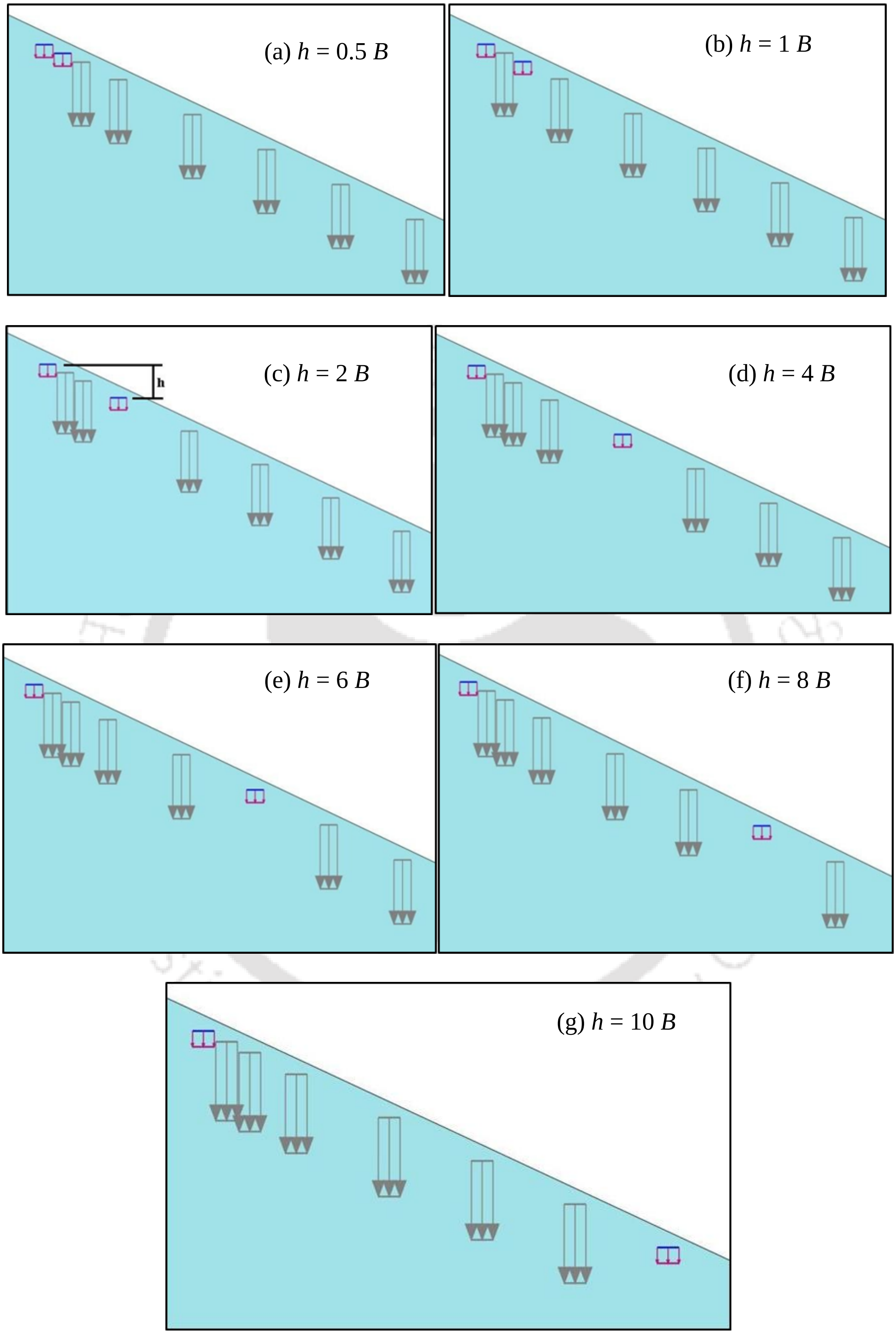

Fig. 5.12 Various position of interacting footings located on slope face

5.4.2.1 Effect of influencing parameters

Reconnaissance of the habitations in the hilly terrains reveal that most of the urbanization have taken place on the hill slopes having slope angle within the range of 20° to 30°. With this background information, three different slope angles (20°, 25°, and 30°) have been considered for the present investigation. The influence of the slope angle on the interaction effects of footings on such slopes are presented in Fig. 5.13. It can be seen that the bearing capacity reduces for the closely located footings within a relative elevation of $2B$, beyond which the bearing capacity of the footings gradually increases to reach an asymptotic constant value (at $h = 8B$) identical to the bearing capacity of isolated strip footing resting on slope. It has also been realised that if slope angle decreases, bearing capacity increases (as expected), although the mechanism associated with interference remains the same for all the slope angles. The associated mechanism is discussed in detail in a later section.

Figure 5.14 describes the effect of the soil typology on the variation of bearing capacity. It is detected that owing to dense packing of the constituent particles leading to higher confinement on the footing, dense sand has provided higher bearing capacity than that provided by medium dense sand. It can be seen that the c-φ soil shows a similar behaviour as that of the dense sand, which may vary depending upon the chosen strength parameters for the soil. It was noted that the mechanisms associated with interference was same for all soil types.

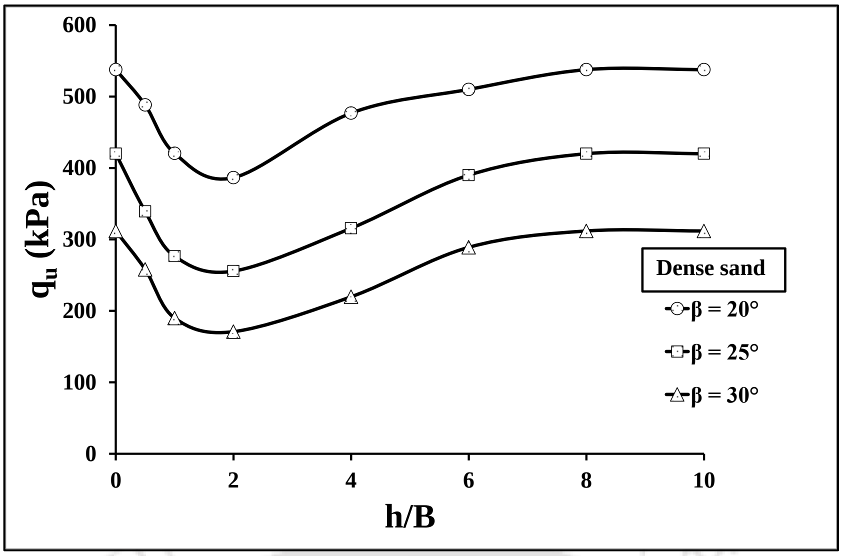

Fig. 5.13 Influence of slope angle on the interaction effects of footings located on slope face

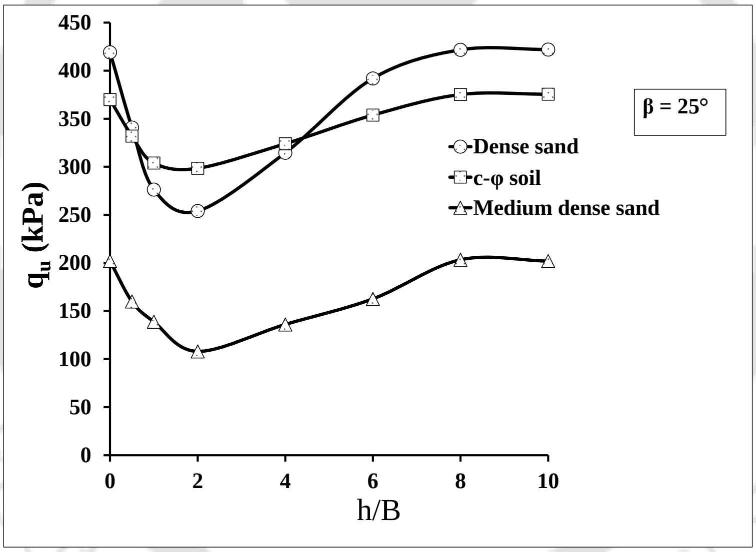

Fig. 5.14 Influence of soil types on the interaction effects of footings located on slope face

Figure 5.15 exhibits the effect of the variation of footing size on the variation of bearing capacity. Although the interaction mechanisms remain the same, it can be realised that, as expected, the increase in the footing width results in the increases in bearing capacity.

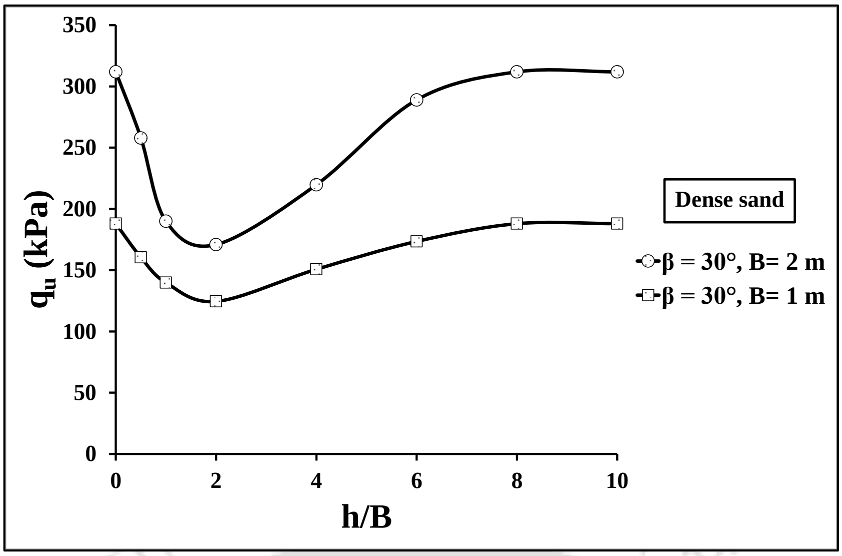

Fig. 5.15 Influence of footing width on the interaction effects of footings on slope face

5.4.2.2 Interaction mechanism of interfering strip footings located on slope face

For investigating the interaction effect of footings on slope using the 2D simulation, a failure displacement of 20% of footing width has been applied on the footings. As mentioned earlier, Fig. 5.13 indicates that the bearing capacity of the footing decreases up to 2*B*, and then gradually increases to reach the bearing capacity of an isolated strip footing beyond 8*B*. Figure 5.16 exhibits the displacement behaviour of the model domain (multiple footings on a slope) for varying levels of interferences. The degree of interaction is quantified by the overlap of the 0.1*B* displacement contour (termed as ‘significant displacement contour) produced by the adjacent footings. In a similar manner, Fig. 5.17 portrays the interference effect of strip footings on the face of the slope in terms of the developed incremental deviatoric strain mechanisms.

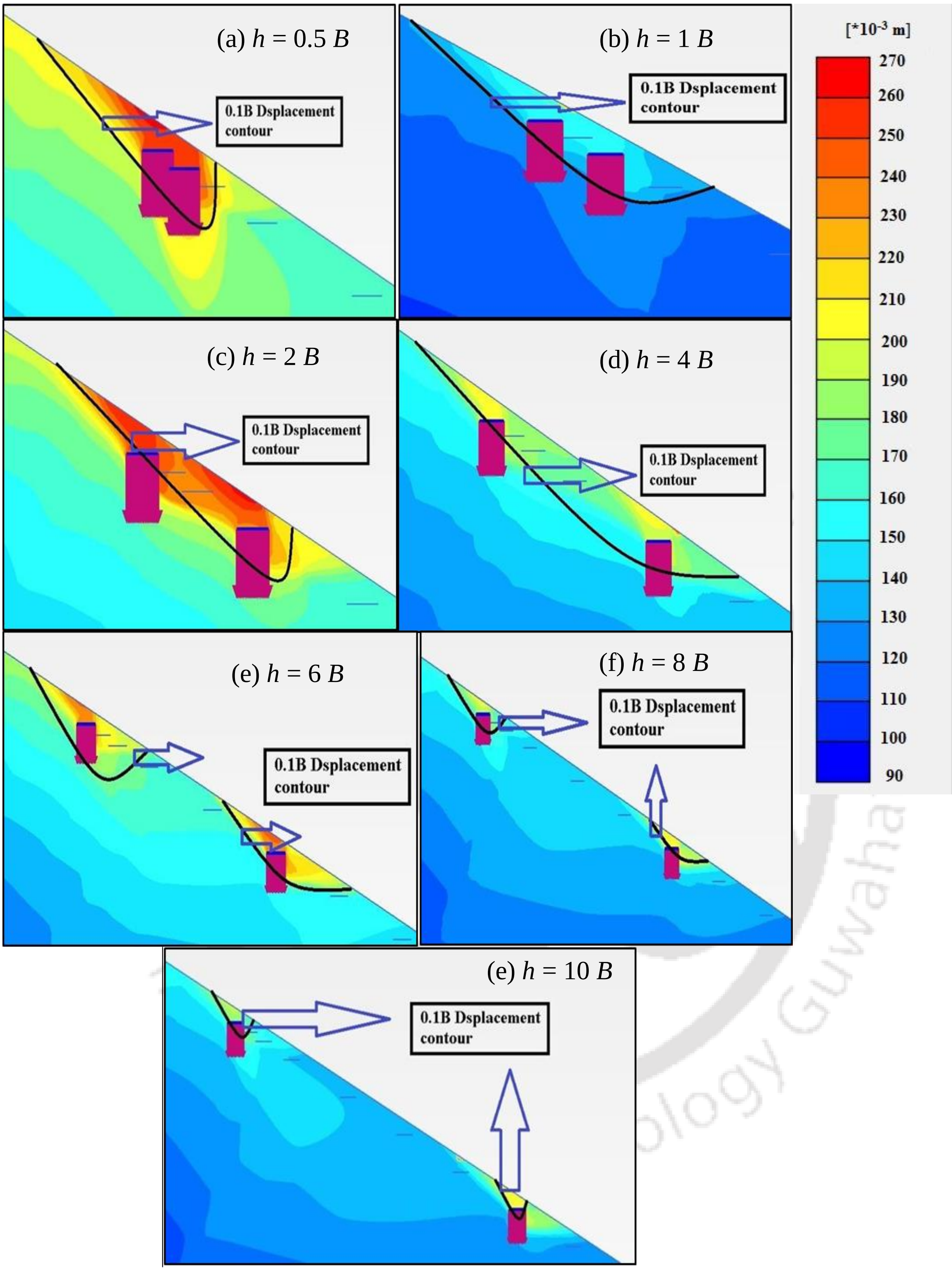

Fig. 5.16 Displacement mechanisms of interfering strip footings located on slope face

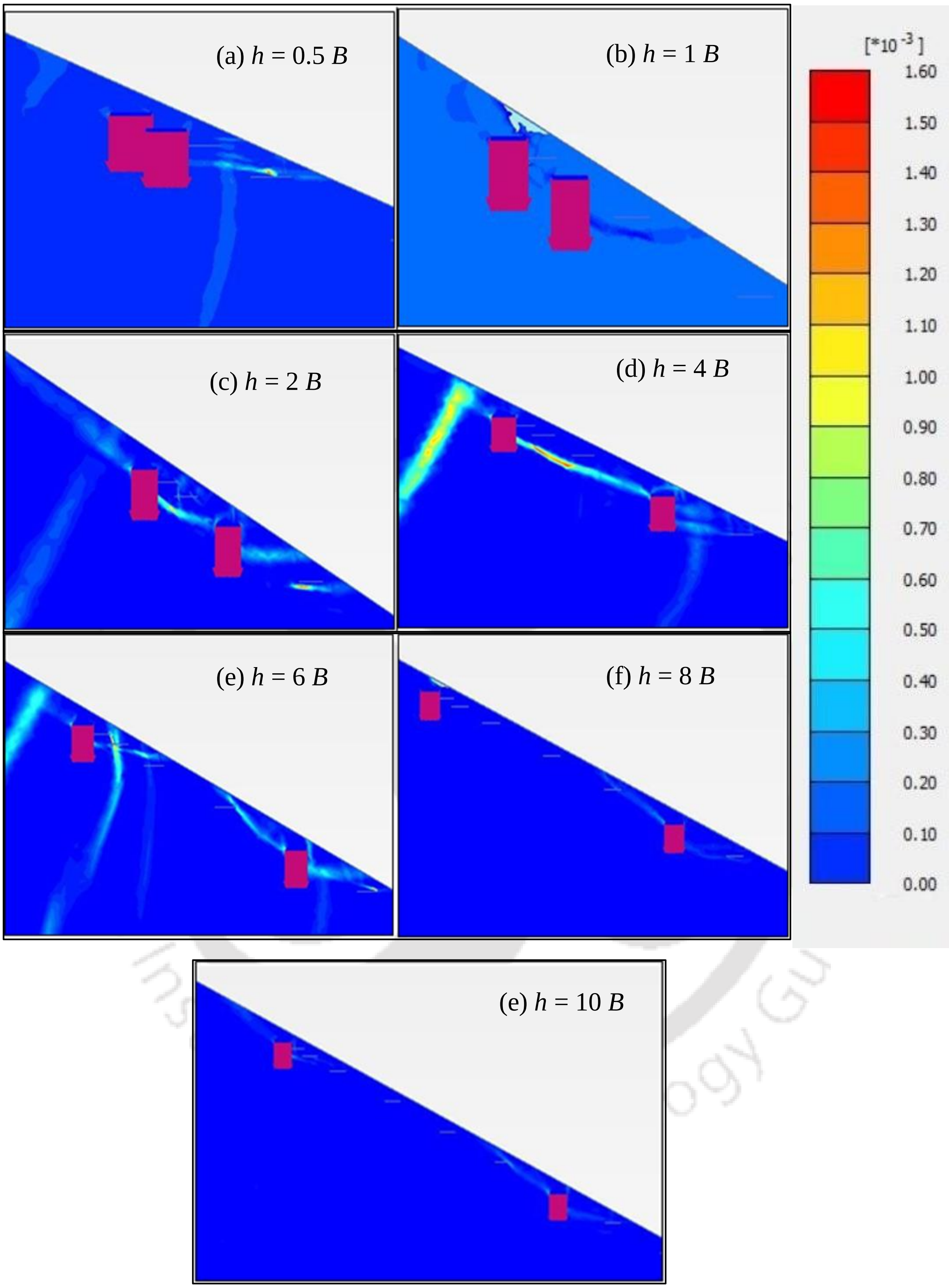

Fig. 5.17 Incremental deviatoric strain mechanism highlighting the failure surfaces for the interfering footings

The incremental deviatoric strain can be calculated from following expression (Eq. 5.1)

$$\Delta \in_q = \sqrt{\frac{2}{3}[(\Delta \in_{xx} - \frac{\Delta \in_v}{3})^2 + (\Delta \in_{yy} - \frac{\Delta \in_v}{3})^2 + (\Delta \in_{zz} - \frac{\Delta \in_v}{3})^2 + \frac{1}{2}(\Delta \gamma^2{}_{xy} \Delta \gamma^2{}_{yz} \Delta \gamma^2{}_{zx})} \tag{5.1}$$

where, $\Delta \in_{xx}$, $\Delta \in_{yy}$ and $\Delta \in_{zz}$ are the incremental Cartesian strains, $\Delta\gamma_{xy}$, $\Delta\gamma_{xy}$ and $\Delta\gamma_{xy}$ are the incremental shear strain. $\Delta \in_v$ is the incremental volumetric strain $\left(\Delta \in_v = \Delta \in_{xx} + \Delta \in_{yy} + \Delta \in_{zz}\right)$. Incremental deviatoric strain mechanism refers to the incremental deviatoric strain pattern at failure or during its evolution. The incremental deviatoric strain and its pattern helps to identify the slip zones developed beneath the footing during the analysis of a coupled stress-deformation problem.

Fig. 5.18 highlights the significant displacement contour produced by the loading of the benchmark footing. The region bounded by the significant displacement contour and slope boundary demarcates the volume of soil that is susceptible to substantial movement upon loading of the footing. Any other footing present in this region, and simultaneously loaded until failure, will result in further drastic movement of the soil in the bounded region. Apart from the above phenomenon, the closely spaced footings when loaded simultaneously also results in the overlap of the displacement zones resulting in an enhanced significant displacement 0.1*B* contour.

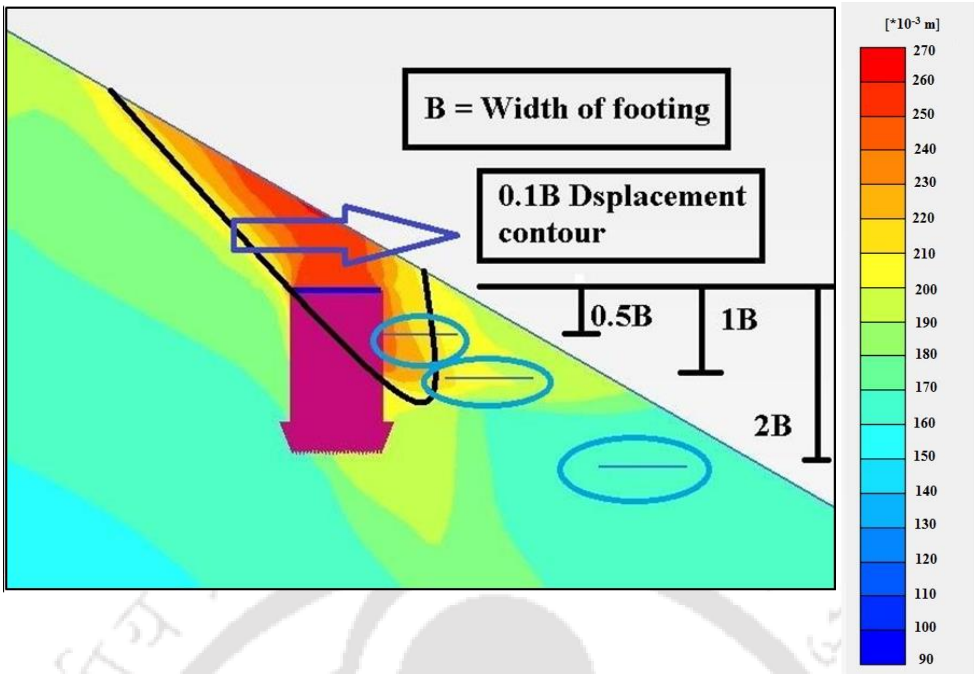

Fig. 5.18 Demarcation of significant displacement contour for the benchmark problem

This behaviour can be observed from the various footing interaction scenarios as depicted in Fig. 5.16 and Fig. 5.17 in terms of the displacement mechanism and incremental deviatoric strain mechanism, respectively. It can be clearly noted that the displacement overlap is significant for the footings within a relative elevation of 2*B*, beyond which increase of the relative elevation reduces the overlap of the significant displacement contour resulting in gradual isolated behaviour of the footing. Beyond $h = 6B$, no significant overlap is manifested, indicating that beyond this distance, the footings commence behaving as independent isolated strip footings. No noticeable changes are noticed any further beyond a relative elevation of 8*B* between the footings.

5.5 Efficacy and Limitation of Developed Numerical Model

From the past researches, it has been clear that there are experimental works conducted for isolated strip footings located on horizontal or sloping grounds. There are very few examples of experimental investigations involving isolated strip footing located on slope crest. However, there has not been a single experimental or theoretical investigation reported for multiple and interfering strip footings located on the crest of a slope. In this regard, to further calibrate and validate the developed numerical model to check its efficacy in predicting the bearing capacity of interfering strip footings on slope, typical experimental studies considering an isolated strip footing on slope crest have been considered. In this context, the experimental study reported by Keskin and Laman (2013) has been taken into account. It is worth mentioning that the interfering effect of the footings completely disappear beyond a spacing ratio, S/B = 3. Hence, proper numerical models were developed in which the footing located away from the crest is kept at a spacing ratio S/B > 8, and the bearing capacity of the foundation is obtained.

Keskin and Laman (2013) had experimentally investigated the ultimate bearing capacity (qu) of strip footing resting on crest of slope. In the experiment, different geotechnical and geometrical parameters had been varied to investigate the influence on qu. For the validation, a strip footing of width (B) 70 mm, located on crest of sand-slope having angle of inclination (β) of 30°, have been considered. The angle of internal friction (φ) and dry unit weight (γd) of the soil were 41.8° and 17 kN/m3 respectively.

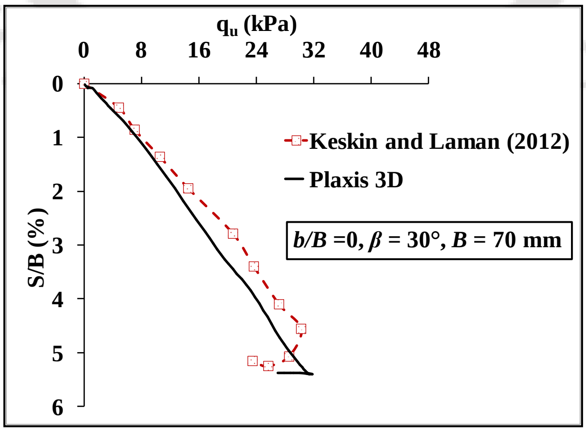

Fig. 5.19 Comparison of pressure-displacement patterns obtained from the numerical model and experimental studies (Keskin and Laman 2013)

In the cases of validation, numerical models comprising a spacing ratio S/B = 10 has been considered so that the footing nearer the slope should behave like isolated strip footing on the crest of slope without having any interference of the far footing on its pressure settlement pattern. Figure 5.19 portrays the load-settlement behavior of the strip footings located on slope crest. It can be perceived that there is excellent agreement in pressure-settlement patterns, as well as the bearing capacity, obtained from present numerical investigation and those estimated from the experimental investigations. As the average difference between the measured and numerical values ranged less than 7%, the developed numerical models can be considered well calibrated and efficient in predicting the bearing capacity of strip footings on slopes.

Further, it is worth mentioning that the FE models were developed only for interfering strip footings resting on the crest or face of the slope. These problems are classified in the domain of plane-strain problems. However, in actual practice, the foundations of an urbanized hillslopes will present a three-dimensional problem and would involve more complex stress and strain distributions considering the erratic geometry and loading features. Hence, the findings from the interfering strip footings can only be applied for restrictive cases. However, the understanding developed from the study of plane-strain problems would be helpful in comprehending the complex three-dimensional interference as well. Some basic studies have been carried out and will be presented in Chapter 7, and further detailed studies in this direction will be taken up as a future scope of the present work.

5.6 Summary

This chapter highlights the influence of different geotechnical and geometrical parameters on the bearing capacity and failure mechanisms of interfering strip footings located at the crest and face of a slope. It has been observed that for strip footings located on the crest of a slope, the interference effect disappears beyond a centre-to-centre spacing of 3*B*; while, for strip footings located on slope face, the interfering feature disappears beyond a relative elevation of 8*B* between the footings. Beyond the critical interfering distances, the footings act as individual footings resting on crest or face of the slope. For footings resting on slope crest, the maximum interference is observed at a spacing of 1.5*B*, owing to the overlap of the significant pressure bulbs beneath the footing. For footings located on slope face, the minimum bearing capacity is observed at a relative height of 2*B*, which is attributed to the maximum effect of the overlapping pressure bulbs leading to the failure of the slope and the foundation. The results obtained from this study will be further used to develop neural network architectures for developing the predictive expression to estimate the bearing capacity of interfering footings, and decide the relative importance of the influencing parameters.

CHAPTER 6

APPLICATION OF ARTIFICIAL NEURAL NETWORKS IN PREDICTING BEARING CAPACITY OF FOUNDATIONS ON SLOPES

6.1 General

Soft computing techniques have gained grounds in the recent times to establish mapping relationships for complex systems which may not be always described by suitable mathematical relationships. Such mapping techniques finds its importance more when there are several parameters influencing the response of the system, many of which might only be qualitative or tangible. In many cases, the parameters might actually be coupled and dependent, and cannot be really decoupled to find their individual importance. Under such cases, different forms of soft computing approaches has been successful in providing meaningful mapping of the contributory inputs to the output from a system, without actually indulging into the complex mathematics defining the system. However, it is worth mentioning that the successful application of all such methods completely depends on the quality real-life data collected from several experimental or numerical studies. Machine learning (ML) is an application of artificial intelligence (AI) that provides systems the ability to automatically learn and improve from experience without being explicitly programmed. Machine learning focuses on the development of computer programs that can access data and use it learn for themselves. Soft computing techniques such as artificial neural networks (ANN), fuzzy logic (FL), evolutionary computation (EC) and probabilistic reasoning (PR) can be resorted for the development of a mapping architecture relating the bearing capacity of such footings and their contributory parameters. ANN, FL, EC and PR belong to different classes of artificial intelligence (AI). ANN comprise adjustable parameters that can be trained using optimization techniques like feed-forward back-propagation algorithms for classification or pattern recognition problems.

The training algorithm of ANNs can be boosted by integrating FL, EC and PR optimization techniques with its training and search schemes. Moreover, the trained weights and biases obtained from the neural network can be utilized for sensitivity analysis of input parameters and to form predictive expression. Although not resorting to any specific reasoning for choosing ANN for the present study, the same has been chosen based on its popularity and simplicity of its usage. Further, the application has been well established in the field of geotechnical engineering and several of the application fields.

Several investigators in distinct area of the civil engineering have recently considered ANNs. Lee and Lee (1996), Das and Basudhar (2006) and Momeni et al. (2014) considered ANN for assessing the pile load carrying capacity. Ghaboussi et al. (1994) presented that ANN was dominant tools for the mathematical constitutive modelling of geomechanics. Shahin et al. (2002) successfully applied the back-propagation Multi-Layer Perceptron's (MLPs) for predicting the settlement and load carrying capacity of shallow foundations placed on horizontal ground. Goh (1994) demonstrated that ANN was capable to arrest the intricate correlation between seismic soil parameters and liquefaction potential considering real field observations. The evaluation of hydraulic conductivity and swelling pressure parameters of clayey soil have been inspected through many scholars (Erzin et al. 2009; Das et al. 2011; Das et al. 2012; Mishra et al. 2016). Noorzaei et al. (2008), Kuo et al. (2009) and Behera et al. (2013a, b) considered ANNs for assessing the bearing capacity of strip footing located on levelled surface and subjected to centric or eccentric loading. In the present research, artificial neural network (ANN) structure has been considered for the estimating of bearing capacity of isolated square footing, isolated strip footing and interfering strip footings placed on the crest of sloping surface. A sensitivity study has been executed for realizing the rank of different input parameters considered for evaluating ultimate bearing capacity. A prediction equation has been generated with aid of biases and weights of the trained neural model. It has been a practice to use the classical theories for the estimation of bearing capacity of footings resting on horizontal ground or slopes. However, as mentioned earlier, bearing capacity of foundations on slopes have received less attention. The classical theory by Meyerhof (1957) aids in the determination of bearing capacity of strip footing resting on crest or face of slope with the aid of bearing capacity factors (N_{cq} and $N_{\gamma q}$), or with the help of established design charts. However, it has already been mentioned earlier that the classical theories follow only the stress-based failure approach for estimating the bearing capacity. However, for footing on slopes, it is immensely important to consider to the coupled stress-deformation based failure approach to address the bearing capacity issues. Moreover, the classical theories provide prediction expressions only for strip footings, thus, rendering the problem to be a plane-strain one. However, for footings on different shapes or for interfering footings, the classical theories are silent in providing any guidelines. Such shortcomings of the classical theory can be effectively overcome by rigorous 2D and 3D FE analyses. However, conducting such intricate FE analyses for any field problem each time is difficult, and it is always helpful for the practising design engineers to be provided with a handy prediction expression. Since the bearing capacity of footings on slopes not only depends on the geotechnical and geometrical parameters, but is also affected by the associated failure mechanism, the simple shear strength-based bearing capacity estimations might not be enough to address the complicacy of the problem. In this regard, development of prediction expressions incorporating both stress and deformation mechanisms is possible with the aid of Artificial Neural Network approach. In this process, dependency on bearing capacity factors and design charts can be resolved, as the developed ANN prediction expressions will be solely dependent on the influencing geotechnical and geometrical factors. Moreover, ANN model provides an idea about most important input parameter used in the modelling. Field engineers can use the same to design for shallow footings resting on or near the slope by considering the importance of the influencing parameter. This would further help in technical and policy making decisions as well.

6.2 Background of ANN Modeling and MatLab ANN Toolbox

Neural networks is an interdisciplinary subject that draws upon the brain metaphor to bring together idea from neuroscience, mathematics and computer science to design and engineer systems whose distinguishing trait is the ability to learn from environmental inputs in order to perform intelligent task. The primary application of neural networks is in area where problems are ill-defined, data is incomplete or noisy in nature and the environment itself is dynamic. Typical applications areas include signal enhancement, noise cancelation, clustering, classification, pattern recognition, system identification, time series prediction and control.

The neural networks employ an approach as shown in Fig. 6.1. An adaptive set of parameters defines the system response. The input presented to the system is processed internally to generate an output, which is further compared with the desired output to estimate the error. The error estimate is provided to a learning algorithm that first estimates and then makes appropriate incremental changes to the system parameters to reduce the error based on the provided input. In neural network, these adaptive parameters are called weights. The input to the network is a vector of numbers that the network processes to generate an output vector of numbers. Weights undergo changes in their values in accordance with a learning algorithm. The architecture of the network has to be chosen in advance, although specialized neural networks can also discover their architectures during the adaption process. Neural network design involves selection of an architecture followed by learning. Learning is a data driven approach. Through an iterative process, or learning, the network learns to estimate the underlying input-output mapping function described by the data that it is presented with (Kumar 2013).

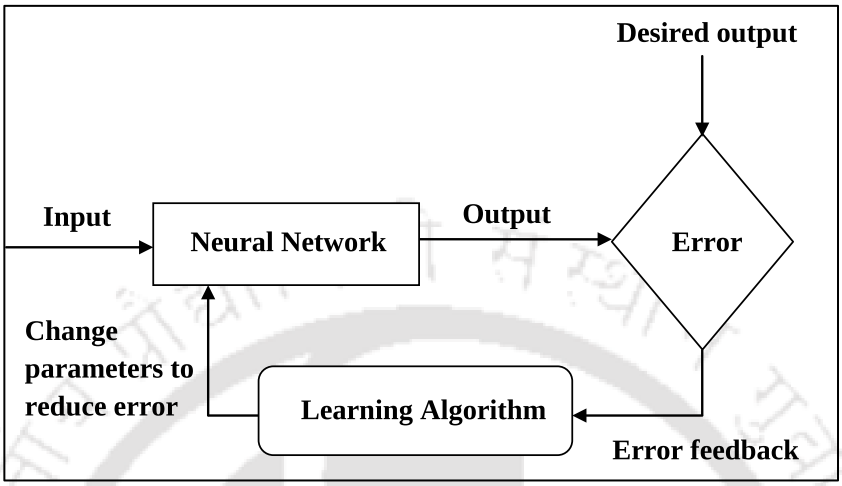

Fig. 6.1 Flow diagram for operation of neural network

Figure 6.2 depicts a typical artificial neuron model in which the j^{th} artificial neuron receives input signal s_i, from possibly n different sources. These signals traverse from neuron i to neuron j along pathways or connections, with an efficiency or weight marked as w_{ij}. It is revealed from Fig. 6.2 that the internal activation x_j is a linear weighted summation of the impinging signals, modified by an internal threshold or bias, θ_j (Eq. 6.1).

$$x_j = \sum_{i=1}^{n} w_{ij} s_i + \theta_j \tag{6.1}$$

Positive weights correspond to excitatory synapses, while negative weights model inhibitory synapses. Impinging signals s_i represents mathematical abstractions of action potentials. The threshold θ_j models the internal firing threshold of a neuron, and the activation x_j models the internal aggregated cell potential. It has been considered that the threshold θ_j as an additional weight $w_{0j} = \theta_j$ fanning into the neuron with constant neuron input $s_0 = +1$ (Fig. 6.2). Hence, w_{0j} has been referred as bias.

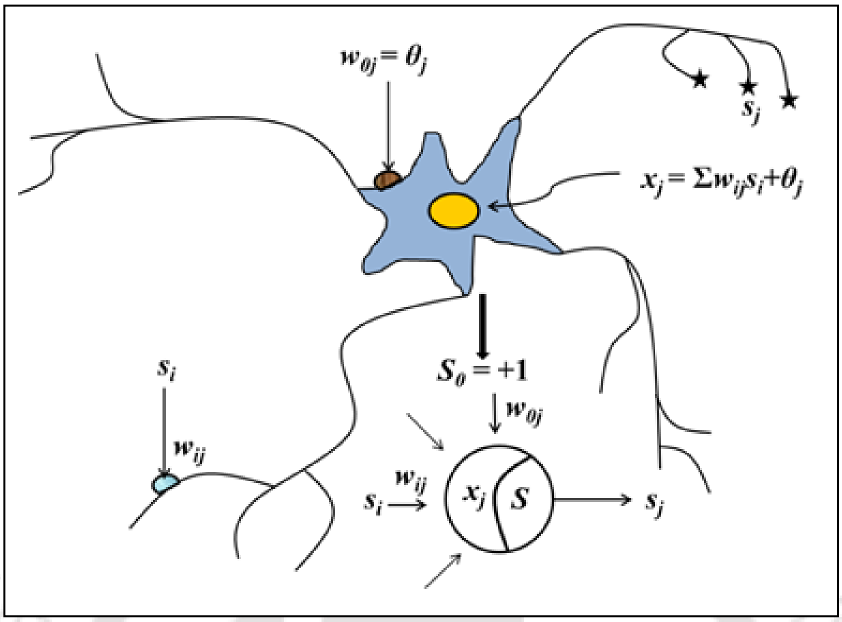

Fig. 6.2 A typical artificial neuron model

The activation of the neuron is subsequently transformed through a signal function *S*(.) to generate the output signal $s_j = S(x_j)$ of the neuron. A plethora of signal functions are available, out of which the most common ones used are binary threshold, linear threshold, sigmoidal, Gaussian or probabilistic.

In the current analysis, sigmoidal signal function has been used. The sigmoid function is by far the most frequently used signal function in neural networks. An example is hyperbolic tangent signal function given by Eq. 6.2.

$$S_j(x_j) = k\tanh(\lambda_j x_j) \tag{6.2}$$

The hyperbolic tangent signal function is formed for some constant $k > 0$ that scales the signal range, and a gain factor λ_j. Figure 6.3 shows the signal function for $\lambda_j = 1$. The hyperbolic tangent signal function is an example of a bipolar signal function since the signal values can become both positive and negative (Koch 1999).

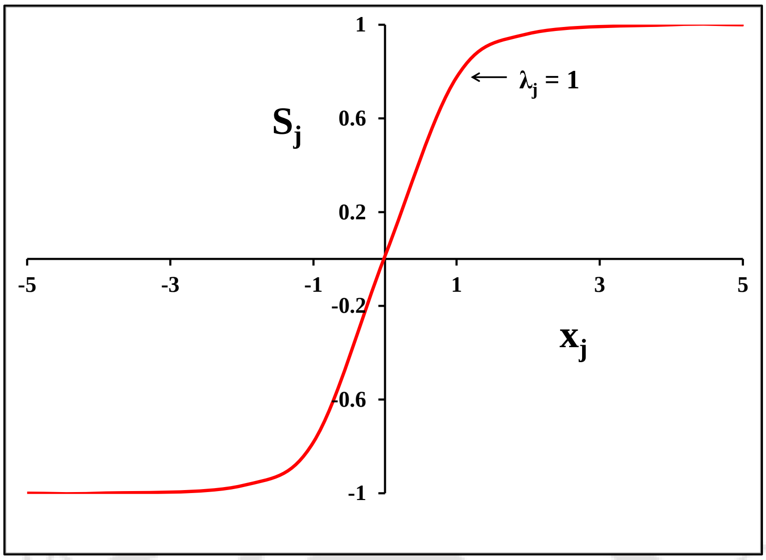

Fig. 6.3 Hyperbolic tangent sigmoidal signal function

Neural network models derive their versatility and computational power primarily from their inherent ability to adapt to changing environment. In the process of adaption, neural networks generate internal models of sampled data. These internal models are represented in variously "structured" weight vector. Most of the neural network models have a well-defined architecture dictated by the pattern of connectivity of neurons. Learning algorithms define an architecture-dependent procedure to encode pattern information into weights to generate these internal models. Learning proceeds by modifying connection weights. There are two types of learning, supervised and unsupervised. Supervised learning encodes a behaviouristic pattern into the network by attempting to approximate the function that underlies the data set. In case of unsupervised learning, the system is simply provided with an input and allowed to self-organize its parameters (i.e. the weights of network) to generate internal prototypes of sample vectors.

It is important to normalize the dataset before utilizing in neural network. Normalization helps the network to learn the pattern faster and provide accurate predicting results. Neural networks perform efficiently when dataset lies in the range of -1 to 1. The influence of normalization is immense because the common activation functions considered in the neural network such as Sigmoid, Hyperbolic tangent and Gaussian produce result that ranges between -1 to 1. It is suggested to normalize the input values to be in that range to achieve better training.

In case of 'Perceptron' learning rule, the actual output of the neural network has to be compared with target output. If the target output does not match with actual output of the network, the weights should be updated based on the amount of error. In the neural network training, various learning algorithms are available specifically, Gradient descent, Newton's method, Conjugate gradient, Quasi-Newton method and Levenberg-Marquardt algorithm. In the current research, for training the neural network, Back-propagation procedure with Levenberg-Marquardt algorithm has been considered. Multi-Layer Perceptrons (MLP) are the well-known type of feed forward network. MLP has generally three layers: One input layer, one or multiple hidden layers, and one output layer. Neurons in the input layer provide input signal x_i to neurons in hidden layer. Each neuron j in the hidden layer sums up its input signals x_i after weighting them with the strength of the respective connections w_{ji} from the input layer, and computes the sum y_j as a function (f) of the inputs and their corresponding weights, and is expressed as Eq. 6.3.

$$y_j = f(w_{ji}x_i) \tag{6.3}$$

where, f is the hyperbolic tangent function.

The output of neurons in output layer is determined similarly. The back-propagation algorithm gives the change in weight ($\vartriangle w_{ji}$) of connection between neurons j and i as given in Eq. 6.4.

$$\vartriangle w_{ji} = \eta \delta_j x_i \tag{6.4}$$

where, η is a parameter called learning rate and δ_j is a factor depending on whether neuron j is an output neuron or a hidden neuron.

For output neurons, the expression is as per Eq. 6.5

$$\delta_j = \left[\frac{\partial f}{\partial net_j}\right]\left[y^t{}_j - y_j\right] \tag{6.5}$$

where, net_j is the total weighted sum of input signals to neuron j, and $y^t{}_j$ is the target output of neuron j.

Levenberg-Marquardt algorithm works by making the assumption that the underlying function being modelled by the neural network is linear. It helps to update the weights obtained from the network to minimize the error. The expression for changing the weights $\left(\vartriangle\overline{w}\right)$ during training in Levenberg-Marquardt method is given below (Eq. 6.6).

$$\vartriangle\overline{w} = (J^T J + \mu I)^{-1} J^T \overline{e} \tag{6.6}$$

where, J is the Jacobian matrix of the first derivatives of the network errors with respect to the weights, μ is a scalar quantity, e is the error vector and I is the identity matrix.

In a nutshell, Neural networks are data mining structures containing huge number of simple, highly interrelated processing elements (artificial neurons) in an architecture encouraged by the structure of the central cortex of the brain. Artificial neurons function as dominant tool to apprehend and study important structures in the datasets. Neural networks create substantial mapping even when the data are not in a pattern, and can generate records rapidly when considered for solving the practical problems.

The commercial ANN toolbox available in Matlab v2015A (MathWorks 2001) has been considered for the investigation. This tool permits the user to choose the number of hidden layers, number of neurons in the hidden layer and the number of iterations considered through the model training, learning algorithms and transfer operators. A multilayer feed-forward cum back-propagation network, which has been formed by generalizing the Levenberg-Marquardt's learning rule to multiple layer networks and nonlinear differential transfer functions (Mishra et al. 2016), has been considered in the current analysis. A typical 2-3-1 network structure has been shown in Fig. 6.4, which comprises an input layer of 2 nodes, an output layer with 1 node, and a hidden layer of 3 nodes. The number of nodes in the input and output layers are governed respectively by the influencing parameters and output estimates to be determined. The number of hidden neurons in the hidden layer is very important for network performance. The quantity of hidden neurons should be optimum because too few neurons can provide under-fitting phenomenon, while too many neurons can hint the system toward remembering the arrangements in the records or absorb noise (Das and Basudhar 2006).

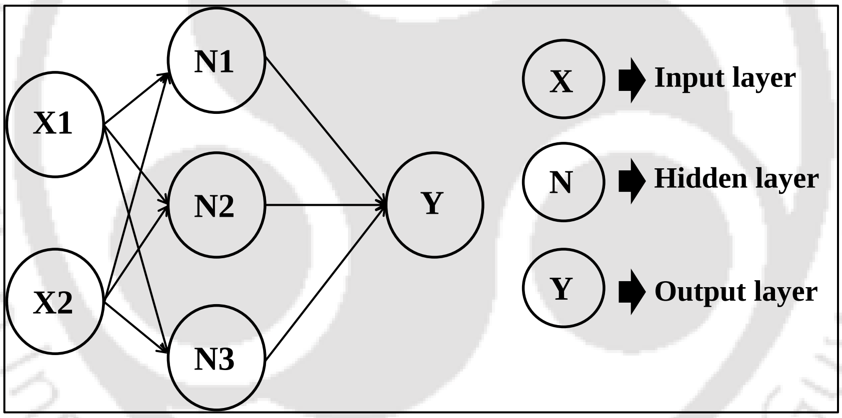

Fig. 6.4 A typical Artificial Neural Network (ANN) architecture

In the current networking, tan-sigmoid transfer operator has been considered for both inputs-to-hidden and hidden-to-output layers. The concept for opting tan-sigmoid operator in the network is that it performs similar to biological neurons. Moreover, the hyperbolic tangent function has some very useful mathematical properties. These include its monotonicity and continuity. Monotonicity means that the function y either always increases or always decreases as x increases. Continuity means there are no breaks in the function, it is smooth. These intrinsic properties renders the networks made of such neurons to be powerful enough approximate and perform apt generalization on functions by learning from the data (Kumar 2013). The maximum iterations have been taken as 50000 as a stopping criterion. The adopted neural network architecture is sequentially trained, validated and tested, by segregating the complete dataset available with the aid of some basic guidelines. Based on the guideline, 80% of the total data are used for training, and the remaining 20% are used for validation of the ANN architecture. The training dataset is further divided, where 70% of the data is used for actual training of the architecture, while the remaining 30% is used as the testing set (Ghaboussi et al. 1994). The training is guided by the Mean Square Error (MSE), which postulates the error produced at time of learning, and can be estimated using Eq. 6.7.

$$MSE = \frac{1}{N_d}\sum_{i=1}^{N_d}(O_{Simulation} - O_{ANN})^2 \tag{6.7}$$

where, $O_{Simulation}$ is the simulated magnitudes, O_{ANN} is the predicted magnitudes of the identical unit and N_d is the total number of records. Once the MSE reduces below a tolerance level, the neural architecture is considered to be trained and is ready to be used for prediction of the output estimates on the basis of the given input estimates. It is worth mentioning that the dataset to be used for training should be random and engross the entire range of inputs of the complete dataset. This is to ensure that the ANN architecture possesses robust prediction capability for any set of input parameters within the range considered for its training. It is advised that that trained ANN architectures should not be used to extrapolate the predictions beyond the training set.

6.3 ANN Model for Predicting the Bearing Capacity of Strip Footing Located on the Crest of *c*-*φ* Soil Slope

This section describes the development of ANN model for predicting the bearing capacity of strip footing located on the crest of a *c*-*φ* soil slope. The data used for the development of the ANN model have been simulated based on PLAXIS FE modelling, and has already been described in Section 4.4. The ANN architecture consists of six input nodes conforming to the input parameters, namely cohesion (c), angle of internal friction (φ), width of footing (B), setback ratio (b/B), slope angle (β) and embedment depth ratio (D_f/B). The output layer consists of only one node showcasing the prediction of the ultimate bearing capacity of strip footing. A single hidden layer has been used for the present study. The numbers of neurons are chosen on the basis of a convergence study, which is described in the following section.

6.3.1 Number of hidden neuron

In the current study, a convergence analysis has been conducted to identify the optimal number of neurons required in the hidden layer to properly characterize the input-output correlation of the analysed dataset. The tolerance is set over a mean squared error (MSE) value of 0.02, which has been attained when the number of neurons in the hidden layer exceeded 9, as shown in Fig. 6.5. To verify the neural network architecture obtained from above convergence analysis, the number of neurons in hidden layer has been varied with the percentage of error found in validation set after analysis. The percentage of error (E) has been calculated from the following expression (Eq. 6.8).

$$E(\%) = ABS\left(\frac{O_{Simulation} - O_{ANN}}{O_{Simulation}}\right) \times 100 \tag{6.8}$$

where, E is the error in percentage, $O_{Simulation}$ is the simulated magnitudes and O_{ANN} is the predicted magnitudes of the identical unit.

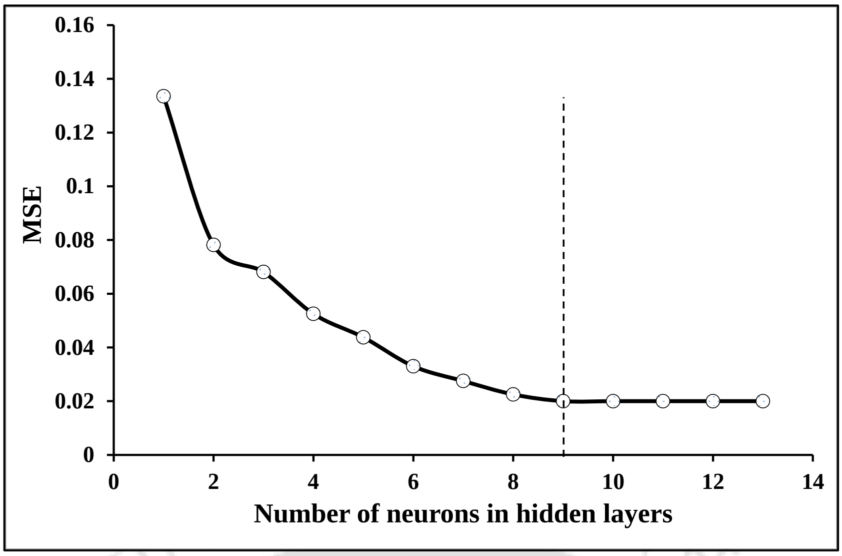

Fig. 6.5 Estimation of optimum number of hidden neurons during the training phase

Figure 6.6 portrays the pattern of error in validation set with increasing the number of neurons in the hidden layer. It has been perceived that the percentage of error reduces with increasing the number of neurons up to 9, beyond this number of neurons in hidden layer the percentage of error increased in validation set. It has been observed that the minimum percentage of error, 0.89%, has been found for 9 numbers of neurons that is same as that obtained from the training set. Thus, the optimality of the hidden layer in the chosen ANN architecture is confirmed. The same has been considered as an optimal value and has been used in further studies. Hence, based on the convergence study, a 6–9–1 ANN architecture has been developed with six input nodes (representing c, φ, B, b/B, β and D_f/B), a single output node (q_{un}) and nine (9) hidden neurons (as shown in Fig. 6.7).

Table 6.1 Number of samples used in various performances

Performance	Number of samples
Training	1120
Testing	480
Validation	400

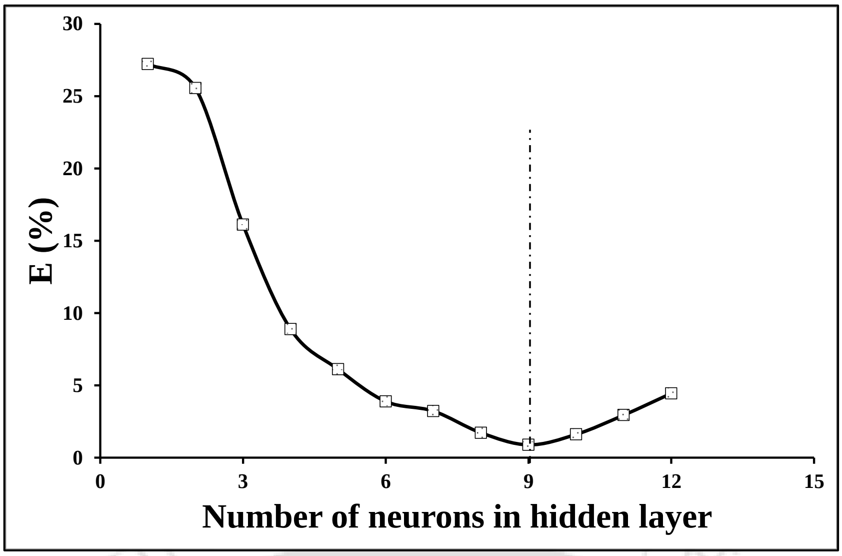

Fig. 6.6 Impact of number of neurons in hidden layer during the validation phase

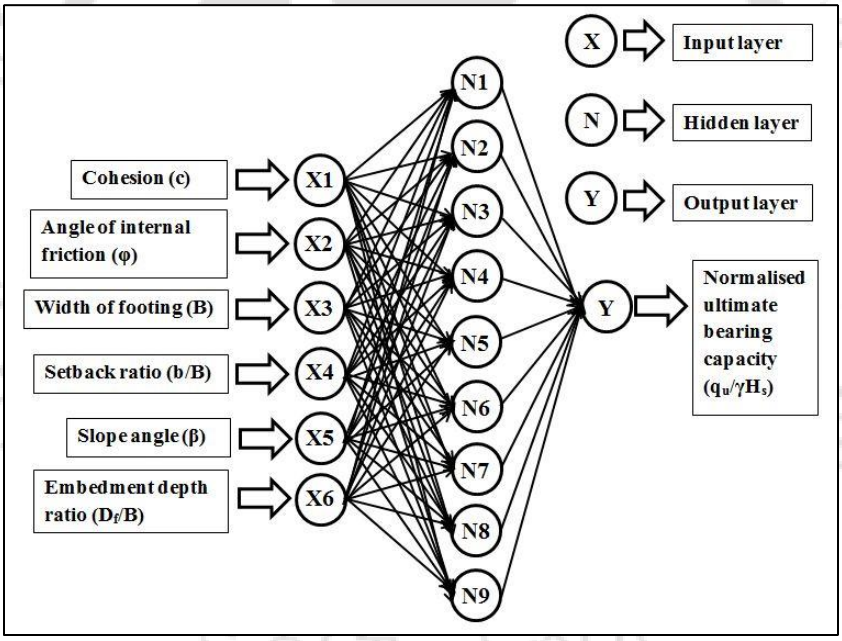

Fig. 6.7 The 6-9-1 ANN architecture to be used for prediction of bearing capacity of a strip footing located on the crest of a *c*-*φ* soil slope

Table 6.2 Training parameters considered in the present study

Training parameters	Magnitudes and nomination
Training function	‘trainlm’ (Levenberg Marquardt)
Transfer function	
a. Hidden layer	a. ‘tansig’ (non-linear function)
b. Output layer	b. ‘tansig’ (non-linear function)
Performance function	‘mse’ (Mean square error)
Error after learning	0.001
Divide function	‘dividerand’
Epochs	50000
Number of neurons in input layer	06
Number of hidden layer	01
Number of neurons in hidden layer	09
Number of output layer	01

6.3.2 Generalization and performance of the ANN architecture

Neural network architecture has the ability to modify its performance with respect to a particular problem. ANN has self-adjusting capability to capture the valid pattern of given dataset, and this process is referred as training. In training, the connection weights of neurons changes systematically to produce the desire outcomes. The main purpose of training is to identify the optimal connection weights which will provide tolerable and minimum MSE (Demuth and Hagan 1996). In neural networking, the separation of samples for training, testing and validation has been done as per the conventional usage (Ghaboussi et al. 1994), and same has been provided in Table 6.1. The optimal weights obtained from training step, have been retained for testing and validation stages. The training parameters used in the study has been tabulated in Table 6.2.

Table 6.3 Stopping parameters and training criteria considered for ANN training

Stopping parameters	Value considered for termination	Stopping value
Epochs	50000	10000
Time (sec)	1800	18
Mu (initial) mu_max	0.001 $1e^{10}$	0.010
Min_grad	$1e^{-07}$	0.0616
Max_fail	10	10

The training has been continued as long as the error decreased in the test data set, and the same has been stopped when the error started growing during the process. The training started considering the default termination values as provided in Table 6.3. The training is halted when the error is lowest in testing data set (early stopping) although the error on training dataset has been found to decrease further as training is continued (Viji et al. 2013). The number of validation checks signifies the number of consecutive iterations that the validation performance fails to decrease. Several termination criteria has been used simultaneously namely epochs, computational time (s), initial and maximum mu (controlling weight perturbations), minimum gradient (Min_grad) and maximum validation fails (Max_fail). The training program is supposed to stop when any of criteria is met. In the present study, the training program terminated when the maximum number of validation fails reached the termination criterion of 10. The magnitudes achieved by rest of the parameters at the event of termination are provided in Table 6.3.

Figure 6.8 depicts the outcome of the training process as an agreement of the magnitudes of q_{un} ($q_u/\gamma H_s$) obtained from Finite Element simulations (simulated q_{un}) with those obtained as predictions of the ANN model (predicted q_{un}). In the training phase, a coefficient of correlation (R^2) has been obtained as 0.998, which signifies a strong agreement between predicted and simulated outcomes, thus highlighting the optimal training of the ANN architecture. Under this condition, the connection weights (input-hidden and hidden-output) obtained as an outcome of the training programme is highlighted in Tables 6.4 and 6.5, which are subsequently used in the testing and validation phases. Table 6.6 highlights the corresponding biases.

Further, the trained ANN structure, with its optimal connection weights, has been considered for the testing phase to check the prediction capacity of the network. Figure 6.9 portrays that there is excellent match (R^2 = 0.996) of q_{un} obtained from numerical investigation (FE simulations) with those predicted by ANN model. The testing phase with a high correlation coefficient provides a confirmatory that the trained neural network has superior prediction ability.

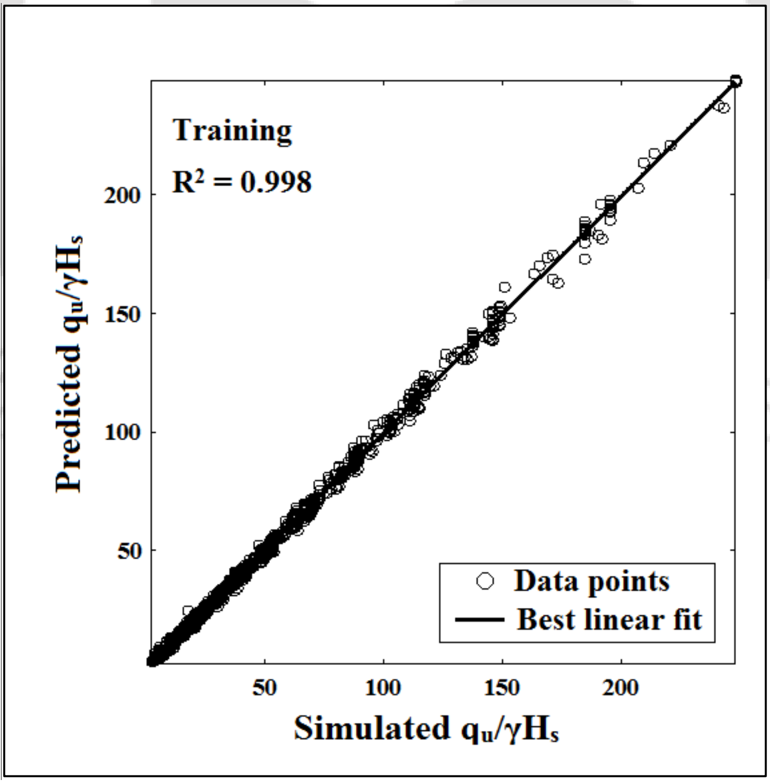

Fig. 6.8 Performance of the 6-9-1 ANN model during training phase

Table 6.4 Connection weights of Input-Hidden layer obtained after training phase of 6-9-1 ANN model

X \ N	Hidden N1	Hidden N2	Hidden N3	Hidden N4	Hidden N5	Hidden N6	Hidden N7	Hidden N8	Hidden N9
c (X1)	4.00	0.39	0.17	-0.25	-0.18	0.85	-0.17	-0.46	0.50
φ (X2)	6.08	0.58	0.041	-1.18	-0.45	-2.57	-0.97	-0.57	0.64
B (X3)	3.18	0.08	0.18	-0.35	-0.88	-0.56	-0.28	0.094	-0.13
b/B (X4)	2.64	0.53	0.050	0.23	0.057	0.069	0.41	-0.14	-0.20
β (X5)	-0.53	-0.17	0.018	-0.12	-0.0075	0.051	-0.18	0.33	-0.16
D_f/B (X6)	3.84	0.086	-0.37	-0.19	-0.15	0.43	-0.16	0.005	-0.033

Table 6.5 Connection weights of Hidden-Output layer obtained after training phase of 6-9-1 ANN model

Y \ N	Hidden N1	Hidden N2	Hidden N3	Hidden N4	Hidden N5	Hidden N6	Hidden N7	Hidden N8	Hidden N9
$q_u/\gamma H_s$	5.66	1.56	-1.83	-4.58	-0.60	-0.17	5.19	1.31	1.71

Table 6.6 Biases in the 6-9-1 ANN model obtained after the training phase

Hidden layer biases (b_{hN})	Output layer biases (b_O)
-19.00	
0.80	
-1.77	
2.10	
-0.70	0.40
0.90	
2.03	
0.51	
0.73	

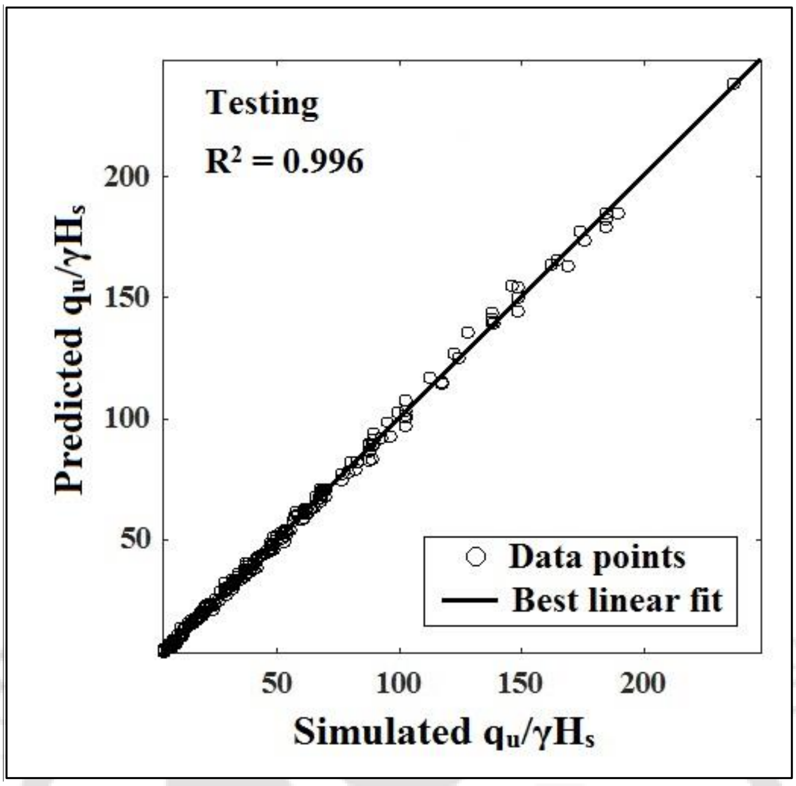

Fig. 6.9 Performance of the 6-9-1 ANN model during testing phase

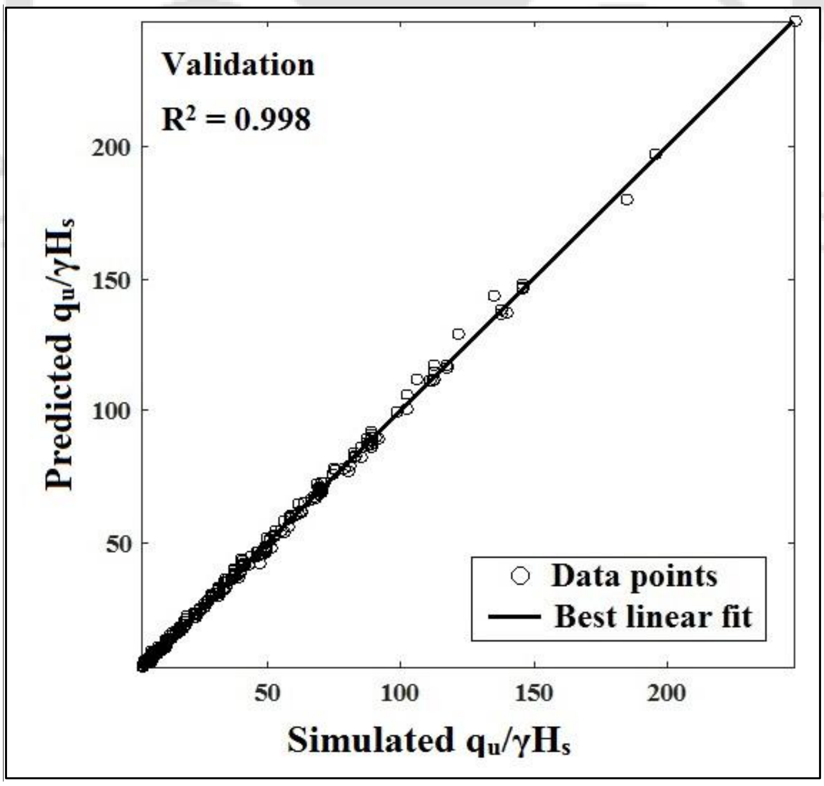

Fig. 6.10 Performance of the 6-9-1 ANN model during validation phase

Subsequently, the trained ANN structure has been engaged with the validation dataset that have not been considered to form ANN architecture, neither in training nor in testing phase. The validation step is useful in checking the aptness of the ANN model to generalize the outcome of the physical problem. Figure 6.10 illustrates excellent match (R^2 = 0.998) between simulated and forecasted magnitudes of q_{un} for strip footing placed near sloping surface, thus highlighting the superior generalization capability and performance of the 6-9-1 ANN architecture.

The progress of training was inspected for the all the above phases, i.e. training, testing and validation, by plotting the variation of MSE with the completed number of iterations, as presented in Fig. 6.11. It is observed that errors obtained from test set and validation sets have identical appearances and hence, there is no over-fitting during the training of the proposed architecture (Noorzaei et al. 2008).

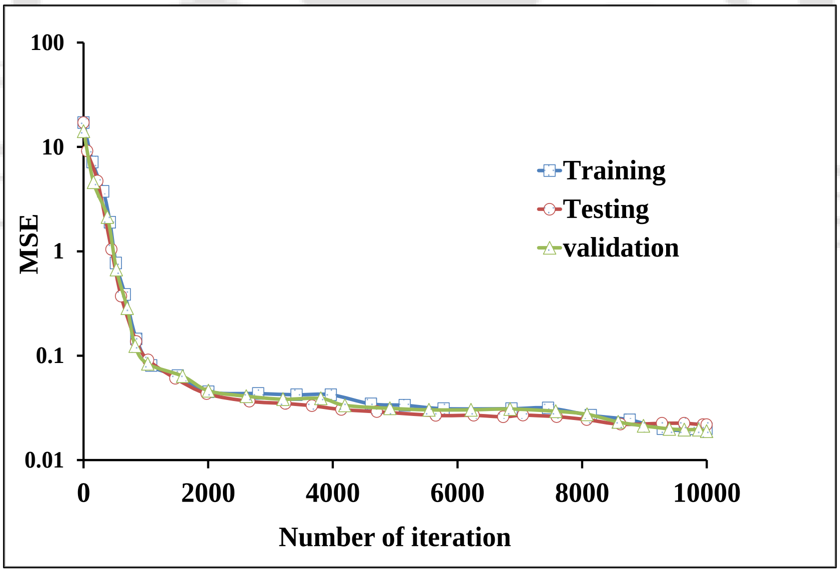

Fig. 6.11 Comparison of MSE with number of iterations for training, testing and validation phases of the 6-9-1 ANN architecture

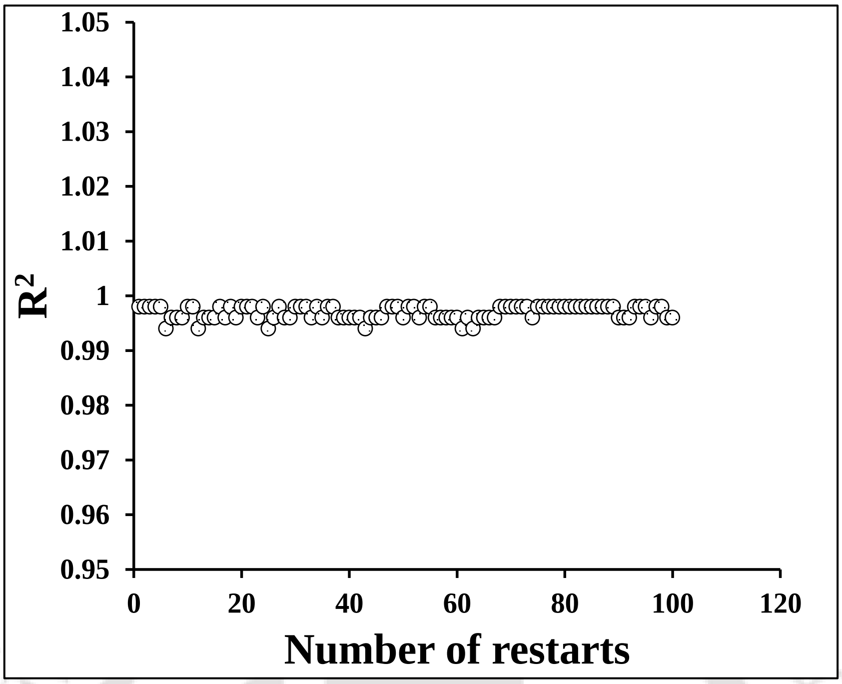

Fig. 6.12 Behaviour of R^2 for several training restarts

In the present investigation, the optimality of the trained network has been checked based n the training statistics over several restarts. Figure 6.12 portrays the pattern of coefficient of correlation (R^2) for several restarts of the network. In the current study, the network has been restarted for 100 times and for each restart the magnitude of R^2 has been recorded. It has been observed that the magnitude of R^2 varies from 0.996 to 0.998. The pattern of R^2 for several restarts confirms the fact that the neural network is optimally trained and the network having excellent capability of prediction.

6.3.3 Sensitivity study

Sensitivity investigation is a necessary research conducted for the ranking of input variables, thus highlighting their sorted influence on the outcome of the physical problem. Such study aids in the 'design of experiments' when large number of the numerical or physical simulations are required, while based on the sensitive influence of the contributing parameters, only few of them are selected for the actual modelling. Thus, sensitivity analysis helps in the reduction in the number of model simulations, without jeopardizing the generality of the obtained results. Various methods have been advised in the articles for identifying the vital input parameter (Shahin et al. 2002; Goh 1994). In the present study, Garson's algorithm (Das and Basudhar 2006; Shahin et al. 2002; Das and Basudhar 2008) has been considered to identify the significance of inputs. In order to apply Garson's algorithm, firstly the input-hidden (Table 6.4) and hidden-output (Table 6.5) weights are segregated, and the absolute magnitudes of weights have been considered to differentiate the rank of input parameters (Eq. 6.9).

$$Input_X = \sum_{N=1}^{9} \frac{|Hidden_{XN}|}{\sum_{Z=1}^{6} |Hidden_{ZN}|} \quad \text{(Garson's algorithm)} \tag{6.9}$$

where, $Hidden_{XN}$ represents the absolute magnitudes of the connection weights between the input nodes and hidden layer nodes (as provided in Table 6.1), and $Hidden_{ZN}$ represents the absolute magnitudes of the product of the connection weights between the input-hidden and hidden-output nodes. The sample $Hidden_{ZN}$ as obtained for the 6-9-1 ANN model developed for the present study is provided in Table 6.7, the values of which are obtained from the corresponding products of the parameter magnitudes provided in Table 6.4 and Table 6.5.

Consequently, Equation 2 indicates the assessment of importance ranking for input predictors X (X = 1-6), utilizing the weights of individual input neurons Z (Z = 1–6) to each of the hidden layer nodes N (N = 1–9), and lastly to a single output node (Y). The outcome of the sensitivity study carried out with the aid of Garson's method to provide the importance ranking to the input parameters is highlighted in Table 6.8. It can be observed that the geotechnical parameters (shear strength parameters) are more sensitive and play a dominant role in deciding the magnitude of q_{un}.

Table 6.7 Product of the input-hidden and hidden-output connection weights after training phase of 6-9-1 ANN model

X \ N	Hidden N1	Hidden N2	Hidden N3	Hidden N4	Hidden N5	Hidden N6	Hidden N7	Hidden N8	Hidden N9
c (X1)	22.67	0.62	-0.32	1.158	0.11	-0.14	-0.89	-0.61	0.87
φ (X1)	34.50	0.91	-0.07	5.43	0.27	0.44	-5.06	-0.76	1.10
B (X1)	18.05	0.12	-0.34	1.61	0.53	0.09	-1.49	0.12	-0.23
b/*B* (X1)	14.98	0.83	-0.09	-1.06	-0.03	-0.01	2.13	-0.18	-0.35
β (X1)	-3.04	-0.27	-0.03	0.55	0.004	-0.008	-0.94	0.44	-0.28
D_f/B (X1)	21.81	0.13	0.68	0.90	0.09	-0.07	-0.85	0.007	-0.05

Table 6.8 Rank of input-parameters as per Garson's algorithm

Input	Relative importance	Relative importance (%)	Rank
c	1.68	18.72	2
φ	3.17	35.27	1
B	1.47	16.39	3
b/*B*	1.02	11.37	5
β	0.60	6.64	6
D_f/B	1.05	11.61	4

According to Garson's method, the angle of internal friction, *φ* has been identified as the utmost significant input parameter lagged by *c*, *B*, D_f/B, *b*/*B* and *β*, according to Garson's method, as shown in Table 8. Hence, it has been revealed from the sensitivity investigation that the angle of internal friction of soil was most significant input parameters to assess q_u of strip footing placed at the crest of a *c*-*φ* slope.

The ranking of input parameters found from Garson's algorithm (1991) has been checked through an alternative local perturbation technique with the graceful degradation of the error curves. The basic concept that has been considered is that each of input parameters of the trained network has been altered slightly and the corresponding change in the output has been recorded, while the remaining input parameters are maintained constant. In the sensitivity investigation, input parameters have been varied from -20% to 20% of their mean value in the predictive network to realize the influence of various geotechnical and geometrical input parameters on the output. Figure 6.13 portrays the percentage change in prediction of $q_u/\gamma H_s$ due to percentage change in input parameters. The graceful degradation technique has been applied to 5 different sets of input parameters, and the results obtained are plotted as error bars in the figure. The small error bars indicate the affirmative consistency of the applied technique. It has been perceived that the angle of internal friction of soil, φ is the most influential input parameter as it has maximum effect on the changes in prediction, followed by the effects of c, B, D_f/B, b/B and β. It can be observed that both the local perturbation technique and Garson's algorithm yields similar results, thus putting confidence on the outcome.

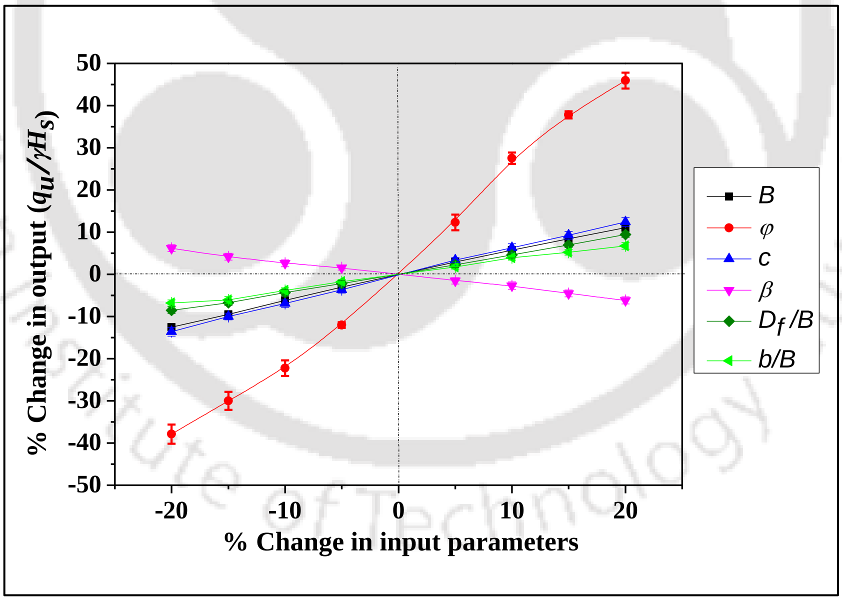

Fig. 6.13 Relative importance of the input parameters by means of graceful degradation

6.3.4 ANN prediction equation for $q_u/\gamma H_s$

A predicting equation is prepared with aid of weights obtained from trained neural network model (Das and Basudhar 2006; Behera et al. 2013a, b; Das and Basudhar 2008; Das et al.

2011). The mathematical expression connecting input parameters (c, φ, B, b/B, β, D_f/B) with output ($q_u/\gamma H_s$) represented in Eq. 6.10.

$$(\frac{q_u}{\gamma H_s})_n = f_{Sig}\{b_O + \sum_{N=1}^{h}[w_N f_{Sig}(b_{hN} + \sum_{i=1}^{m} w_{iN} X_i)]\} \tag{6.10}$$

where, $(q_u/\gamma H_s)_n$ is the normalized magnitude of $q_u/\gamma H_s$ in the variation of [-1,1], X_i is the normalised magnitude of inputs in the variation of [-1,1], f_{Sig} is the Sigmoid transfer function, m is the number of input present as variables, h is the number of neurons present in the hidden layer, , w_{iN} is the connection weight between i^{th} layer of input and N^{th} neuron of hidden layer, w_N is the connection weight between N^{th} neuron of hidden layer and single output neuron, b_{hN} is the bias at the N^{th} neuron of hidden layer and bo is the bias at the output layer.

The model equation for q_{un} of strip footing located at the crest of slope, subjected to vertical loading, has been framed with aid of weights and biases provided in Table 6.4, Table 6.5 and Table 6.6 as per subsequent expressions (Eq. 6.11 – 6.30).

$$A_1 = 4(c) + 6.08(\varphi) + 3.18(B) + 2.64(b/B) - 0.53(\beta) + 3.84(D_f/B) - 19 \tag{6.11}$$

$$A_2 = 0.39(c) + 0.58(\varphi) + 0.08(B) + 0.53(b/B) - 0.17(\beta) + 0.086(D_f/B) + 0.80 \tag{6.12}$$

$$A_3 = 0.17(c) + 0.041(\varphi) + 0.18(B) + 0.05(b/B) - 0.018(\beta) - 0.37(D_f/B) - 1.77 \tag{6.13}$$

$$A_4 = -0.25(c) - 1.18(\varphi) - 0.35(B) + 0.23(b/B) - 0.12(\beta) - 0.19(D_f/B) + 2.10 \tag{6.14}$$

$$A_5 = -0.18(c) - 0.45(\varphi) - 0.88(B) + 0.057(b/B) - 0.0075(\beta) - 0.15(D_f/B) - 0.70 \tag{6.15}$$

$$A_6 = 0.85(c) - 2.57(\varphi) - 0.56(B) + 0.069(b/B) + 0.051(\beta) + 0.43(D_f/B) + 0.90 \tag{6.16}$$

$$A_7 = -0.17(c) - 0.97(\varphi) - 0.28(B) + 0.41(b/B) - 0.18(\beta) - 0.16(D_f/B) + 2.03 \tag{6.17}$$

$$A_8 = -0.46(c) - 0.57(\varphi) + 0.094(B) - 0.14(b/B) + 0.33(\beta) + 0.005(D_f/B) + 0.51 \tag{6.18}$$

$$A_9 = 0.50(c) + 0.64(\varphi) - 0.13(B) - 0.20(b/B) - 0.16(\beta) - 0.033(D_f/B) + 0.73 \tag{6.19}$$

$$B_1 = 5.66(\frac{e^{A_1} - e^{-A_1}}{e^{A_1} + e^{-A_1}}) \tag{6.20}$$

$$B_2 = 1.56\left(\frac{e^{A_2} - e^{-A_2}}{e^{A_2} + e^{-A_2}}\right) \tag{6.21}$$

$$B_3 = -1.83\left(\frac{e^{A_3} - e^{-A_3}}{e^{A_3} + e^{-A_3}}\right) \tag{6.22}$$

$$B_4 = -4.58\left(\frac{e^{A_4} - e^{-A_4}}{e^{A_4} + e^{-A_4}}\right) \tag{6.23}$$

$$B_5 = -0.60\left(\frac{e^{A_5} - e^{-A_5}}{e^{A_5} + e^{-A_5}}\right) \tag{6.24}$$

$$B_6 = -0.17\left(\frac{e^{A_6} - e^{-A_6}}{e^{A_6} + e^{-A_6}}\right) \tag{6.25}$$

$$B_7 = 5.19\left(\frac{e^{A_7} - e^{-A_7}}{e^{A_7} + e^{-A_7}}\right) \tag{6.26}$$

$$B_8 = 1.31\left(\frac{e^{A_8} - e^{-A_8}}{e^{A_8} + e^{-A_8}}\right) \tag{6.27}$$

$$B_9 = 1.71\left(\frac{e^{A_9} - e^{-A_9}}{e^{A_9} + e^{-A_9}}\right) \tag{6.28}$$

$$C_1 = 0.40 + B_1 + B_2 + B_3 + B_4 + B_5 + B_6 + B_7 + B_8 + B_9 \tag{6.29}$$

$$\left(\frac{q_u}{\gamma H_s}\right)_n = \left(\frac{e^{C_1} - e^{-C_1}}{e^{C_1} + e^{-C_1}}\right) \tag{6.30}$$

The $(q_u/\gamma H_s)_n$ magnitude as attained from Eq. (6.30) is in the variation of [-1, 1] and this required to be de-normalized as per following Eq. 6.31.

$$\left(\frac{q_u}{\gamma H_s}\right) = 0.5\left[\left(\frac{q_u}{\gamma H_s}\right)_n + 1\right]\left[\left(\frac{q_u}{\gamma H_s}\right)_{\max} - \left(\frac{q_u}{\gamma H_s}\right)_{\min}\right] + \left(\frac{q_u}{\gamma H_s}\right)_{\min} \tag{6.31}$$

where $(q_u/\gamma H_s)_{\max}$ and $(q_u/\gamma H_s)_{\min}$ are the maximum and minimum magnitudes of $q_u/\gamma H_s$ correspondingly in the records.

6.4 ANN Model for Predicting the Bearing Capacity of Square Footing Located on the Crest of *c*-*φ* Soil Slope

This section describes the development of ANN model for predicting the bearing capacity of square footing located on the crest of a c-φ soil slope. The data used for the development of the ANN model have been simulated based on PLAXIS FE modelling, and has already been described in Section 4.3. The ANN architecture consists of seven input nodes conforming to the input parameters, namely cohesion (c), angle of internal friction (φ), unit weight of soil (γ), width of footing (B), setback ratio (b/B), slope angle (β) and embedment depth ratio (D_f/B). The output layer consists of only one node highlighting the prediction of the ultimate bearing capacity of square footing. A single hidden layer has been used for the present study. The numbers of neurons are chosen based on a convergence study, which is described in the following section.

6.4.1 Determination of number of neurons in hidden layer

In the present investigation, a convergence study has been conducted for ascertaining the optimum number of neurons required in the hidden layer. The number of neurons in the hidden layer is varied and the corresponding MSE is recorded, as shown in Fig. 6.14. It can be observed that the mean square error (MSE) achieves a minimum (0.0126) with the application of minimum ten neurons in the hidden layer; further increase in the numbers of neurons in the hidden layer does not affect the outcome of the neural analysis. The numbers of hidden neurons depend on the complexity of the dataset used in the study. Hence, for the present study, the 7–10–1 ANN architecture is considered to be the 'best model', containing seven (7) input nodes (c, φ, γ, B, b/B, β and D_f/B), ten (10) hidden-layer neurons, and a single (1) output node (q_u); the same is portrayed in Fig. 6.15.

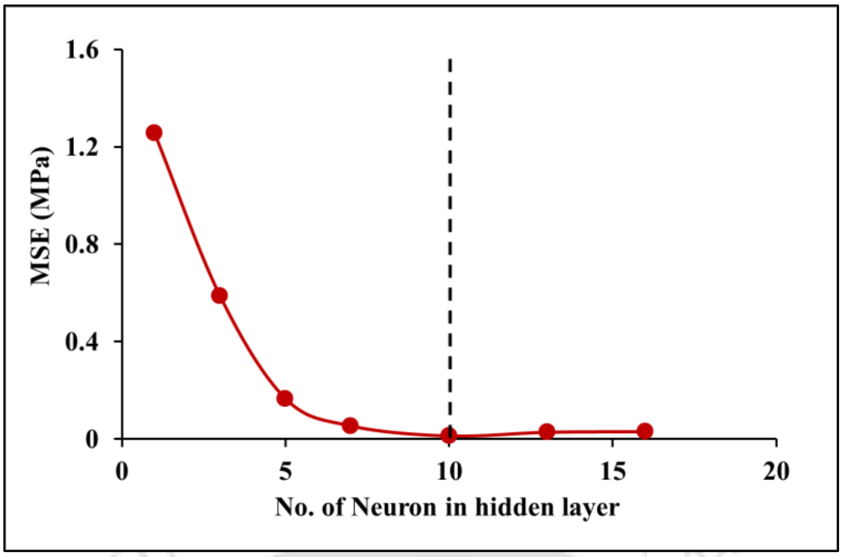

Fig. 6.14 Determination of optimum number of neurons in the hidden layer

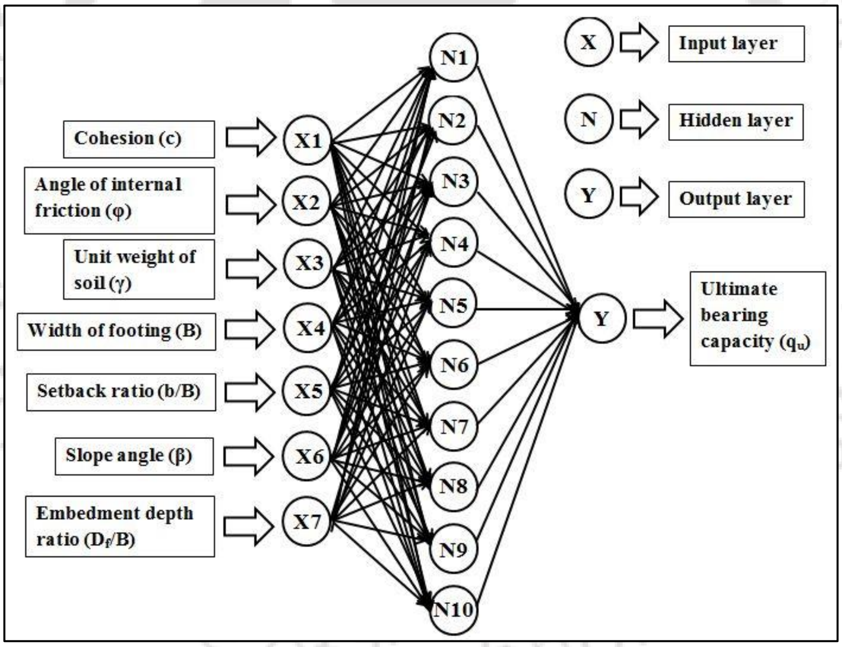

Fig. 6.15 The 7-10-1 ANN architecture to be used for prediction of bearing capacity of a square footing located on the crest of a *c*-*φ* soil slope

6.4.2 Training, testing and validation of the ANN architecture

A neural computing system can adjust its behaviour in response to its environment. When sets of inputs are provided to the network, it will self-adjust to produce reliable mapping through a process called training, wherein the neural (or, connection) weights are methodically altered to attain the desired results. The aim of training is to find a set of connection weights that will achieve the minimum MSE in the shortest possible time (Demuth and Hagan 1996). For the ANN architecture development, a total of 1324 data have been used. In this regard, 80% (1059) of the total data are used for training, and the remaining 20% (265) are used for validation of the ANN architecture. The training dataset is further divided, where 70% (741) of the data is used for actual training of the architecture, while the remaining 30% (318) is used as the testing set (Ghaboussi et al. 1994). In the training process, the connection weights are constantly adjusted to minimize the error between the predicted and the desired outputs. When the training gets complete, the achieved weights are maintained for the subsequent testing and validation phases.

Comparison of the ultimate bearing capacities of a square footing, predicted by ANN and simulation, by using the 70% training datasets, is shown in Fig. 6.16. The coefficient of efficiency (R^2), demarcating the agreeability between the simulated and predicted values, is found to be 0.998 for training phase, which indicates a well-trained neural architecture. After the network is trained, the efficacy of the developed ANN model is checked by exposing it to the testing dataset for the prediction of the ultimate bearing capacity. The result of the testing phase is exhibited in Fig. 6.17, as a comparison between the predicted and simulated q_u values. The simulated and predicted values are found to be in close agreement, the coefficient of efficiency (R^2) achieved in the testing phase being 0.996. This indicates that the developed ANN model is capable of predicting ultimate bearing capacity of foundation soil with highly acceptable accuracy.

Once the training phase of the model has been successfully accomplished, the performance of the trained model is subjected to the validation data, which have not been used as part of the model building process. The purpose of the model validation phase is to ensure that the model has the ability to generalize 'within the limits' set by the training data, rather than simply having memorized the input-output relationships embedded in the training data. The comparison of the target and predicted ultimate bearing capacities, obtained from the validation phase, is presented in Fig. 6.18, and exhibits a high coefficient of efficiency (R^2) equal to 0.998. Under this condition, the connection weights (input-hidden and hidden-output) obtained as an outcome of the training programme is highlighted in Tables 6.9 and 6.10, which are subsequently used in the testing and validation phases. Table 6.11 highlights the corresponding biases.

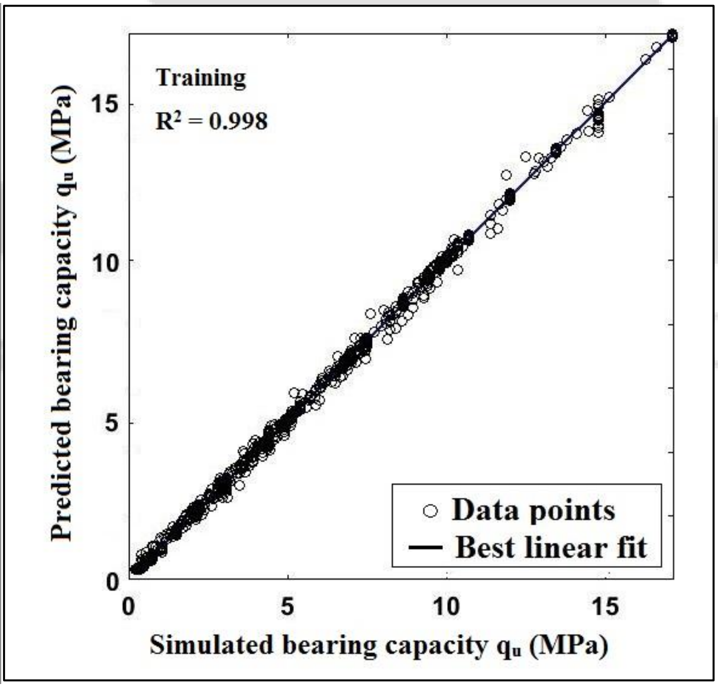

Fig. 6.16 Performance of the 7-10-1 ANN model during training phase

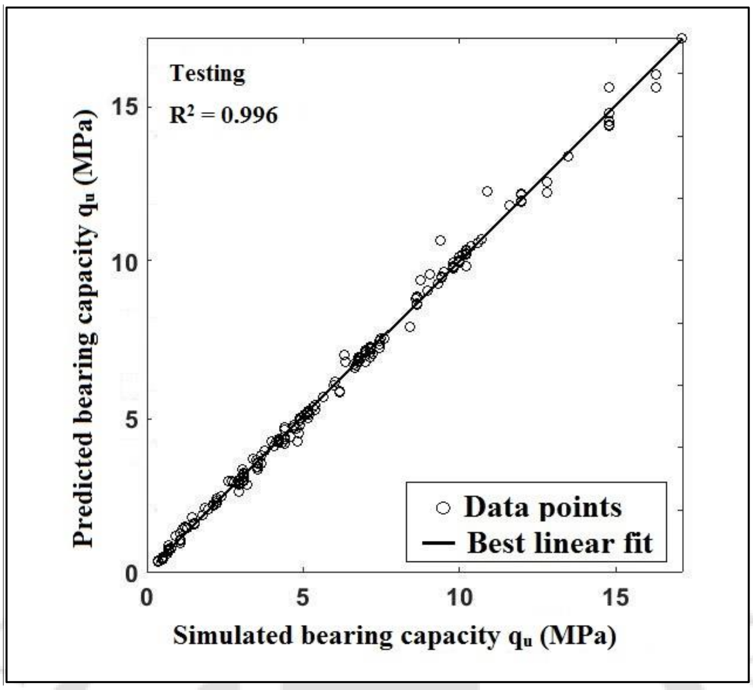

Fig. 6.17 Performance of the 7-10-1 ANN model during testing phase

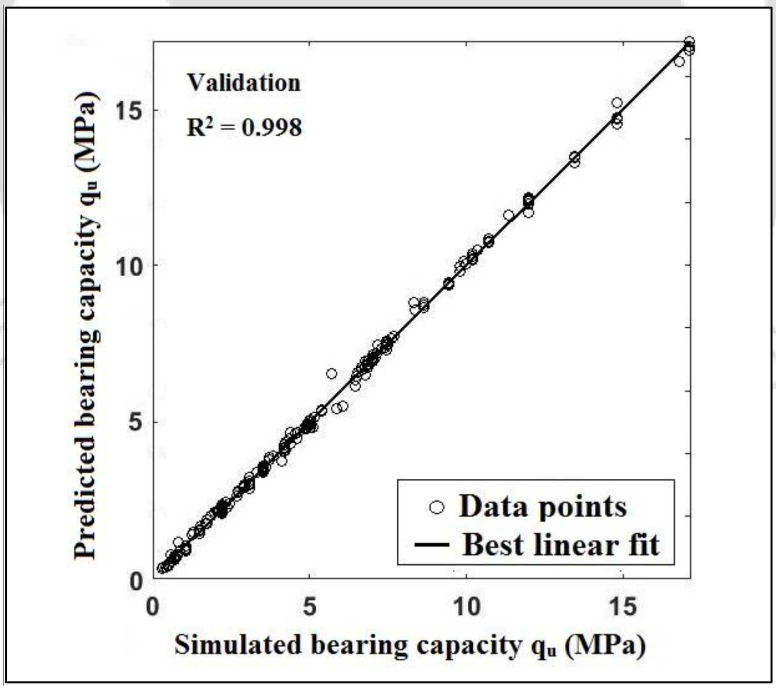

Fig. 6.18 Performance of the 7-10-1 ANN model for validation phase

6.4.3 Sensitivity analysis and importance ranking of influencing parameters

Sensitivity analysis is of extreme importance for selection of influencing input variables. Different tactics have been suggested in the literature to identify the contributory input variables. Goh (1994) and Shahin et al. (2002) have used Garson's algorithm (1991), in which the connection weights of the input-hidden layer (Table 6.9) and the connection-weights of the hidden-output layer (Table 6.10) of the trained ANN model are partitioned, and the absolute values of the weights are taken to distinguish the important input variables (Eq. 6.32). The output from Garson's algorithm provides the ranking of the parameters based on their relative importance. Accordingly, the expression (Eq. 6.32) represents the estimation of variable importance for predictor variable X (where X = 1-7), using the weights connecting each of the input neurons Z (where Z = 1–7) to each of the hidden neurons N (where N = 1–10), and the latter to the single output neuron (Table 6.12).

$$Input_X = \sum_{N=1}^{10} \frac{|Hidden_{XN}|}{\sum_{Z=1}^{7} |Hidden_{ZN}|} \quad \text{(Garson's algorithm)} \qquad (6.32)$$

The sensitivity analysis for the developed ANN model, as per Garson's method (Das and Basudhar 2006; Shahin et al. 2002; Das and Basudhar 2008) to establish the importance ranking of the input parameters, has been presented in Table 6.13. The angle of internal friction, φ has been found to be the most important input parameter followed by c, D_f/B, b/B, B, β and γ as per Garson's method, represented as pie-chart in Fig. 6.19. Hence, based on an overall understanding, the angle of internal friction of the constituent soil is considered the most influencing on the ultimate bearing capacity of the footing resting on the crest of a c-φ slope.

Table 6.9 Connection weights of Input-Hidden layer obtained after training phase of 7-10-1 ANN model

N / X	Hidden N1	Hidden N2	Hidden N3	Hidden N4	Hidde n N5	Hidden N6	Hidden N7	Hidden N8	Hidden N9	Hidden N10
c (X1)	0.55	-0.67	-0.26	0.84	-0.54	0.95	0.58	-3.58	0.004	-0.12
φ (X2)	-0.56	-0.33	8.43	1.30	-0.64	-7.25	1.27	-5.25	-0.29	-0.91
γ (X3)	0.32	0.03	0.02	0.16	-0.09	0.03	0.09	-0.75	-0.01	0.04
B (X4)	0.24	0.11	0.15	0.46	-0.52	-0.06	0.46	4.79	-0.13	-0.13
b/B (X5)	1.45	0.008	2.05	0.14	0.07	-1.74	-0.51	2.64	0.02	2.01
β (X6)	-0.38	-0.01	-0.47	-0.04	-0.01	0.51	0.11	-0.67	0.004	-0.46
D_f/B (X7)	1.30	0.57	-0.66	0.72	-0.35	0.66	0.42	6.50	-0.09	-0.05

Table 6.10 Connection weights of Hidden-Output layer obtained after training phase of 7-10-1 ANN model

N / Y	Hidden N1	Hidden N2	Hidden N3	Hidden N4	Hidden N5	Hidden N6	Hidden N7	Hidden N8	Hidden N9	Hidden N10
Output	0.06	-2.16	0.52	1.91	2.01	0.53	0.83	2.32	-3.58	0.97

Table 6.11 Biases obtained after training phase of the 7-10-1 ANN model

Hidden layer biases (b_{hN})	Output layer biases (b_O)
1.16	
-0.48	
-0.66	
-2.16	
1.34	-0.61
0.03	
-1.79	
-5.15	
-0.03	
3.03	

Table 6.12 Product of the input-hidden and hidden-output connection weights after training phase of 7-10-1 ANN model

Z \ N	Hidden N1	Hidden N2	Hidden N3	Hidden N4	Hidden N5	Hidden N6	Hidden N7	Hidden N8	Hidden N9	Hidden N10
c (X1)	0.04	1.45	-0.13	1.61	-1.09	0.50	0.48	-8.31	0.02	-0.12
φ (X2)	-0.04	0.71	4.40	2.49	-1.29	-3.83	1.06	-12.2	1.03	-0.88
γ (X3)	0.02	-0.07	0.01	0.31	-0.19	0.02	0.08	-1.73	0.02	0.04
B (X4)	0.02	-0.24	0.08	0.87	-1.04	-0.03	0.38	11.10	0.48	-0.12
b/B (X5)	0.09	0.002	1.07	0.26	0.14	-0.92	-0.43	6.13	-0.07	1.94
β (X6)	-0.02	0.03	-0.24	-0.08	-0.01	0.27	0.09	-1.55	0.01	-0.45
D_f/B (X7)	0.08	-1.23	-0.34	1.37	-0.69	0.35	0.35	15.09	0.32	-0.05

Table 6.13 Importance ranking of input-parameters based on Garson's algorithm

Input	Relative importance	Relative importance (%)	Rank
c	1.69	18.07	2
φ	3.54	37.80	1
γ	0.19	2.02	7
B	1.05	11.24	5
b/B	1.23	13.12	4
β	0.30	3.18	6
D_f/B	1.36	14.57	3

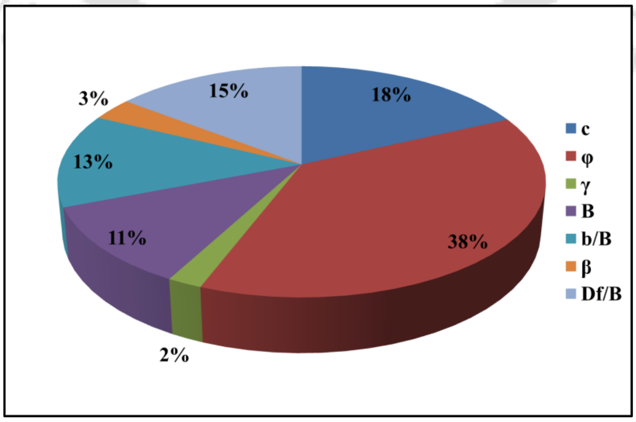

Fig. 6.19 Relative importance of the parameters influencing the bearing capacity of a square footing resting on the crest of a *c*-*φ* soil slope, according to Garson's algorithm (1991)

6.4.4 ANN prediction equation for ultimate bearing capacity (q_u)

A predicting equation is prepared with aid of weights obtained from trained neural network model (Das and Basudhar 2006; Behera et al. 2013 a, b; Das and Basudhar 2008; Das et al. 2011). The mathematical expression connecting input parameters (c, φ, γ, B, b/B, β, D_f/B) with output (q_u) has been represented in Eq. 6.33.

$$(q_u)_n = f_{Sig}\{b_O + \sum_{N=1}^{h}[w_N f_{Sig}(b_{hN} + \sum_{i=1}^{m} w_{iN} X_i)]\} \tag{6.33}$$

where, $(q_u)_n$ is the normalized magnitude of q_u in the variation of [-1,1], X_i is the normalised magnitude of inputs in the variation of [-1,1], f_{Sig} is the Sigmoid transfer function, m is the number of input variables, h is the number of neurons present in the hidden layer, , w_{iN} is the connection weight between i^{th} layer of input and N^{th} neuron of hidden layer, w_N is the connection weight between N^{th} neuron of hidden layer and single output neuron, b_{hN} is the bias at the N^{th} neuron of hidden layer, and b_o is the bias at the output layer.

The ANN model prediction equation for $(q_u)_n$ of strip footing located at the crest of slope, subjected to vertical loading, has been framed with aid of weights and biases provided in Table 6.9, Table 6.10 and Table 6.11 as per subsequent expressions (Eq. 6.34 - 6.56).

$$A_1 = 0.55(c) - 0.56(\varphi) + 0.32\gamma + 0.24(B) + 1.45(b/B) - 0.38(\beta) + 1.30(D_f/B) + 1.16 \tag{6.34}$$

$$A_2 = -0.67(c) - 0.33(\varphi) + 0.03\gamma + 0.11(B) + 0.008(b/B) - 0.01(\beta) + 0.57(D_f/B) - 0.48$$

(6.35)

$$A_3 = -0.26(c) + 8.43(\varphi) + 0.02\gamma + 0.15(B) + 2.05(b/B) - 0.47(\beta) - 0.66(D_f/B) - 0.66 \tag{6.36}$$

$$A_4 = 0.84(c) + 1.30(\varphi) + 0.16\gamma + 0.46(B) + 0.14(b/B) - 0.04(\beta) + 0.72(D_f/B) - 2.16 \tag{6.37}$$

$$A_5 = -0.54(c) - 0.64(\varphi) - 0.09\gamma - 0.52(B) + 0.07(b/B) - 0.01(\beta) - 0.35(D_f/B) + 1.34 \tag{6.38}$$

$$A_6 = 0.95(c) - 7.25(\varphi) + 0.03\gamma - 0.06(B) - 1.74(b/B) + 0.51(\beta) + 0.66(D_f/B) + 0.03 \tag{6.39}$$

$$A_7 = 0.58(c) + 1.27(\varphi) + 0.09\gamma + 0.46(B) - 0.51(b/B) + 0.11(\beta) + 0.42(D_f/B) - 1.79 \quad (6.40)$$

$$A_8 = -3.58(c) - 5.25(\varphi) - 0.75\gamma + 4.79(B) + 2.64(b/B) - 0.67(\beta) + 6.50(D_f/B) - 5.15 \quad (6.41)$$

$$A_9 = 0.004(c) - 0.29(\varphi) - 0.01\gamma - 0.13(B) + 0.02(b/B) + 0.004(\beta) - 0.09(D_f/B) - 0.03 \quad (6.42)$$

$$A_{10} = -0.12(c) - 0.91(\varphi) + 0.04\gamma - 0.13(B) + 2.01(b/B) - 0.46(\beta) - 0.05(D_f/B) + 3.03 \quad (6.43)$$

$$B_1 = 0.06\left(\frac{e^{A_1} - e^{-A_1}}{e^{A_1} + e^{-A_1}}\right) \quad (6.44)$$

$$B_2 = -2.16\left(\frac{e^{A_2} - e^{-A_2}}{e^{A_2} + e^{-A_2}}\right) \quad (6.45)$$

$$B_3 = 0.52\left(\frac{e^{A_3} - e^{-A_3}}{e^{A_3} + e^{-A_3}}\right) \quad (6.46)$$

$$B_4 = 1.91\left(\frac{e^{A_4} - e^{-A_4}}{e^{A_4} + e^{-A_4}}\right) \quad (6.47)$$

$$B_5 = 2.01\left(\frac{e^{A_5} - e^{-A_5}}{e^{A_5} + e^{-A_5}}\right) \quad (6.48)$$

$$B_6 = 0.53\left(\frac{e^{A_6} - e^{-A_6}}{e^{A_6} + e^{-A_6}}\right) \quad (6.49)$$

$$B_7 = 0.83\left(\frac{e^{A_7} - e^{-A_7}}{e^{A_7} + e^{-A_7}}\right) \quad (6.50)$$

$$B_8 = 2.32\left(\frac{e^{A_8} - e^{-A_8}}{e^{A_8} + e^{-A_8}}\right) \quad (6.51)$$

$$B_9 = -3.58\left(\frac{e^{A_9} - e^{-A_9}}{e^{A_9} + e^{-A_9}}\right) \quad (6.52)$$

$$B_{10} = 0.97\left(\frac{e^{A_{10}} - e^{-A_{10}}}{e^{A_{10}} + e^{-A_{10}}}\right) \quad (6.53)$$

$$C_1 = -0.61 + B_1 + B_2 + B_3 + B_4 + B_5 + B_6 + B_7 + B_8 + B_9 + B_{10} \quad (6.54)$$

$$(q_u)_n = \left(\frac{e^{C_1} - e^{-C_1}}{e^{C_1} + e^{-C_1}}\right) \quad (6.55)$$

The magnitude of $(q_u)_n$ as attained from Eq. 6.55 is in the variation of [-1, 1] and this is required to be de-normalized as per expression Eq. 6.56.

$$q_u = 0.5[(q_u)_n + 1][(q_u)_{max} - (q_u)_{min}] + (q_u)_{min} \tag{6.56}$$

where $(q_u)_{max}$ and $(q_u)_{min}$ are the maximum and minimum magnitudes of q_u correspondingly in the dataset.

6.5 ANN Model for Predicting the Bearing Capacity of Interfering Strip Footings Located on the Crest of *c-φ* Soil Slope

This section describes the development of ANN model for predicting the bearing capacity of interfering strip footings located on the crest of a *c-φ* soil slope. The data used for the development of the ANN model have been simulated based on PLAXIS FE modelling, and has already been described in Section 5.3. The ANN architecture consists of six input nodes conforming to the input parameters, namely cohesion (c), Angle of internal friction (φ), width of footing (B), setback ratio (b/B), spacing ratio (S/B) and slope angle (β). The output layer consists of only one node showcasing the prediction of the ultimate bearing capacity of square footing. A single hidden layer has been used for the present study. The numbers of neurons are chosen on the basis of a convergence study, which is described in the following section.

6.5.1 Number of neurons in hidden layer

In the present investigation, a convergence study has been conducted for achieving optimum number of neurons in the hidden layer. The number of neurons in the hidden layer is varied and the minimum mean square error (MSE) value of 0.15 has been obtained with eight hidden neurons as shown in Fig. 6.20. Hence, with six (6) inputs (c, φ, B, b/B, S/B and β), eight (8) hidden neurons and single (1) output ($q_u/\gamma H_s$), a 6–8–1 network architecture is obtained as the best suited ANN model for estimating the bearing capacity of interfering strip footings resting on the crest of a *c*-*φ* slope (Fig. 6.21).

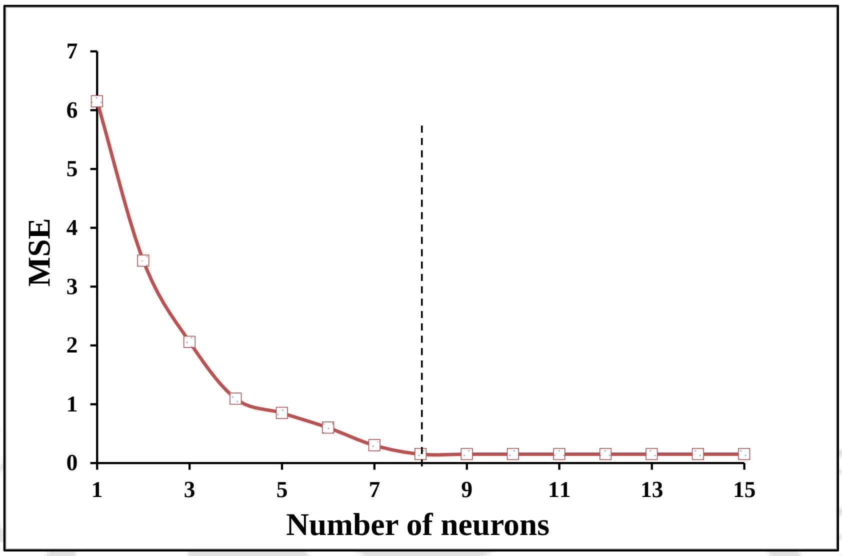

Fig. 6.20 Determination of optimum number of hidden neurons

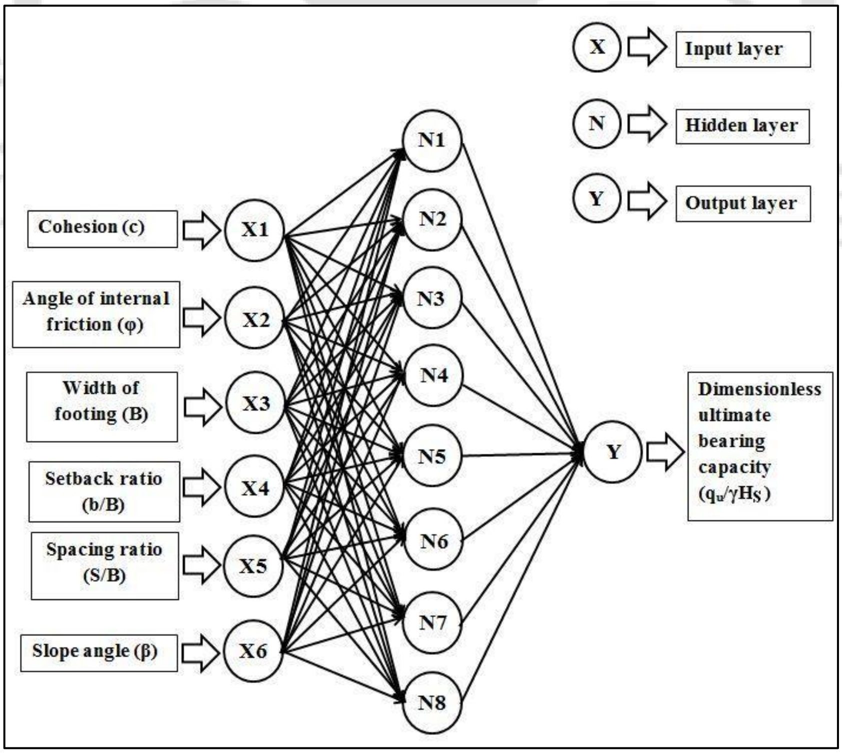

Fig. 6.21 The 6-8-11 ANN architecture to be used for prediction of bearing capacity of interfering strip footings located on the crest of a *c*-*φ* soil slope

6.5.2 Performance of the ANN architecture

Neural network architecture has the ability to modify its performance with respect to a particular problem. ANN has self-adjusting capability to capture the valid pattern of given dataset, and this process is referred as training. In training, the connection weights of neurons changes systematically to produce the desired outcomes. The main purpose of training is to identify the optimal connection weights which will provide tolerable and minimum MSE (Demuth and Hagan 1996). In the network total architecture development, a total of 867 data have been used. In the neural networking adopted herein, 80% (693) of the total dataset has been employed for training and 20% (174) of the remaining dataset has been considered for validation purpose. The 80% of total dataset has been further sub-divided, where 70% (485) of data has been considered for training to construct the neural structure and the remaining 30% (174) of data has been engaged for testing activity (Ghaboussi et al. 1994). The optimal weights obtained from training step have been retained for testing and validation stages.

Figure 6.22 depicts the outcome of the training process as an agreement of the magnitudes of q_{un} obtained from Finite Element simulations (simulated $q_u/\gamma H_s$) with those obtained as predictions of the ANN model (predicted $q_u/\gamma H_s$). In the training phase, a coefficient of correlation (R^2) has been obtained as 0.998, which signifies a strong agreement between predicted and simulated outcomes, thus highlighting the optimal training of the ANN architecture. Under this condition, the connection weights (input-hidden and hidden-output) obtained as an outcome of the training programme is highlighted in Tables 6.14 and 6.15, which are subsequently used in the testing and validation phases. Table 6.16 highlights the corresponding biases. Further, the trained ANN structure, with its optimal connection weights, has been considered for the testing phase to check the prediction capacity of the network. Figure 6.23 portrays that there is excellent match (R^2 = 0.997) of $q_u/\gamma H_s$ obtained from numerical investigation (FE simulations) with those predicted by ANN model. The testing phase with a high correlation coefficient provides a confirmatory that the trained neural network has superior prediction ability.

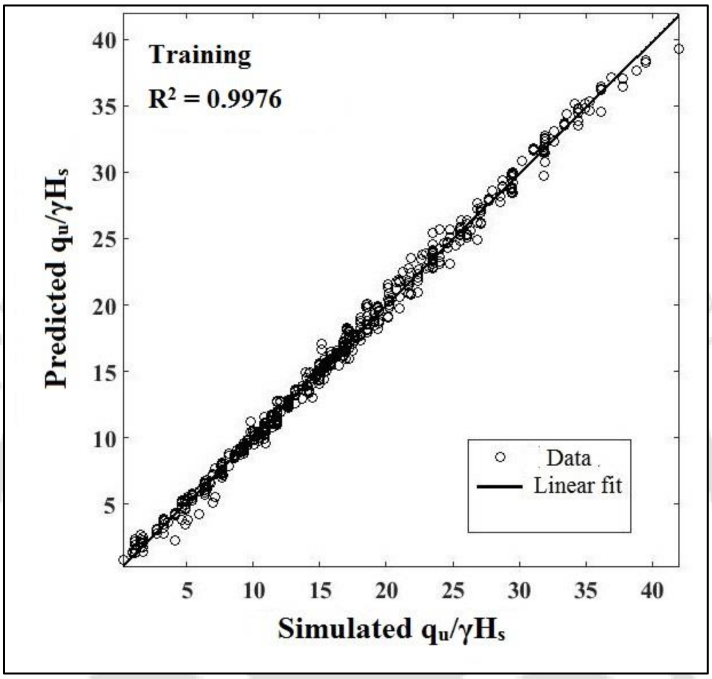

Fig. 6.22 Operational capability of the 6-8-1 ANN model for training phase

Table 6.14 Connection weights of Input-Hidden layer obtained after training phase of 6-8-1 ANN model

N / X	Hidden N1	Hidden N2	Hidden N3	Hidden N4	Hidden N5	Hidden N6	Hidden N7	Hidden N8
c (X1)	0.80	-0.41	0.19	0.15	-0.40	0.44	1.20	0.32
φ (X2)	0.74	-0.40	-0.06	0.19	-0.48	0.26	0.97	0.33
B (X3)	0.10	-0.13	-0.23	0.15	-0.12	-0.14	-2.53	0.02
b/B (X4)	-0.02	2.00	-0.36	-0.005	4.56	-0.21	2.84	-1.29
S/B (X5)	10.88	-0.17	0.064	8.73	0.037	0.017	0.40	0.11
β (X6)	-0.02	-1.14	0.55	-0.040	7.69	0.22	-1.90	0.59

Table 6.15 Connection weights of Hidden-Output layer obtained after training phase of 6-8-1 ANN model

N / Y	Hidden N1	Hidden N2	Hidden N3	Hidden N4	Hidden N5	Hidden N6	Hidden N7	Hidden N8
$q_u/\gamma H_s$	-1.10	-1.13	1.08	1.11	-0.12	-4.27	0.13	-3.38

Table 6.16 Biases obtained after training phase of the 6-8-1 ANN model

Hidden layer biases (b_{hN})	Output layer biases (b_O)
8.81	-0.32
2.53	
0.57	
7.19	
4.99	
0.82	
5.05	
-2.11	

Subsequently, the trained ANN structure has been engaged with the validation dataset that have not been considered to form ANN architecture, neither in training nor in testing phase. The validation step is useful in checking the aptness of the ANN model to generalize the outcome of the physical problem. Figure 6.24 illustrates excellent match (R^2 = 0.998) between simulated and forecasted magnitudes of $q_u/\gamma H_s$ for interfering strip footing placed near sloping surface, thus highlighting the superior generalization and performance of the 6-8-1 ANN architecture.

The progress of training was inspected for the all the above phases, i.e. training, testing and validation, by plotting the variation of MSE with the completed number of iterations, as presented in Fig. 6.25. It is observed that errors obtained from test set and validation sets have identical appearances and hence, there is no over-fitting during the training of the proposed architecture (Noorzaei et al. 2008).

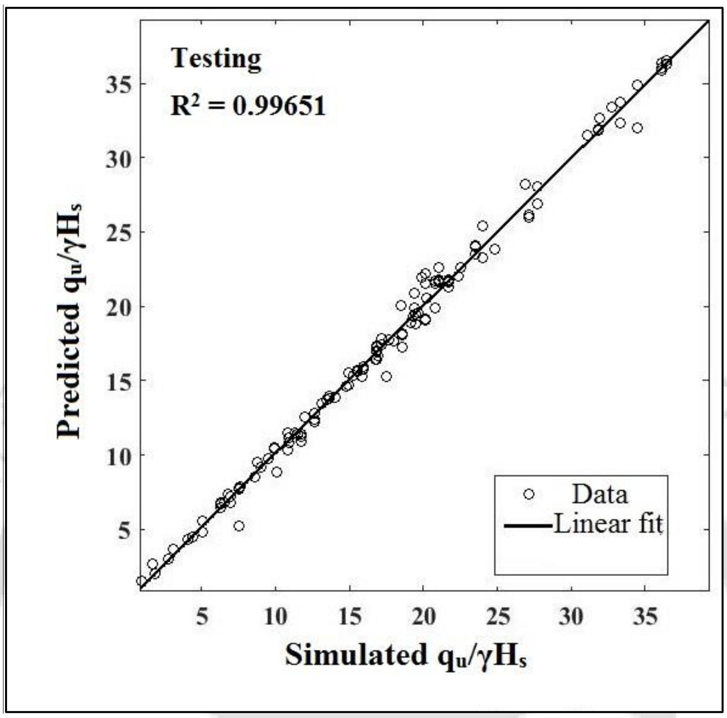

Fig. 6.23 Prediction capability of the 6-8-1 ANN model during testing phase

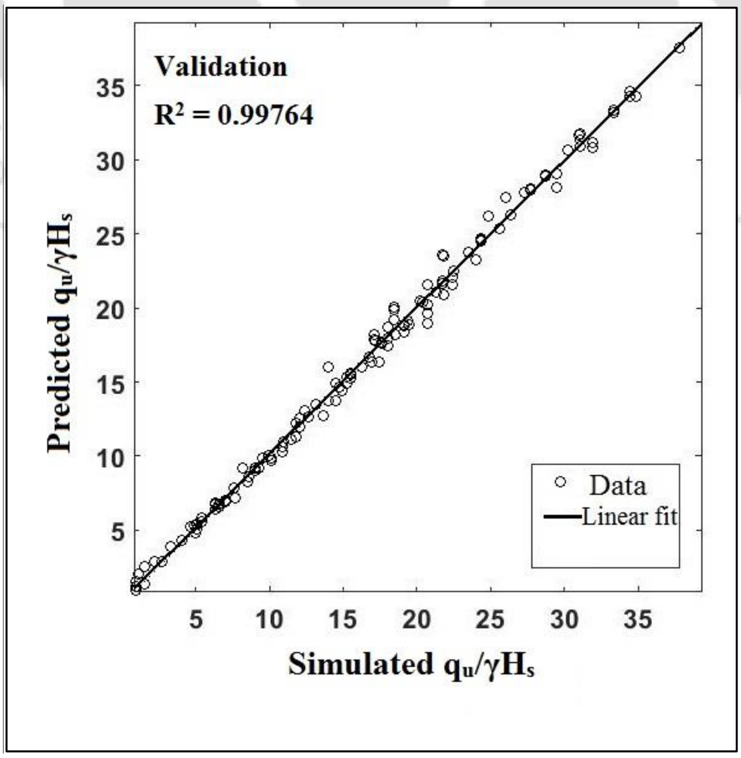

Fig. 6.24 Performance of the 6-8-1 ANN model for validation phase

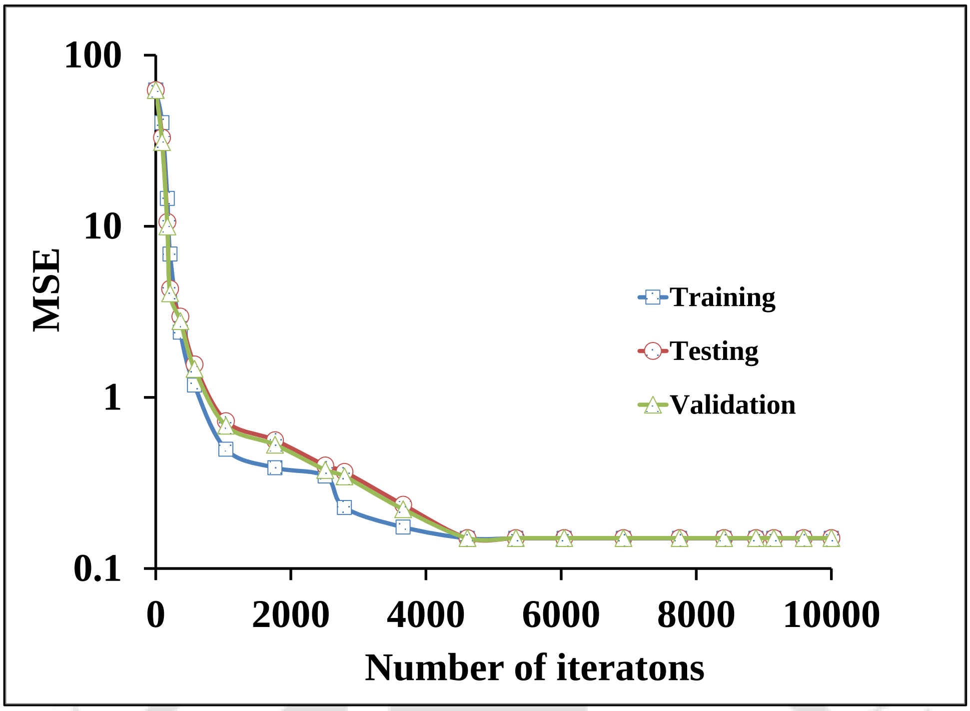

Fig. 6.25 Comparison of MSE during training, testing and validation phases of the 6-8-1 ANN model

6.5.3 Sensitivity analysis and importance ranking of influencing parameters

Sensitivity investigation is a necessary research conducted for the ranking of input variables, thus highlighting their sorted influence on the outcome of the physical problem. Such study aids in the 'design of experiments' when large number of the numerical or physical simulations are required, while based on the sensitive influence of the contributing parameters, only few of them are selected for the actual modelling. Thus, sensitivity analysis helps in the reduction in the number of model simulations, without jeopardizing the generality of the obtained results. Various methods have been advised in the articles for identifying the influential input parameter (Goh 1994; Shahin et al. 2002). In the present study, Garson's algorithm (1991) has been considered to identify the significance of inputs. In order to apply Garson's algorithm, firstly the input-hidden (Table 6.14) and hidden-output (Table 6.15) weights are multiplied, and the absolute magnitudes of weights are considered to differentiate the rank of input parameters (Eq. 6.57).

$$Input_X = \sum_{N=1}^{8} \frac{|Hidden_{XN}|}{\sum_{Z=1}^{6} |Hidden_{ZN}|} \quad \text{(Garson's algorithm)} \tag{6.57}$$

where, $Hidden_{XN}$ represents the absolute magnitudes of the connection weights between the input nodes and hidden layer nodes (as provided in Table 6.14), and $Hidden_{ZN}$ represents the absolute magnitudes of the product of the connection weights between the input-hidden and hidden-output nodes. The sample $Hidden_{ZN}$ as obtained for the 6-8-1 ANN model developed for the present study is provided in Table 7.17, the values of which are obtained from the corresponding products of the parameter magnitudes provided in Table 7.14 and Table 7.15.

Table 6.17 Product of the input-hidden and hidden-output weights after training phase of 6-8-1 ANN model

Z \ N	Hidden N1	Hidden N2	Hidden N3	Hidden N4	Hidden N5	Hidden N6	Hidden N7	Hidden N8
c (X1)	-0.89	0.47	0.21	0.17	0.049	-1.90	0.16	-1.11
φ (X2)	-0.82	0.46	-0.06	0.22	0.058	-1.13	0.13	-1.12
B (X3)	-0.11	0.150	-0.25	0.17	0.015	0.60	-0.34	-0.1
b/B (X4)	0.028	-2.28	-0.40	-0.0059	-0.55	0.917	0.38	4.37
S/B (X5)	-12.06	0.19	0.069	9.72	-0.0046	-0.075	0.055	-0.38
β (X6)	0.024	1.30	0.601	-0.04	-0.93	-0.9403	-0.260	-2.01

Consequently, Eq. 6.57 indicates the assessment of importance ranking for input predictors X (X = 1-6), utilizing the weights of individual input neurons Z (Z = 1–6) to each of the hidden layer nodes N (N = 1–8), and lastly to a single output node (Y). The outcome of the sensitivity study carried out with the aid of Garson's method to provide the importance ranking to the input parameters is highlighted in Table 6.18. It can be observed that the geometrical parameters (spacing of footings, their nearness to the crest and slope inclination) are more sensitive and play a dominant role in deciding the magnitude of $q_u/\gamma H_m$. According to Garson's method, the setback ratio, *b/B* has been identified as the utmost significant input parameter lagged by *S/B*, *β*, *c*, *φ* and *B*, as shown in Fig. 6.26. It is comprehendible that the interference effect of footings is more effective in influencing larger volumes of foundation soil to take part in the resisting bearing mechanism. Moreover, the formation of the resisting passive mechanism and transfer of stresses will be strictly governed by the closeness of the footings to the slope and the steepness of the slope. Closer the footing location to the slope face and higher the slope steepness, lower will be the passive resistance, and hence, lower will be the bearing capacity.

Table 6.18 Rank of input parameters from Garson's algorithm

Input	Importance	Relative importance (%)	Rank
c	0.93	11.61	4
φ	0.68	8.51	5
B	0.60	7.48	6
b/B	2.00	24.95	1
S/B	1.99	24.85	2
β	1.81	22.61	3

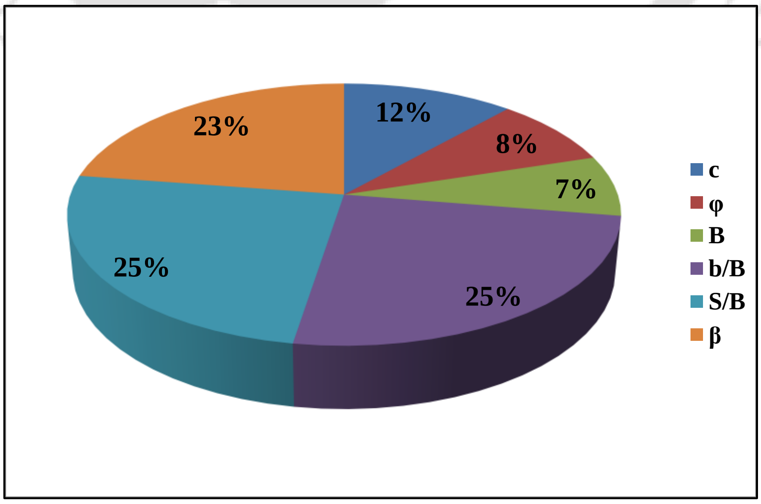

Fig. 6.26 Importance and relative contribution of input parameters, influencing the bearing capacity of an interfering strip footings resting on the crest of a *c*-*φ* soil slope

6.5.4 ANN prediction equation for $q_u/\gamma H_s$

A prediction equation is developed with aid of optimal weights and biases obtained from trained neural network model (Das and Basudhar 2006; Behera et al. 2013 a, b; Das and Basudhar 2008; Das et al. 2011). The mathematical expression connecting input parameters (c, φ, B, b/B, S/B and β) with output ($q_u/\gamma H_s$) is represented in Eq. 6.58.

$$\left(\frac{q_u}{\gamma H_s}\right)_n = f_{Sig}\{b_O + \sum_{N=1}^{h}[w_N\, f_{Sig}(b_{hN} + \sum_{i=1}^{m} w_{iN} X_i)]\} \tag{6.58}$$

where, $(q_u/\gamma H_m)_n$ is the normalized magnitude of $q_u/\gamma H_s$ in the variation of [-1,1], X_i is the normalised magnitude of inputs in the variation of [-1,1], f_{Sig} is the tan-sigmoid transfer function, m is the number of input present as variables, h is the number of neurons present in the hidden layer, w_{iN} is the connection weight between i^{th} layer of input and N^{th} neuron of hidden layer, w_N is the connection weight between N^{th} neuron of hidden layer and single output neuron, b_{hN} is the bias at the N^{th} neuron of hidden layer and b_o is the bias at the output layer.

The ANN model prediction equation for $q_u/\gamma H_m$ of interfering strip footing located at the crest of slope with various setback distance (b) and spacing (S), subjected to vertical loading, has been framed with aid of weights and biases provided in Table 6.14, Table 6.15 and Table 6.16, and is expressed as per subsequent expressions (Eq. 6.59 – 6.76).

$$A_1 = 0.80(c) + 0.74(\varphi) + 0.10(B) - 0.02(b/B) + 10.88(S/B) - 0.02(\beta) + 8.81 \tag{6.59}$$

$$A_2 = -0.41(c) - 0.40(\varphi) - 0.13(B) + 2.0(b/B) - 0.17(S/B) - 1.14(\beta) + 2.53 \tag{6.60}$$

$$A_3 = 0.19(c) - 0.06(\varphi) - 0.23(B) - 0.36(b/B) + 0.064(S/B) + 0.55(\beta) + 0.57 \tag{6.61}$$

$$A_4 = 0.15(c) + 0.19(\varphi) + 0.15(B) - 0.005(b/B) + 8.73(S/B) - 0.040(\beta) + 7.19 \tag{6.62}$$

$$A_5 = -0.40(c) - 0.48(\varphi) - 0.12(B) + 4.56(b/B) + 0.037(S/B) + 7.69\beta) + 4.99 \tag{6.63}$$

$$A_6 = 0.44(c) + 0.26(\varphi) - 0.14(B) - 0.21(b/B) + 0.017(S/B) + 0.22(\beta) + 0.82 \tag{6.64}$$

$$A_7 = 1.20(c) + 0.97(\varphi) - 2.53(B) + 2.84(b/B) + 0.40(S/B) - 1.90(\beta) + 5.05 \tag{6.65}$$

$$A_8 = 0.32(c) + 0.33(\varphi) + 0.02(B) - 1.29(b/B) + 0.11(S/B) + 0.59(\beta) - 2.11 \tag{6.66}$$

$$B_1 = -1.10\left(\frac{e^{A_1} - e^{-A_1}}{e^{A_1} + e^{-A_1}}\right) \tag{6.67}$$

$$B_2 = -1.13\left(\frac{e^{A_2} - e^{-A_2}}{e^{A_2} + e^{-A_2}}\right) \tag{6.68}$$

$$B_3 = 1.08\left(\frac{e^{A_3} - e^{-A_3}}{e^{A_3} + e^{-A_3}}\right) \tag{6.69}$$

$$B_4 = 1.11\left(\frac{e^{A_4} - e^{-A_4}}{e^{A_4} + e^{-A_4}}\right) \tag{6.70}$$

$$B_5 = -0.12\left(\frac{e^{A_5} - e^{-A_5}}{e^{A_5} + e^{-A_5}}\right) \tag{6.71}$$

$$B_6 = -4.27\left(\frac{e^{A_6} - e^{-A_6}}{e^{A_6} + e^{-A_6}}\right) \tag{6.72}$$

$$B_7 = 0.13\left(\frac{e^{A_7} - e^{-A_7}}{e^{A_7} + e^{-A_7}}\right) \tag{6.73}$$

$$B_8 = -3.38\left(\frac{e^{A_8} - e^{-A_8}}{e^{A_8} + e^{-A_8}}\right) \tag{6.74}$$

$$C_1 = -0.32 + B_1 + B_2 + B_3 + B_4 + B_5 + B_6 + B_7 + B_8 \tag{6.75}$$

$$\left(\frac{q_u}{\gamma H_s}\right)_n = \left(\frac{e^{C_1} - e^{-C_1}}{e^{C_1} + e^{-C_1}}\right) \tag{6.76}$$

The $(q_u/\gamma H_s)_n$ value as obtained from Eq. (6.76) is in the range [-1, 1] and this needs to be de-normalized as per Eqn. 7.70.

$$\left(\frac{q_u}{\gamma H_s}\right) = 0.5\left[\left(\frac{q_u}{\gamma H_s}\right)_n + 1\right]\left[\left(\frac{q_u}{\gamma H_s}\right)_{\max} - \left(\frac{q_u}{\gamma H_s}\right)_{\min}\right] + \left(\frac{q_u}{\gamma H_s}\right)_{\min} \tag{6.77}$$

where $(q_u/\gamma H_s)_{\max}$ and $(q_u/\gamma H_s)_{\min}$ are the maximum and minimum magnitudes of $q_u/\gamma H_s$ correspondingly in the dataset.

6.6 Summary

This chapter reports the utilization of artificial neural network (ANN) approach to provide the predicting expressions for the estimation of bearing capacity of strip, square and interfering strip foundations resting on the crest of a *c-φ* soil slopes. For each of the developed ANN models for different foundation scenarios, convergence study has been carried out to decide for the optimal number of hidden neurons and thus develop the best-suited ANN model. For the strip footing, square footing, and interfering strip footings located on the crest of a *c-φ* soil slope, a 6-9-1, 7-10-1 and 6-8-1 ANN architecture has been found to the best suited model to predict the corresponding bearing capacities. Sensitivity analysis, as per Garson's algorithm, has been carried out to identify the importance ranking of the parameter, and decide for the most influential parameter. It has been observed that for isolated square footing or for isolated strip footing resting on crest of *c-φ* slope, the angle of internal friction (*φ*) is most important input parameter of estimating the ultimate bearing capacity. Further, it has been perceived that for interfering strip footing resting on crest of *c-φ* slope, the setback ratio (*b/B*) is most important input parameter of estimating the ultimate bearing capacity.

CHAPTER 7

INFLUENCE OF VARIED TYPOLOGIES OF FOOTINGS LOCATED ON SLOPE CREST

7.1 General

The previous chapters dealt in detail about the response of isolated strip and square foundations located on slope crest or on its face. Studies in earlier chapters have also highlighted the response of interacting strip footings located on the crest or face of a slope. One of the objectives of this study is to extend the understanding of the responses of the individual footing, or interaction of footings of similar typologies, to the cases where footings of different typologies interact with each other. Such a study would help in consequent understanding of the actual scenario encountered in habituated hill-slopes. If the pictures of hill-slopes sustaining human habitation can be seen, as provided in Chapter 1, it can be well understood that the interaction of foundations is far more complex than that illustrated in the earlier chapters of this thesis. Due to the growing demand to cater the needs of development, the uncontrolled practices have led to existence of buildings in close vicinity to each other on the crest or face of the hill-slopes, leading to foundation interaction at same or different elevations. Further, in the presence of a habitation, slopes at the upper or lower levels are being cut for the construction of roadways, railways or further inhabitations, leading to major issues of slope instabilities. Under such growing circumstances, it is necessary to make judicious planning of construction of residential / commercial buildings on hill-slopes, as well as cautious planning of further constructions. In this regard, it is important to understand the interaction of multiple typologies of coexisting footings and their influence on the evolution of failure mechanism on the hill-slopes. At the same time, it is also necessary to understand how different typologies of footings can alter the bearing capacity and resistance to deformation when placed at similar vicinities from the slope face. These understanding would aid in framing guidelines about the safe construction of buildings from a geotechnical point of view, which would subsequently aid in lessening the foundations failures on slopes and its aftermath.

In the above context, this chapter illustrates two topics. Firstly, it addresses the case study as how a 14 m high 220KV transmission tower, located on the crest of hill-slope, supported on isolated square footings, has been jeopardized due to toe cutting of the hill-slope. Further, based on its stability issues, it has been shown how the stability and the bearing capacity can be enhanced by an alternative choice of footing typology, so that the transmission tower is able to sustain higher levels of distress without succumbing to failure. Secondly, further studies are carried out considering coexistence of different types and sizes of footing on the crest of a hill-slope, so that a recommendation can be framed about the possible safest foundation types that could be adopted in the hilly areas, so that they exhibit enhanced bearing capacities and higher resistance to deformation towards the slope.

7.2 Case Study: Electrical Transmission Tower Located on Slope Crest

This case study refers to the Electrical Transmission Tower No. 26 of the 220 kV 4CKT Sarusajai-Jawahar Nagar line, at Sarusajai, Guwahati, Assam. The 14 m high tower, which forms the major component of the electrical supply line to Guwahati city, is supported by isolated square footings of width 2 m beneath each of its legs, having its foundation at a depth of 2 m. The legs of the transmission tower are at a distance of 3 m from each other, forming a square periphery. The tower is located at a hill-slope where a wide bench, created by excavation, forms the slope crest. Figure 7.1 provides a schematic sketch of the stated problem.

In order to support soil filling in the bench, a rubble-masonry guard wall had been constructed for the same. The height of the rubble masonry wall is nearly 3.7 m from its foundation base. During the establishment of the tower in its early days, the rubble masonry wall had sufficient earth cover in the sloping direction on its three sides. The surrounding area had been devoid of human inhabitation. In the recent past, increasing human inhabitation in the surrounding area had led to an intensive amount of the slope and toe cutting, thus removing the supporting soil in masses (Fig. 7.1). Accompanied by removal of the soil from the outward portions of the slope containing the guard wall, instability has resulted in significant outward movement of the guard wall. The stability of overall system has been declined further in the monsoon season due to heavy rain and seepage and percolation induced saturation of the hill-slope.

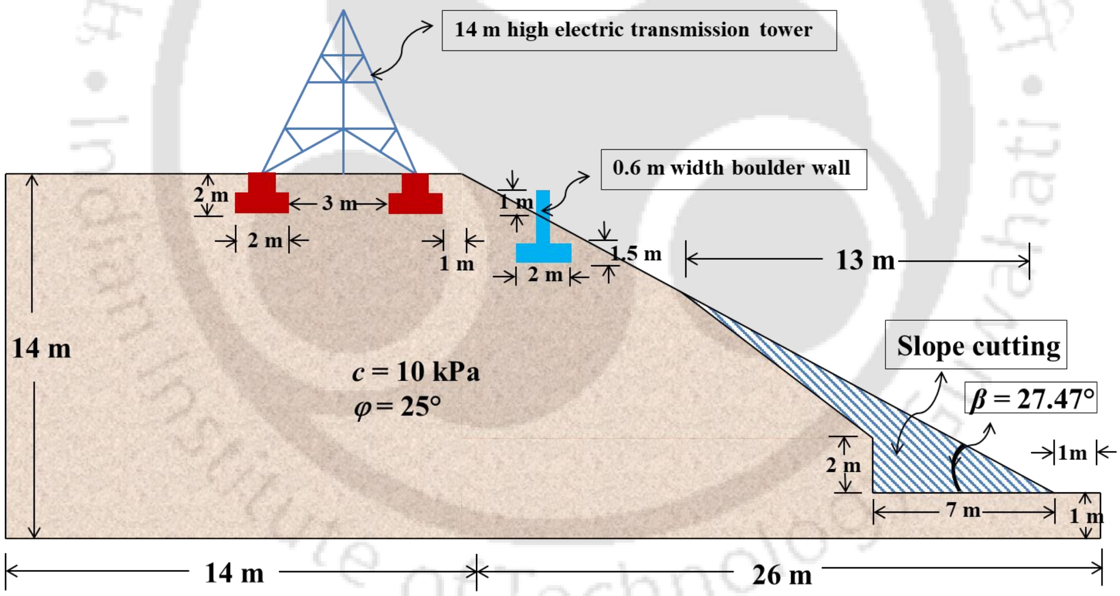

Fig. 7.1 Schematic diagram of Sarusajai transmission tower problem (Not to scale)

7.2.1 FE modelling of the case study

The case study has been investigated through FE modelling of foundations on slopes. In order to model the geometry of the hill-slope, the plan and elevation details were collected, as shown in Fig. 7.1. Further, to model the geotechnical characteristics, undisturbed as well as disturbed samples were collected from two numbers of boreholes of 15 m depth. Soil stratification and subsurface identification were carried out, as well as the shear strength properties ascertained through laboratory tests. From the borehole survey, it has been observed that within 15 m depth of borehole, the soil characteristics are mostly uniform. As a result, homogeneous soil has been considered for the numerical investigation and modelling of the hill-slope. The soil properties are listed in Table 7.1. The structural properties of concrete footing and rubble-masonry boulder wall are provided in Table 7.2.

Table 7.1 Hill-slope soil properties used in FE modelling of the case study

Type of soil	Unit weight (γ) (kN/m^3)	Modulus of elasticity (E) (MPa)	Cohesion (c) (kPa)	φ(°)
Foundation soil	17	10	10	25

Table 7.2 Properties of concrete and rubble masonry used in FE modelling

Material type	Type of material behaviour	Unit weight (γ) (kN/m^3)	Modulus of elasticity (E) (GPa)
Concrete	Liner elastic and non-porous	25	27
Rubble masonry	Liner elastic and non-porous	28	30

The load and moment developed at the base of tower, and as transmitted to the footings, has been calculated with the aid of IS-802 (Part 1/Sec 1) (1995). The weight of tower structure, inclusive of all parts of superstructure (including base plate, anchor bolts, bolts and earth strip) has been determined to impart a vertical load of 63 kN on each of the isolated square footings. The moment transmitted to the footings has been calculated from the design wind pressure and resultant wind load and that was obtained from Eq. 7.1 and Eq. 7.2 respectively.

$$p_d = 0.6 \times V_d^{\,2} \tag{7.1}$$

$$F_{wt} = p_d \times C_{dt} \times A_e \times G_T \tag{7.2}$$

where, p_d is the design wind pressure in N/m^2, V_d is the design speed in m/s, F_{wt} is the resultant wind load in N, C_{dt} is the drag coefficient, A_e is the total net surface area in m^2, and G_T is the gust response factor. According to IS-802 (Part I/Sec I) (1995), Guwahati has been placed under Wind Zone 5, having a prevalent wind speed of 50 m/s. Based on the information, the calculated moment was obtained as 60 kN-m, acting on each footing. These estimated magnitudes of vertical loads and moments have been used as load inputs on the square footings in the Plaxis FE model. The finite element model has been tested through convergence study, as described in earlier chapters, and the optimal mesh size has been determined, which has been used for the rest of the study.

7.2.2 Stability and safety analysis

Phi-c reduction technique has been utilized to compute global safety factor. In the safety approach, the shear strength parameters, φ and c, as well as the tensile strengths are successively reduced until failure of the structure occurs. The dilatancy angle ψ is, in principle, not affected by phi-c reduction procedure. However, the dilatancy angle, in general, is never larger than the friction angle. Thus, when the friction angle φ has been reduced to such extent that it becomes equal to the given dilatancy angle ψ, any further reduction of friction angle leads to identical reduction of dilatancy angle. The strength of interfaces, if used, is reduced in the same way. Optionally, the strength of structural objects like plate and anchors can also be reduced in the safety calculation. The total multiplier $\sum M_{sf}$ is used to define the value of soil strength parameters at a given stage in the analysis, and is determined from Eq. 7.3. Safety factor (SF) can be obtained as per Eq. 7.4.

$$\sum M_{sf} = \frac{\tan \phi_{input}}{\tan \phi_{reduced}} = \frac{c_{input}}{c_{reduced}} = \frac{s_{u,input}}{s_{u,reduced}} = \frac{\text{Tensile strength}_{input}}{\text{Tensile strength}_{reduced}} \tag{8.3}$$

$$SF = \sum M_{sf\ failure} \tag{8.4}$$

In the current investigation, the overall stability of the tower on the crest of slope has been inspected through safety analysis. In the present safety analysis, the safety factors (SF) have been determined for different stages of construction. The stages are as follows.

- Safety factor for virgin slope under both dry and wet, or saturated, conditions
- Safety factor after construction of transmission tower and boulder wall on the crest and slope face, respectively (for both dry and wet conditions)
- Safety factor after toe cutting (for both dry and wet conditions)

The foremost intention for conducting the stability analysis under various conditions was to make a forensic study to infer the condition which led to the impending failure of the slope, and correspondingly validate the FE model with the field information. For analysing the stability of the transmission tower, the safety analysis has been started from the virgin slope and sequentially to the toe cutting. In the analysis, firstly the dry virgin slope has been modelled (Fig. 7.2a) and global safety factor has been determined. Thereafter, the isolated square footings of transmission tower, with incumbent loads and moments, and boulder wall have been activated, and the corresponding safety factor has been estimated (Fig. 7.2b). Finally, the toe cutting has been has been simulated and the safety factor has been assessed (Fig. 7.2c). The above said procedures have been followed for wet conditions as well to illustrate the reduction of stability under the rainfall saturated conditions, and the corresponding safety factors have been assessed.

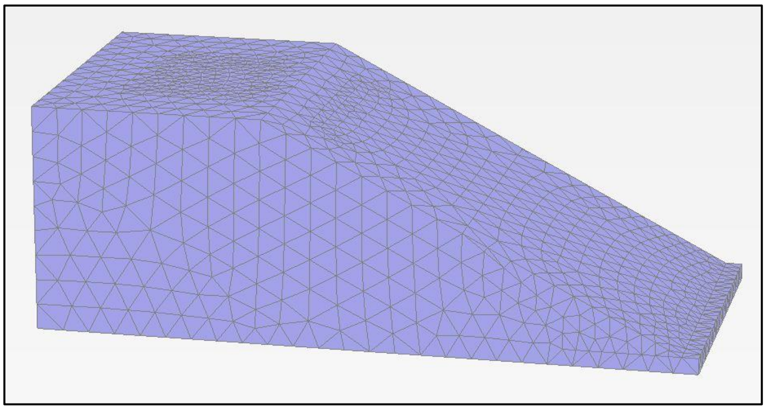

(a) Virgin slope

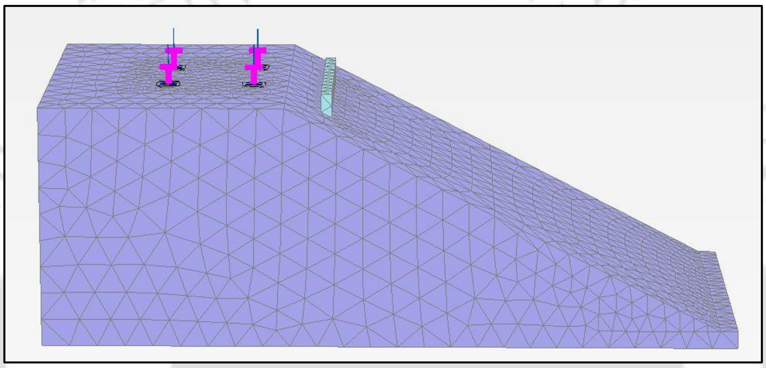

(b) Transmission tower and boulder wall on slope (Arrangement F1)

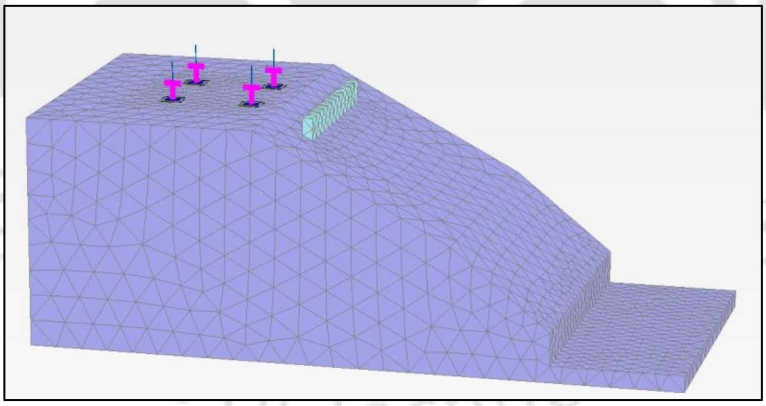

(c) Toe cutting

Fig. 7.2 Different stages of numerical investigation as applied for the case study

Figure 7.3 portrays the safety factors (SF) obtained for different stages of numerical analysis. It can be seen that the SF for dry and wet virgin slopes were 1.57 and 1.51, respectively. Further, after construction of tower and boulder wall on or near the slope, the SFs are reduced to 1.39 and 1.26 for dry and wet slopes, respectively. Finally, due to toe cutting, the SFs have been further reduced to 1.18 and 1.11 for dry and wet slopes, respectively.

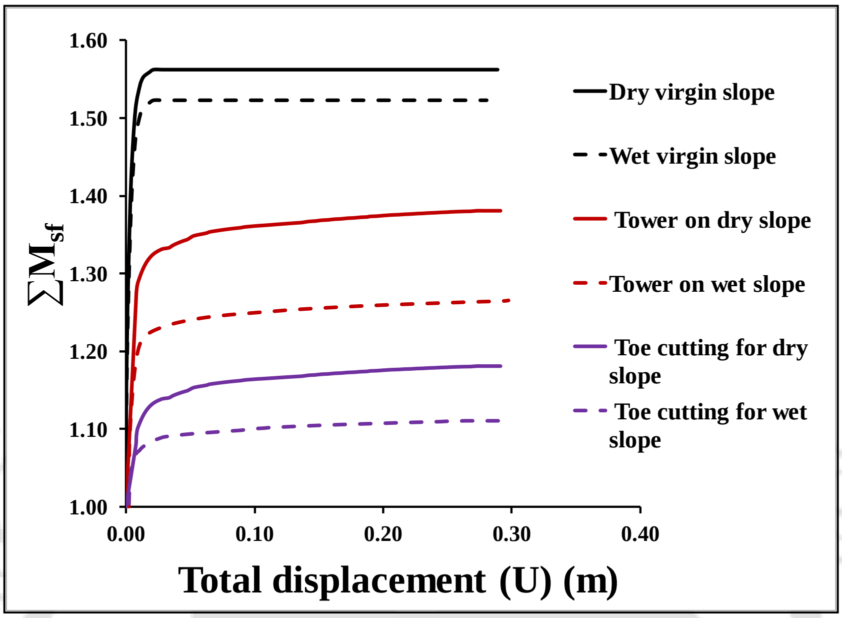

Fig. 7.3 Safety factors for various stages of analysis considering dry and saturated slopes

Based on the results, it can be stated that the virgin slope had been stable under both dry and rainfall saturated conditions. Similarly, it can be observed that the presence of tower and rubble-masonry boulder wall although did reduce the safety factors, the reduction was not sufficient to lead to impending failure under both dry and saturated conditions. Further, it can be noticed that toe cutting led to further reduction in the safety factors, highlighting the same to be a causal factor for impending failure as the reduced SF reached nearly 1.1. It can be observed that even with toe cutting, the dry slope exhibited a SF of approximately 1.18, while the saturated slope showed a SF of 1.1, highlighting impending failure of the wet hill-slope. These observations reinforce the physical observation of the impending failure in the site where major distress and outward movement leading to the cracking of rubble masonry was noted after the monsoon season of 2014.

7.2.3 Influence of alternative footing typology on stability

Apart from the original arrangement of 2 ×2 square footing (Arrangement F1) as used for the transmission tower, the study is further extended to investigate the influence of footings of different shapes and arrangements on the possible enhancement in the stability and the corresponding safety factors. Further numerical investigations have been done for the following arrangements (a) Rectangular footings perpendicular to slope face, obtained by connecting the corresponding square footings (Arrangement F2 as in Fig. 7.4a), and (b) Grid footing formed by connecting all the individual square footings (Arrangement F3 as in Fig. 7.4b). For all the alternative arrangements, the same stages of analysis were followed as considered for isolated square footings, and the corresponding safety factor has been determined. The loads and moments coming from the transmission tower were considered as utilized for isolated square footings.

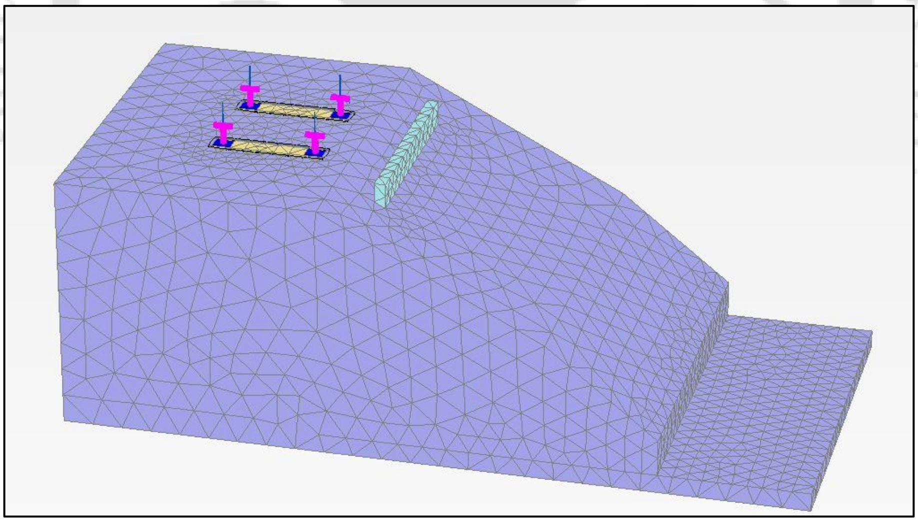

(a) Rectangular footings perpendicular to slope face (Arrangement F2)

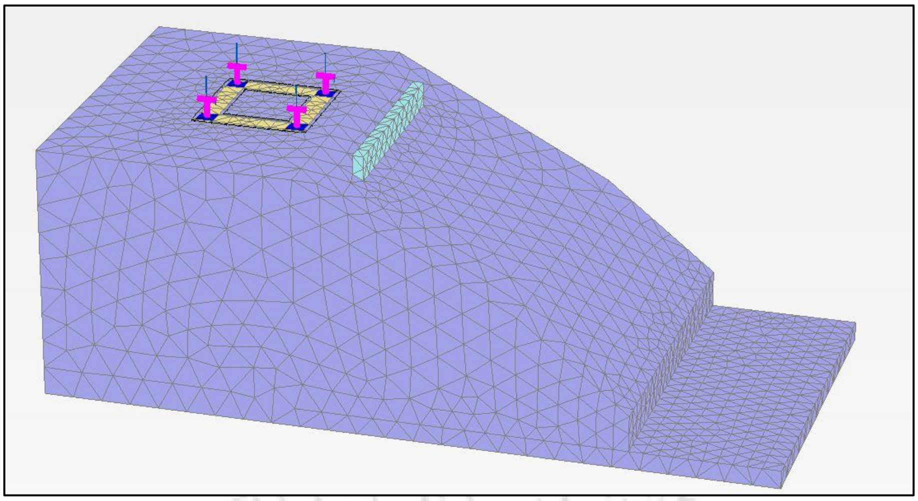

(b) Grid footing formed by connecting isolated square footings (Arrangement F3)

Fig. 7.4 Different footing arrangement and typologies as adopted for case study

Figure 7.5 portrays the safety factors of the fully saturated hill-slope, subjected to toe cutting, while supporting the transmission tower with alternative footing typologies. In the current investigation, only fully saturated condition has been considered, as such condition has yielded the least SF (in the previous analysis) and adjudged the critical condition (Fig. 7.3). It can be observed that for both the arrangements of F2 and F3, the overall stability has increased. When no toe cutting has been carried out in the slope supporting the transmission tower with footing typology F2 and F3, the SF is observed to be 1.35 and 1.48, respectively. Due to toe cutting, the SF values decreased to 1.19 and 1.24, respectively, for footing typology F2 and F3. It can be noted that any of the above SFs are higher than that obtained for the case when the transmission tower is supported on isolated square footings (F1); for such case, the SF was obtained as 1.26 and 1.11, respectively, before and after toe cutting. This confirms that the presence of interconnection between the footings lead to enhanced stability of the foundations on slopes.

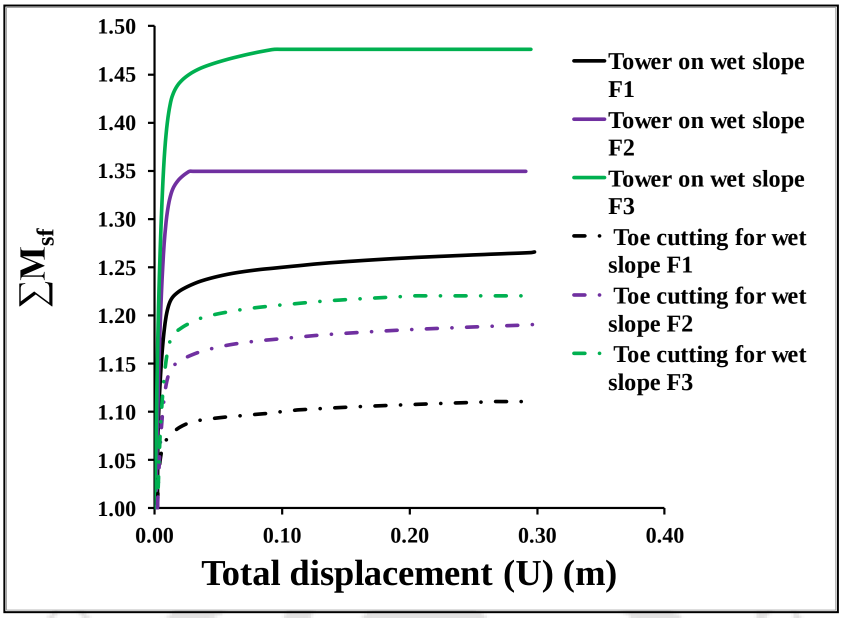

Fig. 7.5 Stability of the fully saturated hill-slope subjected to toe cutting and supporting the transmission tower having various alternative footing typologies

Figure 7.6 exhibits that, even when toe cutting is not considered in the saturated hill-slope, various typologies of footing exhibits varying magnitudes of total displacement towards the slope face. It can be observed that when the footings located near the slope are connected to the ones located away from the slope, the latter produces a tieback mechanism, thus restricting the outward movement of the former ones towards the slope. In this process, the resistance to deformation increases, thus enhancing the stability of the hill-slope against failure and preventing consequent failure of the supported structure. Similar observations in total outward displacement is noted when the toe cutting is carried out, as illustrated in Fig. 7.7. Hence, based on the understanding of reduced outward displacements, it is recommended to interconnect the footings placed near to the slope to those away from the slope, to ensure higher stability to the foundations supported on slopes.

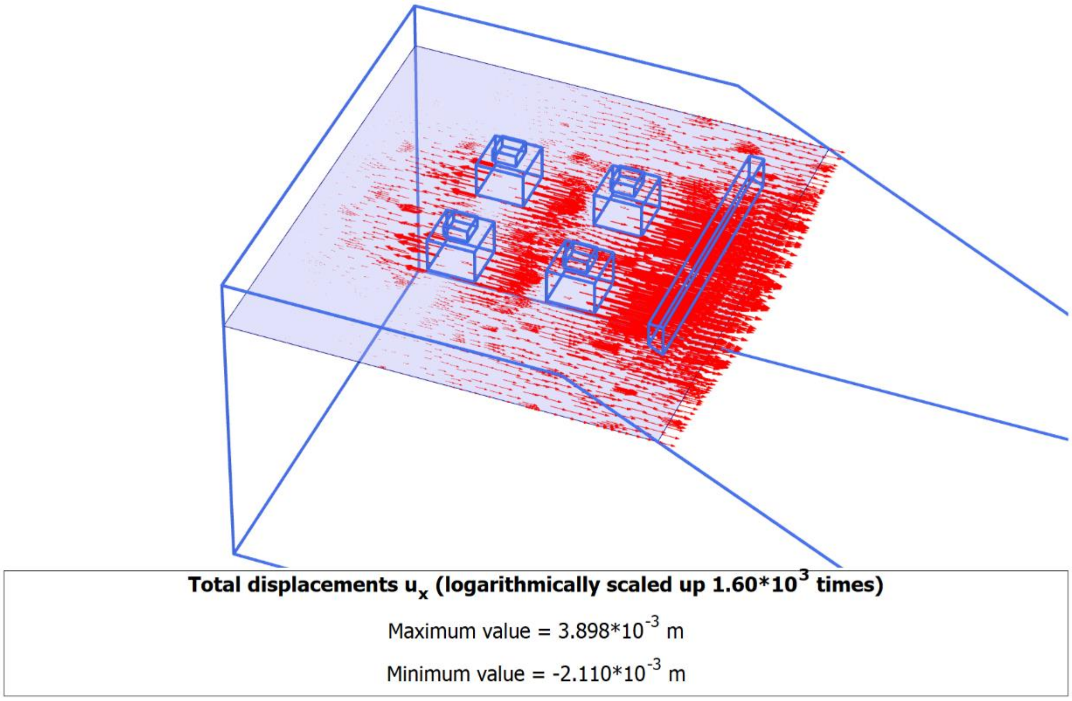
Total displacements u_x (logarithmically scaled up $1.60*10^3$ times)
Maximum value = $3.898*10^{-3}$ m
Minimum value = $-2.110*10^{-3}$ m

(a)

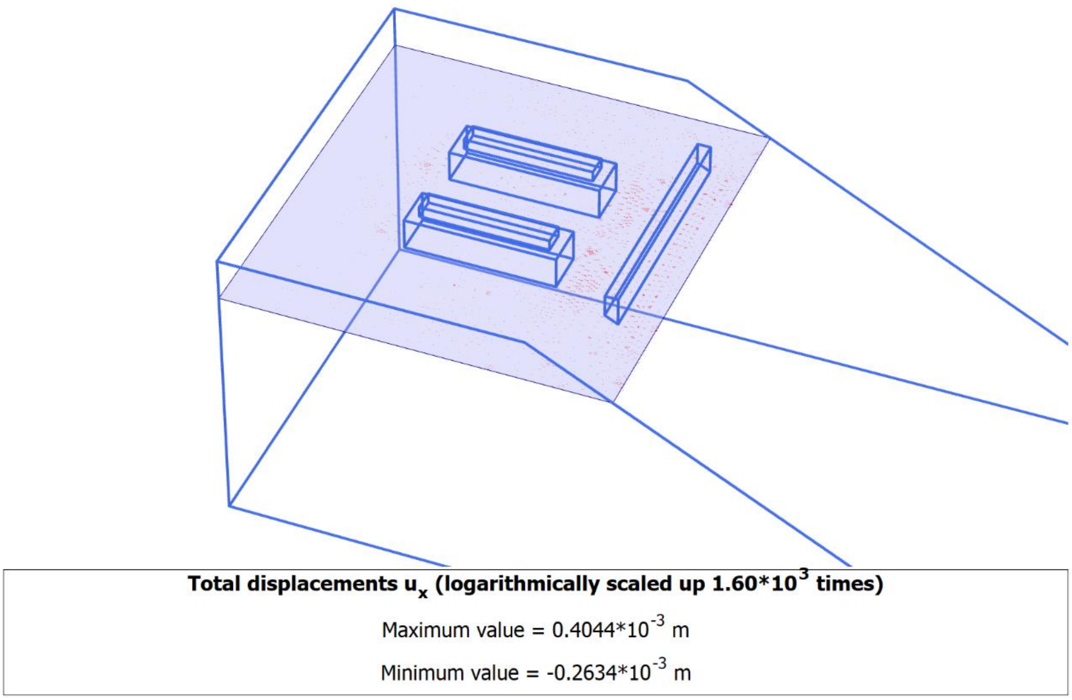
Total displacements u_x (logarithmically scaled up $1.60*10^3$ times)
Maximum value = $0.4044*10^{-3}$ m
Minimum value = $-0.2634*10^{-3}$ m

(b)

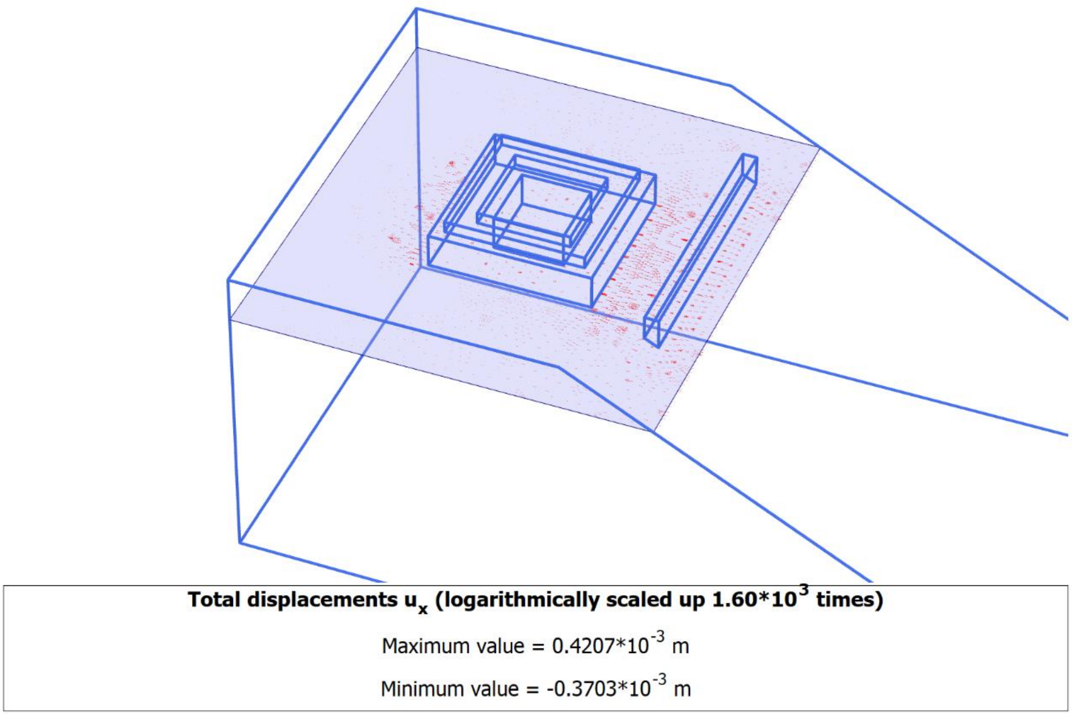

(c)

Fig. 7.6 Total displacement towards the slope face, generated in a typical section of slope passing through the base of the footing, originating due to various footing typologies in absence of toe cutting of hill-slope (a) F1 (b) F2 (c) F3

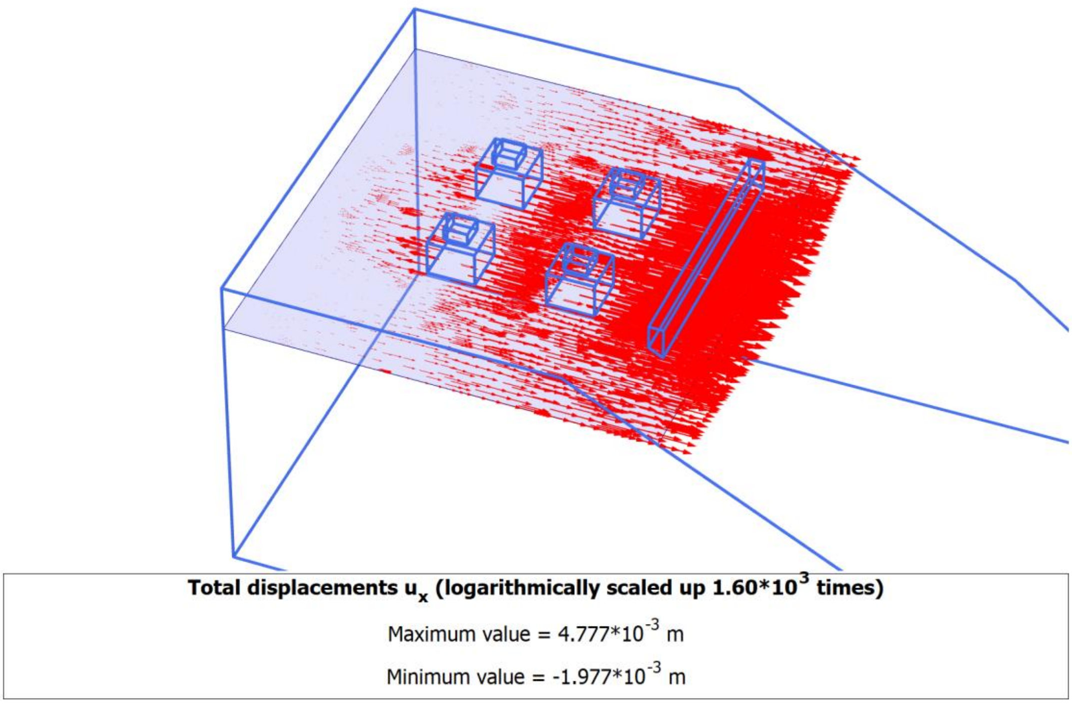

(a)

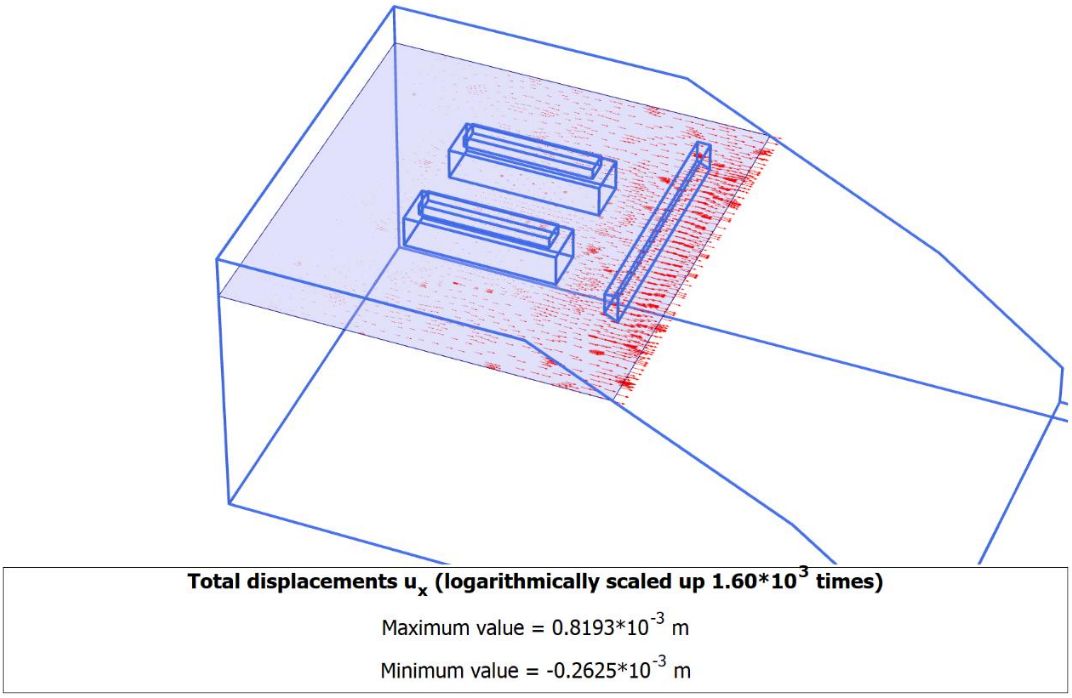

(b)

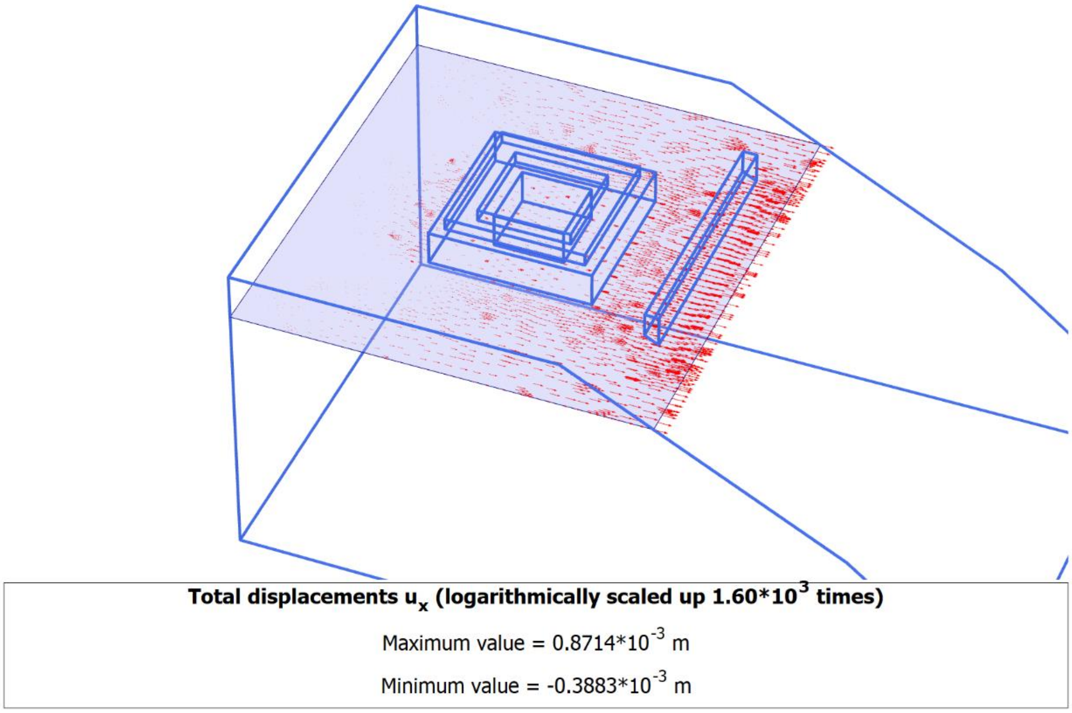

(c)

Fig. 7.7 Total displacement towards the slope face, generated in a typical section of slope passing through the base of the footing, originating due to various footing typologies in presence of toe cutting of hill-slope (a) F1 (b) F2 (c) F3

Figure 7.8 exhibits the total vertical stress generated at a typical section through the base of the footings supporting the electric transmission tower, resting on the hill-slope without any toe cutting. It can be observed that isolated footing arrangement F1 produces the maximum vertical stress owing to the smallest contact area of the individual footings. The rectangular arrangement F2 and the grid arrangement F3 produces the reduced vertical stress owing to higher contact area and larger dissipation of the superstructure load. Similar observation is made when the hill-slope is subjected to toe-cutting; however, for the sake of brevity, the same is not presented here. Thus, it is recommended to interconnect the footings so that the stresses transferred from the superstructure to the foundation soils also are reduced.

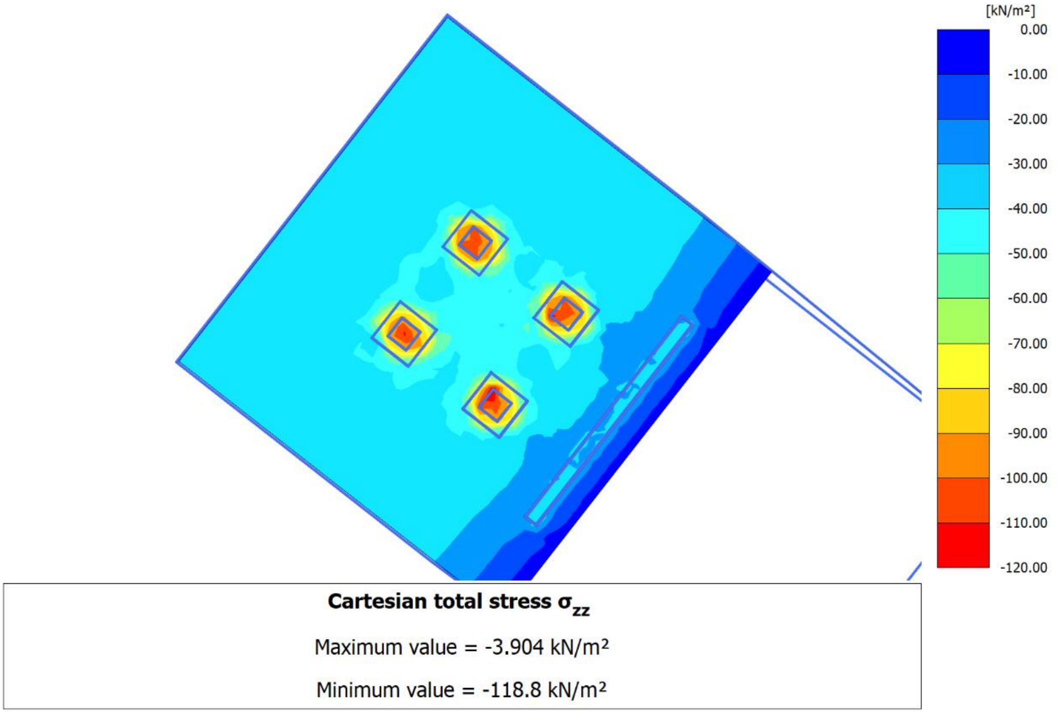

(a)

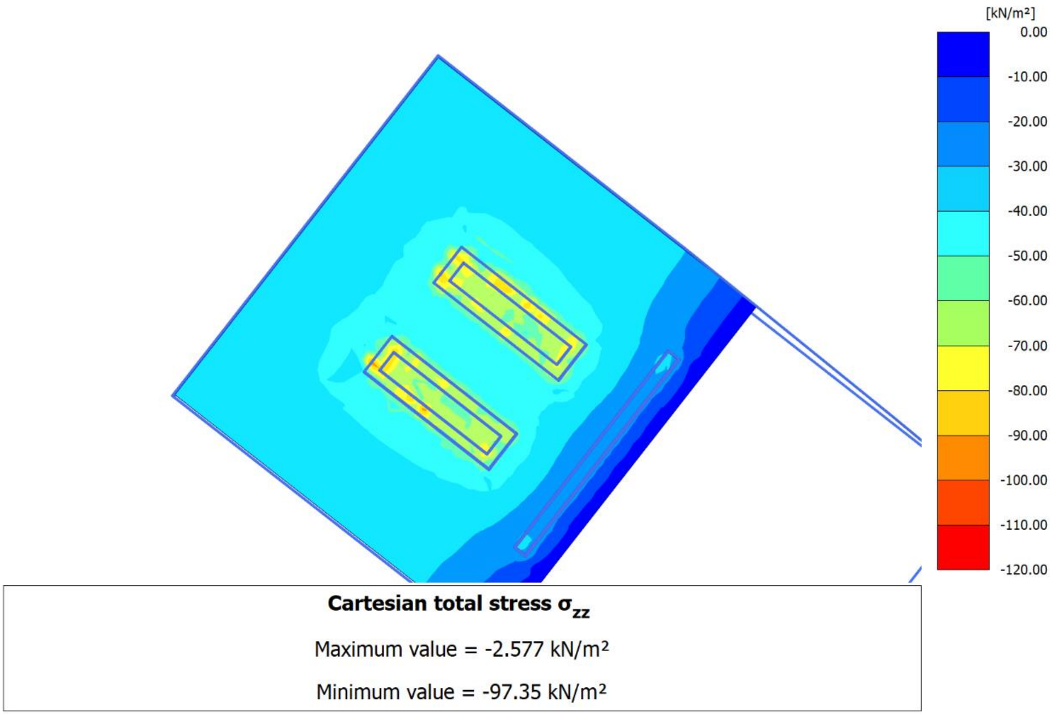

(b)

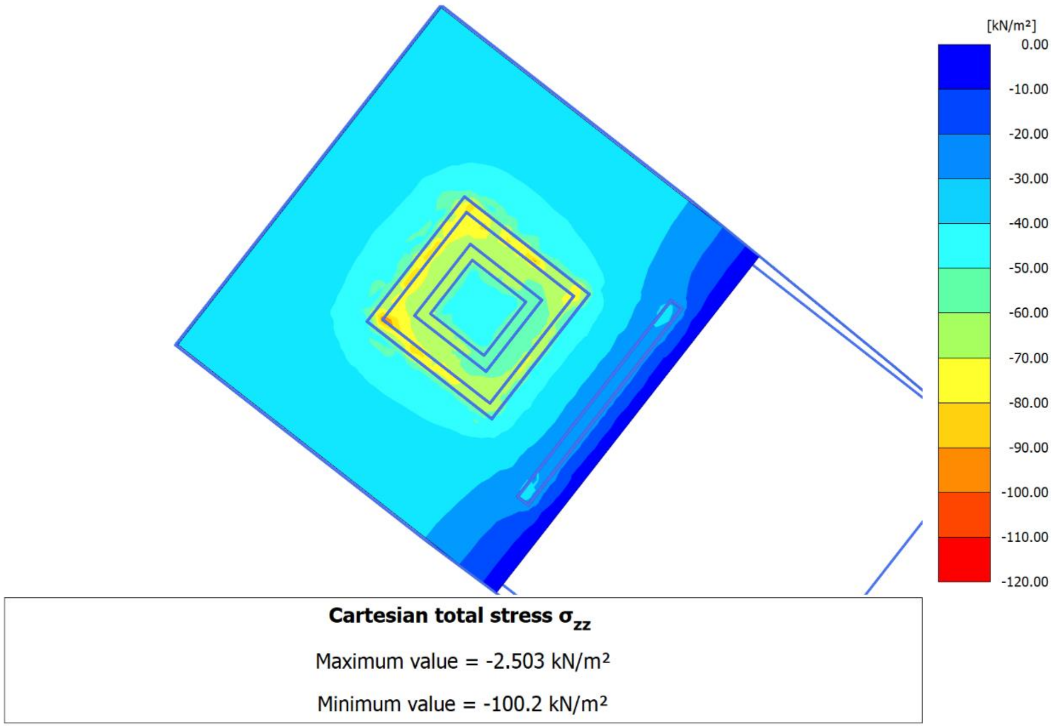

(c)

Fig. 7.8 Total vertical stresses generated in a typical section of slope passing through the base of the footing, originating due to various footing typologies in absence of toe cutting of hill-slope (a) F1 (b) F2 (c) F3

As a consequence of toe cutting, Fig. 7.9 exhibits the total lateral stress towards the slope face, generated at a typical section passing through the base of the footings supporting the electric transmission tower. It can be observed that F1 exhibits the maximum area of large outward horizontal stress towards the slope face, while F3 exhibits it as the least stresses generated. Although the magnitude of maximum lateral stress generated for F2 is the higher than F1, as observed earlier, the area of the section exhibiting higher stresses for F2 is lower as compared to F1. The observations based on vertical and horizontal stresses well conform to the observations made earlier with respect to the displacements. Based on the current findings, it is recommended to use interconnected footings for foundations on slopes, which leads to simultaneous reduction of stress transferred to the foundation as well as generates lesser outward deformation toward the slope face.

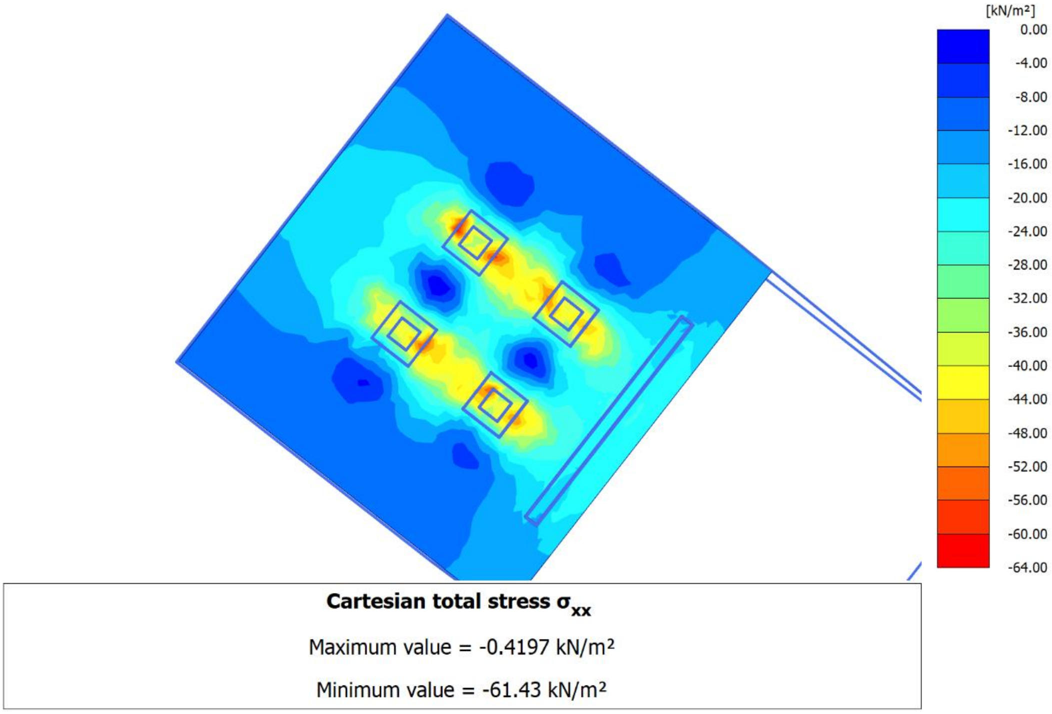

(a)

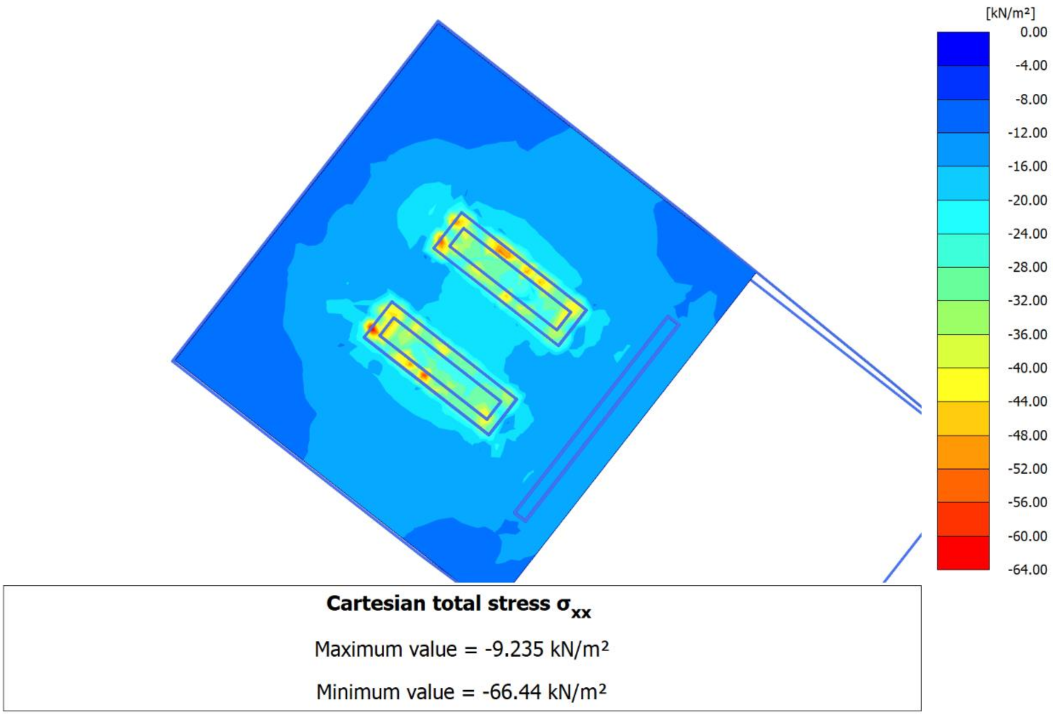

(b)

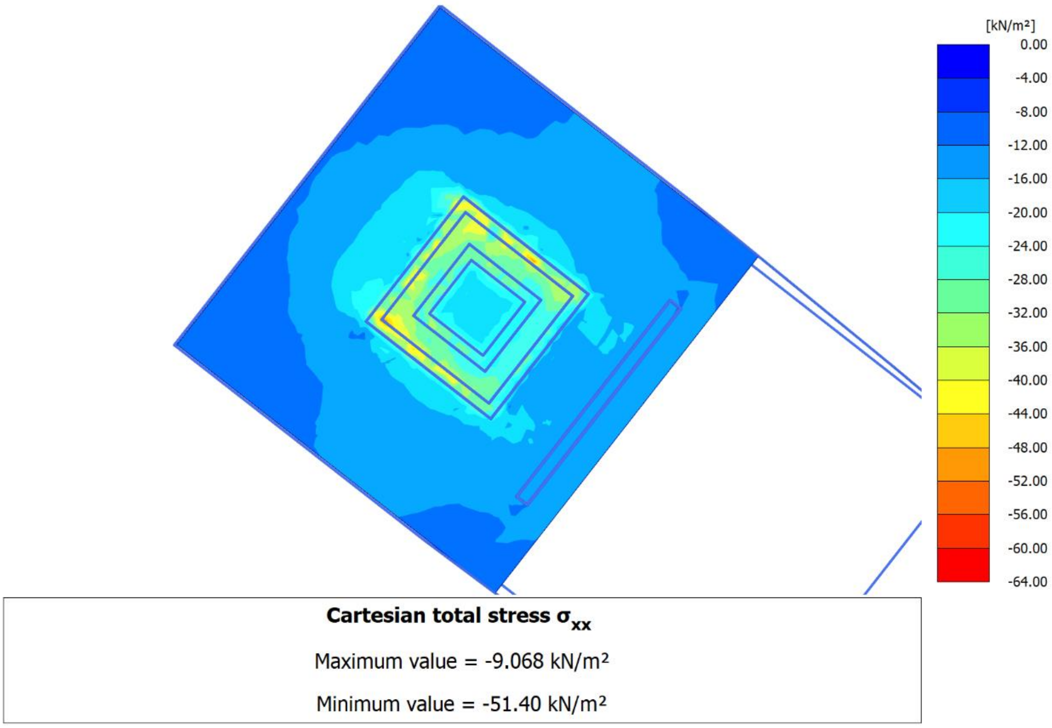

(c)

Fig. 7.9 Total vertical stresses generated in a typical section of slope passing through the base of the footing, originating due to various footing typologies in presence of toe cutting of hill-slope (a) F1 (b) F2 (c) F3

Figures 7.10 and 7.11 depict the incremental displacement mechanism developed beneath the footings of the transmission tower resting on fully saturated slope. The developed mechanism is hereby illustrated for two footing typologies F1 and F2, considering both pre- and post-toe cutting scenarios. When the pre- toe-cutting scenario is considered (Fig. 7.10a and Fig. 7.11a), it can be observed that in comparison to F1, a larger bearing zone is created beneath F2, and a larger volume of foundation soil is involved in producing the resistance to failure.

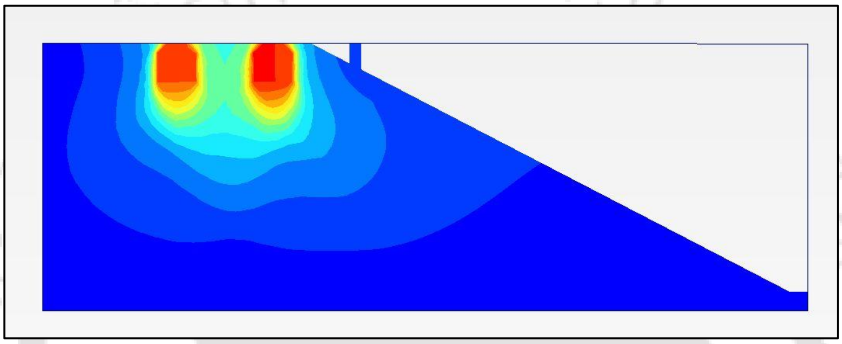

(a) Incremental displacement before toe cut for isolated square footings

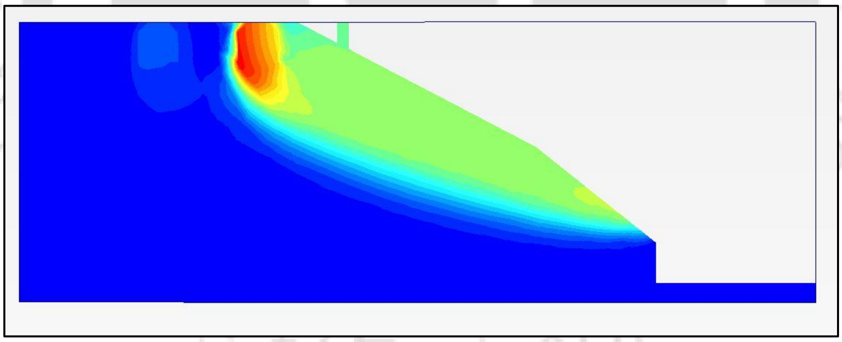

(b) Incremental displacement after toe cut for isolated square footings

Fig. 7.10 Typical failure mechanism of the hill-slope supporting an electric transmission tower resting on isolated square footing (Arrangement F1) (a) Before toe cutting (b) After toe cutting

The mobilization of the shear resistance of this larger volume of soil leads to the enhancement in the bearing capacity. Similar observation can be made for the post- toe-cutting scenario (Fig.

7.10b and Fig. 7.11b), wherein a larger soil mass forms the passive resistance zone, thus leading to greater resistance against the slope failure. Further, from the incremental displacement mechanisms, it can be ensured that for the present case study, the failure has taken place mainly because of the toe cutting, and hence, the failure primarily confirms a slope stability failure rather than a foundation failure.

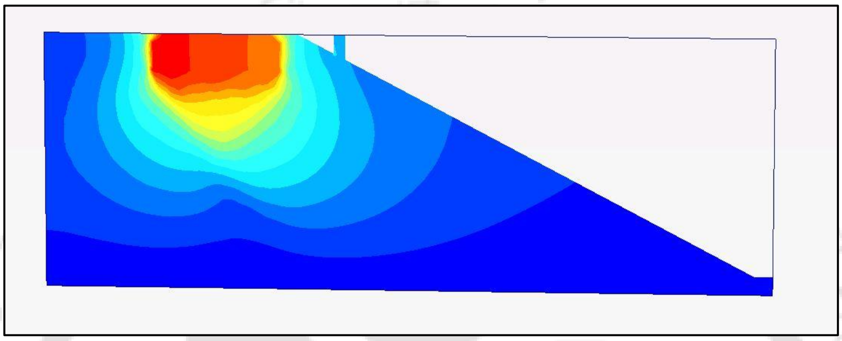

(a) Incremental displacement before toe cut for rectangular footing

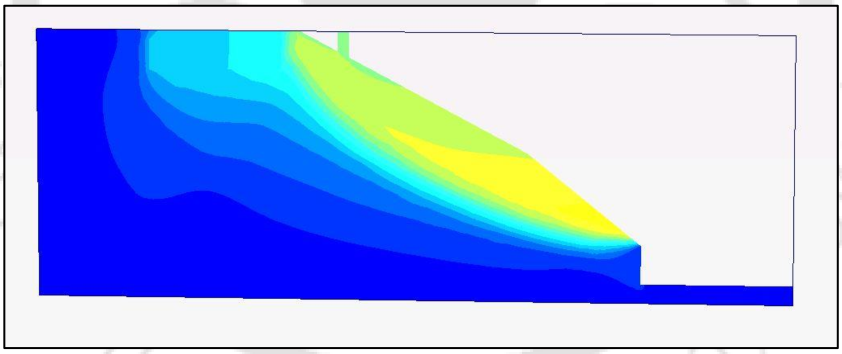

(b) Incremental displacement after toe cut for rectangular footing

Fig. 7.11 Typical failure mechanism of the hill-slope supporting an electric transmission tower resting on rectangular footing (Arrangement F2) (a) Before toe cutting (b) After toe cutting

7.3 Load Carrying Capacity of Different Footing Arrangements for Common Residential Buildings on Hill-slopes

Based on the explanations and discussions of the mechanisms associated with the case study as elaborated earlier, the current section illustrates the different footing arrangements that can be chosen as alternatives for common residential buildings constructed on hills-lopes so that a higher bearing capacity can be ensured. Several footing typologies are investigated, specifically 2×2 and 3×3 arrangements of the square footings, and customized arrangements created out of their interconnections. For each of the different combinations, the bearing load has been estimated. In the current simulation, a constant setback distance (b) of $0.5B$, embedment depth (D_f) of $0.5B$, and spacing between footings (S) of $1.5B$, have been considered (B is the width of square footing). A c-φ soil has been considered for the simulation, the properties of which have been tabulated in Table 7.3. The footing properties have been provided in Table 7.2.

Table 7.3 Soil properties used in assessing the building loads of various footing types

Type of soil	Unit weight (γ) (kN/m^3)	Modulus of elasticity E(MPa)	Cohesion (c) (kPa)	φ (°)
Foundation soil	17	20	20	30

7.3.1 2×2 arrangement of square footing and its various interconnections

In this study, 2×2 square footings, each of size 2 m x 2 m, has been interconnected in various patterns to create various combinations of combined footings (Fig. 7.12), which have been considered for the estimation of its bearing capacity through the FE analysis. The footings are considered to rest on the crest of a hill slope of height 5 m. Several slope inclinations have been considered in the analysis. In all the simulations, centric vertical loading has been considered, and the footing systems have been led to failure.

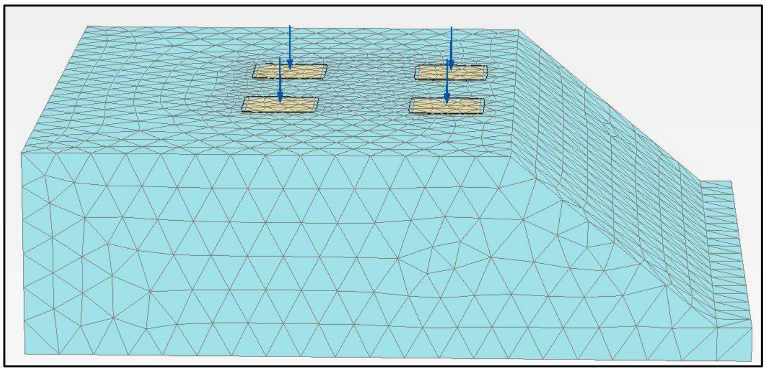

(a) 2×2 isolated square footings on slope crest (Arrangement 2S-I)

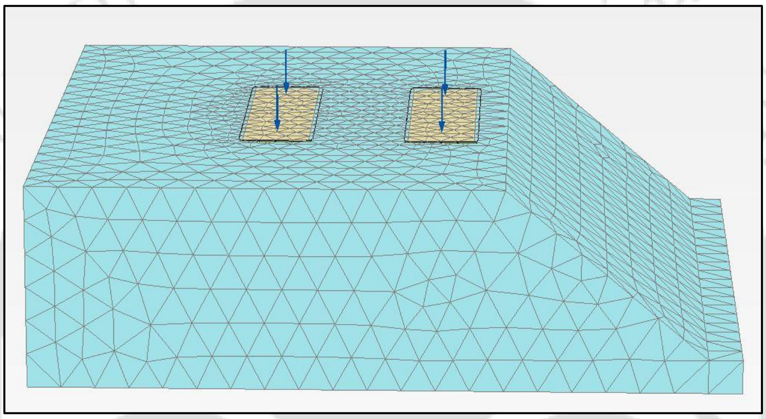

(b) Rectangular footings formed by connecting square footings parallel to the slope face (Arrangement 2S-R1)

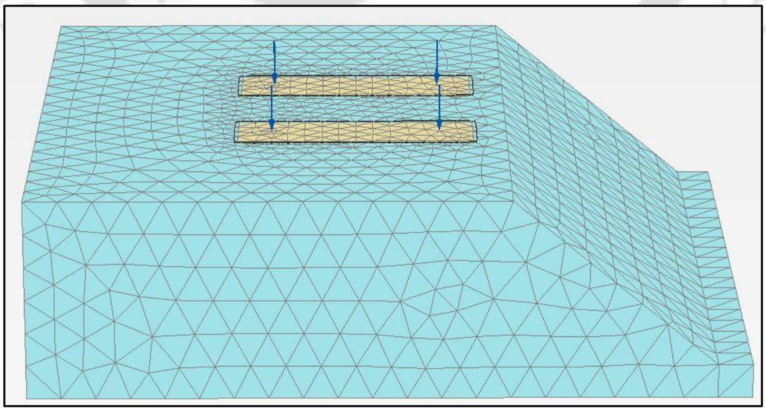

(c) Rectangular footings formed by connecting square footings perpendicular to the slope face (Arrangement 2S-R2)

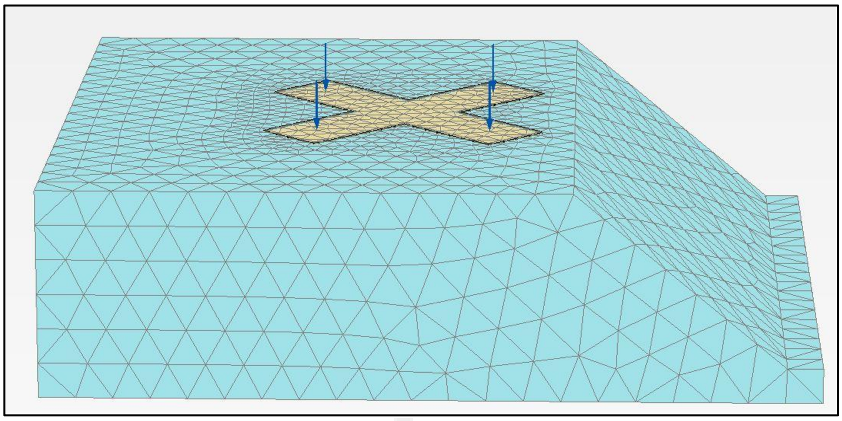

(d) Crossed rectangular footings formed by connecting square footings located opposite to each other (Arrangement 2S-C)

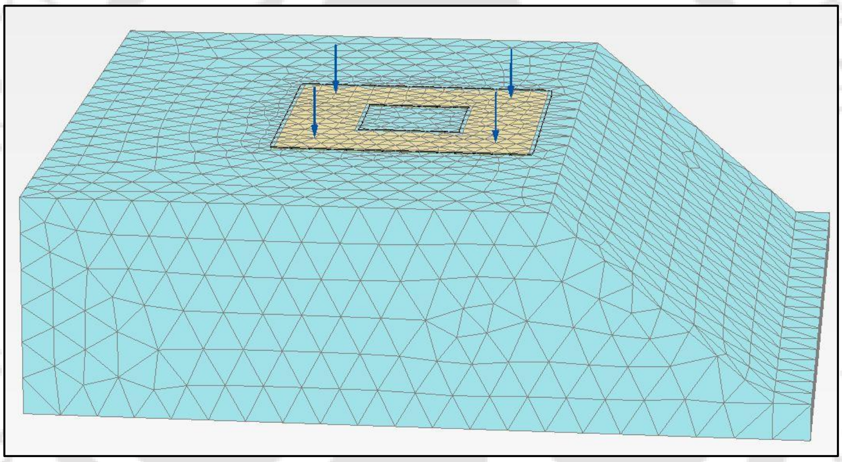

(e) Grid footings formed by connecting all the square footings (Arrangement 2S-G)

Fig. 7.12 Various footing typologies comprising of 2×2 square footings and their various combinations

Table 7.4 portrays the load bearing capacity of different 2 × 2 arrangements of the square footings and their various interconnected forms. The load carrying capacity of different arrangements has been checked for different slope angles (β). The slope angle has been varied from 10° to 40°. It has been observed that the grid footing made by connecting all the square footings (2S-G) possess maximum load carrying capacity than any other arrangements. It is perceived from Table 7.4 that rectangular footings perpendicular to slope face (2S-R2) shows higher load carrying capacity than isolated square footings or the rectangular footings located parallel to slope face (2S-R1). This is attributed to the fact that when rectangular footings are arranged parallel to slope face (2S-R1), higher length of footing interacts with the slope face leading to a bigger active zone of outwards lateral displacement towards the slope face. Such phenomenon reduces the bearing capacity of such arrangement in comparison to the case when rectangular footings are located perpendicular to the slope face (2S-R2). For the latter case, much lesser soil volume participates in the formation of sliding zone towards the slope face. Further, the perpendicularly placed rectangular footings drives its resistance from the far end of the same, thus exhibiting a higher bearing capacity. It is seen from Table 7.4 that the load carrying capacity of cross-connected rectangular (2S-C) footing and footing connecting isolated square footings (2S-G) are more than isolated square footings and rectangular footings. It confirms the fact that as the footing area increases, the load on the footing will spread over the larger area in the subsoil, thereby increasing the bearing capacity.

Table 7.4 Load carrying capacity of various arrangements of 2×2 square footings

Footing typologies obtained from 2×2 arrangement		Slope inclination (β^o)			
		10°	20°	30°	40°
		Load carrying capacity (MN)			
2S-I		10.05	8.13	6.09	4.06
2S-R1	PLAXIS FE	12.6	9.48	6.68	4.41
	ANN	15.4	11.6	8.2	5.4
2S-R2		14.39	13.65	12.38	10.10
2S-C		20.23	17.94	14.79	10.96
2S-G		24.32	21.33	17.46	12.39

Further, for the arrangement 2S-R1, Table 7.4 lists the comparative magnitudes, which shows appreciable agreement. The minor deviations in the magnitudes is primarily attributed to the shape effect of footings: ANN prediction expressions pertain to strip footing, while FE study effectively used rectangular footing. This difference in shape creates a different 3D stress distribution beneath the footing, resulting in the observed difference.

7.3.2 3×3 arrangement of square footing and its various interconnections

Similar to the earlier arrangements, in this section, 3×3 square footings, each of size 2 m × 2 m, has been interconnected in various patterns to create various combinations of combined footings (Fig. 7.13) and investigated for their bearing capacity. As earlier, the footings are considered to rest on the crest of a hill slope of height 5 m. Several slope inclinations have been considered in the analysis. In 3×3 arrangements, different combinations have been taken into account in the numerical study, specifically square footings, strip footings, connected square footings, as well as rectangular, strip and raft footings. In all the simulations, centric vertical loading has been considered, and the footing systems have been led to failure.

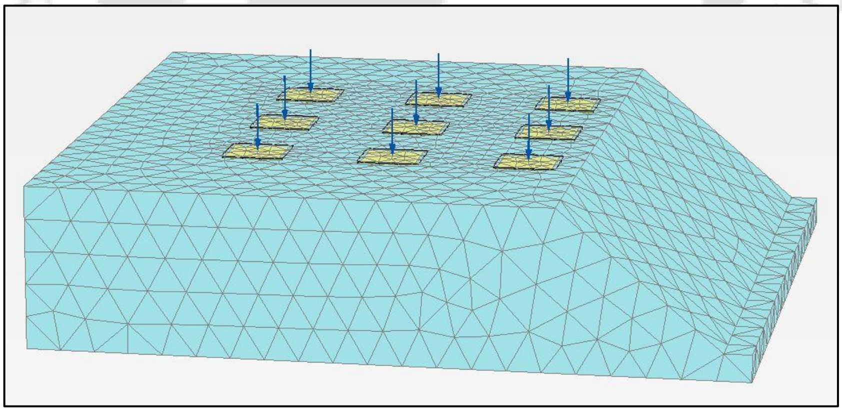

(a) 3×3 isolated square footings on slope crest (Arrangement 3S-I)

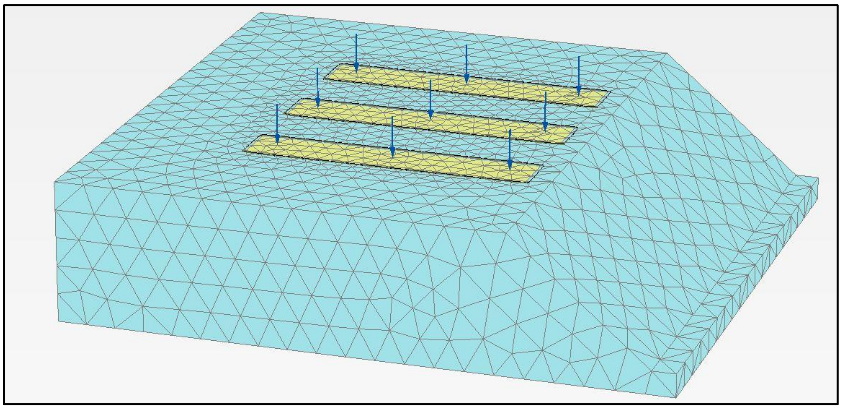

(b) Strip footings formed by connecting square footings perpendicular to the slope face (Arrangement 3S-S)

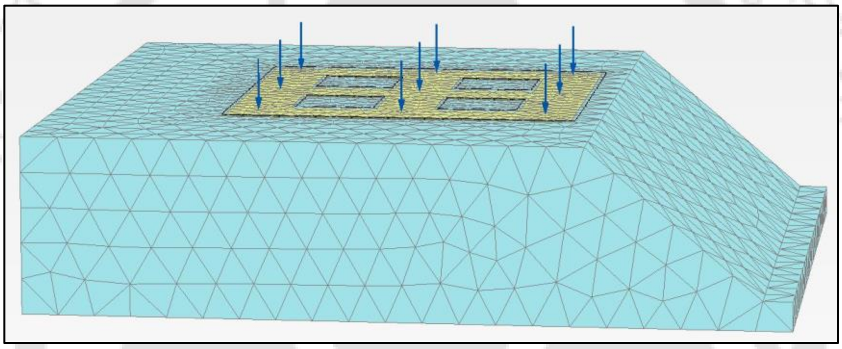

(c) Grid footings formed by connecting square footings (Arrangement 3S-G)

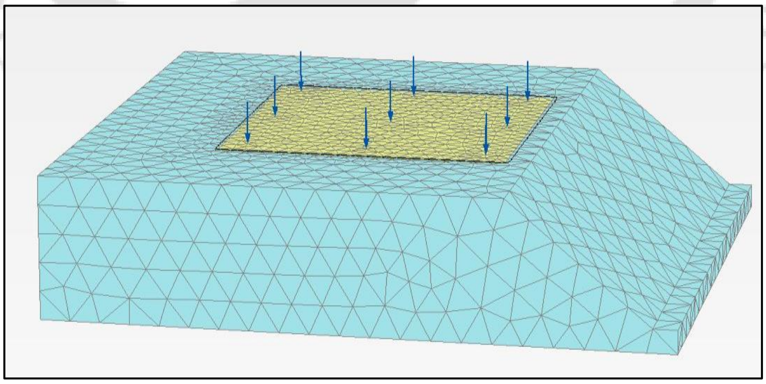

(d) Raft footing formed by connecting all square footings (Arrangement 3S-R)

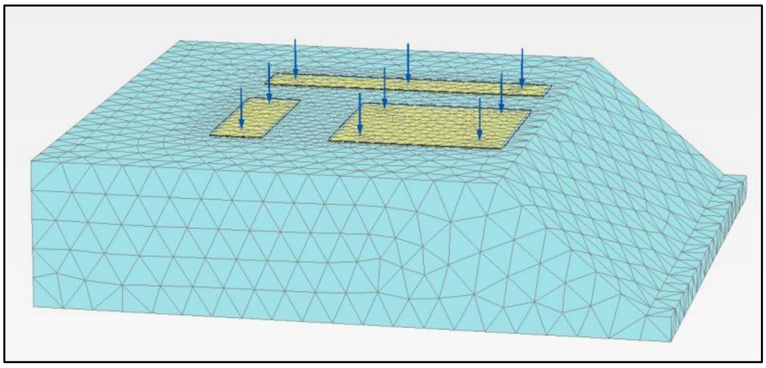

(e) Mixed interconnection to develop combined arrangement of raft and strip footings parallel and perpendicular to slope face (Arrangement 3S-S1-S2-R)

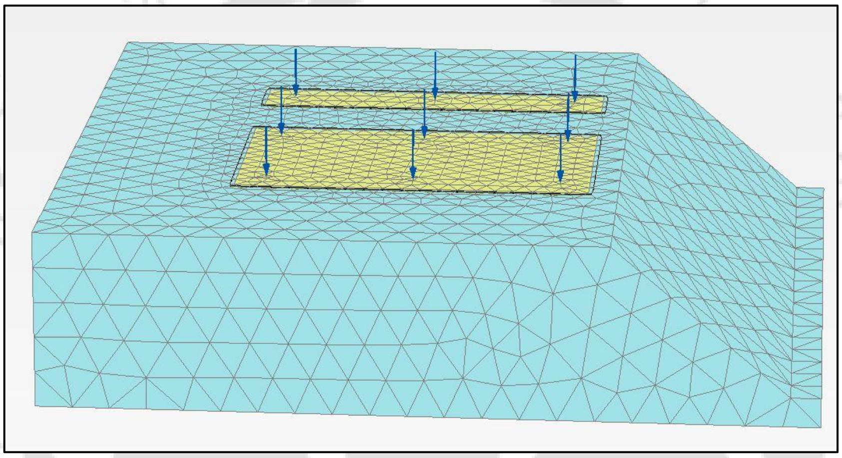

(f) Mixed interconnection to develop combined arrangement of raft and strip footings perpendicular to slope face (Arrangement 3S-S2-R)

Fig. 7.13 Various footing typologies comprising of 3×3 square footings and their various combinations

Table 7.5 depicts the load bearing capacity of different 3 × 3 arrangements of the square footings and their various interconnected forms. It is observed that raft (3S-R) footing having maximum load carrying capacity than all other arrangements used in the simulation. Increase of load bearing capacity confirms the fact that a greater footing width involves a larger soil domain to support the incumbent load. It is observed that the load carrying capacity of strip footings (3S-S) is more than isolated square footing (3S-I). It is perceived that the load bearing capacity marginally varies for Arrangement 3S-S, Arrangement 3S-S1-S2-R and Arrangement 3S-S2-R. It has been revealed that the load carrying capacity of footing connected all square footing is more than isolated square footings (3S-I), or for arrangements 3S-S1-S2-R and 3S-S2-R.

Table 7.5 Load carrying capacity of various arrangements of 3×3 square footings

Footing typologies obtained from 3×3 arrangement	Slope inclination (β^o)			
	10°	20°	30°	40°
	Load carrying capacity (MN)			
3S-I	11.87	9.59	7.07	4.58
3S-S	17.77	16.81	15.46	13.41
3S-S1-S2-R	17.81	17.57	16.69	14.02
3S-S2-R	19.13	18.46	17.42	15.60
3S-G	47.85	42.57	35.12	24.04
3S-R	65.48	52.91	38.90	28.24

7.4 Summary

In the present investigation, a case study has been taken into account to analyse the stability of an electric transmission tower resting on crest of sloping ground, supported on isolated square footings. A forensic study is conducted with the aid of FE simulations to identify the root cause of impending failure of the structure, which was recognized as the toe cutting of the hill-slope. Further, different alternative footing typologies were used to check the possibility in enhancing the bearing and deformation resistance of the system. It was understood that presence of interconnecting the footings placed near the slope crest with those located away from the slope crest would provide a tieback mechanism and generate more restraint against free outward and lateral deformation towards the slope face. Further, the increased area of the footing due to the interconnection, the increase in the footing area reduces the stress transferred to the foundations, thus also aiding in increase of the bearing capacity of the foundations on slopes.

Further, in order to investigate the influence of coexistence of the multiple footing typologies on the load carrying capacity, as commonly experienced in closely spaced habitations in the hill-slopes, the study is enhanced to consider various arrangements of 2×2 and 3×3 square footings and their interconnections. It is noted that raft footing exhibits maximum bearing capacity than any other arrangements. Based on this study, it is also prescribed to interconnect footings to enhance their load carrying capacity and resistance against deformation towards slope.

CHAPTER 8

INFLUENCE OF DILATANCY ON FAILURE MECHANISM OF STRIP FOOTING RESTING ON HORIZONTAL AND SLOPING GROUND

8.1 General

This chapter reports about the finite element based numerical analysis of the failure mechanism developed beneath a strip footing resting on horizontal and sloping ground. The observed failure mechanism is manifested in terms of incremental displacement and incremental deviatoric strain patterns. The evolution of failure mechanism is substantially affected by the shear dilatancy of the soil. In order to investigate the effect of dilatancy, both associated and non-associated flow rule had been considered in the present study.

The plastic flow of a material - gets governed by the rate of plastic strain increment tensor. In order to estimate the incremental plastic strain $\left(d\varepsilon_{ij}^{p}\right)$ generated within a stresses soil continuum, an assumption is made about the existence of a plastic potential function $g\left(\sigma\right)$ from which the plastic strain increment at current stress state (σ_{ij}) is evaluated by Eq. 8.1.

$$d\varepsilon_{ij}^{p} = \lambda \frac{\partial g}{\partial \sigma_{ij}} \tag{8.1}$$

where, g is the plastic potential, and λ is a scalar multiplier whose magnitude defines the magnitude of plastic strain. The gradient of the plastic potential $\frac{\partial g}{\partial \sigma_{ij}}$ defines the direction of plastic flow, which is essentially normal to the plastic potential. Such flow rule is termed as non-associated flow rule.

For the elastic-perfectly-plastic Mohr-Coulomb model, and similar class of constitutive models, where the plastic potential function is represented by the yield function $\left(\text{i.e. } g = f\right)$, the flow rule is represented as Eq. 8.2.

$$d\varepsilon_{ij}^{p} = \lambda \frac{\partial f}{\partial \sigma_{ij}} \tag{8.2}$$

where, the gradient of the yield function, $\frac{\partial f}{\partial \sigma_{ij}}$, indicates that as per the normality rule, the direction of plastic flow is along the normal to the yield surface. Such flow rule is represented as associated flow-rule.

In the case of associated flow rule, since the yield function represents the plastic potential, there remains no control on the dilatancy, i.e. the evolution of plastic volumetric strain during shearing and hence, the angle of dilatancy is considered equal to the angle of internal friction $\left(\text{i.e. } \psi = \varphi\right)$. However, in case of considering non-associated flow rule, the flow becomes normal to the plastic potential, whose slope can be lesser than the yield function of the M-C model. In such case, the angle of dilatancy becomes less than the angle of internal friction $\left(\text{i.e. } \psi < \varphi\right)$. The angle of dilatancy is defined as the ratio of the components of the gradient of plastic potential in the *p'*-*q* space, as shown in the corresponding figure.

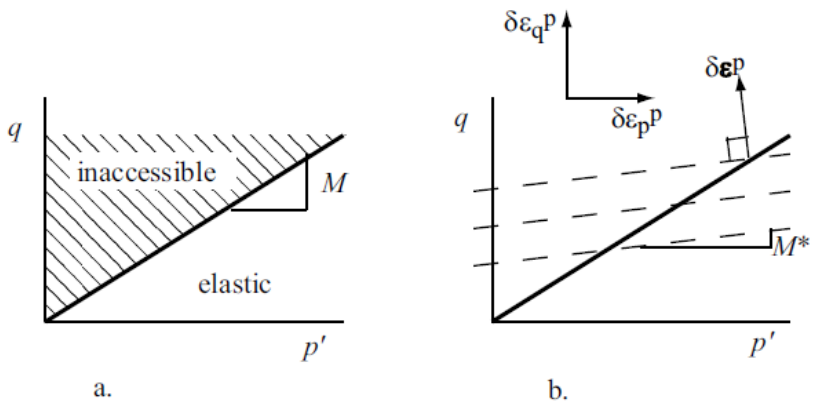

Fig. 8.1 Elastic-perfectly plastic Mohr-Coulomb model (a) yield or failure locus (b) plastic potentials (Wood, 2004)

Plasticity theory indicates that, if the dilatancy angle is not similar to the angle of internal friction, the material follows non-associated flow rule (Xiao-Li et al. 2007). The dilatancy angle varies from zero to the soil friction angle. Similarly, dilative coefficient η, which relates the dilatancy angle to soil friction angle, is defined by Eq. 8.3.

$$\eta = \psi / \varphi \tag{8.3}$$

Where, φ is the soil friction angle and ψ is the dilatancy angle. Theoretically, the value of dilative coefficient is $0 \leq \eta \leq 1$. The situation $\eta = 1$ indicates the material follows an associated flow rule. For a coaxial non-associated flow rule, if the soil mas is assumed to follow Mohr-Coulomb failure criterion, the following relationships (Eq. 8.4 and Eq. 8.5) can consider the dilatancy of the material.

$$\tan\varphi^{*} = \tan\varphi \frac{\cos\psi \cos\varphi}{1 - \sin\psi \sin\varphi} \tag{8.4}$$

$$c^{*} = c \frac{\cos\psi \cos\varphi}{1 - \sin\psi \sin\varphi} \tag{8.5}$$

where, c is the cohesion in the Mohr-coulomb failure, c^{*} and φ^{*} are the modified cohesion and friction angle.

A series of simulation on foundation models have been carried out to examine the influence of mesh refinement schemes, shape of mesh element and soil shear strength properties on the failure mechanism. The numerical outcomes have been verified against experimental investigations available in literature. It has been observed that angle of dilatancy (ψ) plays a significant role in influencing the evolution of the failure mechanism.

8.2 Strip Footing Resting on Horizontal Ground

As already elaborated in Chapter 3, PLAXIS 3D Finite Element (FE) simulation has been conducted for a strip footing resting on horizontal ground. This particular section illustrates the characteristic response of footing resting on a non-dilatant sandy soil following non-associative flow rule (ψ = 0). As it is imperative that the response of FE numerical models is strongly influenced by the mesh configuration (shape and coarseness), the influence of mesh parameters on the evolution of failure mechanism has been investigated. A convergence study has been conducted to decide for an optimum meshing scheme that would provide in order to arrive at a reliable estimate of the characteristic response of the foundation.

8.2.1 Typical failure mechanism obtained from FE simulation

Figure 8.2 represents the typical failure mechanisms developed beneath a rough strip footing resting on non-dilatant medium dense sandy soil (φ = 30°, γ = 17 kN/m^3, E = 20 MPa), represented in terms of the incremental displacement and incremental deviatoric strain contours. Based on analyses conducted using non-associated flow rule (ψ = 0°), it is noted that even when the footing is resting on the horizontal ground and is subjected to a vertical centric load, the footing exhibits tilting (rigid rotation) during its failure, exhibited by the asymmetric formation of the incremental displacement and incremental deviatoric strain patterns. Conventional bearing capacity theories illustrate otherwise, wherein the development of the failure zones are always assumed symmetric for symmetric geometry and loading conditions, as exhibited in Fig. 8.3. As per the ultimate bearing capacity theories, the slip lines represent the path of mobilized stress in the foundation soil at the verge of failure. For a numerical analysis, the same is represented by the developed incremental deviatoric strain contours. It is observed that the failure mechanism obtained from the FE simulation (Fig. 8.2) is different with respect to the conventional failure mechanisms (Fig. 8.3). Such difference may originate due to the influence of meshing schemes adopted in finite element simulation, or due to the dissimilar assumptions in considering the effect of dilatancy. This difference in the findings between the conventional theory and numerical simulation is further investigated and presented in the subsequent sections.

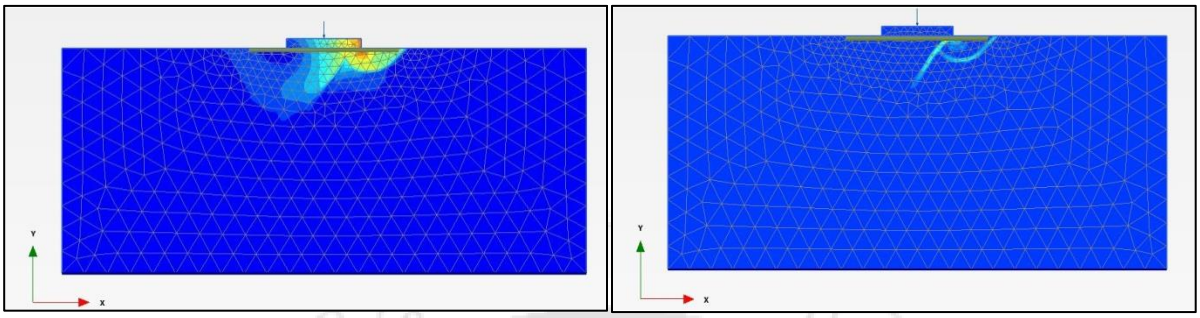

(a) (b)

Fig. 8.2 Typical failure mechanism developed beneath footing resting on medium dense sandy soil considering ‘Fine mesh’ (a) incremental displacement contours (b) incremental deviatoric strain contours

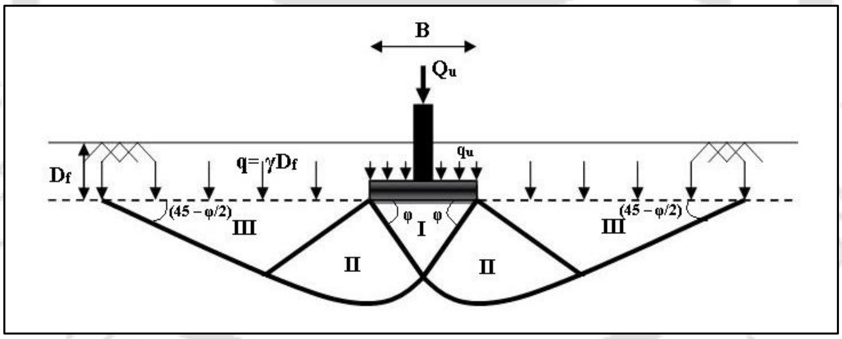

Fig. 8.3 Standard illustration of the classical failure mechanism developed beneath a shallow strip footing resting on a horizontal ground and undergoing general shear failure (as per Terzaghi 1943)

8.2.2 Influence of meshing scheme on results from FE analysis

It is well established that the outcome of any FE analysis will be governed by the mesh element size, which can be variedly adopted using different mesh refinement techniques. In order to further verify whether the asymmetrical failure mechanism is an outcome of the particular meshing scheme, supporting studies have been conducted on the same problem considering varied meshing schemes. In Plaxis 3D, the standard meshing schemes available are 'very coarse', 'coarse', 'medium', 'fine' and 'very fine', which are differentiated on the basis of their average element size (AES), arising from the adopted global refinement strategy. Local refinements have not been considered at the present stage of analysis. Figure 8.4 provides the results as obtained from the investigation for medium dense sand, which shows that independent of the adopted meshing scheme, the failure mechanism obtained beneath the footing resting on non-dilatant soil is always asymmetrical, in contradiction to the classical failure mechanism considering fully dilatant soil (Chen 2010). For a better portrayal of the progressive development of the asymmetric failure mechanism beneath the footing, Fig. 8.5 depicts the ratio of the maximum leftward to the maximum rightward incremental displacement of the footing for progressive loading on the footing, for two typical meshing schemes, namely 'Very coarse' and 'Fine'(others are not presented for the sake of brevity). For a symmetric development of the failure mechanism (resulting in symmetric rightward and leftward settlement), the ratio for successive loading stages would closely follow the magnitude of 1 (the horizontal black line passing through 1 represents ideal development of symmetric failure mechanism). However, it can be observed that for the present problem (considering two typical meshing schemes), the ratio for successive loading stages exhibit significant deviation from the symmetric phenomenon. Moreover, the ratio continuously switches on both sides of '1', indicating an oscillating footing deformation with monotonic load increase. This phenomenon has also been observed in similar experimental investigations, and has been termed 'Mode switching'. The phenomenon has been attributed to the alternating densification of sandy soil due to a larger deformation towards one side, leading to the switching of the larger deformation towards the opposite side of the footing in the successive loading cycle (Michalowski and Shi 2003).

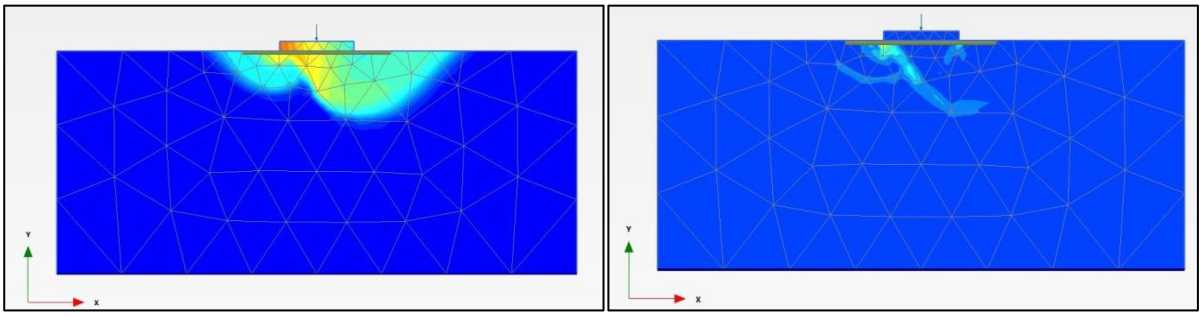

(a)

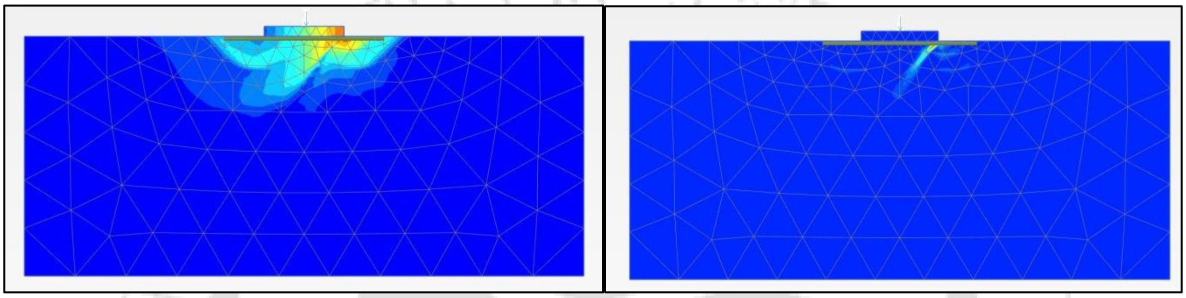

(b)

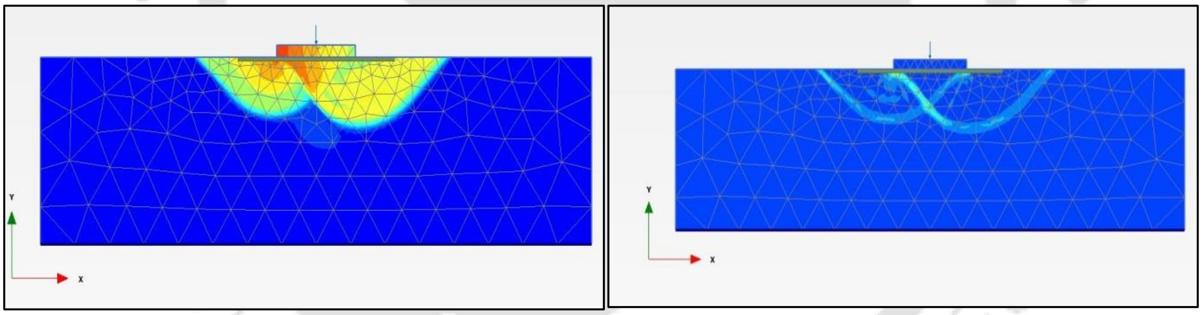

(c)

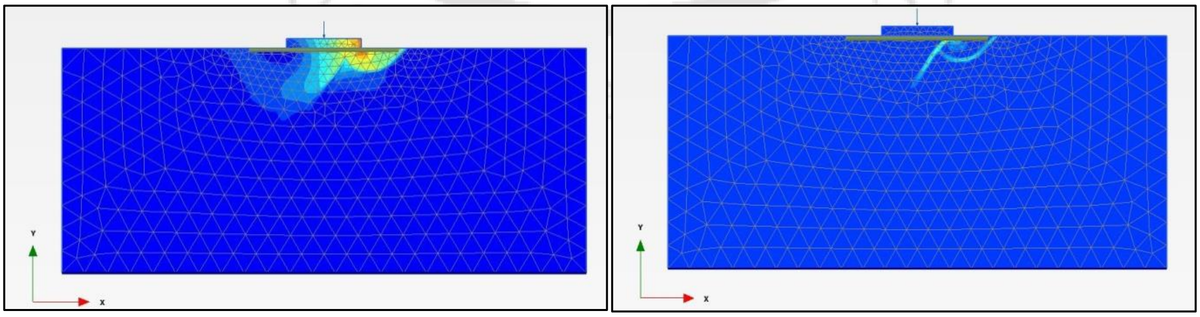

(d)

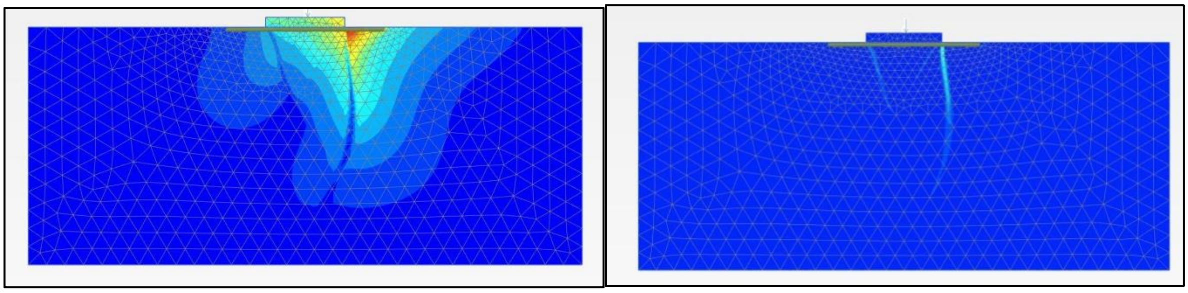

(e)

Fig. 8.4 Typical failure mechanism represented by incremental displacement and incremental deviatoric strain contours for medium dense sand based on different meshing schemes (a) Very coarse mesh (b) Coarse mesh (c) Medium mesh (d) Fine mesh (e) Very fine mesh

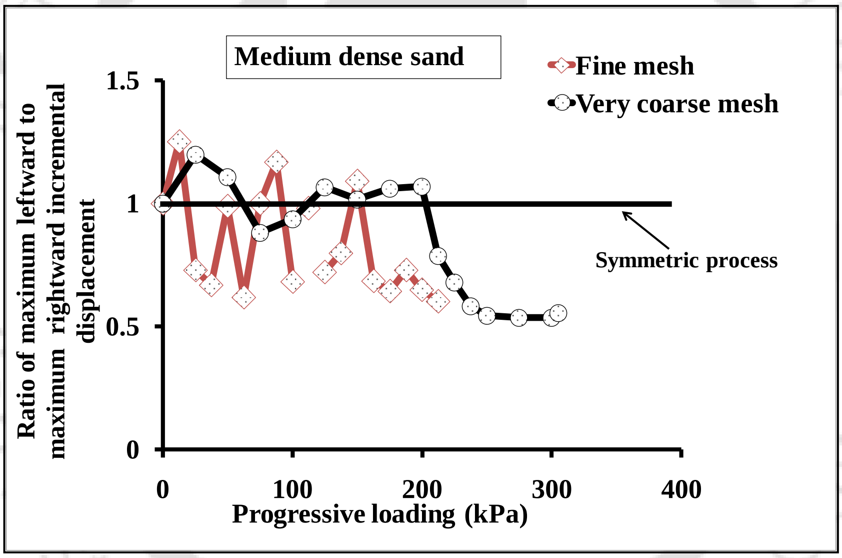

Fig. 8.5 Typical variation of the ratio of maximum leftward to maximum rightward incremental displacements with progressive loading of the footing resting on medium dense sand

8.2.3 Influence of mesh element type on the results of FE analysis

PLAXIS FE modelling allows adopting only triangular elements (either 6-noded or 15-noded). Moreover, the discretization of a problem domain into a set of FE mesh elements is auto-controlled by a scheme referred as ‘Robust triangulation technique’, which is beyond the scope of modification by the user. It has been noted that, even for a geometrically symmetric problem, the triangulation technique does not generate a perfectly symmetric mesh, and leaves a minor asymmetry in the developed mesh itself. Although in the PLAXIS manual (Reference Manual Plaxis 2D v2015.02) it has been stated to be a necessity, however, it was necessary to check whether the minor asymmetry in the developed mesh structure was actually instrumental in leading to the asymmetric behaviour. However, as PLAXIS does not allow for any other mesh or discretization technique, GeoStudio (another similar FE software suite) was resorted to check the issue. Despite having its own limitation in addressing complex geotechnical problems, GeoStudio v2007 (GeoStudio Manual 2007) offers a wide variety of mesh elements and meshing schemes for domain discretization. The present problem being a simple geotechnical verification problem, GeoStudio v2007 has been utilized to examine the influence of different structured mesh types (symmetric and asymmetric) on the obtained numerical solutions. Two different meshing schemes have been adopted, namely ‘Rectangular grid of Quads’ (a symmetric meshing scheme, Fig. 8.6a) and ‘Triangular grid of Quads/Triangles’ (an asymmetric meshing scheme, Fig. 8.6b). The remaining features (boundary conditions and model dimensions) of the numerical model adopted in GeoStudio FE model remains to be the same as that adopted for PLAXIS 2D FE model. Considering the above-mentioned meshing schemes, the response of the surface footing subjected to uniform load is reported in terms of deformed meshes and displacement vectors, as shown in Figs. 8.7a and 8.7b. It is observed that for both the cases, the failure mechanism of the footing exhibited an inadvertent tilting in one direction even after applying a symmetric loading. Figure 8.8 depicts the typical load-displacement characteristics of the two edges of the strip footing, which reveals that the displacement of extreme points (left and right) on both sides of the strip footing is noticeably different, indicating a tilt or rigid rotation of the footing.

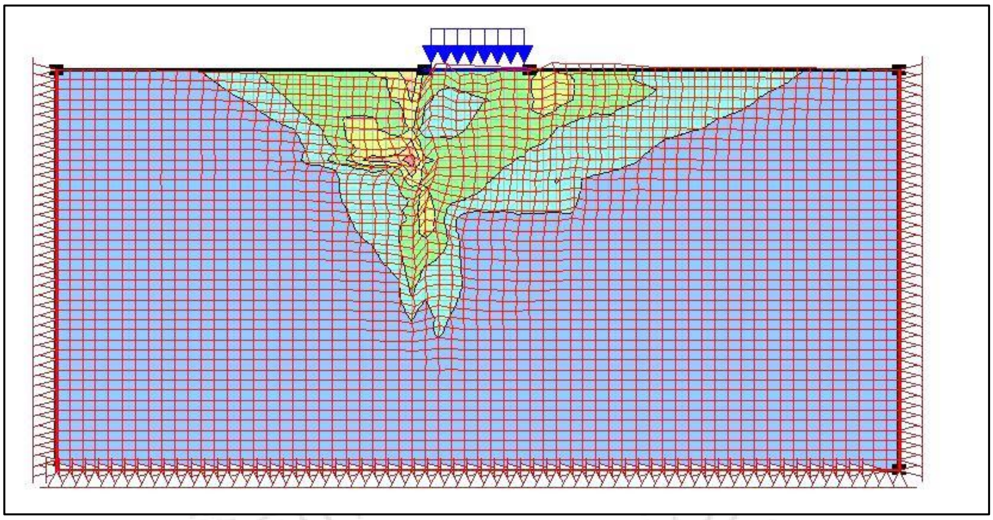

Fig. 8.6a Response of surface footing obtained using 'Rectangular grid of Quads' element: Mesh deformation from GeoStudio analysis

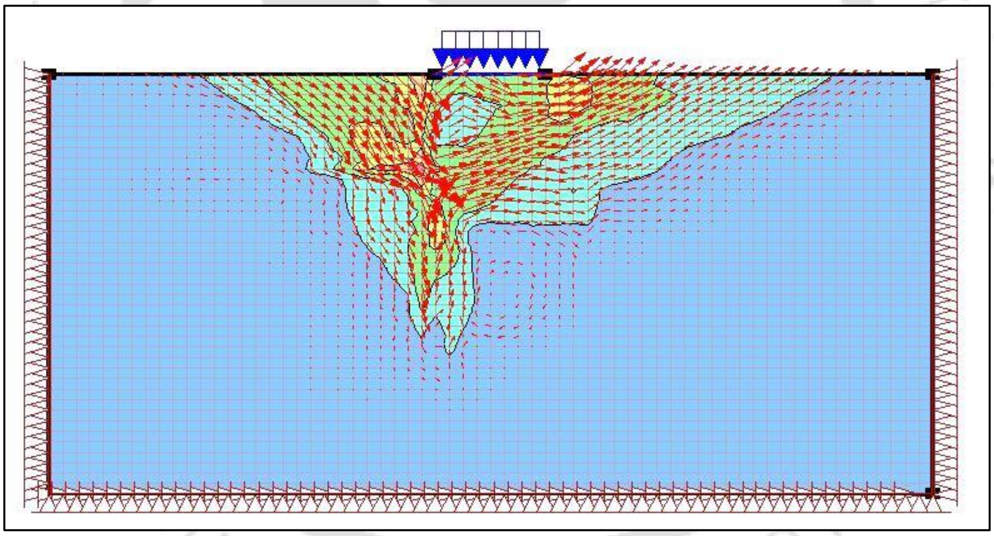

Fig. 8.6b Response of surface footing obtained using 'Rectangular grid of Quads' element: Displacement vector from GeoStudio analysis

From the stated qualitative and quantitative representations, it is understandable that the exhibition of asymmetric development of failure mechanism is independent of the meshing scheme, whether structured or unstructured, symmetric or asymmetric, and comprising triangular or rectangular elements, in any arrangement. The tilt or the rigid rotation of the footing, hence, can be considered as an inadvertent numerical representation of the physical mechanism associated with the stresses and strains developed progressively within the model domain during the FE simulation. The same will be explained in detail in subsequent sections.

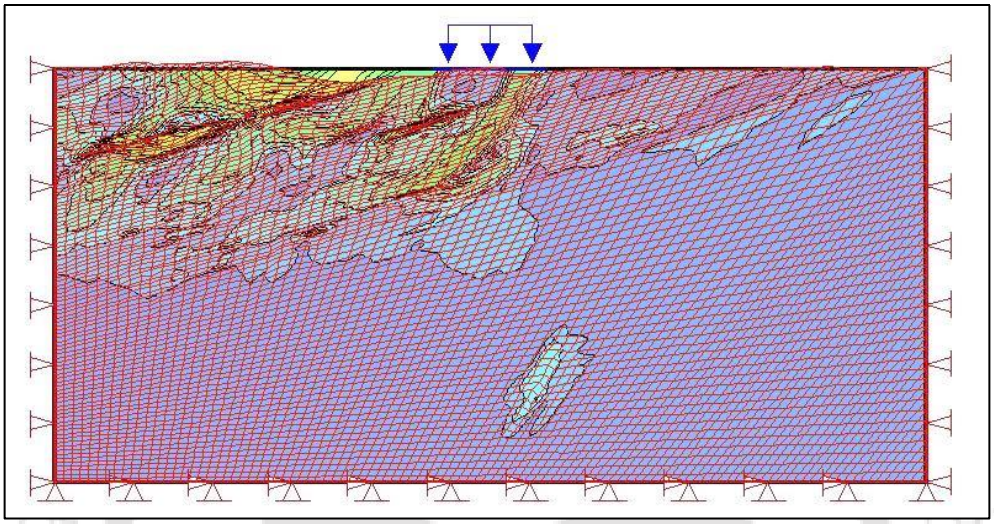

Fig. 8.7a Response of surface footing obtained using 'Triangular grid of Quads/Triangles' element: Mesh deformation from GeoStudio analysis

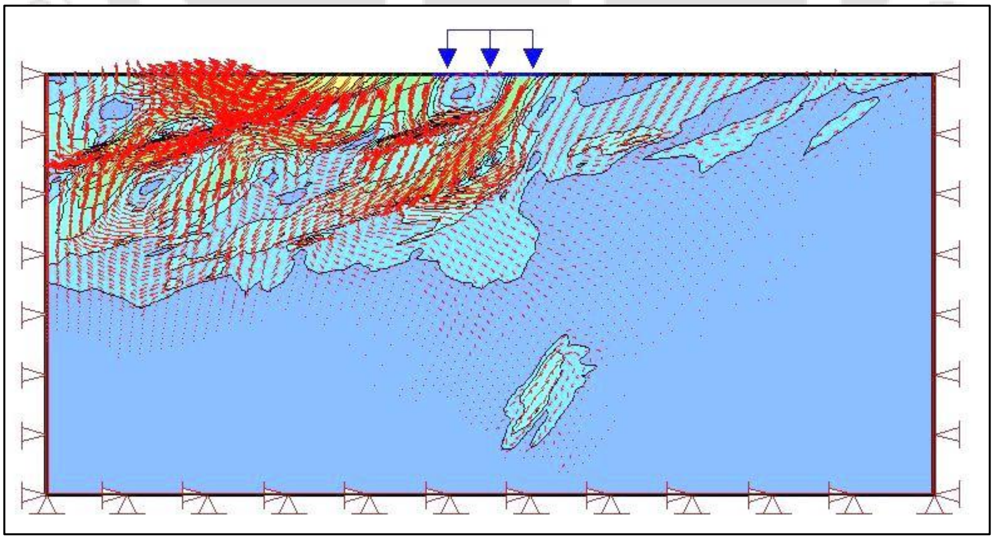

Fig. 8.7b Response of surface footing obtained using 'Triangular grid of Quads/Triangles' element: Displacement vector from GeoStudio analysis

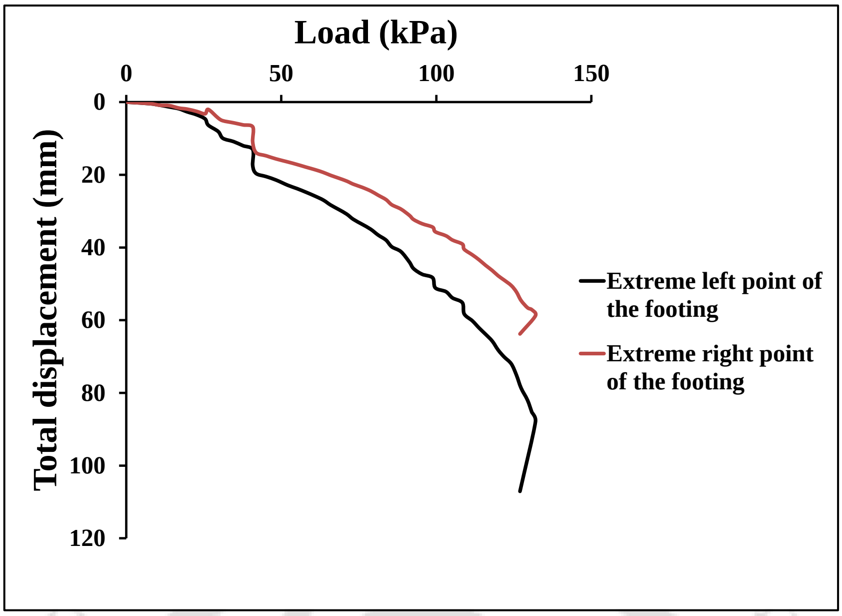

Fig. 8.8 Typical load-displacement pattern of extreme ends of the footing indicating differential settlement of footing

8.2.4 Convergence study to determine optimal meshing scheme

In order to identify the optimal meshing configuration for the numerical model, convergence studies had been carried out (considering different foundation soils). Five different meshing schemes, differentiated and represented by their non-dimensional average element length (defined as the ratio of the AES to the largest geometrical dimension of the model), have been investigated for their effect on the ultimate bearing capacity of the strip footing. To determine the non-dimensional mesh size, the largest dimension of the model for this study has been considered the width of the model, i.e. 14 m, which remains invariant for all the simulation scenarios. Figure 8.9 represents the result of a typical convergence study for a footing resting on a typical foundation soil comprising medium dense sand. It can be observed that the result is nearly identical for any mesh size lesser than fine mesh (conforming to non-dimensional average element length approximately 0.03); similar results have been obtained for other configurations as well; however, they are not presented here for the sake of brevity. Thus, for the further study adopted, ‘fine mesh’ is considered optimum, and the same has been used in further studies for footings resting on horizontal ground.

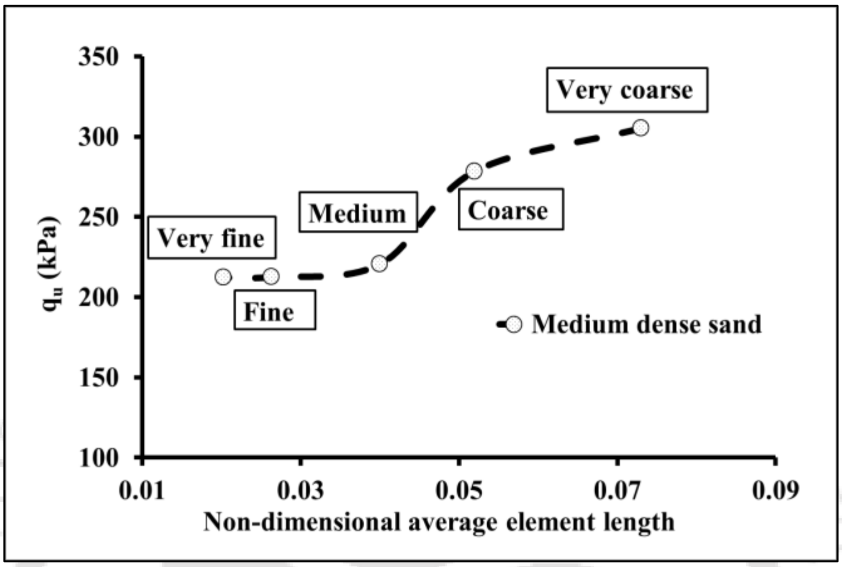

Fig. 8.9 A typical mesh convergence study for identifying the optimum mesh element size

8.2.5 Effect of soil characteristics on failure mechanism: Non-associated flow neglecting dilatancy

In order to check the effect of shear strength and stiffness characteristics of soil on the observed failure mechanism, typical categories of foundation soil have been considered beneath the footing, the characteristics of which are listed in Table 8.1.

The outcomes of the analyses have been presented in terms of total incremental displacement and incremental deviatoric strain (Fig. 8.10). For all the cases of foundation soil considered, the formation of the failure zones beneath the footing are found to be asymmetric for foundation soil following non-associated flow rule (ψ = 0°). This asymmetric development of failure mechanism is illustrated in Fig. 8.11 (a-b) for loose and dense sand (ψ = 0°), in terms of the ratio of the maximum leftward to the maximum rightward incremental displacements for successive load stages. Hence, it can be stated that the developed failure mechanism of a strip footing resting on horizontal ground will be inadvertently asymmetric. Conventionally, differential soil movements resulting in tilting and rotation of footing, when subjected to loading, are primarily dependent on the vertical displacement of the foundation soil. However, it is to be understood that the vertical displacements will always be associated with horizontal displacements due to volumetric changes in the foundation soil, and corresponding outward radial or horizontal shear displacement of the adjacent soil. This is exactly the phenomenon responsible for the formation of the radial shear zone beneath a footing when subjected to failure, and consequential occasional heaving of the soil adjacent to the footing. Depending on the degree of dilatancy of the foundation soil, there is a significant variation of the outward radial or shear displacement of the soil. Hence, it is always reasonable to consider the resultant displacement at any location in the foundation soil, which accounts for the resolved influences of horizontal and vertical displacement.

Table 8.1 Different types of foundation soil as used in the present investigation

Soil types	Cohesion (c) (kPa)	Angle of internal friction (φ)°	Unit weight (γ) (kN/m^3)	Modulus of elasticity (E_s) (MPa)	Poisson's ratio (ν)
Dense sand	0	40	19	40	0.3
Medium dense sand	0	30	17	20	0.28
Loose sand	0	20	16	15	0.25
c-φ soil	20	30	18	20	0.3

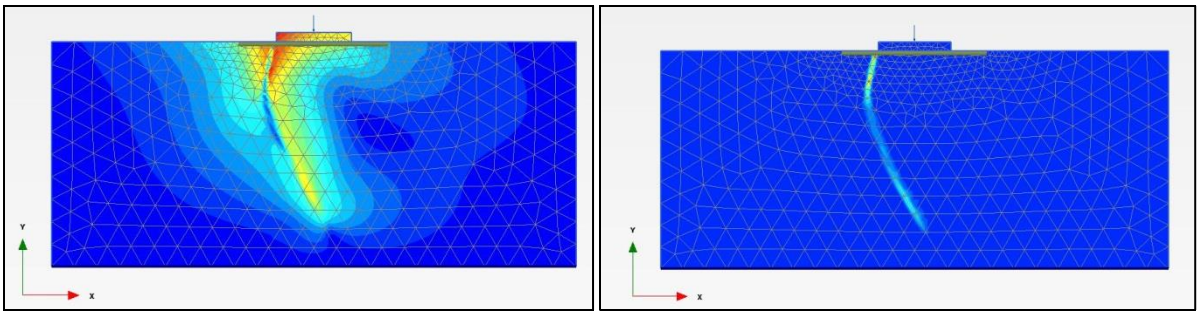

(a)

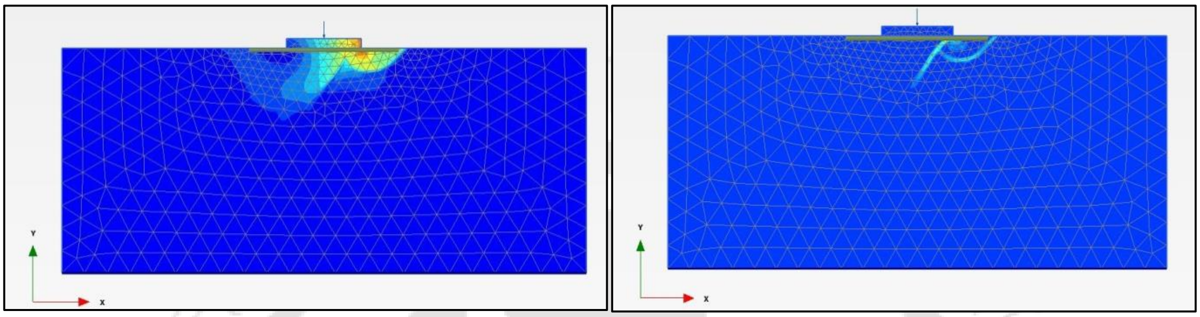

(b)

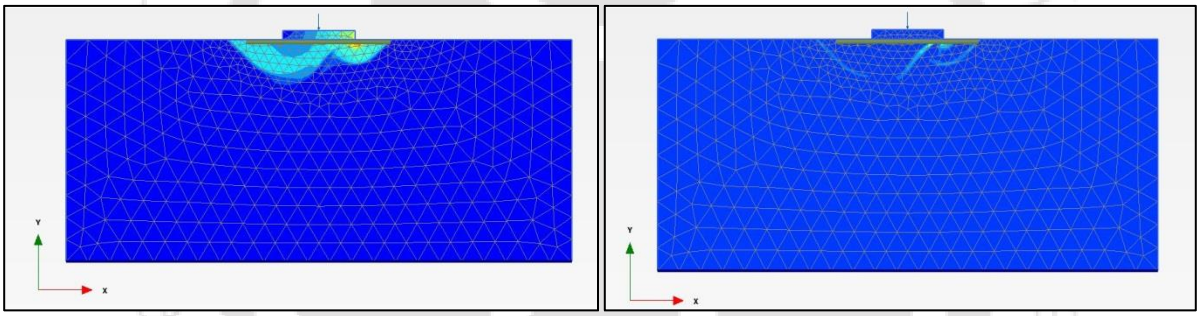

(c)

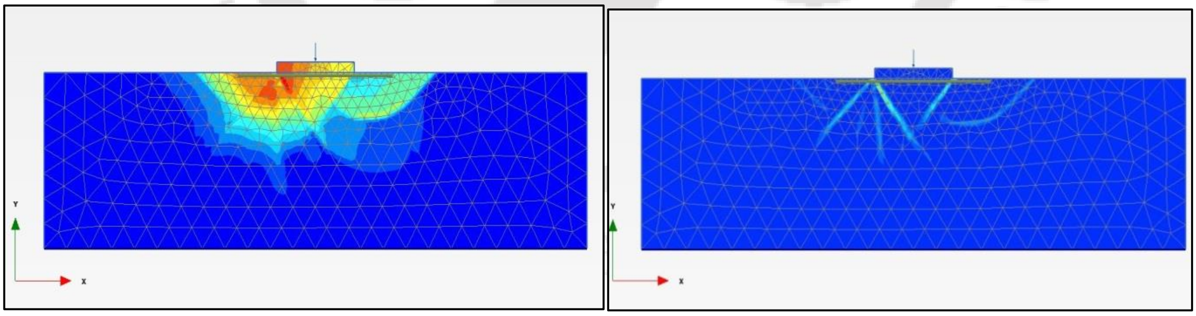

(d)

Fig. 8.10 Incremental displacement and incremental deviatoric strain for various soil types with ψ = 0°, considering fine mesh; (a) Dense sand (b) Medium dense sand (c) Loose Sand (d) *c*-*φ* soil

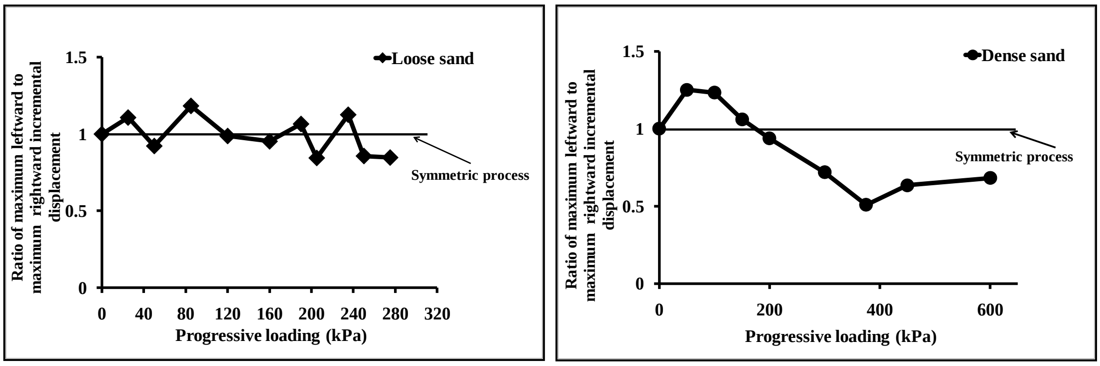

(a) (b)

Fig. 8.11 Typical ratio of maximum leftward to maximum rightward incremental displacements for non-dilatant soils (a) loose sand (b) dense sand

8.2.6 Failure mechanism considering varying flow rules: Effect of dilatancy of soil

Figure 8.12 depicts that the failure mechanism beneath the surface and embedded strip footing resting on horizontal ground is asymmetrical for foundation soils following non-associated flow rule ($\psi \neq \varphi$). It can be also noticed that with the increasing dilatancy angle (ψ), the shape of the slip lines beneath the footing becomes progressively symmetrical. As it has been seen for Terzaghi's bearing capacity theories for general shear failure, as shown in Fig. 8.3, exact symmetrical nature of the failure lines beneath the footing is obtained when the dilatancy angle attains the magnitude of angle of internal friction (φ). It has been perceived that the symmetric failure mechanism initiates beyond $\psi = 3\varphi/4$. Figure 8.13 illustrates the asymmetric behaviour of footing with varying angles of dilatancy of foundation soil. It is observed that for $\psi = 3\varphi/4$ and $\psi = \varphi$, the ratio of the maximum leftward to the maximum rightward horizontal displacement increments for progressive load increments conforms nearly to the symmetrical line, thus indicating the formation of symmetrical failure mechanism beneath the footing. Figure 8.13 also highlights that there is a prominent effect of non-associative flow rule in developing the asymmetrical formation of failure zones, the effect being exemplary for lower values of dilatancy angle.

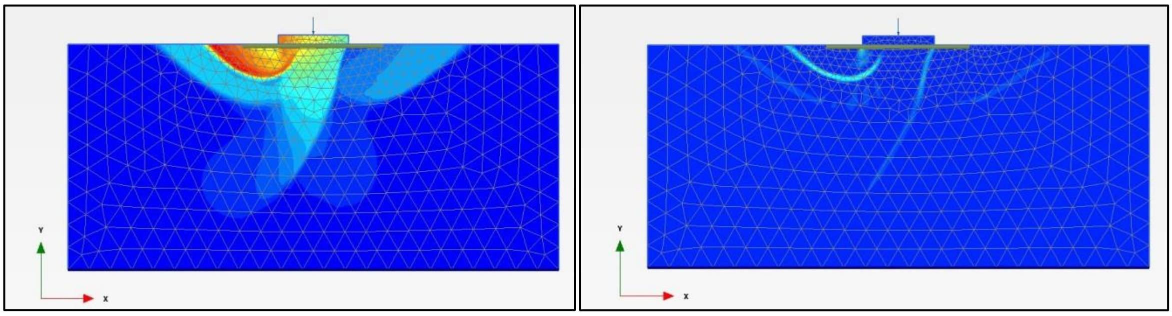

(a)

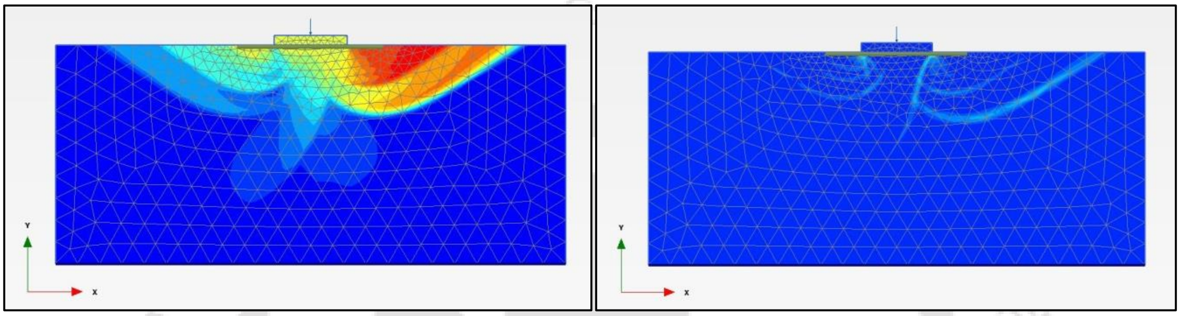

(b)

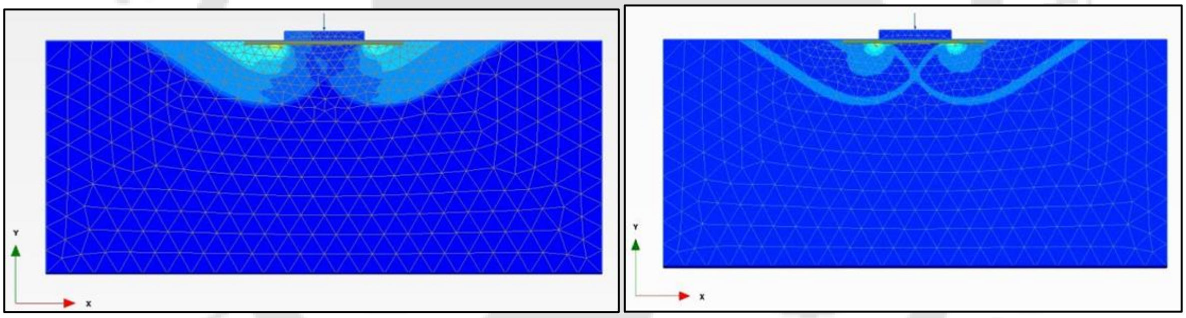

(c)

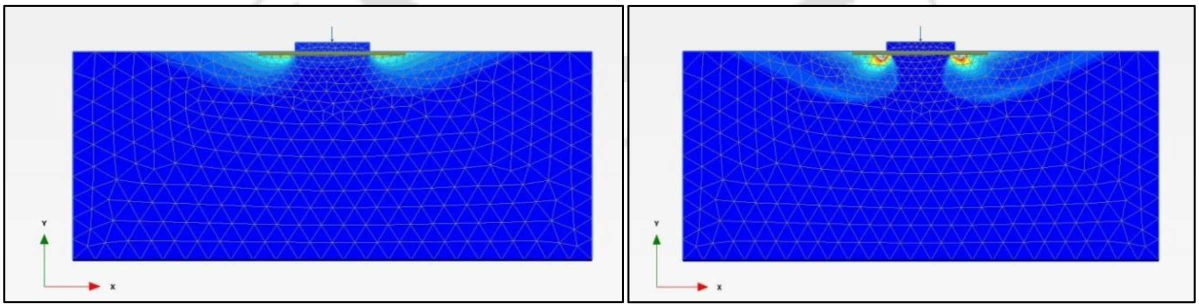

(d)

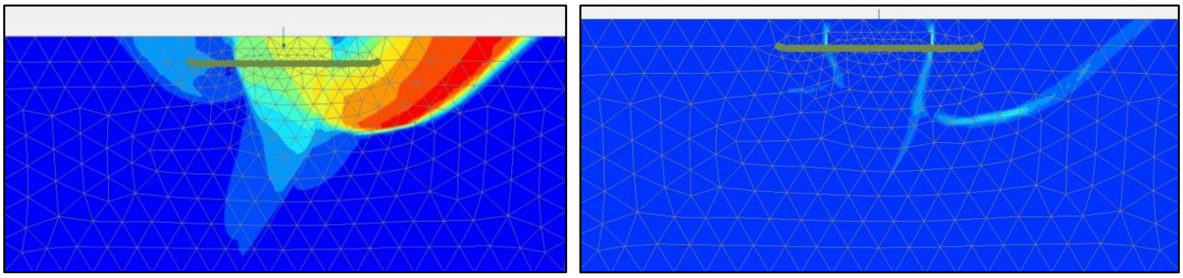

(e)

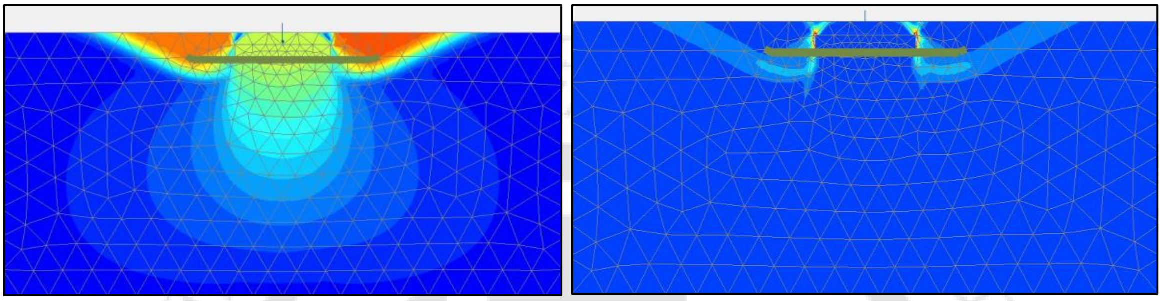

(f)

Fig. 8.12 Incremental displacement and incremental deviatoric strain for dense sand (a) $\psi = \varphi/4$ (b) $\psi = \varphi/2$ (c) $\psi = 3\varphi/4$ (d) $\psi = \varphi$; Embedded footings [$D_f/B = 0.25$] (e) $\psi = \varphi/4$ (f) $\psi = \varphi$

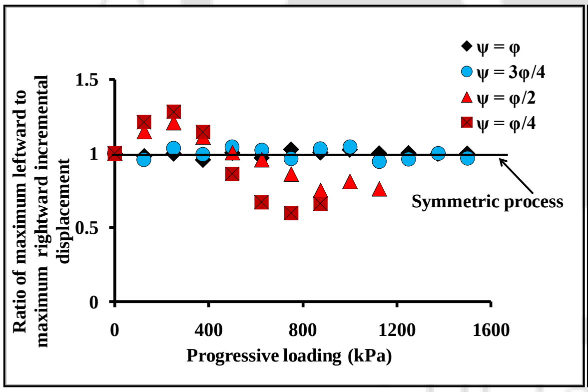

(a)

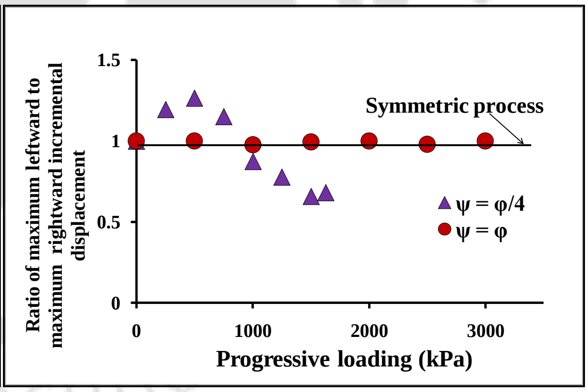

(b)

Fig. 8.13 Ratio of maximum leftward to maximum rightward incremental displacement for dense sand with different dilation angles (ψ); (a) Surface footing (b) Embedded footing

8.2.7 Evolution of failure mechanism: Non-persistent shear strain localization

The essence of the generated asymmetry and the randomness in the results (termed as 'mode switching') is related to the evolution of shear band localization and development of the failure mechanism, and is explained herein based on the purview of geomechanics. As conducted in the model experiments with a stepped increase in the loading on the footing until failure, the numerical simulation in PLAXIS advances through an automated load-stepping algorithm. This technique is especially used when soil plasticity is involved rendering the solution of nonlinear finite element equations to obtain the failure capacity and failure mechanisms. Until a specific load step, the solution remains linear, as the dominant volume of foundation soil maintains its elastic state. However, with the loading advancement, at each load step, several iterations of nonlinear finite element solutions are required to reach a convergent solution. These iterations and consecutive load-steps involve stress redistribution and local plastic volume change in the foundation soil during the entire process of the numerical simulations, as well as during the prototype experiments. The amount of local plastic volume change depends on the degree of dilatancy present in the soil medium. A soil material having no dilatancy (ψ = 0, non-associated flow rule), i.e. if it is a perfectly plastic volume preserving model (Vermeer and de Borst 1983), any stress redistribution would result in the adjustment of the plastic volume in the near vicinity of the stress concentration zones so that the total plastic volume is preserved. As a result, the formation of plastic volumetric strain becomes random within the foundation soil. Such random concentrations of volumetric strain results in the non-persistent shear strain localizations within the foundation soil, which is well established in several classic literatures providing a geomechanics perspective to the failure of sandy soils under drained and undrained loading (Finno et al. 1996; Mokni and Desrues 1998; Guo and Stolle 2013). Non-persistent shear bands modify their orientations randomly during the progressive loading, especially at the earlier stages that mark the onset of localization, and are often termed as mode-switching (Han and Vardoulakis 1991; Mokni and Desrues 1999; Michalowski and Shi 2003). The onset of shear banding in a homogeneous dry soil, subjected to a homogeneous load history, has been illustrated in several literature based on the elasto-plastic constitutive models (Rudnicki and Rice 1975; Vardoulakis and Sulem 1995; Kodaka et al. 2007; Lu et al. 2011). Based on the triaxial tests on Hostun sand, Mokni and Desrues (1998) have explicitly highlighted the randomness in the development of incremental plastic deviatoric and volumetric strains at the onset and post-onset localization stage, which marks the non-preferred orientation of the localized plastic volume change and shear banding during the progressive loading. It has also been clarified (Mokni and Desrues 1998) that the non-persistent shear band localization continues until a preferred shear banding develops, which, marks the attainment of the peak shear stress in the stress-strain curve. Such observations have been reported in experimental (Michalowski and Shi 2003) and numerical (van Baars 2015, 2016, 2018) investigations. If the sandy medium is dense, the attainment of the preferred shear banding is shortly followed by sudden reduction in the shear stress, while, for loose sands, the attainment of directional shear banding is followed by an asymptotic progress in the stress levels with increasing strain (Mokni and Desrues 1998). Such phenomenon of onset and progression of non-persistent strain localization results in the continuously varying ratio of leftward-to-rightward displacement of the footing as illustrated in Figures 8.5, 8.11 and 8.13.

For sands, or any cohesionless materials, having maximum dilatancy, and following the associated flow rule ($\psi = \varphi$), the stress redistribution during the load advancement steps becomes uniform, and hence, the preferred shear banding becomes nearly symmetric and is attained right at the early stages of onset of strain localization. As a result, for highly dilative soils, the generated incremental deviatoric and volumetric strains remain symmetric, and as a consequence, the ratio of leftward-to-rightward displacement of the footing resting on such soils exhibit a ratio nearly equal to 1 (one) during the entire progression of load advancement, till the attainment of failure. The incremental displacement at the nodes depends on the flow rule (Salgado 2011). Such observation has been highlighted in Fig. 8.13. Hence, based on the above discussion, it can be stated that the progressive development of non-persistent shear localization is the causative phenomenon for the observation of randomness in the strain localization (also termed as mode-switching) and formation of asymmetric shear banding during failure of the dilative soils, as well as to some extent for the non-dilative soils.

8.2.8 Validation of asymmetric failure mechanism obtained from PLAXIS 3D FE simulation based on experimental investigation

The verification of the numerically obtained asymmetric one-directional failure mechanism for non-associated flow rule is established based on the outcomes of the experimental investigation conducted by Michalowski and Shi (2003). Based on sophisticated laboratory tests, the evolution of progressive failure mechanism of a strip footing resting on homogeneous sandy foundation (both loose and dense states having angle of internal friction, φ = 34.9° and 44.1°, respectively) is exhibited with respect to the obtained failure deformation patterns. The dimensions of the test container were 61 cm × 61 cm × 30.5 cm (length × height × thickness). A three-piece aluminum model of a strip footing was used, each piece 10 cm long and 3.18 cm wide, and having a thickness of 1.02 cm. With the application of incremental monotonic loading, the movement of the deformed sand bed was recorded with an extremely high-resolution digital camera and subsequently subjected to motion detection computations. The vertical and horizontal components of the incremental displacement vector field were presented on the basis of correlation-based motion detection technique. In addition, the maximum incremental shear strain and incremental volumetric strains were estimated. In the numerical investigation, identical model dimension and soil properties have been opted as considered in the experimental investigation (Michalowski and Shi 2003). To replicate the 3D effect of the experimental investigation, Plaxis 3D vAE.01 has been chosen for thenumerical exploration. The basic soil elements of 3D finite element mesh are the 10-noded tetrahedral elements, as shown in Fig. 8.14. The same boundary conditions, material models and 'fine' meshing scheme have been chosen as considered for 2D analysis. It is perceived from Fig. 8.15 that there is appreciable agreement of load-displacement patterns (for footing resting on dense sand) obtained from the numerical results (considered with non-associated flow rule, $\psi = \varphi/8 = 5.5°$) and the experimental observations (Michalowski and Shi 2003), thus ascertaining the efficacy of the developed 3D numerical model.

The dilatancy angle of the soil used in experimental investigation has not been mentioned in the literature (Michalowski and Shi 2003). Hence, in the present study, in order to back-estimate the probable dilatancy angle, different values of the same were chosen in the range $\psi = 0 - \varphi$, and the corresponding load-displacement curves were compared with that of the experimental observation (Fig. 8.16). Based on the appreciable agreement of the curves (with minimal tolerance), the most probable dilatancy angle was identified thatcould represent the experimentally obtained load-deformation pattern. In this case, a dilatancy angle $\psi = \varphi/8$ provided a very agreeable match throughout the entire load-displacement behavior till failure.

Based on the shaded contours of incremental displacement and incremental deviatoric strain, it can be understood from Fig. 8.17(a-d) that for non-associated flow rule ($\psi \neq \varphi$), the failure slip lines underneath the footing remains asymmetrical. It can also be appreciated from Fig. 8.16(e) that for associated flow rule ($\psi = \varphi$), the failure slip mechanisms are exactly symmetrical beneath the footing. It can be stated from Fig. 8.18 that the maximum leftward to maximum rightward incremental displacements of the soil beneath the footing is definintely not identical when non-associated flow rule is considered, while the same is observed to be symmetrical and encourgingly similar to the conventional understandings while considering associated flow rule.

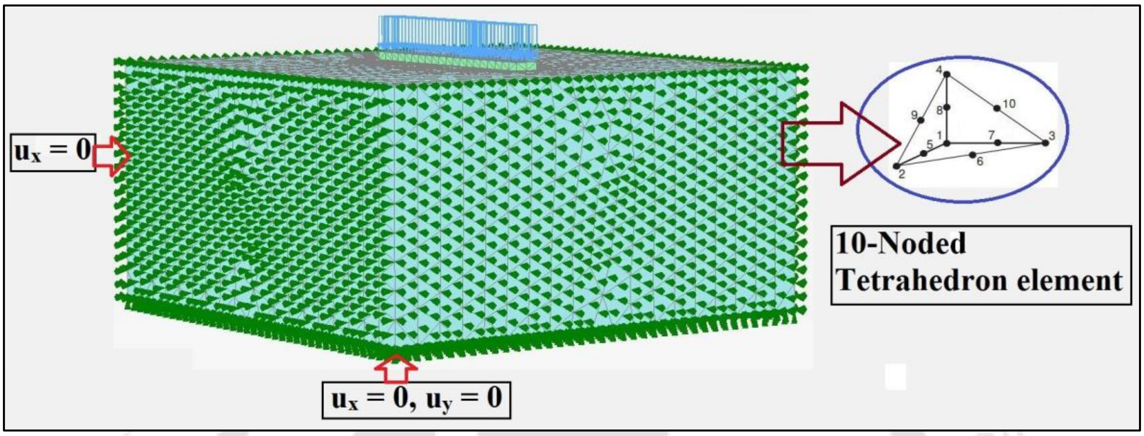

Fig. 8.14 Plaxis 3D model for the simulation of experimental work of Michalowski and Shi (2003)

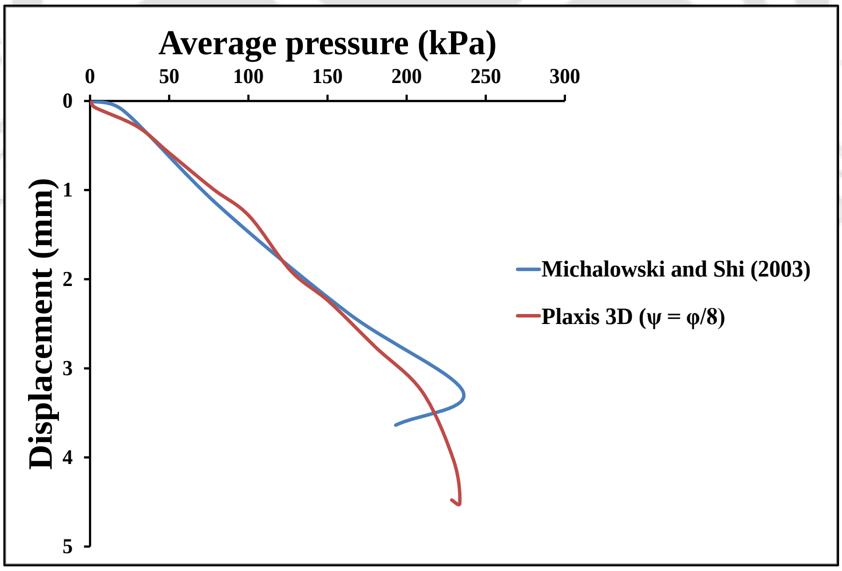

Fig. 8.15 Comparative load-displacement diagram of footing resting on dense sand as observed for expreimental and numerical outcomes

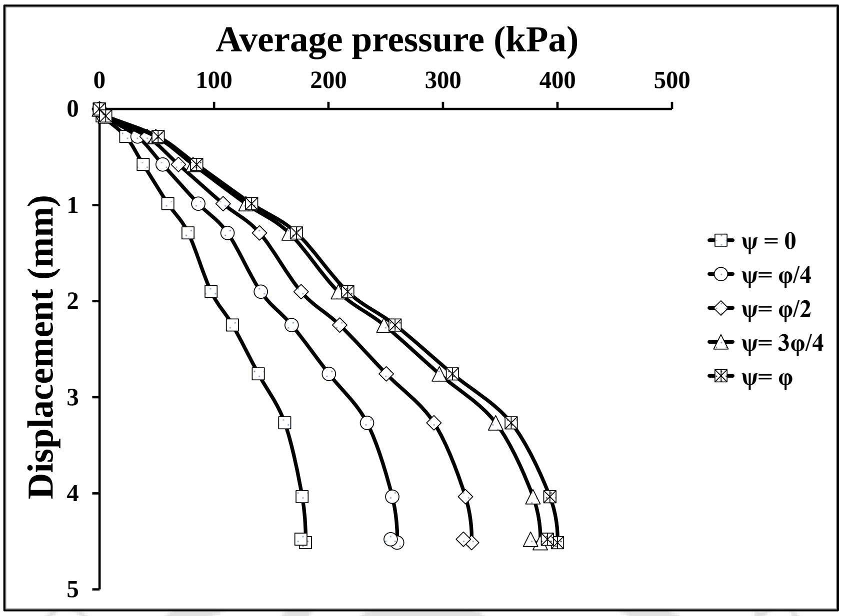

Fig. 8.16 Load–displacement pattern for different dilatancy angles (ψ) of dense sand

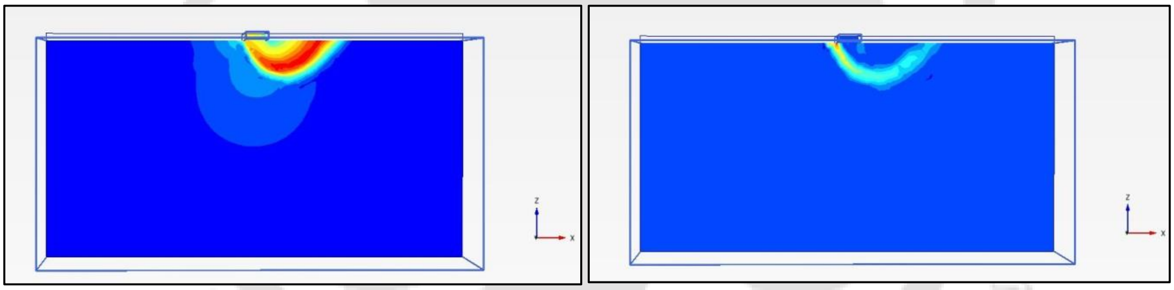

(a)

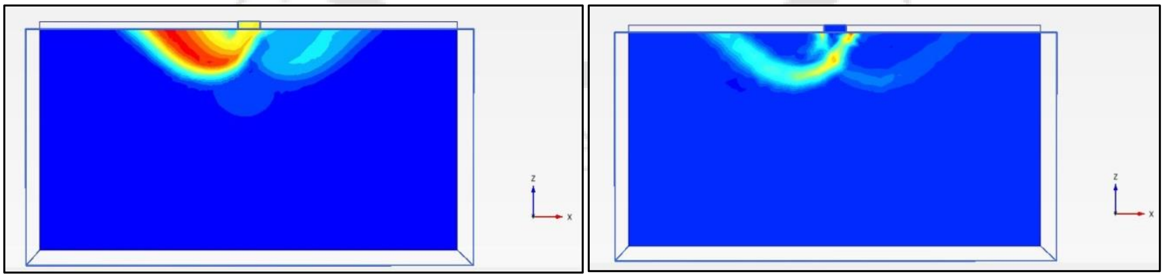

(b)

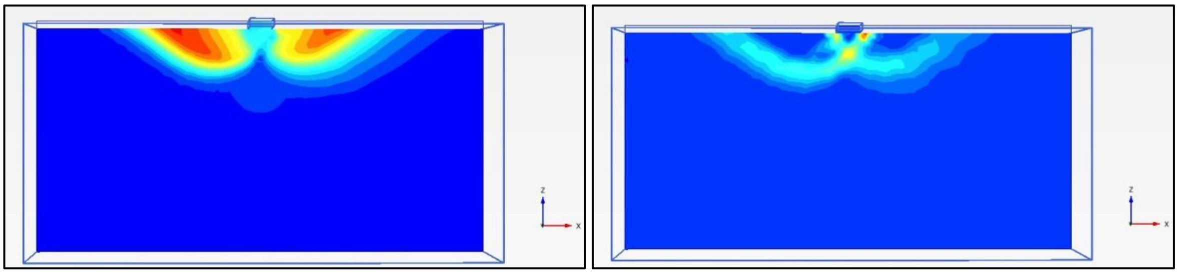

(c)

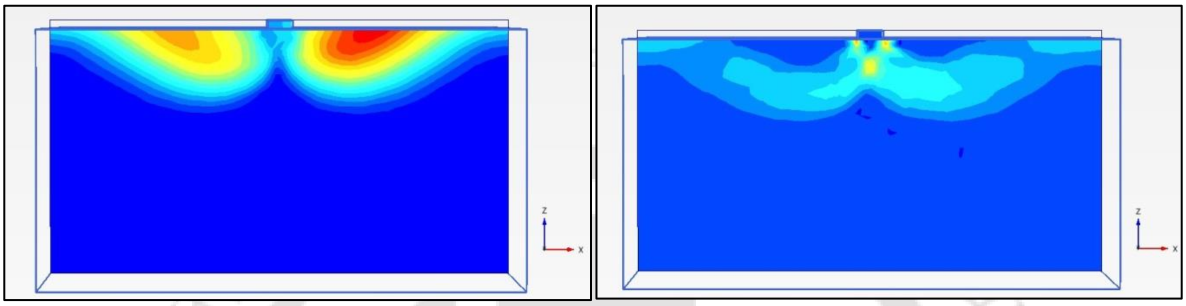

(d)

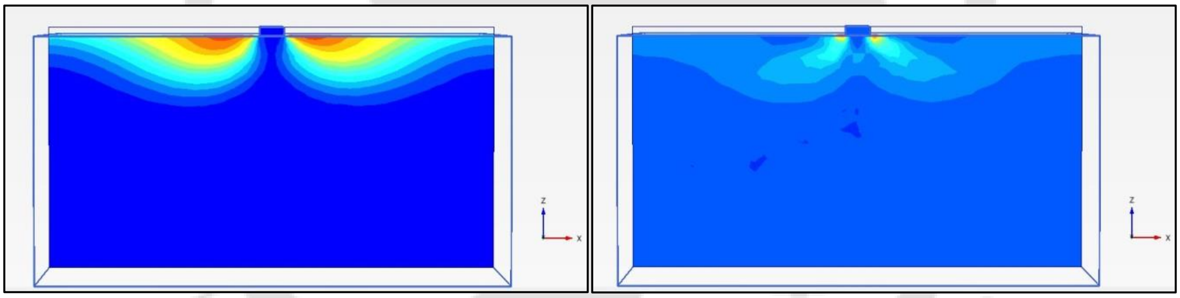

(e)

Fig. 8.17 Typical incremental displacement and incremental deviatoric strain patterns for dense sand used in investigation (Michalowski and Shi 2003); (a) $\psi = 0$ (b) $\psi = \varphi/4$ (c) $\psi = \varphi/2$ (d) $\psi = 3\varphi/4$ (e) $\psi = \varphi$

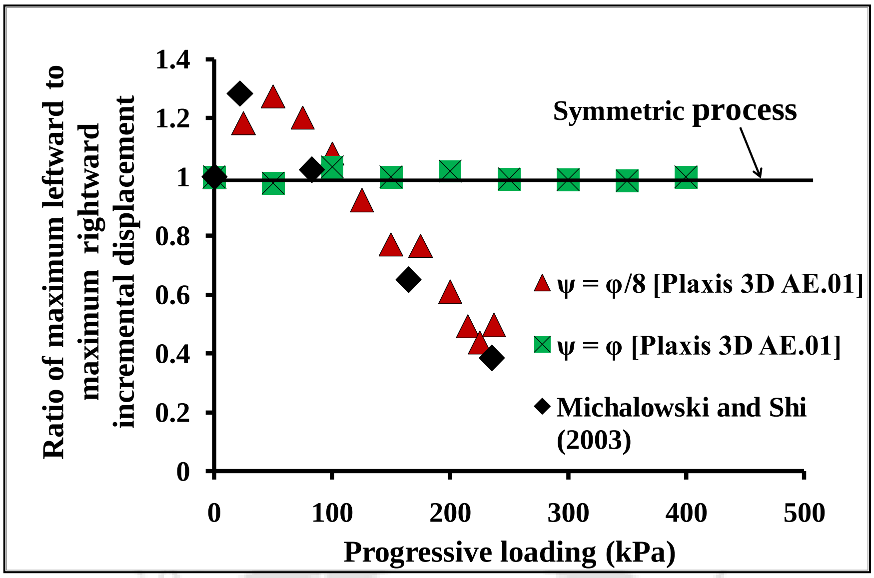

Fig. 8.18 Ratio of maximum leftward to maximum rightward incremental displacements for dense sand with different dilation angles (ψ)

8.3 Strip Footing Resting on Sloping Ground

The previous sections amply highlighted the importance of dilatancy on the evolution of failure mechanism of surface or embedded footings in horizontal ground. The scenario of the development of failure characteristics of a loaded footing become even more critical when the same rests on the edge of a slope, either on the crest or near the slope face. The limited literature that deals with the bearing capacity of such footings does not consider the influence of soil dilatancy on the failure characteristics. Owing to the understanding of the importance of dilatancy for footing on horizontal ground, this section addresses the similar issue for footings resting on sloping grounds, which has remained unaddressed yet in the prevailing literatures related to the subject.

8.3.1 FE analysis of footing resting on slopes: Validation study

Similar to the FE model developed for strip footing resting on horizontal ground, the FE simulation of a strip footing resting on sloping ground has been developed with Plaxis 3D vAE.01, and the same has been validated with the experimental work conducted by Keskin and Laman (2013). For the validation study, the soil properties adopted are φ = 41.8°, D_r = 65%, and γ = 17 kN/m^3, identical as considered by Keskin and Laman (2013). The dilatancy angle (ψ) is considered equal to the angle of internal friction of soil (φ), i.e. the soil is assumed to follow 'associated flow rule'. A strip footing of 70 mm width resting on the crest of the slope (β = 30°) with setback distance of *b/B* =0 has been simulated, where 'setback distance' is the clear distance of the footing from the face of the slope at the crest level. In the numerical investigation, identical model dimension (1.140 m × 0.475 m × 0.50 m), as considered by the researchers for laboratory experimentation, has been considered. Figure 8.19 illustrates the Plaxis 3D model as used in the validation work.

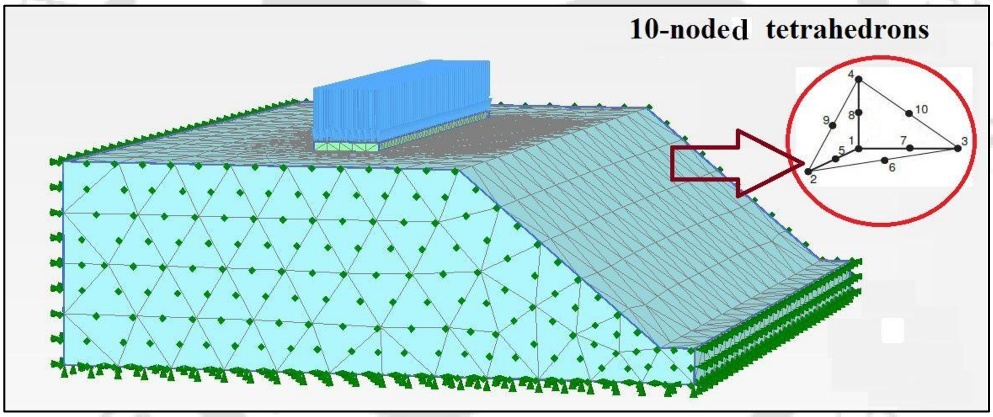

Fig. 8.19 Representative model geometry considered in Keskin and Laman (2013) and the adopted discretization and meshing scheme

In order to choose a suitable mesh for the numerical simulation, a convergence test has been conducted. It has been found that for the present study, the choice of the fine mesh (having a non-dimensional average length of the element as 0.04) is sufficient to provide the optimal results, as shown in Fig. 8.20. Based on the chosen optimal mesh, the stress-deformation plot for the loaded footing, as obtained from the FE simulations, is presented in Fig. 8.21. It can be observed that there is appreciable match between the bearing capacity obtained from the numerical result and experimental observations, indicating the correctness of the developed FE model.

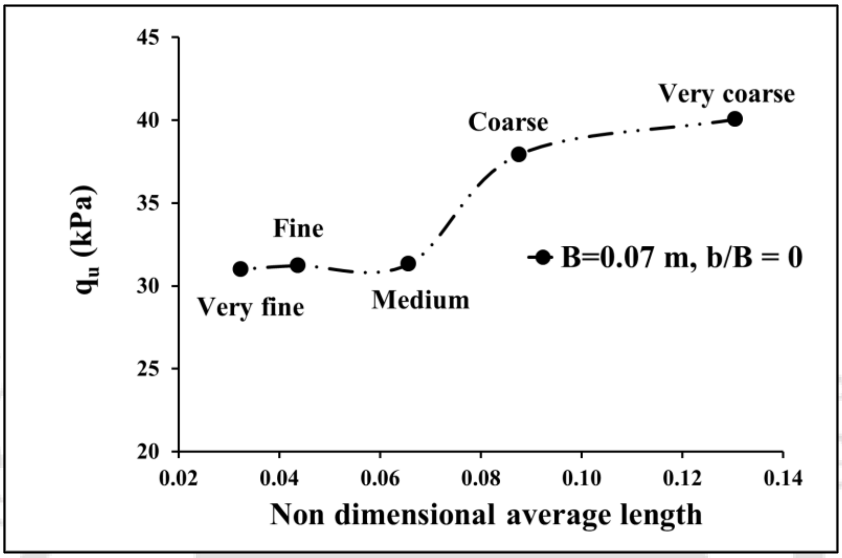

Fig. 8.20 Mesh convergence study for determining the optimum mesh element size

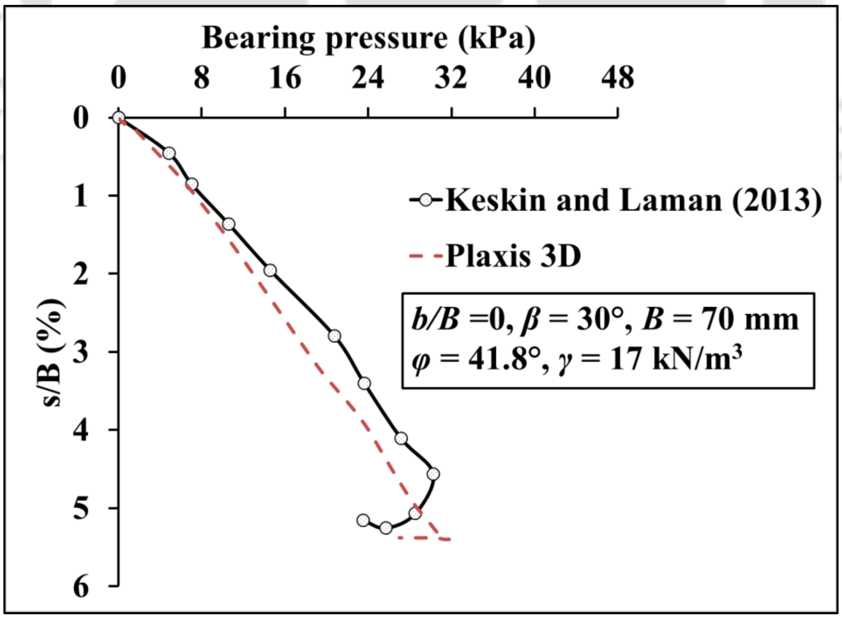

Fig. 8.21 Comparative study of the stress-deformation behaviour obtained from the Plaxis 3D FE model and experimental observations by Keskin and Laman (2013)

8.3.2 Typical response of footing on slope crest: Effect of setback distance

Considering the slope material to follow the associated flow rule (i.e. $\psi = \varphi$), for strip footings located at various setback distances from the slope face, Figure 8.22 exhibits that the passive zone formed beneath the footing is affected by the nearness of the footing to the slope face. It can be perceived that for a footing placed at the crest of the slope ($b/B = 0$), the formation of passive zone is largely one-directional and curtailed by the slope face, due to the dominant free deformation of the soil induced by the footing load. Such phenomenon results in a considerable decrease of the confinement pressure, and hence, attenuation of the bearing capacity. As the setback ratio increases, the influencing effect of the slope face on the development of the passive mechanism gradually diminishes, as can be observed from the Fig. 8.22. It is noted that beyond a critical setback ratio $(b/B)_{critical} = 6$, the footing behaves as if resting on horizontal ground, wherein the developed displacement contours for the passive zone remains unaffected from the influence of the slope face. Further, owing to the consideration of associated flow rule, it can be noticed that the development of failure mechanism beneath the footing is perfectly symmetrical for the cases when there is no influence of the slope face on the developed mechanism.

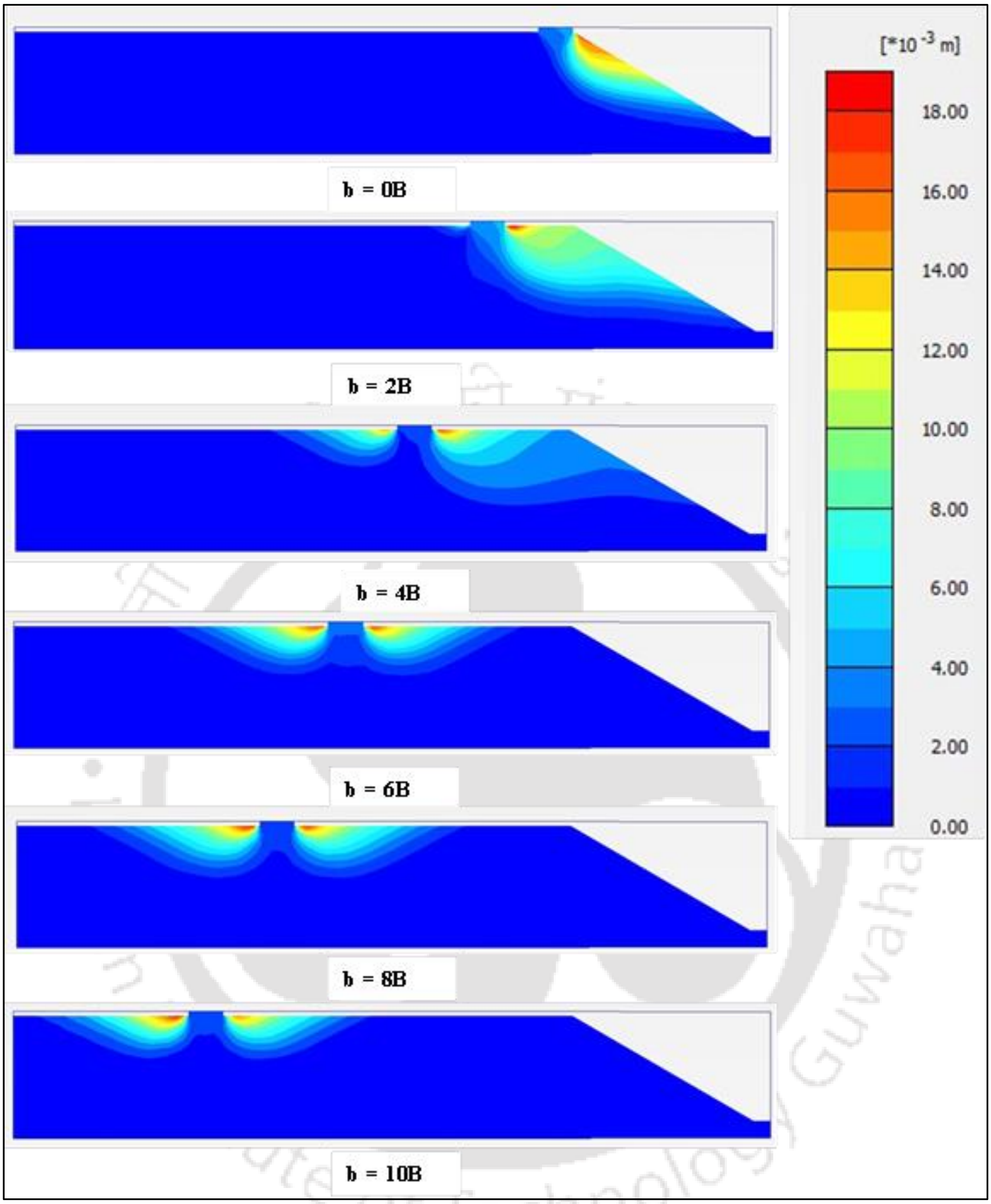

Fig. 8.22 Typical formation of passive zones conforming associated flow rule (ψ = φ) for various setback ratios (*b/B*) at failure

8.3.3 Influence of dilatancy on the bearing capacity of footing resting on slope crest and the deformation response of slope face

An attempt has been made to understand the influence of varying angles of dilatancy, signifying different flow rules, on the ultimate bearing capacity, displacement and failure mechanism of strip footings resting on crest of the slope. For this purpose, various dilation angles (ψ) have been used namely $\psi = \varphi/4$, $\varphi/2$, $3/4\varphi$ and φ. Three different slope angles (β = 20°, 30° and 40°) and two typical setback distances (b = 0.5B and 2B, B is the width of the footing) were taken into account for the numerical investigation. The influence of the angle of dilatancy on the obtained bearing capacity is depicted in Fig. 8.23. It can be observed that that the ultimate bearing capacity (q_u) increases with increasing dilation angle (ψ), and that lower magnitudes of dilation results in sufficiently lower bearing capacity. It can also be noticed that the ultimate bearing capacity increased with increasing setback distance (b) and decreasing slope angle (β), the reason of which is explained in the previous section. Figure 8.24 depicts the total resultant displacement of the slope face (U_{max}) as obtained for various dilation angles, slope angles and setback distances at failure. It can be clearly noticed that the total resultant displacement increases with increasing dilation angle, thus indicating the influence of dilatancy on the deformation behaviour of slope face.

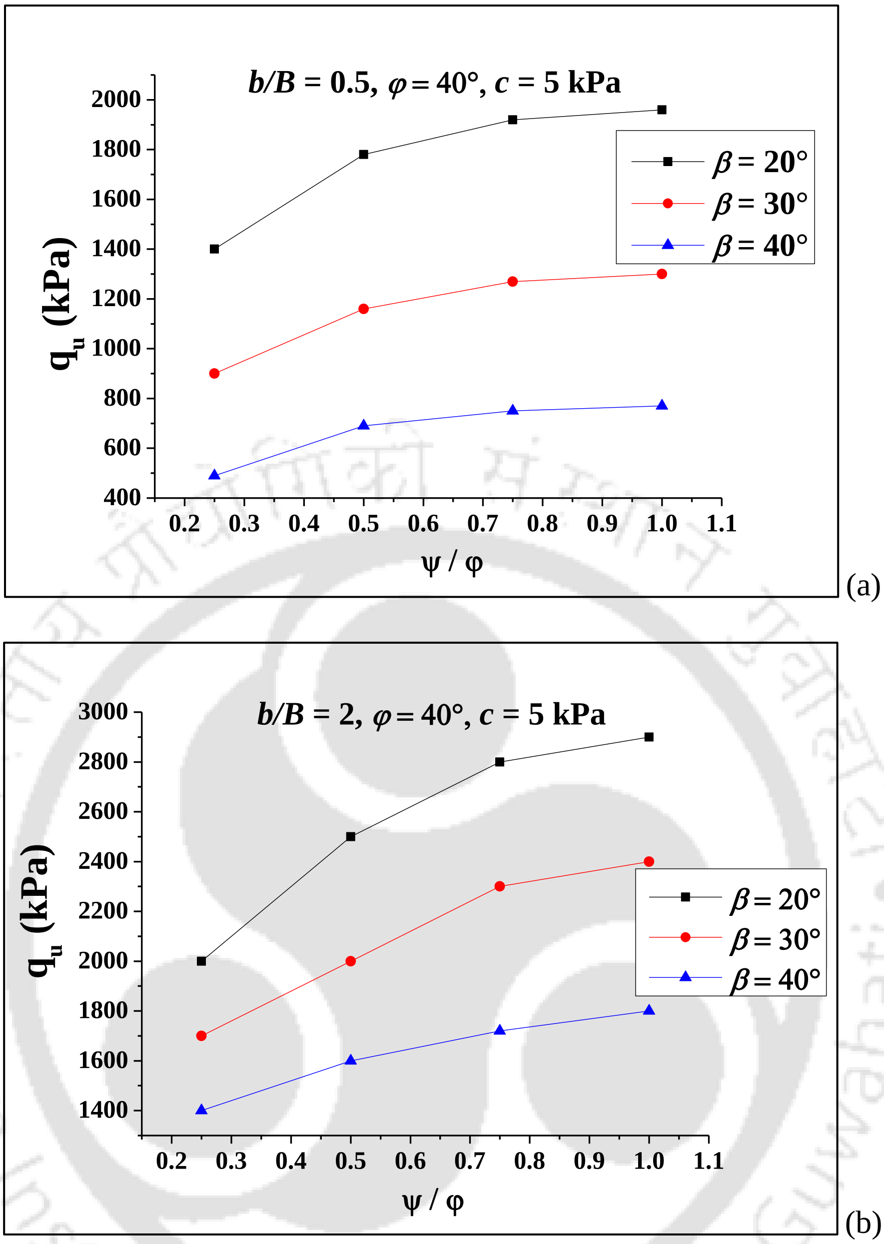

Fig. 8.23 Influence of angle of dilatancy on ultimate bearing capacity of a footing resting on the crest of a slope having (a) *b/B* = 0.5 (b) *b/B* = 2

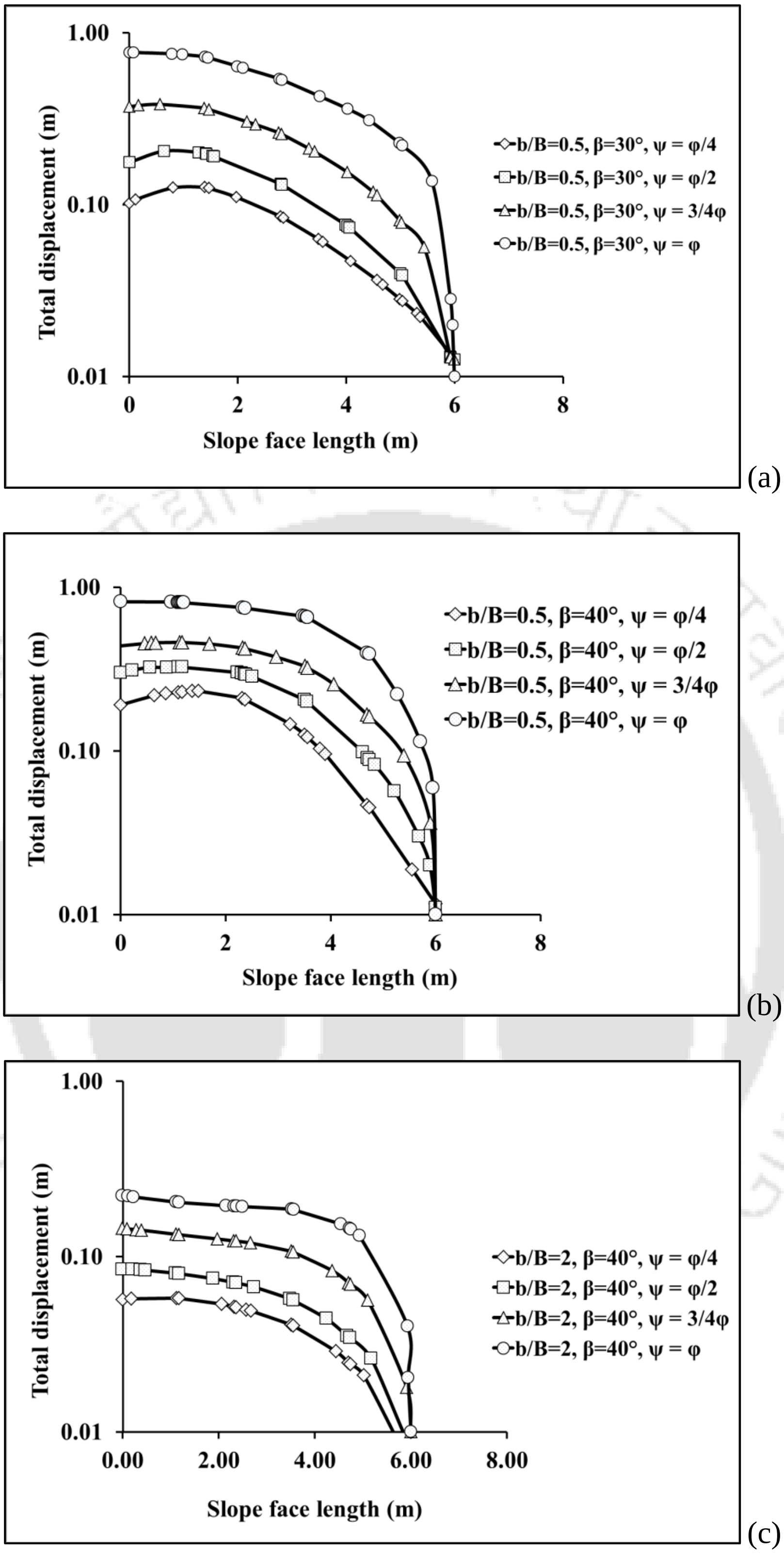

Fig. 8.24 Influence of angle of dilatancy on the total resultant displacement of slope face for various setback ratios and slope angles (a) b/B = 0.5, β = 30° (b) b/B = 0.5, β = 40° (c) b/B = 2, β = 30°

8.3.4 Influence of dilatancy on the failure mechanism of footing resting on slope crest

Figure 8.25 portrays the failure displacement pattern through incremental displacement vectors for various slope angles, dilation angles and setback distances. It can be observed that for the chosen slope angles, dilation angles and setback distances, as expected, the soil movement has always taken place expectedly towards the slope face during the failure. This is primarily attributed to the incomplete development of the passive zone near the slope face where there is not enough lateral restraint on the soil to resist its outward lateral movement. Moreover, it can be noticed that higher dilation angles result in larger outward movement of the slope face, as indicated by larger size of the incremental displacement vectors for higher dilation angles. This overall phenomenon indicates that for a footing resting on the slope crest, higher angles of dilatancy will lead to higher bearing capacity and failure deformations.

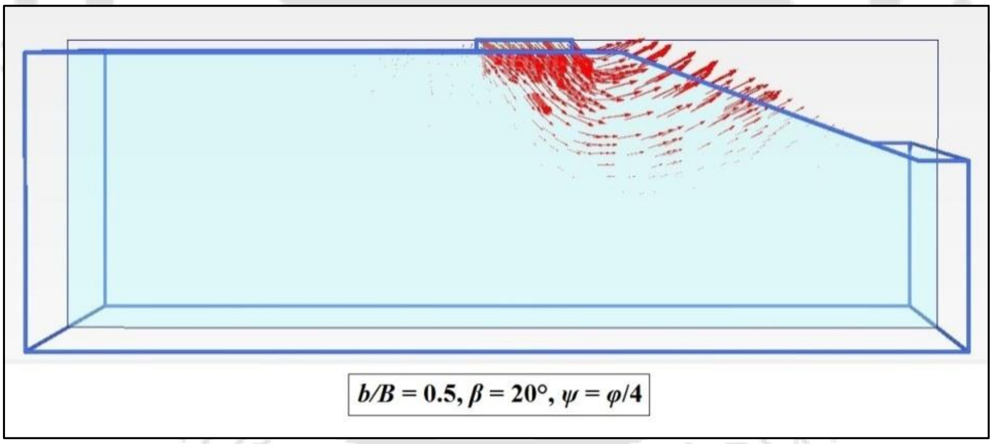

(a)

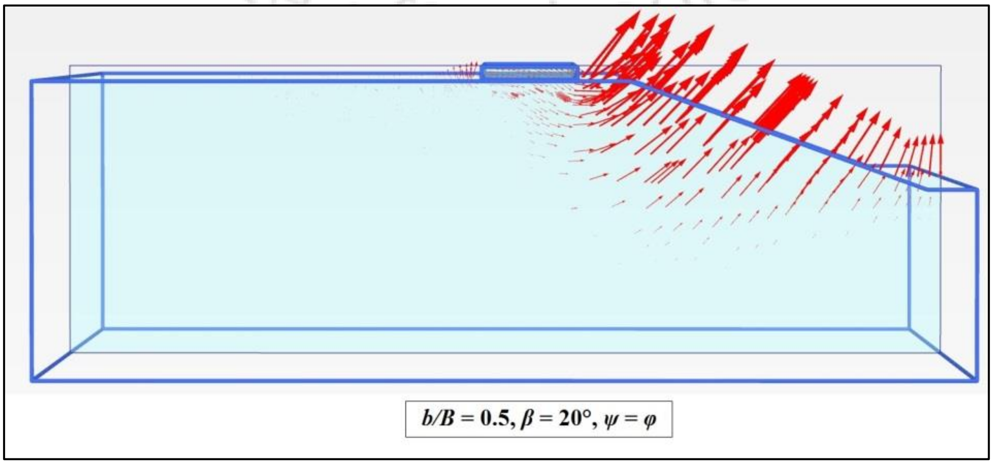

(b)

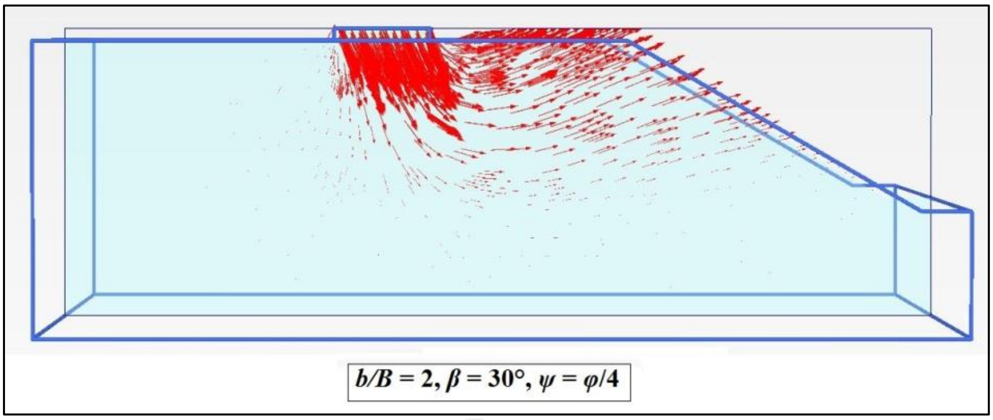

(c)

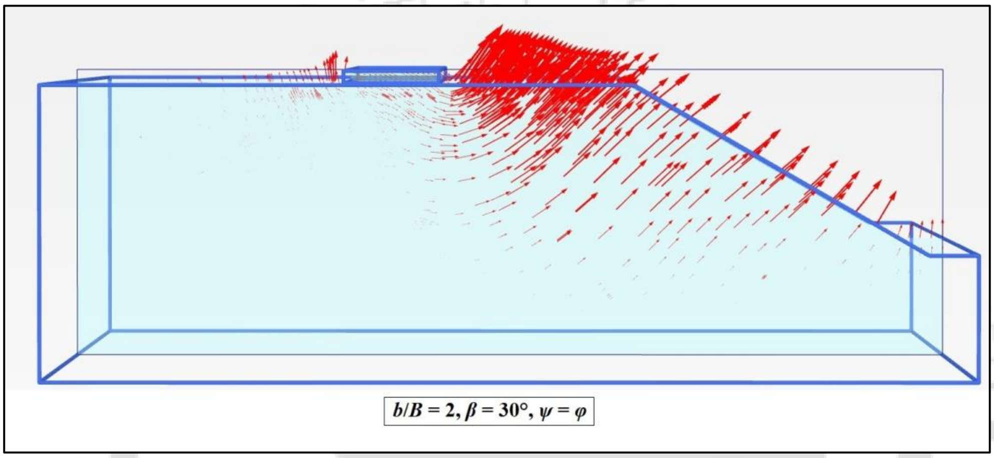

(d)

Fig. 8.25 Incremental displacement pattern of strip footing resting on slope at its failure (a) b/B = 0.5, β = 20°, $\psi = \varphi/4$ (b) b/B = 0.5, β = 20°, $\psi = \varphi$ (c) b/B = 2, β = 30°, $\psi = \varphi/4$ (d) b/B = 2, β = 30°, $\psi = \varphi$

8.4 Summary

This chapter summarizes the influence of dilatancy on the response of footings resting on horizontal or sloping grounds. In the present investigation, the influence of flow rules over bearing capacity, displacement and failure mechanism of strip footing resting on horizontal ground or near the sloping ground have been inspected by considering Mohr-Coulomb soil model. From the above discussions, it can be stated that if the foundation soil follows a non-associative flow rule, even a uniformly loaded footing resting on horizontal ground will exhibit differential settlement (tilting or rigid rotation) along with the formation of asymmetrical and one-directional slip mechanisms at or near failure. On the contrary, for footings resting on soil following associated flow rule, the developed failure mechanism will be symmetrical, as adopted in the conventional bearing capacity theories. The trend of the failure mechanism, and its evolution, remains independent of the type of soil and mesh refinement scheme adopted for the numerical simulation. For footings resting on sloping ground, it is comprehended that the bearing capacity and deformation of slope face at failure increases with increasing dilatancy angle. This study highlights the importance of considering the angle of dilatancy as a design parameter for estimating the bearing capacity of footings, which has not been considered in the existing bearing capacity theories.

CHAPTER 9

CONCLUSIONS AND RECOMMENDATIONS

9.1 Brief Summary of the Dissertation

This dissertation reports about the overall response of isolated and interfering shallow footings located on or near the slope. 2-D and 3-D Finite element analyses have been resorted to for conducting the numerical investigations for deciphering the bearing capacity and failure mechanisms of the foundations located on slopes. Based on an earlier conducted building survey, foremost, the ultimate bearing capacity and failure pattern of square footing resting on dry sandy-soil slope has been investigated by altering the various geotechnical and geometrical parameters. Further recognizing the prevalent presence of c-φ soils in most of the hilly terrains, the study was extended for the square footings resting on such sloped. Apart from square footing, strip footing being the other most common typology of shallow foundations for buildings in hill-slopes, the previous study was further extended to recognise the bearing capacity and failure mechanism of the same. Considering the practical scenarios of building construction in the hill-slopes, it was revealed that single isolated strip or square footing does not represent the building foundation characteristics. In this regard, the impact of interference of strip footings located on crest of c-φ soil slope on their bearing capacity and failure mechanisms has been examined. In all the simulations of various typologies, the influence of the geotechnical and geometrical parameters were vividly studied. With the aid of ANN technique, the quantitative influences of the geotechnical and geometrical parameters were used to develop expressions for bearing capacity prediction. These expressions can serve as a ready-made handy tool for the geotechnical engineers for assessing the bearing capacity of isolated and interfering shallow footings located on the hill-slopes. Additionally, ANN technique had been further used to provide importance ranking of the influencing parameters.

Such ranking would help the geotechnical engineers to give due attention to the important parameters while designing and constructing foundations on slopes. Further, with the aid of a case study, the overall stability of a hill-slope supporting an electric transmission tower had been investigated. Based on the outcomes, recommendations to enhance the bearing capacity commonly adopted isolated footings has been provided through the application of alternative typologies of interconnected shallow footings. The study has been further extended to study the bearing capacity of complex arrangement of shallow footings that may be suitably adopted to harness their benefit of enhanced bearing capacity and lessened outward deformation of slope when placed on the crest of a slope. Finally, the influence of flow-rules (associated and non-associated) and soil dilatancy has been inspected on the bearing capacity, displacement and failure mechanism of strip footing resting on horizontal ground as well as near the sloping ground. Such study aids in the understanding the practical conditions of bearing capacity of foundations on slopes as well as the overall failure mechanisms, which are left unaddressed by the conventional classical bearing capacity theories.

9.2 Conclusions and Recommendations

Based on the studies and outcomes reported in the present dissertation, the relevant conclusions and recommendations are provided as follows:

- For an isolated shallow square or strip footing resting on the crest of the slope, bearing capacity increases with the increase in the shear strength parameters of constituent soil (c and φ), footing width (B) and the embedment depth (D_f), while it reduces with the increase in the slope inclination (β). Unit weight of soil (γ) is found to have negligible effect on the ultimate bearing capacity.

- Bearing capacity of an isolated shallow footing increases with the increasing setback distance (b). Beyond a critical setback ratio $(b/B)_{critical}$ = 4, an isolated square footing located on the crest of a slope behaves as if resting on a horizontal semi-infinite medium, Similar behaviour is exhibited by a strip footing beyond $(b/B)_{critical}$ = 6. Beyond these critical distances, the influence of the slope face on the developed bearing mechanism complete disappears. These limiting setback distances are recommended to be adopted, wherever possible, for constructing shallow foundations on slopes to generate the maximum bearing capacity.

- Bearing capacity of interfering shallow footings resting on the crest of a slope is significantly affected by the centre-to-centre spacing (S) between the individual footings, apart from the other geotechnical and geometrical parameters. The maximum magnitude of ultimate bearing capacity was obtained at a spacing ratio S/B = 1.5. Beyond a spacing ratio S/B = 3, the ultimate bearing capacity of interfering footings attain the magnitude exhibited by an individual isolated footing, thus indicating the complete disappearance of the interference effect. It is recommended to maintain the spacing ratio, S/B = 1.5, while constructing adjacent footings so that the maximum bearing capacity of interfering footings can be harnessed.

- Bearing capacity of interfering shallow footings resting on the face of a slope is influenced by the relative elevation between the footings (h). The least bearing capacity is obtained for relative elevation h/B = 1.5, when the maximum overlap of the significant stress isobars is attained, leading to failure of the slope and the foundation. Beyond a relative elevation of h/B = 8, individual response of the footings are exhibited without any mutual interference. Whenever required, it is recommended to construct footings at higher magnitude of relative elevations (h/B > 6) so that the distress in the slope face due to mutually interfering foundations is avoided, and greater stability and bearing capacity is ensured.

- Artificial Neural Network (ANN) modelling effectively brings out the characteristic relationship between the various influencing parameters and the bearing capacity of the isolated and interfering shallow footings located on the crest of slope. Based on network sensitivity studies, ANN models with 7-10-1, 6-9-1 and 6-8-1 architectures has been found to be the best suitable ones for predicting the bearing capacity of isolated square footing, isolated strip footing and interfering strip footings located on the crest of hill-slopes.

- Bearing capacity expressions are developed based on the best suitable trained ANN architectures proves to be efficient and are recommended for their application in predicting the ultimate bearing capacity of isolated or interfering shallow footings on slopes, provided the geometrical and geotechnical parameters are known. These prediction expressions will provide a quick tool for the practicing and consulting engineers involved in the design of hillside urbanizations and constructions.

- Sensitivity studies using Garson's algorithm reveals that angle of internal friction of constituent foundation soil and setback distances are the most influential parameters governing the bearing capacity of isolated square and strip footings resting on the crest of a slope. Apart from the above parameters, spacing ratio proves to be substantially influencing the bearing capacity of interfering strip footings in slopes. It is recommended to provide due attention to these parameters while designing foundations on slopes to make proper assessment of the bearing capacity.

- Interconnecting shallow footings located near the crest of a slope with those located away from the slopes provides an effective means of enhancing the bearing resistance of the shallow foundation for buildings located on hilly terrains. Footings located away from the crest act as additional ties to those located near the crest, and prevents the latter from free deformation towards the slope face, thus enhancing the overall bearing resistance of the foundation. It is recommended to provide such interconnections perpendicular to the slope face, or develop an interconnected grid, for more sustainable foundations on slopes.

- Foundation soil characteristically following non-associated flow rule (i.e. $\psi \neq \varphi$) result in the development of non-persistent shear banding beneath a uniformly loaded footing, resulting in the formation of asymmetrical and one-directional slip mechanisms. Such phenomenon exhibiting differential settlement (tilting and rotation) of even a uniformly loaded footing. Such evolution of the failure mechanism remains independent of the type of soil and mesh refinement scheme adopted for the numerical simulation.

- Foundation soils closely following the associated flow rule (i.e. $0.75\varphi < \psi \leq \varphi$) exhibit symmetrical failure mechanism beneath a uniformly loaded footing, and pertains similarity to the classical and conventional solutions.

- For footing resting on slopes, the bearing capacity and displacement enhances with increasing the dilatancy angle of soil, up to a limit of $\psi = 0.75\varphi$.

- The evolution of failure mechanism beneath a uniformly loaded footing resting on horizontal is substantially affected by the angle of dilatancy of the foundation soil. It is recommended to determine the angle of dilatancy of foundation soil through carefully conducted suitable laboratory tests, and apply the same for finite-element (FE) based numerical simulations to obtain the best results.

9.3 Significant Contribution of Present Study

The following are the significant contributions from the present study which leads to an advanced understanding of the response of foundations on slopes, as well as on the horizontal ground, beyond the existing conventional knowledge.

- Detailed presentation of the influence of various parameters on the evolution of failure mechanism and bearing capacity of isolated square and isolated strip footings resting on the crest of slope. Being an output from the coupled stress-deformation FE analysis, the results and inferences incorporate the evolution of failure mechanism which is beyond that is addressed in the conventional studies following the stress-based approaches comprising limit equilibrium or limit analysis techniques.
- Detailed response and bearing capacity of interfering strip footings located on the crest and face of slope based on finite element analysis and interpreted in terms of the evolving failure mechanism. Such studies are attempted for the first time and has not reported earlier in any literature.
- Application of ANN to develop predictive expressions to determine the bearing capacity of isolated square, isolated strip and interfering strip footings resting on the crest of a soil slope. Such expressions, defined on the data obtained from coupled stress-deformation approach, can be effectively used in the design and analysis of such foundations on hill slopes.
- Comprehensive response of coexisting multiple footing typologies on the crest of hill-slope have been illustrated. Such understanding would be extremely fruitful in quickly ascertaining the bearing capacity of foundations on urbanized hillslopes where different types of foundations are expected to be present in vicinity. Such studies have not been attempted till date and not reported in any literature.

- The influence of dilatancy on the bearing capacity on the footings resting on horizontal and sloping grounds have been elucidated. The variation of results observed from such studies effectively highlighted the importance of the role of geomechanics in the comprehensive understanding of the bearing capacity of foundations. Such studies have not been attempted earlier, and opens up the domain of geomechanics and its applications to such problems.

This section also presents few design examples to illustrate the applicability of the prediction expressions developed for the evaluation of bearing capacity of different types of footings resting on the crest of the slope. In the present investigation, design examples for estimating the ultimate bearing capacity of square footing, strip footing and interfering strip footings have been considered as shown in Figure 9.1, 9.2 and 9.3.

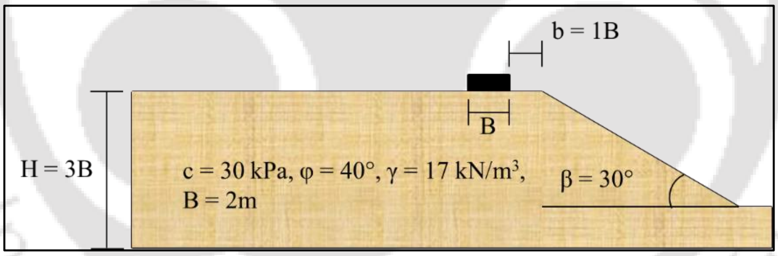

Fig. 9.1 Schematic diagram for the design example for isolated square footing (not to scale)

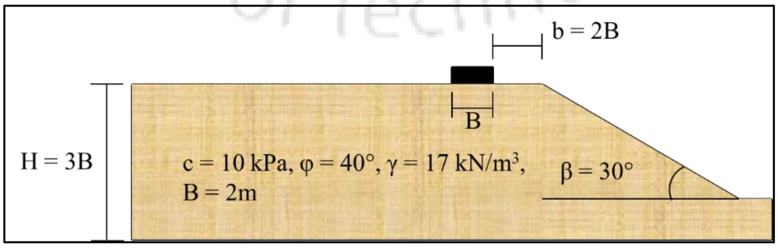

Fig. 9.2 Schematic diagram for the design example for isolated strip footing (not to scale)

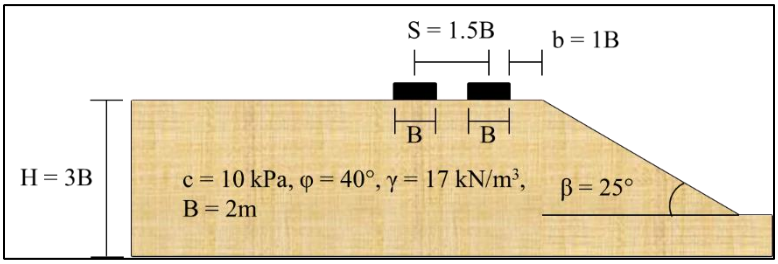

Fig. 9.3 Schematic diagram for the design example of interfering strip footings (not to scale)

9.3.1 Design example for square footing resting on crest of a slope

Isolated square footing of width 2 m resting on the crest of a slope of 6 m height inclined at an angle of 30° to the horizontal. The slope comprises of soil possessing cohesion and angle of internal friction as 30 kPa and 40°, respectively. The unit weight of soil is 17 kN/m^3. The setback distance of the footing nearest to the crest of the slope is 2 m as shown in Fig. 9.1.

Table 9.1 Parameters used in the analysis of square footing resting on crest of a slope

Parameters	Range
c (kPa)	0-80
φ (°)	10-40
B (m)	0.08-2
b/B	0-10
β (°)	10-40
D_f/B	0-1
q_u (MPa)	0.25-17.14

The initial step in the assessment of bearing capacity is to normalize the input and output parameters between 1 to -1. The maximum and minimum magnitudes of input and output parameters have been tabulated in Table 9.1. Further, the normalized input parameters have been used in the expressions (Eq. 6.34 – 6.55) to get the normalized output. For the present design example problem, the normalized output [(q_u)n] magnitude has been found as -0.307. The actual magnitude of q_u has been calculated with the aid of expression Eq. 6.56.

$$q_u = 0.5\times(-0.307+1)\times(17.136-0.25)+0.25 = 6.1 \text{ MPa} \tag{9.1}$$

The ultimate bearing capacity of strip footing (q_u) for current design problem has been found as 6.1 MPa.

9.3.2 Design example for strip footing resting on crest of a slope

Isolated strip footing of width 2 m resting on the crest of a slope of 6 m height inclined at an angle of 30° to the horizontal. The slope comprises of soil possessing cohesion and angle of internal friction as 10 kPa and 40°, respectively. The unit weight of soil is 17 kN/m^3. The setback distance of the footing nearest to the crest of the slope is 4 m as shown in Fig. 9.2.

Table 9.2 Parameters used in the analysis of strip footing resting on crest of a slope

Parameters	Range
c (kPa)	0-80
φ (°)	10-40
B (m)	0.04-2
b/B	0-10
β (°)	10-40
D_f/B	0-1
$q_u/\gamma H_s$	4.05-145.55

The initial step in the assessment of bearing capacity is to normalize the input and output parameters between 1 to -1. The maximum and minimum magnitudes of input and output parameters have been tabulated in Table 9.2. Further, the normalized input parameters have been used in the expressions (Eq. 6.11 – 6.30) to get the normalized output. For the present design example problem, the normalized output [($q_u/\gamma H_s$)n] magnitude has been found as -0.63. The actual magnitude of $q_u/\gamma H_s$ has been calculated with the aid of expression Eq. 6.31.

$$\begin{aligned} q_u/\gamma H_s &= 0.5(-0.63+1)(145.55-4.05)+4.05=30 \\ \Rightarrow q_u &= 30\times17\times6=3.06 \text{ MPa} \end{aligned} \tag{9.2}$$

The ultimate bearing capacity of strip footing (q_u) for current design problem has been found as 3.06 MPa.

9.3.3 Design example for interfering strip footings resting on crest of a slope

Two strip footings of width 2 m resting on the crest of a slope of 6 m height inclined at an angle of 25° to the horizontal. The slope comprises of soil possessing cohesion and angle of internal friction as 10 kPa and 40°, respectively. The unit weight of soil is 17 kN/m^3. The centre-to-centre spacing between the footings is 3 m, leaving a clear spacing of 1 m between the interfering footings. The setback distance of the footing nearest to the crest of the slope is 2 m as shown in Fig. 9.3.

Table 9.3 Parameters used in the analysis of interfering strip footing resting on slope crest

Parameters	Range
c (kPa)	0-80
φ (°)	10-45
B (m)	0.05-2
b/B	0-10
β (°)	10-40
S/B	0-10
$q_u/\gamma H_s$	1.092-38.79

The initial step in the assessment of bearing capacity is to normalize the input and output parameters between 1 to -1. The maximum and minimum magnitudes of input and output parameters have been tabulated in Table 9.3. Further, the normalized input parameters have been used in the expressions (Eq. 6.59 – 6.76) to get the normalized output. For the present design example problem, the normalized output [($q_u/\gamma H_s$)n] magnitude has been found as -0.194. The actual magnitude of $q_u/\gamma H_s$ has been calculated with the aid of expression Eq. 6.77.

$$\begin{aligned} &q_u/\gamma H_s = 0.5(-0.194+1)(38.79-1.092)+1.092 = 16.28 \\ &\Rightarrow q_u = 16.28 \times 17 \times 6 = 1.66 \text{ MPa} \end{aligned} \tag{9.3}$$

The ultimate bearing capacity of interfering strip footings (q_u) for current design problem has been found as 1.66 MPa.

9.4 Limitation and Future Scope

Any research work performed has its own setbacks and thus paves the way and scope for future investigation. Some of them, as applicable for the present study, are listed as follows:

- In the present study through numerical simulations, the bearing capacity and the evolution of failure mechanism of shallow footings resting on slope have been evaluated using Mohr-Coulomb (M-C) constitutive relations for the foundation soil. Hilly terrains of the North-eastern India and many other parts of the world largely comprise soil material that manifests creep movements and rainfall induced failures. Such behaviours cannot be explicitly represented by the adopted M-C relations. In this regard, it is extremely important to apply advanced constitutive models such as soft soil creep (SSC), Cam-clay (CC) or Modified cam-clays (MCC), and elucidate the more critical responses of foundations on slopes.

- Incessant rainfall and strong seismic shocks often rattle the inhabitations in hilly regions causing large damages to life and property. The present investigations only address the basic static aspects of the foundations on slopes. It is important to investigate the progressive evolution of the failure mechanism under the cases of dynamic loading and failures induced due to rainfall.

- In the present investigation, the bearing capacity and failure mechanism of shallow footing resting over slope have been estimated by considering only vertical centric loading. Further, no lateral loading has been considered in the present study that is prevalent in hill-slope structures due to the lateral load generate by winds. Hence, it is required to investigate the influence of eccentric, lateral and oblique loadings, along with the prevalent moment loadings, over the bearing capacity and failure mechanism of foundations for tall structures resting near the slope.

- In the current investigation, only shallow footings have been considered as building foundations. With the growing habitations in the hilly regions and progressive urbanization, there are ample instances where voluminous structures being raised over pile foundations. Although pile foundations are supposed to carry the load to deep bearing stratum, such foundations may also lead to slope failure during to the installation of the piles and consequent weakening of the slope face resulting in induced failure. Hence, the suitability and response of deep foundations, specifically piles and sheet piles, located on or near the slope, is essential to be looked into.

- The influence of the various footing arrangements, conforming to 2 x 2 and 3 x 3 arrangements, has been investigated on the alteration of ultimate bearing capacity has been emphasized to identify the possible arrangement which can provide higher bearing capacity instead of isolated foundations as commonly practiced in the urbanized hill slopes. The settlement criterion has not been vividly considered in the study. However, it is imperative that more detailed study and inferences should be carried out on the basis of complex interactions of the coexisting multiple typology footings.

- There are instances of usage of special types of shallow foundations on horizontal ground, such as skirted foundations or foundations with micro-piles, in order to enhance the bearing capacity of the basic typologies of shallow foundation resting on horizontal ground. It would be interesting to investigate whether such adoptions can lead to enhanced bearing capacity and lead to a sustainable foundation system on the hill-slopes.

- In the analysis, only unreinforced slope has been considered for determination of bearing capacity and failure mechanism of shallow footing located on slope. Therefore, the overall response of shallow footings on reinforced soil slope need to be inspected.

- In the numerical simulation, only homogeneous soil has been taken into account. The effect of stratification of soil layers or spatial variation of soil properties on bearing capacity of footing resting on sloping ground has to be investigated.

- A large number of hill-terrain inhabitations suffer from the progressive construction that involves development of buildings, roads or railways through the inhabited areas. Such activities involve cutting and filling strategies, which may lead to destabilization due to either removal basal material or addition of surcharge weight on the existing structures. It would be intriguing to scrutiny such aspects in detail so that a proper planning strategy may be developed focussing on the progressive development of the habitations in hilly terrains without the jeopardizing the existing habitations.

* Although the present investigation highlighted the influence of soil dilatancy on the bearing capacity and failure mechanism, an in-depth analysis regarding the same for footings on slopes has not been investigated. Such study is important to understand the deformation of the slope face due to dilatancy and its implication on the overall stability and foundation failure.

REFERENCES

1. AASHTO (American Association of State Highway and Transportation Officials) (2012) Specifications of LRFD bridge design. Washington, DC, USA.
2. Arora KR (2011) Soil Mechanics and Foundation Engineering. Standard Publishers Distributors, Nai Sarak, Delhi, India.
3. Ausilio E, Conte E (2005) Influence of groundwater on the bearing capacity of shallow foundations. Canadian Geotechnical Journal 42: 663–672.
4. Azzam WR, El-Wakil AZ (2015) Experimental and numerical studies of circular footing resting on confined granular subgrade adjacent to slope. International Journal of Geomechanics, ASCE 16(1): 1-15.
5. Azzam WR, Farouk A (2010) Experimental and numerical studies of sand slopes loaded with skirted strip footing. Electronic Journal of Geotechnical Engineering 15(H): 795-812.
6. Bakir N (1993) Etude sur modeles centrifuges de la capacite portante de fondations superficielles (in French), Doctoral Thesis, Ecole Centrale de Nantes, France.
7. Bauer GE, Shields DH, Scott JD, Gruspier JE (1981) Bearing capacity of footing in granular slope. Proceedings of 11th International Conference on Soil Mechanics and Foundation Engineering, Balkema, Rotterdam, Netherlands, 2: 33-36.
8. Behera RN, Patra CR, Sivakugan N, Das BM (2013) Prediction of ultimate bearing capacity of eccentrically inclined loaded strip footing by ANN. Part I, International Journal of Geotechnical Engineering 7(1): 36-44.
9. Behera RN, Patra CR, Sivakugan N, Das BM (2013) Prediction of ultimate bearing capacity of eccentrically inclined loaded strip footing by ANN. Part II, International Journal of Geotechnical Engineering 7(2): 165-172.

10. Benmebarek S, Remadna MS, Benmebarek N, Belounar L (2012) Numerical evaluation of the bearing capacity factor N'_γ of ring footings. Computers and Geotechnics 44: 132–138.

11. Bolton MD, Lau CK (1993) Vertical bearing capacity factors for circular and strip footings on Mohr–Coulomb soil. Canadian Geotechnical Journal 30: 1024–1033.

12. Castelli F, Lentini V (2012) Evaluation of the bearing capacity of footings on slopes. International Journal of Physical Modelling in Geotechnics 12(3): 112-118.

13. Cerato AB, Lutenegger AJ (2006) Bearing capacity of square and circular footings on a finite layer of granular soil underlain by a rigid base. Journal of Geotechnical and Geoenvironmental Engineering, ASCE 132(11): 1496–1501.

14. Chakraborty D, Kumar J (2013) Bearing capacity of foundations on slopes. Geomechanics and Geoengineering 8(4): 274-285.

15. Chen WF (2010) Limit Analysis and Soil Plasticity. J. Ross Publishing, Noida.

16. Clark JI, McKeown S, Crawford CB (1988) Field measurements of the behavior of inclined footings on a natural slope. Canadian Geotechnical Journal 25(4): 662-674.

17. Das BM (2009) Shallow Foundations. CRC Press, Taylor and Francis Group, New York.

18. Das BM, Larbi-Cherif S (1983) Bearing capacity of two closely-spaced shallow foundations on sand. Soils and Foundations 23(1): 1–7.

19. Das SK, Basudhar PK (2006) Undrained lateral load capacity of piles in clay using artificial neural network. Computers and Geotechnics 33: 454-459.

20. Das SK, Basudhar PK (2008) Prediction of residual friction angle of clay using artificial neural network. Engineering Geology 100: 142-145.

21. Das SK, Samui P, Sabat AK (2011) Application of artificial intelligence to maximum dry density and unconfined compressive strength of cement stabilized soil. Geotechnical and Geological Engineering 29: 329-342.

22. Das SK, Samui P, Sabat AK (2012) Prediction of field hydraulic conductivity of clay liners using an artificial neural network and support vector machine. International Journal of Geomechanics 12: 606-611.

23. de-Buhan P, Garnier D (1998) Three dimensional bearing capacity analysis of a foundation near slope. Soils and Foundations 38(3): 153-163.

24. Demuth HB, Hagan MT (1996) Neural Network Design. PWS Publishing Company, Boston.

25. Drescher A, Detournay E (1993) Limit load in translational failure mechanisms for associative and non-associative materials. Geotechnique 43(3): 443–456.

26. El-saied AE (2014) Performance of footing with single side micro-piles adjacent to slopes. Alexandria Engineering Journal 53(4): 903-910.

27. Erickson HL, Drescher A (2002) Bearing capacity of circular footings. Journal of Geotechnical and Geoenvironmental Engineering, ASCE 128(1): 38–43.

28. Erzin, Y, Gumaste SD, Gupta AK, Singh DN (2009) Artificial neural network (ANN) models for determining hydraulic conductivity of compacted fine-grained soils. Canadian Geotechnical Journal 46: 955-968.

29. Finno RJ, Harris WW, Mooney MA, Viggiani G (1996) Strain localization and undrained steady state of sand. Journal of Geotechnical Engineering, ASCE 122(6): 462-473.

30. Garson GD (1991) Interpreting neural-network connection weights. Artificial Intelligence Expert 6(7): 47-51.

31. Gemperline MC (1988) Centrifuge modeling of shallow foundation. Proceedings of the ASCE Spring Convention, ASCE 45-70.

32. Georgiadis K (2010) Undrained bearing capacity of strip footings on slopes. Journal of Geotechnical and Geoenvironmental Engineering, ASCE 136(5): 677-685.

33. GeoStudio (2007). GeoSlope International Limited.

34. Ghaboussi J, Sidarta DE, Lade PV (1994) Neural network based modelling in geomechanics. Computer Methods and Advances in Geomechanics, Balkema, Rotterdam Publishing 153-164.

35. Giroud JP (1971) Force portant d'une foundation sur une pente. A.I.T.B.T.P. juillet-aout, Serie: Therie et methods de calcul, 142: 283-284.

36. Goh ATC (1994) Seismic liquefaction potential assessed by neural networks. Journal of Geotechnical and Geoenvironmental Engineering, ASCE 120(9): 1467-1480.

37. Guo P, Stolle DFE (2013) Coupled analysis of bifurcation and shear band in saturated soils. Soils and Foundations 53(4): 525-539.

38. Han C, Vardoulakis I (1991) Plane-strain compression experiments on water-saturated fine-grained sand. Geotechnique 41(1): 49–78.

39. Hanna A, Rahman AME (1990) Ultimate bearing capacity of triangular shell strip footings on sand. Journal of Geotechnical and Geoenvironmental Engineering, ASCE 116(12): 1851–1863.

40. Hanna AM (1982) Bearing capacity of foundations on a weak sand layer overlaying a strong deposit. Canadian Geotechnical Journal 19(3): 392–396.

41. Hanna AM, Meyerhof GG (1981) Experimental evaluation of bearing capacity of footings subjected to inclined loads. Canadian Geotechnical Journal 18(4): 599–603.

42. Hansen JB (1970) A revised and extended formula for bearing capacity. Danish Geotechnical Institute, Bulletin 28: 5-11.

43. Hjiaj M, Lyamin AV, Sloan SW (2005) Numerical limit analysis solutions for the bearing capacity factor $N\gamma$. International Journal of Solids and Structures 42 (5): 1681–1704.

44. Huang CC, Menq FY (1997) Deep-footing and wide-slab effects in reinforced sandy ground. Journal of Geotechnical and Geoenvironmental Engineering, ASCE 123(1): 30-36.

45. IS (Indian Standard) (1986) IS 1904: Code of practice for design and construction of foundations in soils: general requirements. BIS, New Delhi, India.

46. IS (Indian Standard) (1995) IS 802-1-1: Use of structural steel in overhead transmission line tower - code of practice. BIS, New Delhi, India.

47. Islam MA, Ganendran CT (2013) Slope stability under cyclic foundation loading - effect of loading frequency. Geo-Congress, ASCE 750-758.

48. Jao M, Ahmed F, Muninarayana G, Wang MC (2008) Stability of eccentrically loaded footings on slopes, Geomechanics and Geoengineering 3(2): 107-111.

49. Keskin MS, Laman M (2013) Model studies of bearing capacity of strip footing on sand slope. KSCE Journal of Civil Engineering 17(4): 699-711.

50. Koch C (1999) Biophysics of Computation: Information Processing in Single Neuron, Oxford University Press, New York.

51. Kodaka T, Higo Y, Kimoto S, Oka F (2007) Effects of sample shape on the strain localization of water saturated clay. International Journal for Analytical and Numerical Methods in Geomechanics. 31: 483-521.

52. Kumar J (2009) The variation of N_γ with footing roughness using the method of characteristics. International Journal for Numerical and Analytical Methods in Geomechanics 33: 275–284.

53. Kumar J, Rao VBKM (2003) Seismic bearing capacity of foundations on slopes. Geotechnique 53(3): 347–361.

54. Kumar S (2013) Neural Networks, McGraw Hill Education (India) Private Limited, New Delhi.

55. Kuo YL, Jaksa MB, Lyamin AV, Kaggwa WS (2009) ANN-based model for predicting the bearing capacity of strip footing on multi-layered cohesive soil. Computers and Geotechnics 36: 503-516.

56. Kusakabe O, Kimura T, Yamaguchi H (1981) Bearing capacity of slopes under strip loads on the top surfaces. Soils and Foundations 21(4): 29-40.

57. Lebegue Y (1973) Essais de fondations super ficielles sur talus. Proceedings of 8th International Conference on Soil Mechanics and Foundation Engineering, 4(3): 313.

58. Lee MI, Lee HJ (1996) Prediction of pile bearing capacity using neural networks. Computers and Geotechnics 18(3): 189-200.

59. Leshchinsky B, Xie Y (2017) Bearing capacity of footings placed adjacent to c′–φ′ slopes. Journal of Geotechnical and Geoenvironmental Engineering, ASCE 141(6): 1–13.

60. Loukidis D, Chakraborty T, Salgado R (2008) Bearing capacity of strip footings on purely frictional soil under eccentric and inclined loads. Canadian Geotechnical Journal 45: 768–787.

61. Loukidis D, Salgado R (2009) Bearing capacity of strip and circular footings in sand using finite elements. Computers and Geotechnics 36: 871–879.

62. Lu X, Huang M, Qian J (2011) The onset of strain localization in cross-anisotropic soils under true triaxial condition. Soils and Foundations 51(4): 693-700.

63. Manoharan N, Dasgupta SP (1995) Bearing capacity of surface footings by finite elements. Computer and Structure 54(4): 563–586.

64. Manzari MT, Nour MA (2000) Significance of soil dilatancy in slope stability analysis. Journal of Geotechnical and Geoenvironmental Engineering, ASCE 126(1): 75–80.

65. Manzari MT, Nour MA (2000) Significance of soil dilatancy in slope stability analysis. Journal of Geotechnical and Geoenvironmental Engineering, ASCE 126(1): 75-80.

66. Mayne PW, Kulhawy FH (1982) K_0-OCR relationships in soils. Journal of the Geotechnical Engineering Division, ASCE 108(6): 851-872.

67. Meyerhof GG (1951) The ultimate bearing capacity of foundations. Geotechnique 2: 301-332.

68. Meyerhof GG (1957) The ultimate bearing capacity of foundation on slopes. Proceedings of 4th International Conference on Soil Mechanics and Foundation Engineering I: 384-386.

69. Meyerhof GG (1963) Some recent research on the bearing capacity of foundations. Canadian Geotechnical Journal 1(1): 16-26.

70. Meyerhof GG (1978) Bearing capacity of anisotropic cohesionless soil. Canadian Geotechnical Journal 15(4): 592–595.

71. Meyerhof GG, Koumoto T (1987) Inclination factors for bearing capacity of shallow footings. Journal of Geotechnical and Geoenvironmental Engineering, ASCE 113(9): 1013–1018.

72. Michalowski RL (1997) An estimate of the influence of soil weight on bearing capacity using limit analysis. Soil and Foundation 37(4): 57-64.

73. Michalowski RL, Shi L (1995) Bearing capacity of footings over two-layer foundation soils. Journal of Geotechnical and Geoenvironmental Engineering, ASCE 121(5): 421–428.

74. Michalowski RL, Shi L (2003) Deformation patterns of reinforced foundation sand at failure. Journal of Geotechnical and Geoenvironmental Engineering, ASCE 129(6): 439–449.

75. Mishra AK, Kumar B, Dutta J (2016) Prediction of hydraulic conductivity of soil bentonite mixture using hybrid-ANN approach. Journal of Environmental Informatics 27(2): 98-105.

76. Mittal S, Shah MY, Verma NK (2009) Experimental Study of Footings on Reinforced Earth Slopes." International Journal of Geotechnical Engineering 3: 251–260.

77. Mizuno T, Tokumitsu Y, Kawakami H (1960) On the bearing capacity of a slope on cohesionless soil. Japanese Society of Soil Mechanics and Foundation Engineering 1(2): 30-37.

78. Moayedi H, Hayati S (2018) Modelling and optimization of ultimate bearing capacity of strip footing near a slope by soft computing methods. Applied Soft Computing 66: 208-219.

79. Mokni M, Desrues J (1998) Strain localization measurements in undrained plane-strain biaxial tests on Hostun RF sand. Mechanics of Cohesive Frictional Materials 4: 419-441.

80. Momeni E, Nazir R, Armaghani D.J. Maizir H (2014) Prediction of pile bearing capacity using a hybrid genetic algorithm-based ANN. Measurement 57: 122-131.

81. Murthy VNS (2008) Principles and Practices of Soil Mechanics and Foundation Engineering. Marcel Dekker Inc, New York.

82. Naderi E, Hataf H (2014) Model testing and numerical investigation of interference effect of closely spaced ring and circular footings on reinforced sand. Geotextiles and Geomembranes 42: 191-200.

83. Nainegali LS, Basudhar PK, Ghosh P (2013) Interference of two asymmetric closely spaced strip footings resting on non-homogeneous and linearly elastic soil bed. International Journal of Geomechanics 13(6): 840-851.

84. Narita K, Yamaguchi H (1990) Bearing capacity analysis of foundations on slopes by using log-spiral sliding surfaces. Japanese Society of Soil Mechanics and Foundation Engineering. 30(3): 144-152.

85. Nasr AM (2014) Behaviour of strip footing on fiber-reinforced cemented sand adjacent to sheet pile wall. Geotextiles Geomembranes 42: 599–610.

86. NDMA (2013) Catalogue of building typologies in India: seismic vulnerability assessment of building types in India. A report submitted by the Seismic Vulnerability Project Group

of IIT Bombay, IIT Guwahati, IIT Kharagpur, IIT Madras and IIT Roorkee to the National Disaster Management Authority.

87. Noorzaei J, Hakim SJS, Jaafar MS (2008) An approach to predict ultimate bearing capacity of surface footings using artificial neural network. Indian Geotechnical Journal 38(4): 513-526.

88. Nova R, Montrasio L (1991) Settlements of shallow foundations on sand. Geotechnique 41(2): 243–256.

89. PLAXIS (2015) Reference Manual, 2D-Version 2015.02, Plaxis, Delft, The Netherlands.

90. PLAXIS (2015) Scientific Manual, 2D-Version 2015.02, Plaxis, Delft, The Netherlands.

91. PLAXIS (2017) Reference Manual, 3D-Version AE.01, Plaxis, Delft, The Netherlands.

92. Reddy AS, Singh AK, Karnik SS (1991) Bearing capacity of clays whose cohesion increases linearly with depth. Journal of Geotechnical and Geoenvironmental Engineering, ASCE 117(2): 348–353.

93. Rudnicki JW, Rice JR (1975) Conditions for localization of deformation in pressure-sensitive dilative materials. Journal of the Mechanics and Physics of Solids 23: 371-394.

94. Salgado R (2008) The Engineering of Foundations. McGraw-Hill, New York.

95. Saran S, Sud VK, Handa SC (1989) Bearing capacity of footings adjacent to slopes. Journal of Geotechnical Engineering, ASCE 115(4): 553-573.

96. Shahin MA, Maier HR, Jaksa MB (2002) Predicting settlement of shallow foundations using neural networks. Journal of Geotechnical and Geoenvironmental Engineering, ASCE 128(9): 785-793.

97. Shiau JS, Lyamin AV, Sloan SW (2003) Bearing capacity of a sand layer on clay by finite element limit analysis. Canadian Geotechnical Journal 40: 900–915.

98. Shiau JS, Merifield RS, Lyamin AV, Sloan SW (2011) Undrained stability of footings on slopes. International Journal of Geomechanics, ASCE 11(5): 381-390.

99. Shields D, Chandler N, Garnier J (1990) Bearing capacity of foundation in slopes. Journal of Geotechnical Engineering 116(3): 528-537.

100. Shields DH, Scott JD, Bauer GE, Deschenes JH, Barsvary AK (1977) Bearing capacity of foundation near slopes. Proceedings of the 10th International Conference on Soil Mechanics and Foundation Engineering. Japanese Society of Soil Mechanics and Foundation Engineering, Tokyo, Japan, 1: 715–720.

101. Shukla RP, Jakka RS (2016) Discussion on Experimental and numerical studies of circular footing resting on confined granular subgrade adjacent to slope by WR Azzam and AZ El-Wakil. International Journal of Geomechanics, ASCE 17(2): 1-3.

102. Siva Reddy A, Mogaliah G (1976) Bearing capacity of strip footings on partly saturated soils. Indian Geotechnical Journal 6(4): 220-245.

103. Skempton AW (1951) The bearing capacity of clay. Building Research Congress, England.

104. Stuart JG (1962) Interference between foundations, with special reference to surface footings in sand. Geotechnique 12(1): 15-21.

105. Terzaghi K (1943) Theoretical Soil Mechanics. John Wiley and Sons Inc., New York, USA.

106. Van Baars S (2015) The Bearing Capacity of Footings on Cohesionless Soils. The Electronic Journal of Geotechnical Engineering 20: 12945-12955.

107. Van Baars S (2016) Failure mechanisms and corresponding shape factors of shallow foundations. 4th International Conference on New Developments in Soil Mechanics and Geotechnical Engineering, Nicosia, Cyprus 1-7.

108. Van Baars S (2018) Numerical check of the Meyerhof bearing capacity equation for shallow foundations. Innovative Infrastructure Solutions 3: 9.

109. Vardoulakis I, Sulem J (1995) Bifurcation Analysis in Geomechanics. Chapman and Hall, London.

110. Vermeer PA, de Borst R (1984) Non-associated plasticity for soils, concrete and rock. Heron 29(3): 1–64.

111. Vesic AS (1973) Analysis of ultimate loads of shallow foundation. Journal of Soil Mechanics Found Division, ASCE 99(SM1): 45-73.

112. Vesic AS (1975) Bearing capacity of shallow foundations. Foundation Engineering Handbook, New York, Van Nostrand Reinhold, 121.

113. Viji VK, Lissy KF, Sobha C, Benny MA (2013) Predictions on compaction characteristics of fly ashes using regression analysis and artificial neural network analysis. International Journal of Geotechnical Engineering 7(3): 282–291.

114. Wood, R. D. (2004) Geotechnical Modeling. E&FN Spon Press, London, UK.

115. Xiao-Li Y, Nai-Zheng G, Lian-Heng Z, Jin-Feng Z (2007) Influences of non-associated flow rules on seismic bearing capacity factors of strip footing on soil slope by energy dissipation method. Journal of Central South University and Technology 14: 842–847.

116. Yang F, Zheng XC, Zhao LH, Tan YG (2016) Ultimate bearing capacity of a strip footing placed on sand with a rigid basement. Computers and Geotechnics 77:115–119.

117. Yin JH, Wang YJ, Selvadurai APS (2001) Influence of non-associativity on the bearing capacity of a strip footing. Journal of Geotechnical and Geoenvironmental Engineering, ASCE 127(11): 985–989.

118. Zhao L, Yang F, Dan H (2014) The influence of horizontal confinement on the bearing capacity factor N γ of smooth strip footing. Computers and Geotechnics 61: 127–131.

119. Zhou H, Zheng G, Yin X, Jir R, Yang X (2018) The bearing capacity and failure mechanism of a vertically loaded strip footing placed on the top of slopes. Computers and Geotechnics 94: 12-21.

LIST OF PUBLICATIONS FROM THIS DISSERTATION

Journal (Published)

1. Acharyya R, Dey A (2017) Finite element investigation of the bearing capacity of square footings resting on sloping ground. INAE Letters 2(3): 97-105.
2. Acharyya R, Dey A, Kumar B (2018) Finite element and ANN-based prediction of bearing capacity of square footing resting on the crest of *c*-*φ* soil slope. International Journal of Geotechnical Engineering. DOI: 10.1080/19386362.2018.1435022.
3. Acharyy R, Dey A (2018) Assessment of failure mechanism of a strip footing on horizontal ground considering flow rules. Innovative Infrastructure Solution 3(49): 1-16.
4. Acharyya R, Dey A (2018) Importance of dilatancy on the evolution of failure mechanism of a strip footing resting on horizontal ground. INAE Letters 3(3): 131-142.
5. Acharyya R, Dey A (2018) Assessment of bearing capacity for strip footing located near sloping surface considering ANN-model. Neural Computing and Applications. DOI: 10.1007/s00521-018-3661-4.
6. Acharyya R, Dey A (2018) Assessment of bearing capacity of interfering strip footings located near sloping surface considering Ann-technique. Journal of Mountain Science 15(12): 2766–2780.
7. Acharyya R, Dey A (2018) Assessment of bearing capacity and failure mechanism of single and interfering strip footings on sloping ground. International Journal of Geotechnical Engineering. DOI: 10.1080/19386362.2018.1540099.

Conference (Published)

1. Acharyya R, Dey A (2018) Evaluation of slip mechanism beneath the shallow footing resting on plane ground by altering flow-rules. Advanced Construction And Computational Tools In Geotechniques – Practice To Theory. IGS Kolkata Chapter, Kolkata, West Bengal, India, pp. 1-8.
2. Acharyya R, Dey A (2017) Bearing capacity of strip footing resting on the crest of a slope: FE Simulation. Indian Geotechnical Conference: IGC 2017, Pune, India, pp. 1-4.
3. Acharyya R, Dey A (2016) Square footings on unreinforced sandy slopes: Numerical modeling using PLAXIS 3D. National Seminar on Geotechnics for Infrastructure Development, Indian Geotechnical Society, Kolkata Chapter, West Bengal, India, pp. 1-8.
4. Acharyya R, Dey A (2015) Site characterization and bearing capacity estimation for a school building located on hillslope. Indian Geotechnical Conference: IGC 2015, Pune, India, pp. 1-10.
5. Anand A, Acharyya R, Dey A (2014) Finite Element Analysis of Footings on Unreinforced Slopes. Indian Geotechnical Conference: IGC-2014, Kakinada, India, pp. 1490-1497.
6. Anand A, Acharyya R, Dey A (2014) Foundations on Unreinforced slopes: Numerical modeling using GeoStudio. National Seminar on Geotechnique Today: Modeling, Prediction and Construction, Indian Geotechnical Society, Kolkata Chapter, West Bengal, India, pp. 64-68.

Journal (Under review)

1. Acharyya R, Dey A, Kumar B (2018) Prediction of bearing capacity of strip footing resting on sloping surface using multi-gene genetic programming. Soft Computing.
2. Acharyya R, Dey A (2019) Bearing Capacity and Failure Mechanism of Shallow Footings on Slopes: A State-of-the-Art Review. International Journal of Geotechnical Engineering.
3. Acharyya R, Dey A (2019) Suitability of the typology of building foundations on hillslopes. Indian Geotechnical Journal.